MODELLING OF RADIOACTIVE PARTICLE RESUSPENSION AFTER A DIRTY BOMB EVENT

by

Sharman Perera, P.Eng.

A thesis submitted to the
School of Graduate and Postdoctoral Studies in partial
fulfillment of the requirements for the degree of

Doctor of Philosophy in Nuclear Engineering

The Faculty of Engineering and Applied Science

University of Ontario Institute of Technology (Ontario Tech University)

Oshawa, Ontario, Canada

Ph.D. thesis examination information

Submitted by: Sharman Perera

Doctor of Philosophy in Nuclear Engineering

Thesis title: Modelling of Radioactive Particle Resuspension after a Dirty Bomb event

An oral defense of this thesis took place on July 12, 2022, in front of the following examining committee:

Examining Committee:

Chair of Examining Committee:	Dr. Jennifer McKellar, Ontario Tech University
Research Supervisor:	Dr. Edward J. Waller, Ontario Tech University
Examining Committee Member:	Dr. Anthony Waker, Ontario Tech University
Examining Committee Member:	Dr. Igor Pioro, Ontario Tech University
University Examiner:	Dr. Lennaert van Veen, Ontario Tech University
External Examiner:	Dr. Luke Lebel, Canadian Nuclear Laboratories

The above committee determined that the thesis is acceptable in form and content and that a satisfactory knowledge of the field covered by the thesis was demonstrated by the candidate during an oral examination. A signed copy of the Certificate of Approval is available from the School of Graduate and Postdoctoral Studies.

Abstract

The primary hazard of a Dirty Bomb emanates not from the initial detonation but from the subsequent re-suspension of deposited radioactive particles. Although radiological contamination is substantial on surfaces initially, the biological risk intensifies through ingestion or inhalation due to re-suspension. Experimental simulations in a 10 m wind chamber unveiled average bin-by-bin resuspension factors for particle sizes between 0.9 and 6.5 µm downstream from the initial fallout. Calculated values were 4.12E-05 × (1 ± 46.8%) m^{-1} and 4.56E-05 × (1 ± 79.5%) m^{-1}, indicating the magnitude of the resuspension process. In a prototypical study using data from a full-scale dirty bomb experiment by DRDC Canada, maximum committed effective inhalation radiation doses were calculated as 1.89E+02 µSv for the public and 1.89E-2 µSv for first responders, considering a 35.2 × (1 ± 10%) GBq dirty bomb.

Subsequently, Computational Fluid Dynamics (CFD) was applied via FLUENT software, incorporating Regional and Global models to simulate particle resuspension. The unsteady Large Eddy Simulation viscous model with Smagorinsky-Lilly Subgrid-Scale models effectively captured turbulent flow dynamics. CFD resuspension factors at specific locations were computed as 4.14E-04 × (1 ± 13.3%) m^{-1} and 4.01E-4 × (1 ± 16.3%) m^{-1} for particle sizes between 0.9 and 6.75 µm. Notably, an order of magnitude difference between CFD and experimental results highlights the intricacies in modelling particle resuspension.

Future refinements may include incorporating surface roughness elements in both downstream and transverse directions in the Regional CFD model to capture particle saltation, enhancing resuspension predictions' accuracy, and introducing a multilayer resuspension model. This study underscores the complex nature of Dirty Bomb scenarios, emphasizing the need for a holistic understanding that combines experimental insights with advanced computational modelling for effective risk assessment and response planning.

Keywords: Resuspension, RDD, Dirty Bomb, CFD, Radiological

Author's declaration

I hereby declare that this thesis consists of the original work that I have authored. This is a true copy of the thesis, including any required final revisions, as accepted by my examiners.

I authorize the University of Ontario Institute of Technology (Ontario Tech University) to lend this thesis to other institutions or individuals for the purpose of scholarly research. I further authorize the University of Ontario Institute of Technology (Ontario Tech University) to reproduce this thesis by photocopying or by other means, in total or in part, at the request of other institutions or individuals for the purpose of scholarly research. I understand that my thesis will be made electronically available to the public.

Sharman Perera, P.Eng.

Statements of contributions

The work described in Chapter 3 was performed at Wehrwissenschaftliches Institut für Schutztechnologien (WIS) facility in Munster, Germany, managed by Dr. Schneider, N and the Aerosol Research lab at Ontario Tech University, Oshawa, Ontario, managed by Dr. Waller, E. I was responsible for setting up the wind chamber, running resuspension tests with non-radioactive La_2O_3 powder during the WIS facility experiment, and measuring powder particle size distributions using the analytical instrumentation available at the Aerosol laboratory facility at Ontario Tech University.

The experimental work and data analysis presented in Chapter 3 has been published as:

- Perera, S., Waller, E., & Akhtar, A. (2015). Experimental Modeling of Wind-Driven bin-by-bin Resuspension Factors of Freshly Fallen Radionuclides After an Energetic Release From a Radiological Dispersal Device. ASME, Journal of Nuclear and Radiation Science, 1(1):011005-011005-10. doi:10.1115/1.4026390.
- Akhtar, A., Perera, S., & Waller, E. (2013). Investigation of the variation of resuspension factor for multiple wind profiles. 38th Annual CNS/CAN Student Conference at the 19th Annual PBNC.
- Perera, S., & Waller, E. (2013). Experimental modelling of radioactive particle resuspension. Canadian Nuclear Society, 34th Annual Conference.

The particle analysis techniques developed during the experimental work presented in Chapter 3 of the thesis were used to contaminate the nasal swabs used in the following publications:

- Ko, R., Shew. C., Perera, S., Mattson, K., Nielsen, K., Kelly, D., Waller, & E., Li, C. (2014). Investigation of internal radionuclide contamination from the analysis of nasal swabs and facial swipes, Journal of Radioanalytical and Nuclear Chemistry, 301(1), 147-152.

- Ko, R, Li, C, Shew, C, Waller, E, & Perera, S. (2012). The efficacy of facial swipes and swabs for determination of lung deposition in simulated aerosol exposure, American Nuclear Society International Topical Conference, 9th International Conference on Methods and Applications of Radioanalytical Chemistry.

- Waller, E., Shew, C. & Perera, S. (2012). Experiments in Support of Determining Orofacial-to-Lung Ratio (OLR) for Radiological Dispersal Device Events. Health Physics Society 57th Annual Meeting.

- Weijia, L., Skinner, R., Megna, K., Chen, J., Perera, S., Murimboh, J., Waller, E., Erhardt, L., & Cornett, R. J. (2009). In vitro dissolution study of uranium dioxide and uranium ore with different particle sizes in simulated lung fluid. Journal of Radioanalytical and Nuclear Chemistry, 279(1), 209-218.

Initial literature review and aerosol dispersal studies discussed in Chapter 1 of the thesis were published in the following conference proceeding:

- Waller, E., & Perera, S. (2008). Assessing Risk from Low Energy Radionuclide Aerosol Dispersal. 12th International Congress of the International Radiation Protection Association

- Li, C., Skinner, R., Chen, J., Kiser, S., Cornett, R., Megna, K., Perera, S., Waller, E., Murimboh, J. & Erhardt, L. (2007). Uranium in Natural Water and in Lung Fluid, Canadian Society of Chemistry Conference (CSC2007).

- Waller, E., Perera, S., Satgunanathan, R., Erhardt, L. & Cousins, T. (2007). Phenomenology of Resuspension: Radioactive Particles and Aerosols – Implications to Radiological Dispersal Device Events. DRDC-Ottawa Technical Report.

- Waller, E., Perera, S., Erhardt, L. & Haslip, D. (2007). Risk from Low Energy Radionuclide Dispersal. Health Physics Society 52nd Annual Meeting.

The papers below present the initial work conducted at the WIS facility to establish the experimental procedure used in the thesis.

- Waller, E., Perera, S., Chaput, J., Roberts, C., Kearnan, A. & Hart, S. (2007). Analysis of the $^{152m}Eu_2O_3$ Resuspension Experiments Conducted at the WIS Decontamination Facility in Munster, Germany. DRDC-O, UOIT-ARRL-01-07

- Waller, E., Perera, S., Megna, K., McGill, K. & Satugunanathan, R. (2007). Experimental Characterization of Risk from Radiological Dispersal Devices – Investigation on Non-Explosive Dispersal of the Ceramic Compounds $SrTiO_3$ and CeO2. UOIT-ARRL-03-07 for Department of National Defence.

- Satgunanathan, R., Waller, E. & Perera, S. (2007). Phenomenology of Resuspension: Radioactive Particles and Aerosols - Implications to Radiological Dispersal Device (RDD) Events. CRTI, UOIT.

- Waller, E., Perera, S., Satgunanathan, R. & Megna, K. (2006). Risk Assessment from Non-Explosive Aerosol Dispersal of Commonly Utilized Radioisotopes – CsCl and $CoCl_2$, SAIC Canada & CRTI, UOIT.

The 2D CFD modelling of the Radioactive Particle resuspension presented in Appendix B was published in the following conference proceedings:

- Perera, S, Waller, E, Akhtar, A, & Doxtator, A. (2015), 2D CFD Modelling of Radioactive particle Resuspension, 39th CNS/CNA Student Conference at 35th Annual CNS Conference.

- Perera, S, & Waller, E. (2010). Computational Modeling of Radionuclide Resuspension, European Nuclear Conference.

Acknowledgment

I would like first to thank my supervisory committee members, Dr. Waller, E., Dr. Pioro, I. and Dr. Waker, T., chair of the examination committee, Dr. McKellar, J., external examiner, Dr. Lebel L., and university examiner, Dr. van Veen, L. They have provided helpful feedback and support throughout my academic life at OnTechU. Second, I would like to thank Satgunanathan, R. for his help with the literature review process at the beginning of this project and Dr. Cousins, T., Dr. Schneider, N., Hill J., Rambousky, R., Shinn, J., Desrosiers, M., Jones, T., Brown, J., Chaput, J. for their help with experiments conducted at the WIS facility, in Germany. Third, I would like to thank the founding dean of FESNS, Dr. Bereznai, G., for encouraging me to start my Ph.D. Also, I would like to thank Dr. Meneley, D. (1935-2018), Dr. Lewis, B., Dr. Tokuhiro, A., Goldman, G., and my thesis supervisor Dr. Waller, E., for their continuous support and guidance. Fourth, I would like to thank my students, colleagues and friends, Akhtar A., Ali, F., Brown, C., Brown, K., Chen, J., Cornett, R., Doxtator, A., Erhardt, L., Hart, S., Haslip, D., Kearnan, A., Kelly, D., Kiser, S., Ko, R., Krowchuk, Z., Labana, T., Li, C., Mattson, K., McGill, K., Megna, K., Murimboh, J., Nielsen, K., Roberts, C., Shew, C., Skinner, R., Dr. Walsh, P., Weijia, L. They have helped me or published with me on topics related to my Ph.D. thesis work.

My special thanks go to my wife, Suareen, P., and my children, Kaylan P. and Jaydan P. They have supported me and have made countless sacrifices to get me to this point. In addition, my parents, Mervin P. (1939-2022) and Beatrice P. (1942-2022), deserve special thanks for their support and encouragement.

Funding for this work was provided, in part, by the Chemical, Biological, Radiological and Nuclear (CBRN) Research and Technology Initiative, Defense R&D Canada, and the Natural Sciences and Engineering Research Council of Canada (NSERC).

Table of Contents

List of tables

List of Figures

Nomenclature

Symbols and Abbreviations

′	fluctuating component around the mean
~	Instantaneous quantity (tide over a symbol) and Einstein summation convention
–	mean quantity (bar over a symbol)
*	coefficient of friction
A	area, m^2
a	parameter, m
b	constant
d	days
B	force due to buoyancy, N
C	airborne concentration, μg m^{-3} or Bq m^{-3}or coefficient
C_a	concentration of species in air, g m^{-3} or Bq m^{-3}
C_d	drag coefficient
C_s	concentration of species in soil, g g^{-1} or Bq g^{-1}
D	cross-diffusion (for *k*, kg m^{-1} s^{-3} and for ω, kg m^{-3} s^{-2}) or hydraulic diameter, m
d	diameter, μm
DF	deposition fraction
e	coefficient of restitution
F	force, N or blending functions used in *k*-ω, SST model
G	gravitational acceleration, m s^{-2} or amplitude of fluctuating velocity component (m s^{-1}), the generation of turbulent kinetic energy, specific dissipation rate of turbulence, effective diffusivities for *k*-ω model
gsd	geometric standard deviation
H	height, m
I	turbulent intensity, %

K or RF	resuspension factor, m^{-1}
k	constant, the average thickness of roughness elements, μm or turbulent kinetic energy, $m^2\ s^{-2}$ per unit mass
L	length, m
l	turbulent length scale, m
l_s	Kolmogorov length scale
m	mass, kg
n	number of particles in a bin
N	total number of particles
p	perimeter, m or pressure, Pa
r	radius of a particle, m or radius of a vortex, m
R	resuspension flux, μg $m^{-2}\ s^{-1}$ or Bq $m^{-2}\ s^{-1}$ or a constant use in SST *k-ω* turbulence model or gas constant for air ~ 29.04 J $kg^{-1}\ K^{-1}$
R_{ij}	Reynolds stress tensor
S	user-defined source term in SST *k-ω* turbulence model or Strain rate magnitude/strain invariant (s^{-1}), surface contamination or activity density on the ground, μg m^{-2} or Bq m^{-2} respectively or strain rate magnitude, s^{-1}
SE	equivalent soil concentration, kg m^{-3} or Bq m^{-3}
T	time after deposition for Garland formula, days or Temperature, K
t	time, s
U	continuous flow velocity, m s^{-1}
u	velocity, m s^{-1}
U_0 or U^*	friction velocity, m s^{-1}
u_P	particle velocity, m s^{-1}
U_{PL}	particle launching velocity, m s^{-1}
v	particle velocity, m s^{-1}
Vg	deposited velocity, m s^{-1}
W	force due to gravity, N, Width
Y	dissipation rate term in SST *k-ω* turbulence model

y	distance to the next surface, m or time in years
z	elevation, m
Z	symbol for integers such as {..., -3, -2, -1, 0, 1, 2, 3...}
z_0	roughness length, m

Greek letters

ρ	constant mass density, kg m^{-3}
ε	dissipation rate per unit mass of fluid, m^2 s^{-3}
σ	standard deviation
ν	kinematic viscosity, m^2 s^{-1}
τ	shear stress, Pa
κ	von Kármán constant [~ 0.41]
Γ	effective diffusivity, Pa s
Φ_1	a function use in SST *k*-ω turbulence model
Λ	resuspension rate, s^{-1}
α	constant use in SST *k*-ω turbulence model
β	constant use in SST *k*-ω turbulence model
γ	adiabatic index/isentropic expansion factor (C_p/C_v) ~ 1.4
ϕ	shape factor of a particle
δ_{ij}	Kronecker delta
μ	dynamic viscosity, Pa s
λ	radioactive decay constant, day^{-1}
θ	particle launching angle with respect to +ve X-axis, degrees
σ	standard deviation, turbulent Prandtle number, a constant use in SST *k*-ω turbulence model
ω	specific dissipation rate, s^{-1}
ζ	constant use in SST *k*-ω turbulence mode

1 INTRODUCTION

A radiological Dispersal Device (RDD) is a device that can disperse radioactive material purposely without using a nuclear detonation. RDD can disperse material using explosives or other dispersion methods, such as spraying radioactive material using aircraft. The device that disperses radioactive material using explosives is called a dirty bomb.

The radioactive sources in a dirty bomb can be solid, aerosol, gas or liquid. The explosion of a dirty bomb will not cause mass casualties compared to a nuclear explosion, but the radioactive material dispersed by a dirty bomb to densely populated areas around ground zero (GZ) can contaminate people to a level that requires medical treatment. The consequences to the environment and personnel near GZ will depend on the design of the dirty bomb, the radioactive material used and the pattern of dispersion following the release of the dirty bomb (Levi & Kelly, 2002). The contamination of people may occur through air, water, soil or food. The immediate health effects on people living in the areas close to GZ would depend on the amount and the type of radiation exposure. Factors such as distance from GZ, the barriers/shielding between the radiation sources and people, the amount of radiation infiltration through the building envelopes, the ground shine, the exposure time, rate of exposure and the area of the body exposed are some of the factors that would contribute the amount of radiation exposure.

The Defense Research and Development Canada (DRDC) conducted Full-Scale Radiological Dispersal Device (RDD) experiments at the DRDC Suffield experimental proving grounds to characterize the real effect of a dirty bomb to prepare Canada for potential terrorist attacks (Green, et al., 2016). These experiments used ^{140}La as a radioactive surrogate because of its ease of production in required quantities and ease of detection without risking humans and the environment due to its short half-life. The radioactive surrogate with the activity of 35.2 × (1 ± 10%) GBq at the shot-time was dispersed using an explosive device at ground zero (GZ) under 2.9 × (1 ± 0.4) ms^{-1} wind in the direction as shown in Figure 1. The design information of the explosive device used in Suffield experiments is classified as SECRET (Erhardt, Quayle, & Noel, Full-Scale RDD Experiments and Models, 2013).

Figure 1 shows the beta radiation contour plots of the highly contaminated area at GZ immediately after the explosion of the dirty bomb during the DRDC Suffield experiment.

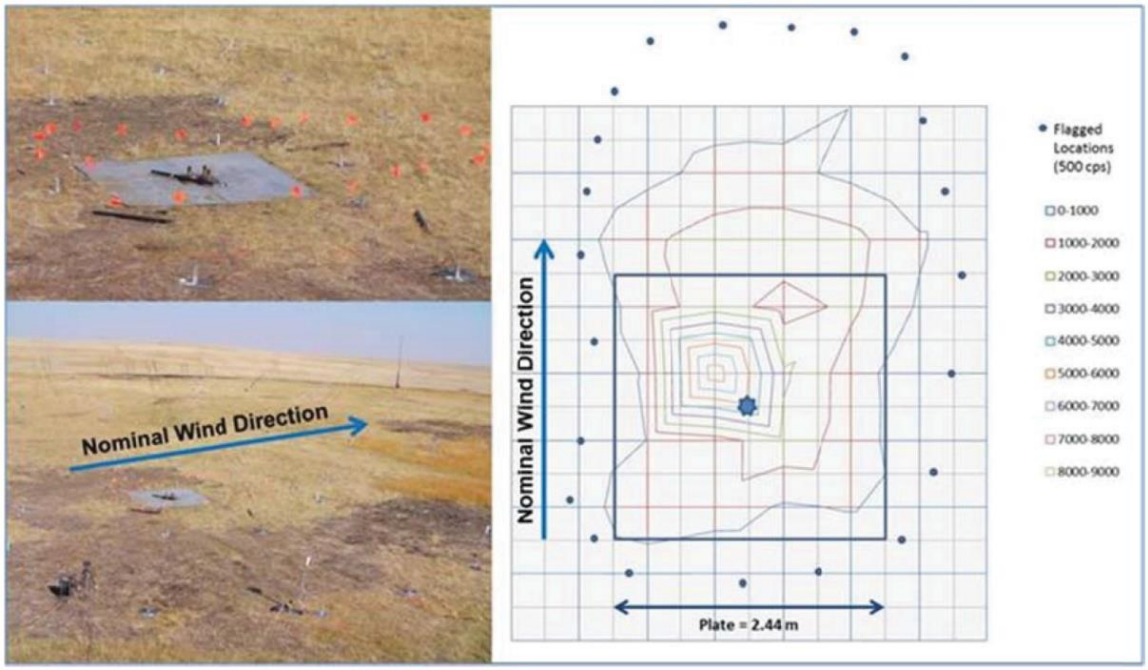

Figure 1: The figure on the right shows the beta contour plot around ground zero of the dirty bomb: The big blue star marks the GZ, the blue square represents the metal base plate, and the blue dots represent the flagged locations on the photo which demark the edge of the highly contaminated area (500 cps) (Erhardt, Quayle, & Noel, Full-Scale RDD Experiments and Models, 2013).

Figure 2 shows the fireball generated by the dirty bomb in the field studies. The average diameter of the fireball during the dirty bomb experiment at the DRDC Suffield event was approximately 2.5 to 3 m, with a central upward protrusion extending 4 to 5 m above ground.

Figure 2: The photo on the left shows the GZ before the detonation, and the still photo taken from a high-speed camera on the right shows the fireball at its maximum size (Erhardt, Quayle, & Noel, Full-Scale RDD Experiments and Models, 2013).

Roughly one-third of the dispersed mass of radioactive tracer power used in the dirty bomb at the DRDC Suffield experiment was in the respirable range (< 10 µm), one-third in the "intermediate" size range (10-100 µm) and one-third in the "ballistic" size range (>100 µm) (Erhardt, Quayle, & Noel, Full-Scale RDD Experiments and Models, 2013). During the explosion of the dirty bomb, radioactive tracer particles interact with the surrounding soil and sand in the GZ, resulting in bigger particles due to particle fusing, depositing onto one another, and forming agglomerates (Lebel, Brousseau, Erhardt, & William, 2011).

Figure 3 shows the ground concentration profile of deposited radioactive ^{140}La based on in situ gamma measurements after the dirty bomb explosion conducted at the DRDC Suffield experiment in 2012. As per Erhardt, Lebel, et al. (2016), 3% of the radioactive material used in the source was deposited close to GZ, and 15-30% was deposited within a 450 m radius of GZ.

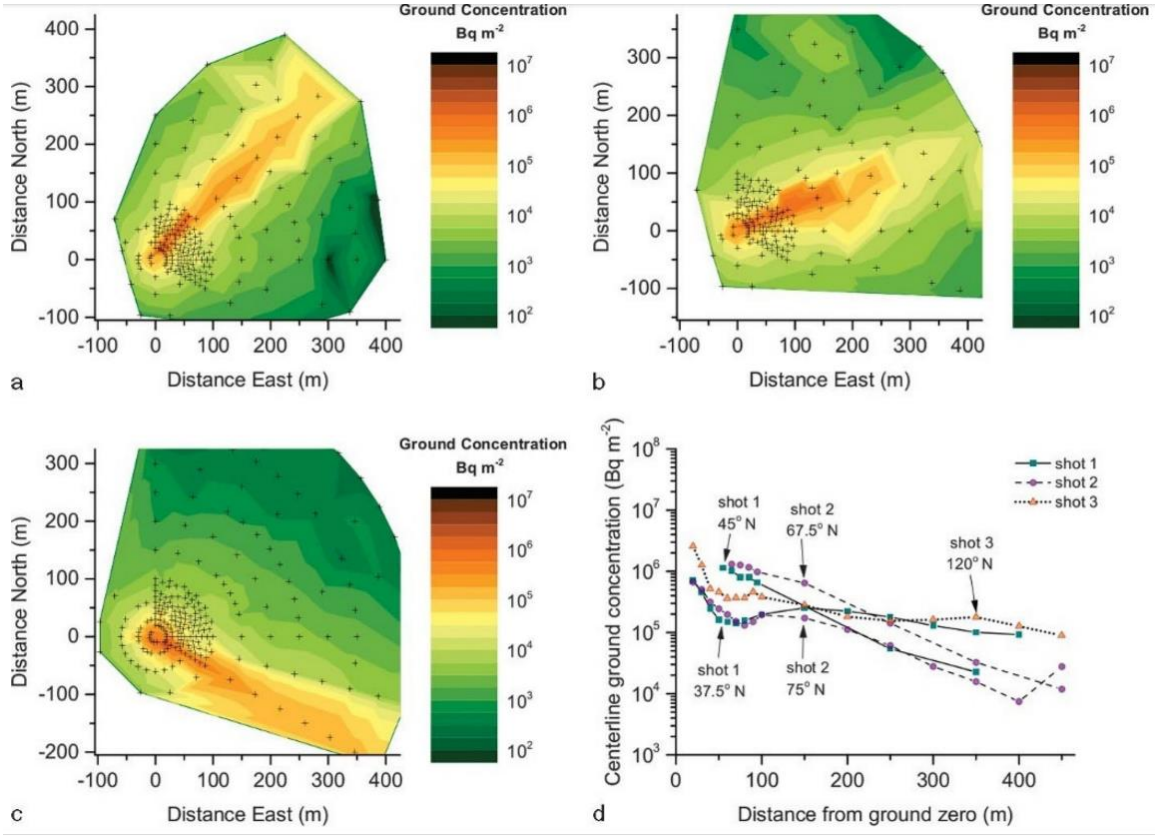

Figure 3: In situ gamma measurements profiles of ground contamination from ^{140}La deposited as a result of dirty bomb explosion for 3 trails (shots) (a) Shot 1 measurement map, (b) Shot 2 measurement map, (c) Shot 3 measurement map and (d) Centerline measurements (Erhardt, et al., 2016)

Once a dirty bomb explodes, it is important to respond in a timely manner to reduce the spread of radioactive contamination. Figure 4 shows the US Homeland Security preferred Time-Phased Response Missions when responding to a dirty bomb.

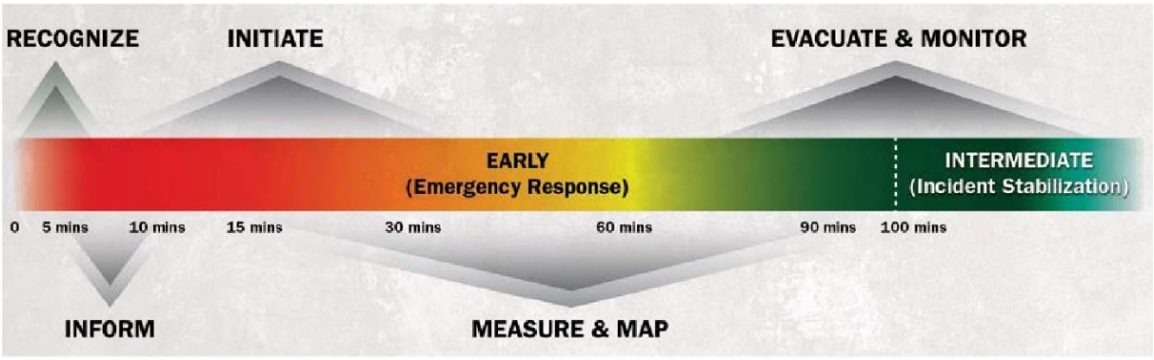

Figure 4: Response time for a dirty bomb according to the US Home Land Security (US Homeland Security, 2017)

During the Recognize phase (0 - 5 mins), the first responders attending the explosion will recognize the presence of radiation levels above the background based on the radiation readings they get from their radiation detectors. Then, during the 5 - 10 mins period, the incident commander will inform command centers and emergency personnel attending the scene that there is radiation in the area due to an explosion of a dirty bomb. At the same time, people who are living within a 500 m radius of GZ will be asked to take shelter-in-place inside buildings and close all the doors and windows, or those who cannot get into a building will be asked to cover their noses and mouths using dry cloths and quickly move away from the contaminated area. Figure 5 shows the extent of the initial Hot Zone and Shelter-in-Place areas.

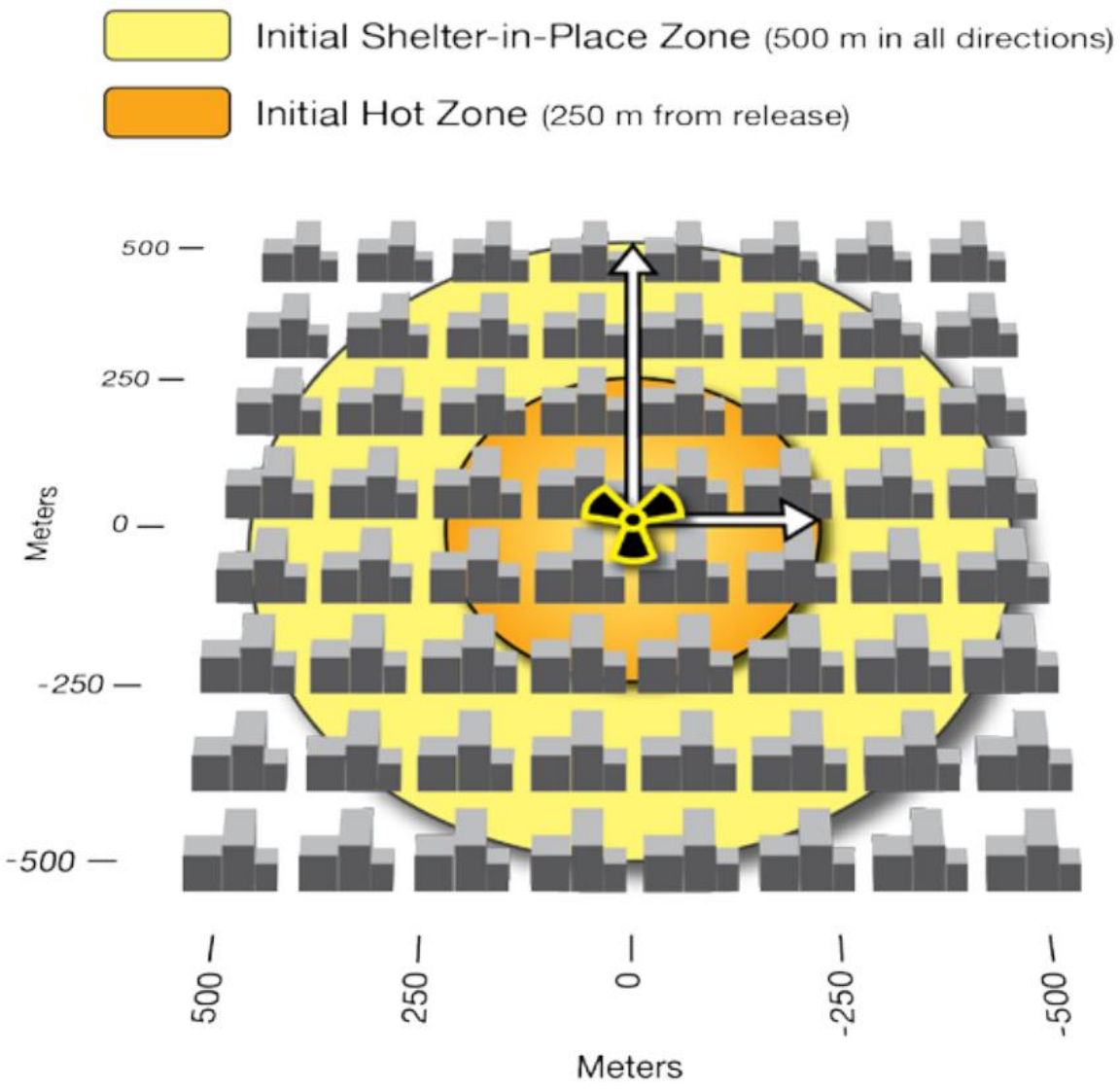

Figure 5:Initial Hot Zone and Shelter-in-Place Zone, with Unknown Direction of Contamination (US Homeland Security, 2017)

Between 5 and 40 minutes, the first responders will attend the scene wearing full personnel protective equipment (PPE), which protects them against most potential hazards until the hazard on the scene is identified. Then, the first responders initiate search and rescue, fire suppression, and medical triage and treatment without delay. Next, the police

and bomb squad clear the area, remove all hazards, including secondary bombs, establish a 20 m radius area as the initial public safety boundary, and designate this area as a crime scene.

Initially, the area within a 250 m radius will be designated as a Hot Zone until the radiation measurements are taken to define the actual Hot Zone boundary area 10 mR hr^{-1} (0.1 mGy hr^{-1}) or 60,000 dpm cm^{-2} at 1.5 cm above ground for the beta and gamma or 6,000 dpm cm-2 at 0.5 cm above ground for alpha). During the Measure & Map phase (15 - 90 mins), the incident commander, with the help of strike teams, will characterize the radiological contamination near the GZ and downwind, locate high radiation areas, and finally provide measured radiation data to the analyst to map the extent of radiological contamination. The analyst will use real-time, ground truth data to model the radiation plume to predict the direction and extent of the radiological contamination. Finally, during the Evacuation and Monitor phase (> 70 mins), the first responders will set up evacuation routes based on measured radiation data, avoiding highly contaminated areas. The first responders will quickly screen the people evacuating the Hot Zones, and those who are contaminated will be decontaminated without slowing the evacuation process (US Homeland Security, 2017).

Analysts need to know how the contamination will spread immediately after a dirty bomb and provide that information to the first responders, helping people evacuate the area as soon as possible. The analyst must use efficient computational tools to predict the airborne concentration of radioactive material due to particle resuspension using the computer power available to them. Not every analyst will have access to a supercomputer

to model the radioactive particle resuspension and advection through physical space. However, many of them will have access to high-end desktop computers where they can combine resuspension data with a simple plume model to predict the direction and the extent of the radiological contamination immediately after a dirty bomb.

According to the US Homeland Security guidelines document, the concentration of acute exposure levels of airborne radioactivity will dissipate after 10 minutes, and the remaining hazard to the population living near GZ will be from the resuspension of deposited radioactive particles (US Homeland Security, 2017). Resuspension, in the immediate aftermath of a dirty bomb incident, can be defined as the process where radioactive particles become dislodged from their deposited surfaces and are carried away from those surfaces.

The resuspension of radioactive particles in the Hot Zone may occur due to air jets or mechanical forces. The air jets can be generated by the winds, vehicles driving by, or people walking over the Hot Zone. The mechanical forces generated by the rotating tires of vehicles, lifting or kicking of particles due to people walking or impacting raindrops onto contaminated surfaces can also initiate particle resuspension in the Hot Zone, as shown in Figure 6.

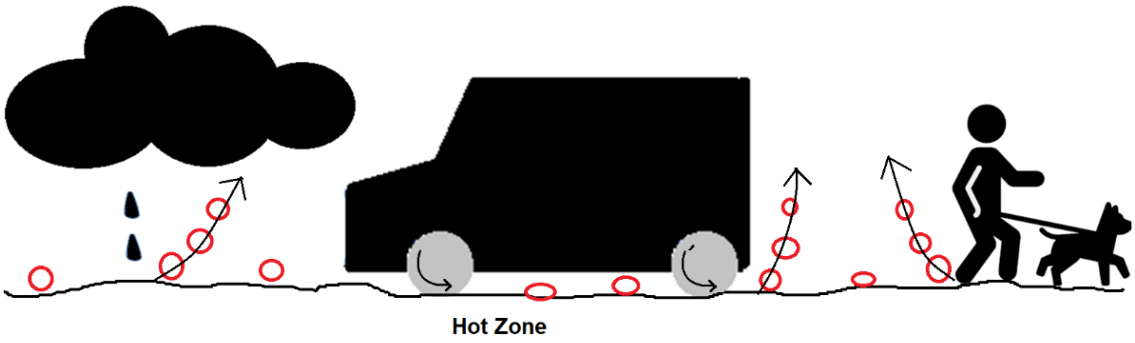

Figure 6: Mechanical resuspension examples (raindrop impact, rotating tires and walking)

Resuspension of particles due to air currents is often called re-entrainment or blow-off (Hinds, 1999). According to Hinds (1999), re-entrainment of particles is a stochastic process. For a given condition of air velocity, only a fraction of specific sizes of particles will be removed from the contaminated surfaces. The aerodynamic forces acting on the particles due to air jets will initiate particle movement against the particles' weight and adhesive forces. Particles will start rolling/creeping and leaping/saltation until they gain enough inertia to move into fast-moving air currents. In turbulent airflow, the boundary layer close to the surface area is called the laminar sub-layer, where the flow is laminar. The particles smaller than the laminar sublayer are protected by re-entrainment, but they will get lifted off from the surfaces by the air jets generated due to turbulent bursts. The particles moved into fast-moving air currents by re-entrainment, or turbulent burst, will eventually move them into human breathing height.

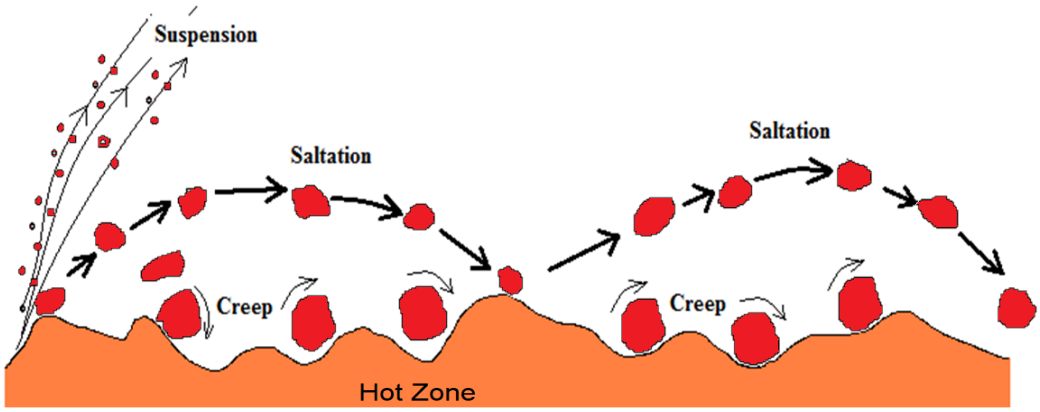

Figure 7: Particles in the Hot Zone will go through saltation, creep or immediate suspension due to air jets

In the context of the dirty bomb, the resuspension factor will provide the ratio of mass or radioactivity of material at a unit volume of air to mass or radioactivity of the same material deposited on the ground on a unit surface area.

The health effects of resuspended particles occur mainly due to inhalation of respirable range particles (< 10 µm) at human breathing height. Since different sizes of particles are deposited in different compartments of the human respiratory tract, it is essential to find out how many particles in respective particle size bins, especially in the respirable range, are available at human breathing height (Hinds, 1999). Therefore, a bin-by-bin (Bin 1: 0.25 - 0.45 µm, Bin 2: 0.45 - 0.58 µm, Bin 3: 0.58 - 1.00 µm, Bin 4: 1.00 - 5.00 µm, Bin 5: 5.00 - 10.00 µm and Bin 6: 10.00 - 32 µm) resuspension factors were introduced in the thesis to provide the ratio of radioactive particles in respective particle bin sizes available at human breathing height compared to what was deposited on the surfaces as a result of a dirty bomb. The respiratory tract deposition fraction provides the

ratio of particles that will deposit in the lungs compared to what was available at the human breathing height. The respiratory deposition fractions for different regions of the human respiratory tract are available for a wide range of particle sizes (Hinds, 1999). Multiplying the bin-by-bin particle resuspension factor by the respiratory tract deposition fractions, one can find the number of radioactive particles deposited onto respective lung compartments due to the particle resuspension process immediately after a dirty bomb.

Parameters influencing the resuspension process are numerous. It is vital to consider each of these parameters to understand resuspension comprehensively. Sehmel (1986) has divided the possible parameters into six main categories: particle soil interaction, surface properties, pollutant particle properties, soil properties, meteorological variables, and topography. There have only been a few relevant studies conducted under each category, indicating the necessity for more resuspension experiments to be designed specifically to understand the influence of each of these categories and the other possible groups that are not yet listed (Sehmel, 1980).

Previous reviews on radioactive particle resuspension have included references describing wind's role in soil erosion and sand movement. This result has been of great intrigue to the nuclear industry since radioactive particles can mix with soil and sand, especially during an explosion of a dirty bomb (Anspaugh, Kennedy, Phelps, & Shinn, 1975) (Lebel, Brousseau, Erhardt, & William, 2011). Wind can suspend much smaller particles (< 100 μm), while the very smallest of these particles (< 10 μm) may end up being suspended for a substantial amount of time and travel vast distances from the location of the initial fallout (Nicholson K. W., 1988).

Figure 8 illustrates the resuspension factors found due to wind stresses during the studies conducted from 1967 to 1975.

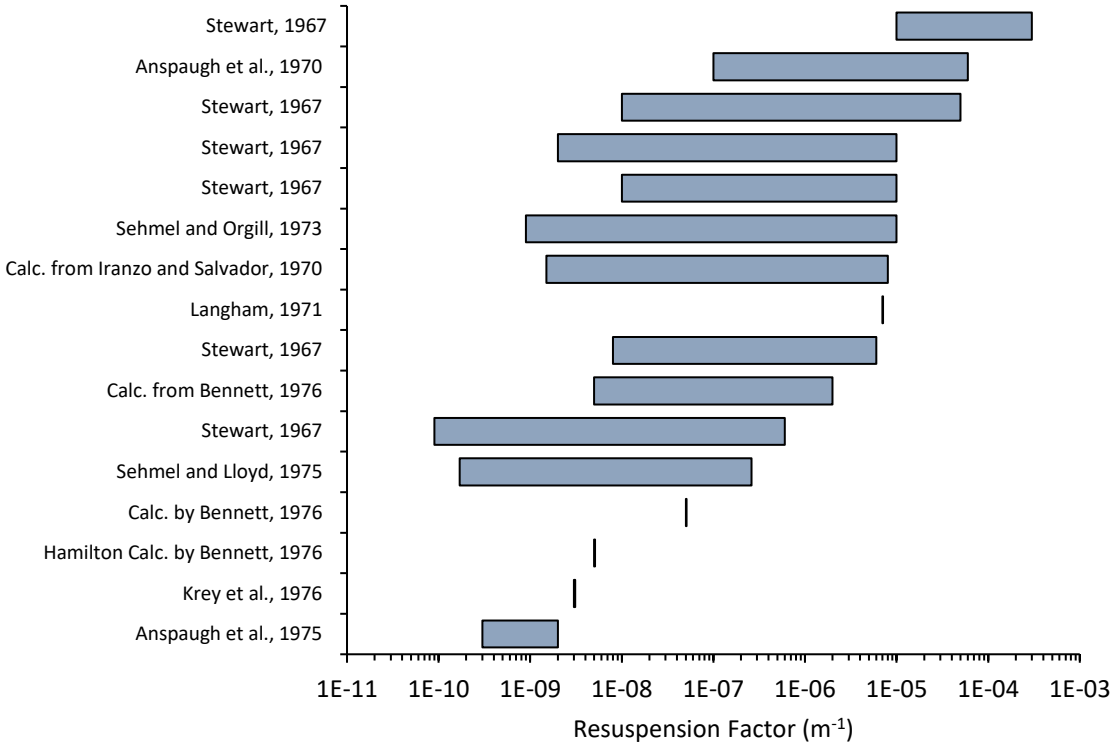

Figure 8: Comparison of resuspension factor studies conducted from 1967 to 1975 due to wind stresses (Sehmel, 1980).

Among the results reviewed in Figure 8, a variation across multiple magnitudes for wind stress-driven resuspension factors was observed (Sehmel, 1980) (Perera, 2015). Furthermore, the results presented in Figure 8 were corroborated by independent reviews of long-term resuspension factor studies conducted by Anspaugh et al. (1975), Linsley (1978), Garland (1979) and Makhon'ko (1992) following the Chornobyl accident. The

resuspension factors found in these studies vary by 2 to 3 orders of magnitude (Garger, Hoffman, & Thiessen, 1997). Therefore, the review was carried out with an additional objective to estimate the uncertainty of the resuspension factors.

As the nuclear industry developed, the interest in radioactive particle resuspension has expanded to investigate the health effects associated with deposited material generated due to fission products. These fission products may result from the material being released from nuclear weapon tests or accidental releases from the nuclear power plant or facility (Nicholson K. W., 1988). The environmental samples collected at the Ontario Tech University in Oshawa (OnTechU), Ontario, Canada, by the author measured anthropogenic ^{137}Cs in soil samples that may have travelled across the globe due to repeated resuspension processes from wind stresses.

The resuspension phenomenon of radioactive aerosols is by no means a new topic, although this topic remains relatively untouched regarding potential terrorist attacks from a dirty bomb. Walsh (2002) has created a resuspension factor model for predicting the dose level for an emergency response situation. However, it is likely appropriate for countries with weather conditions similar to the United Kingdom's and has limited application for many other parts of the world.

A critical analysis by Ziskind, Fichman, and Gutfinger (1995) reveals that presently available experimental resuspension data is insufficient to support the existing theoretical models. Hence, detailed theoretical and experimental research is required to identify and quantify the essential parameters that influence the resuspension factor; this will lead to the

development of a general resuspension factor model applicable to most situations. Until then, the accuracy of the predicted values using the reported resuspension factors may not be within acceptable levels.

1.1 Objectives of the Thesis

There are three objectives for this Ph.D. thesis:

1. The first objective is to develop an experimental procedure to measure the radioactive particle resuspension following a dirty bomb event using a wind chamber.
2. The second objective is to develop a Computational Fluid Dynamics (CFD) model to simulate the experimental setup using computer resources available for an average analyst helping the first responders.
3. The third objective is to develop an innovative bin-by-bin resuspension factor model (resuspension factor for a selected group of particle sizes) that can be used to calculate the amount of radioactive material that will deposit different compartments of the human respiratory tract immediately after a dirty bomb.

Radionuclide particle resuspension after an energetic release from a dirty bomb event was successfully modelled using a custom-built 10 m long wind chamber, and the resuspension factors at two downstream locations from the initial fallout were calculated to be 4.12E-05 × (1 ± 46.9%) m^{-1} and 4.56E-05 × (1 ± 79.5%) m^{-1}.

Subsequently, the experimental configuration was effectively simulated through Computational Fluid Dynamics (CFD) utilizing both Global and Regional methods to incorporate the impact of coherent turbulent structures in particle resuspension. The primary objective of this Computational Fluid Dynamics (CFD) analysis was to develop a methodology for computing the resuspension factor swiftly, utilizing a high-performance personal computer. This time-sensitive task was crucial to enable the analyst responsible for this calculation to furnish the resuspension factor data to first responders, promptly facilitating the creation of effective evacuation plans (US Homeland Security, 2017). The resuspension factors at the same locations as the experiment using the innovative CFD method were found to be 8.29E-05 × (1 ± 24.3%) m^{-1} and 7.95E-5× (1 ± 28.1%) m^{-1}, respectively.

Finally, the bin-by-bin resuspension factors were calculated using experimental and CFD methods. The bin-by-bin resuspension factors will help the analysts to find the amount of radioactive material that will be deposited in different compartments of the human respiratory tract due to the dirty bomb.

The guidelines used to recreate resuspension experiments will provide innovative tools and methodologies for the scientific community to create radioactive particle

resuspension following a dirty bomb. Additionally, the innovative methods introduced in the CFD modelling process of the particle resuspension will serve as valuable tools for analysts, first responders, scientists, and engineers to calculate resuspension factor values in a timely manner so first responders can generate evacuation plans to safely evacuate people from contaminated areas in the aftermath of a dirty bomb incident.

The literature review in Chapter 2 reveals the past studies on particle resuspension due to nuclear weapon tests and accidental releases from the nuclear industry. This literature review intends to draw numerous sources to elucidate the complexities of the resuspension process, particularly the resuspension of radioactive materials and the various factors affecting this process. Past resuspension studies are presented here in two categories: large-scale and small-scale resuspension studies. Recent literature review studies show that researchers use Computational Fluid Dynamics (CFD) to model small-scale particle suspension and entrainment.

Towards the end of Chapter 2, the movements of microscopic particles and forces acting on them are presented using available models in the literature. Radioactive particles undergo three prominent suspension stages during the resuspension process before entering the human respiratory tract. The first stage involves the initial resuspension. In this stage, particles are lifted off, rolled or saltated due to the coherent structure of the turbulent boundary layer near the floor. During the second stage of resuspension, particles are transited through the laminar sub-layer to the end of the turbulent region. Finally, the particles are transited from the local turbulent boundary layer into the free-stream region

during the third stage. In the free-stream area, particles are transited up to the respirable height or can eventually be entrained downstream through the atmospheric boundary layer.

Chapter 3 discusses the radioactive particle resuspension experiments conducted at Wehrwissenschaftliches Institut für Schutztechnologien (WIS) facility in Munster, Germany. Radioactive particle resuspension experiments were conducted in a 10 m long, open-ended wind chamber built exclusively for radioactive particle resuspension studies. In addition, the WIS facility was equipped with an appropriate ventilation system to handle live agent radioactive materials experiments. The bin-by-bin resuspension factors of freshly fallen radioactive materials resulting from a simulated RDD event were calculated using experiments conducted inside the WIS facility using radioactive Lanthanum Oxide powder as a surrogate.

Chapter 4 is devoted to the CFD modelling of the experimental setup and the use of CFD to visualize the microscopic process of wind-driven particle resuspension processes. The 3D computational domain of the WIS facility wind chamber was built using a hybrid mesh using Gambit software. A very fine mesh was generated close to the wind chamber wall surfaces to ensure there are an adequate number of mesh nodes in the viscosity-dominated boundary layer region model turbulent properties. The original mesh was refined until the non-dimensional wall distances (y+) for wall-bounded flows of all wall surfaces were less than 2.5. Solving the governing equations and post-processing of results was performed using a FLUENT double-precision solver. Best practice guidelines in CFD modelling were followed to ensure grid independence and the use of higher-order schemes. Fluent uses the control volume numerical technique to discretize the

computational models. The momentum equations (Navier-Stokes equations) are considered in their conservative integral form in the control volume technique. The governing equations were integrated into the individual control volumes (mesh elements) to construct a set of linear algebraic equations consisting of discrete dependent variables such as velocities, pressures, and turbulent parameters (Fluent Inc., 2006). These solutions for the linear set of algebraic equations provided the updated values of the dependent variables.

Regional and Global CFD models were introduced to simplify the CFD modelling process to simulate the particle suspension across all three stages of the resuspension processes to reduce the mesh size to solve the CFD model utilizing the computational power available. Initial CFD work performed using the 2D WIS facility model showed that the k-ω SST turbulence model could be used successfully to model the turbulent transport properties close to the wall surfaces where initial particle resuspension would occur. Based on the experience gained from modelling the 2D WIS facility CFD model, the k-ω SST turbulence model was used to find the turbulent transport properties of the 3D WIS facility CFD model domain before using the Large Eddy Simulation (LES) to simulate the flow patterns inside the WIS facility wind chamber including in the regions close to the wind chamber floor. The Regional CFD model was located close to the wind chamber floor. The ceiling of the Regional CFD model was modelled as a velocity inlet boundary based on the velocity and turbulent intensity properties acquired from the 3D Global WIS facility CFD model. The boundary condition of the ceiling was modelled to simulate the cylindrical vortex formations, and the vortex burst to simulate the coherent structure of the vortices

close to the floor utilizing the Spectral Synthesizer Algorithm. This chapter also compares the CFD velocity results against the experimental results and shows the converged CFD models' velocity contours and vector plots.

Chapter 5 explains the particle tracking process and showcases the bin-by-bin particle resuspension factor results. Particles were introduced to the converged CFD domain and tracked in a Lagrangian frame of reference using the Discrete Phase Model (DPM) available in FLUENT software until particles for the same duration as the experiment. This chapter also explains how particles interact with different computational domain boundaries. For example, particles escape in pressure-inlet, velocity-inlet, and exhaust-fans and reflect when they come across a wall or symmetry boundary conditions.

This chapter shows how particles are entrained inside the Global 3D WIS facility domain, the Regional domain, and the corresponding bin-by-bin resuspension factor and fraction results. The resuspension fraction was defined as the ratio of the number of particles crossing a boundary and the number of particles released into the computation domain.

The flow inside the Regional model was simulated by introducing constant velocity components found from the Global model, and the turbulent structure in the boundary layer was introduced using the Spectral Synthesizer algorithm available in the Fluent software under Large Eddy Simulation (LES) option (Fluent Inc., 2006). The resuspension fraction at the ceiling of the respective particle bin size was calculated by dividing the number of particles that crossed the ceiling as a result of turbulent vortex structure in the Regional

model by the particles released in the respective bin on the floor surfaces. Finally, the CFD bin-by-bin particle resuspension factor values were found by multiplying the Regional resuspension fraction values by the corresponding Global resuspension transfer factor.

Chapter 6 concludes the main discoveries found as a part of the thesis. This chapter summarizes the detailed experimental procedures and CFD methods used to calculate the particle resuspension factors resulting from an RDD event. This chapter also discusses the validity of experimental and CFD procedures used in the thesis and recommendations for future work.

Several appendices are appended to the thesis, including a list of publications generated during the study. Appendix A lists the parameters used in the particle resuspension studies, particle information, and particle behaviour due to coherent structure near the floor. Appendix B shows the initial works done by the author at the beginning of the thesis study to lay the foundation for the work presented in the thesis, and Appendix C provides numerous computer codes used during the thesis.

2 LITERATURE REVIEW

Resuspension after an RDD event is a complex phenomenon, and a method of accurately measuring its magnitude has not been fully developed. Therefore, selecting a suitable measurement approach to measure radioactive particle resuspension immediately after an RDD event requires a proper understanding of the measured parameters, primarily how they represent the resuspension process, strengths, weaknesses, and ease of measurement. In previous works, measurements of resuspension are often expressed in one or a combination of the following forms: resuspension factor, resuspension rate, and equivalent soil concentration (Nicholson K. W., 1988) (Perera, 2015). Each of these measurement approaches is discussed in the following sections.

2.1 Resuspension Factor

The resuspension factor, K or RF (m^{-1}), was the traditional method of quantifying the results of early resuspension work; for example, Stewart (1967) defined K using Equation (1).

$$K = \frac{C}{S} \qquad (1)$$

where, C (μg cm^{-3}) represents the airborne concentration at a reference height, and S (μg cm^{-2}) represents the surface contamination. When the scope of measurement is radioactivity instead of mass, C and S are measured in units of Bq m^{-3} and Bq m^{-2}, respectively (Perera, 2015).

Two distinct complications arise when measuring airborne concentration (C). Firstly, the resuspended material's dilution rate due to the wind, and secondly, the airborne resuspended material concentration variation with respect to the elevation and the distance downstream. Further, surface contamination (S) requires knowing the depth of the surface material sampled, which is used to determine the value of K. The resuspension factor method assumes that any material below the surface does not contribute to resuspension. This method of measuring resuspension has also been criticized due to its failure to account for the advection of particles into the testing zone as a result of upwind resuspension for large deposits [(Horst, (1976a); (Sehmel, 1977a); (Sehmel, 1977b)]; downwind surface contamination concentration was observed to have a minor influence on resuspension for firmly deposited species (Horst, 1976b). Due to these reasons, the resuspension factors should strictly be considered applicable to the determined conditions. In addition, the geographic variation of the deposit strongly influences the resuspension factor, and in many cases, the use of the same resuspension factor for different geometries could lead to non-representative results.

For an infinitely large contaminated area, both C and S will be constant; hence, the resuspension factor will be constant. There is no such thing as an infinitely large contaminated area; it is only a theoretical concept. In a finitely large contaminated area, the resuspension factor will reduce as time progresses, having an asymptotic solution for the resuspension factor. The resuspension factor stabilizes over time as the contaminants disperse, settle, and adhere to surfaces.

Although the resuspension factor has limitations, it has traditionally been considered the universal parameter to measure the resuspension process (Perera, 2015). The resuspension factor method will also be helpful for locations where contamination concentration in the air is dominated by local resuspension (Garland & Pomeroy, 1994).

There have been attempts to identify the influence of time on the resuspension factor. The temporal dependence of the resuspension factor, K(t), was approximated and summarized by Evgenii, Garger, Hoffman and Thiessen (1997). The predictability of time-dependent resuspension factor models was analyzed using the soil and air concentrations collected over several years around the Chornobyl accident area in Ukraine. The most observed realistic time-dependent resuspension factor models utilize an inverse power function. The inverse power function was developed by comparing existing models with empirical data collected for long-term resuspension factors. Hatano Y. and Hatano N. (2003) have proposed a theoretical formula for the time dependence of the resuspension factor, which is also an inverse power function. This formula agrees well with data collected from short and long periods, such as field observations in Chornobyl.

Garland (1979) derived a formula for long-term resuspension, which was recommended as the appropriate formula for emergency response by the report NRPB-W1 produced by Public Health England and its predecessor organizations for UK emergency situations (Walsh, 2002) (Wellings, Bedwell, Hywood, & Charnock, 2019), (Yu, Cheng, Kamboj, Domotor, & Wallo, 2009). The recommended formula is given by Equation (2)

$$\boldsymbol{K(t) = \left(\frac{1.2 \times 10^{-6}}{t} + 10^{-9}\right) e^{-\lambda \cdot t}} \qquad \textbf{(2)}$$

here, λ (day^{-1}) represents the radioactive decay constant, $K(t)$ (m^{-1}) represents the time-dependent resuspension factor, and t represents the time after deposition measured in days. Equation (2) is valid for times greater than 1 day. The resuspension factor of 1.2×10^{-6} m^{-1} was assumed during the first day (Yu, Cheng, Kamboj, Domotor, & Wallo, 2009). The time-dependent modified Garland equation accounts for wind shear typical to UK weather (light-medium wind). The time-dependent resuspension factor will go down over time starting day 1 of an RDD event due to particle settling, deposition, environmental factors, particle adhesion and agglomeration, natural degradation and transformation. Particles that were initially released by an RDD event into the air can stay suspended for a certain period before settling down due to gravity. Larger and heavier particles tend to settle down more quickly than smaller and lighter particles. As time progresses, the larger and more mobile particles settle out, reducing the number of readily available particles for resuspension.

During resuspension, particles can deposit onto surfaces such as ground, vegetation, or buildings due to gravity, electrostatic forces or other mechanisms. As the particles deposit over time, the available pool of airborne particles decreases, decreasing the resuspension factor. Environmental conditions such as wind and rainfall can also influence the resuspension factor. The high wind can facilitate the transport of particles away from the contaminated area, and rain can wash out particles from the atmosphere and on surfaces, reducing the available particles for resuspension. The presence of moisture will increase the adhesion of insoluble particles due to the surface tension effect, reducing the particle resuspension factor for a given condition (Nicholson & Branson, 1990). Over time, particles may undergo processes of adhesion and agglomeration due to moisture present, chemical reactions and electrostatic forces forming larger particles that are less prone to resuspension. The natural degradation and transformation of some contamination will alter particles' physical, chemical and radiological properties, affecting resuspension characteristics and making the particles less likely to become airborne.

The resuspension factor at a given time may go up due to disturbances to the old deposits due to environmental and human activities. Equation (2) was empirically derived for wind-driven resuspension in climates typical to the UK, and it does not consider mechanical resuspension. A list of rule-of-thumb multiplication factors presented in Table 1 was suggested to be used to account for various environmental conditions (Garland J. , 1979) (Walsh, 2002) (Yu, Cheng, Kamboj, Domotor, & Wallo, 2009).

Table 1: Mechanical stress multiplication factors that can be used with Garland's equation (Garland J. , 1979) (Yu, Cheng, Kamboj, Domotor, & Wallo, 2009).

Condition	**Multiplier**
Rural conditions; light-medium winds	x1
Arid climate	x10
Urban conditions; light traffic; light pedestrian activity	x10
Urban conditions; heavy traffic	x100
Plowing in dry conditions	x100
High winds	additional x2

According to the Beaufort Wind Scale, light-medium winds will have speeds between 1 to 38 kmh $^{-1}$, and High Winds will have speeds between 39 to 49 kmh $^{-1}$ (Government of Canada, 2017).

The presence of moisture will increase the adhesion of insoluble particles due to the surface tension effect reducing the particle resuspension factor for a given condition (Nicholson & Branson, 1990).

2.2 Resuspension Rate, Λ

The resuspension rate, Λ (s^{-1}), is an alternative way of quantifying the resuspension. It is defined as the fraction of surface species being removed per unit of time (Kim, Gidwani, Wyslouzil, & Sohn, 2010):

$$\Lambda = \frac{R}{S} \qquad (3)$$

where, R (μg cm^{-2} s^{-1}) represents the resuspension flux, S (μg cm^{-2}) represents the surface contamination. R and S are measured in Bq m^{-2} s^{-1} and Bq m^{-2}, respectively, when the goal is to measure radiological contamination.

Sehmel (1984) commented that S is subjected to comparable limitations, as discussed under the resuspension factor Section 2.1. Compared to the resuspension factor approach, airborne concentrations across areas of varying contamination levels can be modelled using the resuspension rate approach, but the challenge is to find the local source term that can change from location to location. For most of the work done in the past regarding old radioactive deposits, the source term at the contaminated sites was not available and has been found in collaboration with the results found using numerical models of airborne dispersion and deposition (Qian & Andrea, 2008).

As mentioned earlier, particle resuspension is a function of wind speed and mechanical disturbances. Therefore, local mechanical resuspension due to the movement of vehicles or people walking in the contaminated area will affect the local resuspension rate compared to the wind-driven resuspension rate, which usually affects the entire contaminated area (Sehmel, 1977a). Since the resuspension rate provides information about local resuspension, even a person setting up equipment to measure the resuspension rate can enhance the resuspension rate by an order of magnitude (Garger , Gordeev , Holländer , & Kashpur, 1996). According to Garger E (1996). the variability of the resuspension rates was much greater than the resuspension factor. The resuspension rate at a specific location, as measured with the same equipment, exhibited a significant variability spanning up to two orders of magnitude.

The purpose of resuspension measurements during a dirty bomb event is to determine the amount of respirable range radioactive particles available at an average person's height resulting from the resuspension events. So, it is essential to have a well-defined source term and a reliable way of measuring the resuspension phenomenon that will not be affected by local activities; hence, using a resuspension rate after a dirty bomb event is questionable.

2.3 Mass Loading Approach

The mass loading approach assumes that particulates in air and soil contain the same proportion of contaminants (Linsley G. S., 1978). The resuspension of substances mixed thoroughly with the soil can be described by this method. The most common way of representing equivalent soil concentration, SE (mass per unit volume or radioactivity per unit volume), is given by Equation (4).

$$S_E = \frac{C_a}{C_s} \qquad (4)$$

where, Ca and Cs represent species concentrations in the air (g m^{-3}) and soil (g g^{-1}), respectively. When measuring radioactive resuspension, Ca and Cs are measured in Bq m^{-3} and Bq g^{-1}, respectively.

This type of measurement is more beneficial for deposits that have been distributed in the soil over several years. A significant problem in this method is that upwind sources affect atmospheric concentration, similar to the resuspension factor and resuspension rate (Perera, 2015). Despite the limited application of the mass loading approach, long-term resuspension consequences could be predicted using this method. This method has been

shown to correlate well with measured values on several sites where there were aged deposits of contaminants, but it has not been used for fresh deposits (Linsley G. S., 1978).

The mass loading approach has been found useful when considering human-made disturbances and aged deposits. However, this approach assumes that radionuclide is closely associated with soil. As this is not the condition after the initial deposit flowing an RDD event, the mass loading approach has been determined inappropriate for emergency response situations. Further, there is no time dependence consideration in the mass loading approach.

2.4 Resuspension Studies

Resuspension studies can be categorized into two distinct sections: large-scale studies in which details of resuspension are empirically represented as a whole, and small-scale studies that examine the resuspension of particles at the microscopic scale (Gillette, Robert, Lawson, & Thompson, 2004a) (Perera, 2015).

2.5 Large-Scale Resuspension Studies

Large-scale studies are communicated in terms of a resuspension factor and resuspension rate. These studies focus on large-scale hazardous substance contamination, predicting contamination spread, and the total lifetime of dangerous air-borne concentrations (Perera, 2015).

G. S. Linsley (1978) reviewed various models developed to represent the large-scale resuspension process. A review of resuspension mechanisms, resuspension in an urban environment, and resuspension from the sea surface are also covered in this review. Most previous research on mechanical resuspension was reviewed, and a list of corresponding resuspension factors was presented. However, most of these results are related to UK weather conditions, and a thorough analysis of local urban conditions is required if one wants to use these results in a different urban location.

Sehmel (1980), Nicholson (1988), Ziskind, Fichman, and Gutfinger (1995) have reviewed previous work on large-scale resuspension work as well. Sehmel (1984) has shown by experimental studies that airborne concentration of resuspended particles from aged deposits is a function of sampling location, wind speed, high wind direction with the highest frequency, and host particle size diameter.

Shinn, Homan, and Hofmann (1986) have compared the resuspension studies of plutonium aerosol for four Nevada Test Sites with similar studies in South Carolina, California, and the Pacific Atolls. Related reviews were directed towards the measurement

of inhalation dose of radioactive aerosols from weapon test sites and nuclear accident sites found in the literature; for example, Gavrilov, Klepikova, Troyanova, & Roden (1995), Shinn (2003), Rosner & Winkler, (2001), Sehmel G. (1977a) and Sehmel (1977b). These studies provide valuable information about the behaviour of radioactive aerosols in the atmospheric environment with time. The most helpful information is the resuspension factor, K, which can be used to predict the environmental radioactive dose in the event of possible future accidents.

Radioactive ^{137}Cs powder resuspension to the urban area was discussed by Do Rio, Amaral, & Paretzke (1994) after the Goiânia accident in Brazil. The accidental opening of a stolen teletherapy radiation capsule contaminated the urban area, imposing health risks on many people handling this source and living in the initial fallout area. Restricted contamination in this urban area allowed one to study the local resuspension factor without the influence of subsequent resuspensions due to previously deposited radioactive material and human activities. Based on air activity data, resuspension factors near the initial contamination areas were measured to be 10^{-8} to 10^{-9} m^{-1}.

Schershakov (1997) has derived expressions for the resuspension factor and resuspension rate, including their dependence on time since the release of radioactive dust, chemical species, wind speed, roughness length, type of the underlying surface, the moisture of the soil, and intensity of anthropogenic activity. These expressions agree well with experimental data. However, these semi-empirical model parameters were derived from data collected from a nuclear weapon test site for many years. This approach's usefulness in predicting the resuspension from a fresh deposit requires further research.

Garcia-Olivares and Iranzo (1997) devised a compartmental approach to model the transport and resuspension of radionuclides from the Palomares area in southern Spain caused by wind actions. This area was contaminated by plutonium and americium as a result of an aerial accident involving two US military aircraft during a mid-air refuelling operation, one carrying nuclear weapons. The resuspension model developed as a part of this work was capable of predicting the resuspension factor based on radioactive material concentration in air, C (Bq m^{-3}) within a boundary layer at the height of h (m), based on the resuspension rate, Λ (s^{-1}), soil activity contamination, S (Bq m^{-2}), and deposition velocity, v_g (m s^{-1}). Garcia-Olivares and Iranzo assumed the resuspension rate depends on the wind velocity as presented by Anspaugh et al. (1975); where $\Lambda = a{u_*}^3$ here, u_* (m s^{-1}) is the friction velocity and a = 10^{-10} (s^2 m^{-3}). Using a logarithmic velocity profile, the friction velocity based on measured velocity at height h (m) was calculated using the equation: $u_* = {u.\kappa}/{ln(z/z_0)}$, here u (m.$s^{-1}$) is the wind speed at height z, κ is the von Kármán constant [0.41], and z_0 is the roughness length (5-14 cm for cultivated areas and 0.5 - 1 m for urban areas).

Figure 9 shows the comparison of resuspension factor data of the Palomares area due to accidents compared to previously derived resuspension factor models such as Anspaugh (1975), USAEC (1974), USAEC (1975), Linsley (1978), Garland (1982) and European data collected following Chornobyl accident.

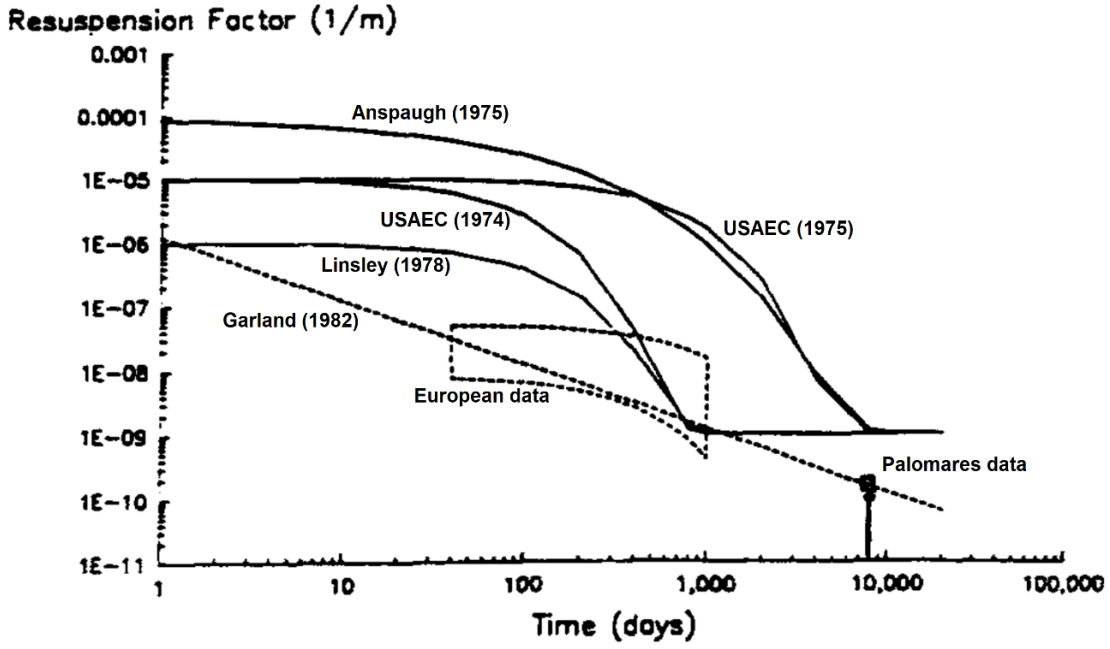

Figure 9: Palomares data compared to European data following Chornobyl accident and some selected of resuspension factor models (Garland et al. (1990), p. 23). Models: USAEC (1974), k= $10^{-5}e^{-0.0139t} + 10^{-9}\,m^{-1}$; USAEC (1975), k= $10^{-5}e^{-0.00185t} + 10^{-9}\,m^{-1}$; Anspaugh (1975), k= $10^{-4}e^{-0.15\sqrt{t}} + 10^{-9}\,m^{-1}$; Linsley (1978), k= $10^{-6}e^{-0.01t} + 10^{-9}\,m^{-1}$; Garland (1982), $k = 1.2 \times 10^{-6}\,t^{-1}$[Garcia-Olivares and Iranzo (1997)]. Note: Graph names were added to the original figure

This data fits generated a rough theoretical resuspension factor, Kth (=Λ/v_g) of 4×10-11 (m^{-1}); the observed resuspension factor was 10-10 (m^{-1}). Here, the resuspension rate, Λ was found using equation $\Lambda = Cu_*{}^k$, where C is the proportionality constant, u_* is friction velocity, exponent k, is between 2 and 6.5 (Till & Meyer, 1983) (Garcia-Olivares & Iranzo, 1997).

E. K. Garger, et al. (1999) evaluated existing mathematical models based on measurements collected after the Chornobyl accident. Most of the mathematical models calculate the surface contamination of radionuclides at the time of initial release, $C_s(0)$ (Bq

m^{-3}) using the equation, $C_a(t) = K(t)C_s(0)$, where $C_a(t)$ (Bq m^{-3}) is the concentration of radionuclides in air and $K(t)$ is the resuspension factor. A summary of these models can be found in Table 2. E. K. Garger, et al. (1999) stated that the process of finding the relative decrease of the resuspension factor was very complicated, and the selection of the initial resuspension factor was very subjective. In addition, most of the parameters used in these mathematical models would depend highly on physical or geographical conditions. Simple exponential models would provide a good prediction of annual air concentrations for homogeneous conditions, but for heterogeneous situations, Garger et al. (1999) recommended using more complicated models that would account for heterogeneous conditions.

Table 2: Resuspension models used by participants (Garger E. K., et al., 1999)

Model and Participant	Model Description	Units of time
Anspaugh et al. (1975) model	$K(t) = K(0)e^{-\lambda\sqrt{t}} + a$	d
Antoshina	$K(0) = 1 \times 10^{-6}\ instead\ of\ 1 \times 10^{-4}$ $\lambda = 0.15$ and $a = 1 \times 10^{-9}$	
Linsley (1978) model	$K(t) = K(0)e^{-\lambda t} + a$	d
Galata	$K(0) = 1 \times 10^{-6}$ $\lambda = 0.01$ and $a = 1 \times 10^{-9}$	
IAEA (1992) model	$K(t) = K(0)e^{-Bt}$	
Miller	$K(0) = 3.6 \times 10^{-9}\ to\ 4.9 \times 10^{-8}$ (log uniform distribution) $B = 8.7 \times 10^{-4}\ to\ 4.1 \times 10^{-3}$ (uniform distribution)	d
Galeriu	$K(0) = 1 \times 10^{-8}$ $B = 0.09$	d
NRPB/CEA Makhonko (1992) model	$K(t) = Ae^{-(a+b+\lambda)t} + Be^{-(b+\lambda)t}$	d
Malyutyak	$A = 1 \times 10^{-5}$, $\lambda = \lambda_R = 6.33 \times 10^{-5}$, $a = 1.26 \times 10^{-2}$, $b = 3.0 \times 10^{-5}$ and $B = 1 \times 10^{-10}$	
Garland (1982) model	$K(t) = At^{-1}$	d
Semenova	$A = 1.2 \times 10^{-6}$	
Nair	$A = 1 \times 10^{-6}$ for t >1000, $K(t) = 1 \times 10^{-9}$	
Makhonko/ Garland/ Kryshev (1992) model	$K(t) = A(u) \times (e^{-at} + bt^{-1})$	y
Kryshev	$A(u) = (5 \times 10^{-15}) \times (2620u^3 + u^8)$ where u = wind velocity, a = 0.9 and b = 0.1	

Wagenpfeil (1999) has concluded some beneficial resuspension factor results based on anthropogenic enhanced and wind-driven resuspension measurements in areas of proximity to Chornobyl. The magnitude of resuspension has been quantified through the use of ^{137}Cs. For coarse particles (d_{ae} > 10 μm), the mean resuspension factor was observed to reside between 1×10^{-10} – 6×10^{-10} (m^{-1}) for wind-driven resuspension and three orders of magnitude increase during agricultural activities. An exponential decrease in the resuspension factor was seen as the relative moisture content in the soil increased. The coarse particle concentrations in the air at respective heights were measured using a Rotating Arm Impactor (RAI). The vertical flux of the contamination, Q (Bq m^{-2} s^{-1}), was derived using Equation (5).

$$\boldsymbol{Q = \frac{\kappa u_* \left(A_V(Z_1) - A_V(Z_2)\right)}{ln\left(Z_1/Z_2\right) + correction}} \qquad \textbf{(5)}$$

where, κ is the von Kármán constant [0.41], u_* (m s^{-1}) is the friction velocity, $A_V(Z_1)$ and $A_V(Z_2)$ are concentrations of ^{137}Cs in air (Bq.m^{-3}) at elevations Z_1 and Z_2.

Reshetin (2005) predicted the radioactivity (Bq), maximum inhalation dose (mSv), and the spatial extent (km^{-2}) of contamination by using a Gaussian Plume model. This model applies to urban areas affected by a terrorist event releasing ^{90}Sr radiological dispersion. The dispersal of ^{90}Sr was used as an RDD event because of its ease of access by the former Soviet Union (USSR) countries where orphaned ^{90}Sr sources with limited

security may be accessible to terrorists. Typical Radioisotope Thermoelectric Generators (RTG) were used for remote power applications in these countries. A 3.7×104 GBq (1000 Ci) or 7g of ^{90}Sr (typical commercial Sr source) dirty-bomb release at 50 m and 100 m above ground level was evaluated and analyzed using this semi-empirical method modelling. The conclusions drawn from this simulation revealed that the above conditions would have the highest probability of inflicting adverse health effects on the target population. The conclusions also indicated that low wind velocity combined with a stable atmosphere (prolonging the particles' residence time in the air) and particle geometry and size (~ 1 μm) would maximize inhalation exposure.

Besides many simplifying assumptions made in resuspension modelling, one significant phenomenon that has not been considered in semi-empirical resuspension models is the effect of radioactive fallout in radioactive particle resuspension. This questions the model validity for an actual application as radionuclides resuspended into the atmosphere can spread contamination outside the initial release location and act as a secondary contamination source (Garger E. , et al., 1999). Not incorporating the resuspension mechanism in the analysis mentioned above was likely due to the limited knowledge of the phenomenology of resuspension of radioactive particles and aerosols from a general and RDD perspective.

Resuspension factor models and associated physical processes that affect the movement of radionuclides, such as interception by vegetation, resuspension, and vertical migration in soil, were established by Anspaugh (2002). A large scatter was found to exist

in the experimental data. It was determined that the resuspension process could not be understood solely by saltation models; instead, it was recognized that multiple factors affected the particle resuspension process. Another complication described in this study was the inability of current models to describe empirical results adequately. The proposed temporal model by Anspaugh et al. (2002), presented in Equation (6), accurately predicts the entire data span.

$$S_F = \left[10^{-5}e^{-0.07t} + 6 \times 10^{-9} \times e^{-0.003t} + 10^{-9}\right]10^{\pm 1} \qquad (6)$$

here, S_F (m^{-1}) is the resuspension factor, and t (d) is the elapsed time.

Maxwell & Anspaugh (2011) used previous resuspension models and data collected across three continents to derive two improved empirical models using a data- fitting technique. The collected resuspension data varies over six orders of magnitude. Therefore, power law and the modified double exponential Anspaugh et al. model (2002) given in Equation (7) were selected as the most suitable fit for data found at the early moments of the resuspension process ($t < \sim 100$ days). Also, the modified Anspaugh model does not suffer from undefined resuspension factor values when $t = 0$.

$$S_F = \left[10^{-5}e^{-0.07t} + 7 \times 10^{-9} \times e^{-0.002t} + 10^{-9}\right] \times 4.2^{\pm 1} \qquad (7)$$

Figure 10 shows previously observed resuspension factor data and five models of resuspension, Anspaugh et (2002), Power Law, Double-Exponential, Anspaugh modified, and NCRP. (Maxwell & Anspaugh, 2011).

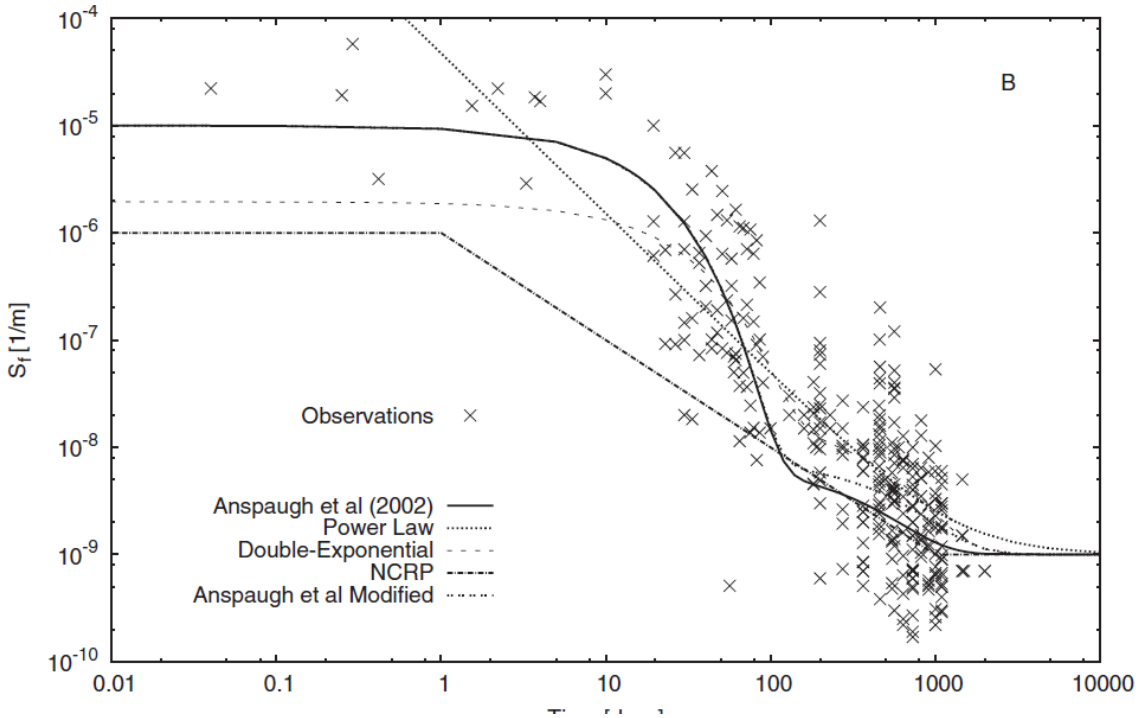

Figure 10: Plot of SF vs. time for previsly observed data and five models of resuspension, Anspaugh et (2002), Power Law, Double-Exponential, Anspaugh modified, and NCRP. (Maxwell & Anspaugh, 2011)

Most large-scale resuspension studies were conducted via observations or experiments conducted using aged atomic bomb sites and nuclear accidents. Parameters, such as initial resuspension factors at time=0, were calculated using mathematical models.

Ishizuka, et al. (2017) used a resuspension scheme to evaluate the resuspended radioactive material associated with mineral dust particles from the ground surfaces near the Fukushima Daiichi Nuclear Power Plant (F1NPP). Equation (8) was used to find the radioactive dust concentration due to the resuspension of radioactive dust.

$$\boldsymbol{C_r(D) = B_S(D) F_N(D) \frac{T_d}{H_d}} \qquad \textbf{(8)}$$

here, $C_r(D)$ (Bq m^{-3}) is radioactive dust concentration, $B_s(D)$ (Bq) is the radioactivity of soil particles, $F_N(D)$ (number m^{-2} s^{-1}) is size-resolved dust number, T_d (s) is the duration of dust event, H_d (m) is the mixing layer height. The 1-D resuspension scheme developed by Ishizuka (2017) was in good agreement with the measured ^{134}Cs and ^{137}Cs concentrations found in highly contaminated school grounds in Tsushima District, Namie Town, Fukushima, resulting from the Fukushima Daiichi Nuclear Power Plant (F1NPP) accident between Dec 2012 and March 2013. The environmental samples at the school grounds were collected using a seven-stage cascade impactor placed at 1.2 m height above ground connected to a high-volume sampler.

Kaneyasu (2017) calculated the resuspension factor of radiocesium adsorbed on soil particles between April 28 and September 21, 2011, in Tsukuba city, located 170 km south of F1NPP. The airborne particle size concentrations were calculated using a 12-stage cascade impactor placed 15 m above ground. The activity-based resuspension factor was calculated assuming that the ^{137}Cs radioactivity absorbed on soil was the sum of ^{137}Cs

particles with diameters greater than 2.1 μm aerodynamic diameter. The bar graph in Figure 11 shows the resuspension factor calculated at 6 different time periods and a comparison of resuspension factors calculated at Chornobyl city during the first two years after the Chornobyl Nuclear Power Plant (ChNPP)accident. It was observed that the resuspension factors calculated during testing periods 1 and 2 were similar to European city resuspension factor results found in the months following the ChNPP accident.

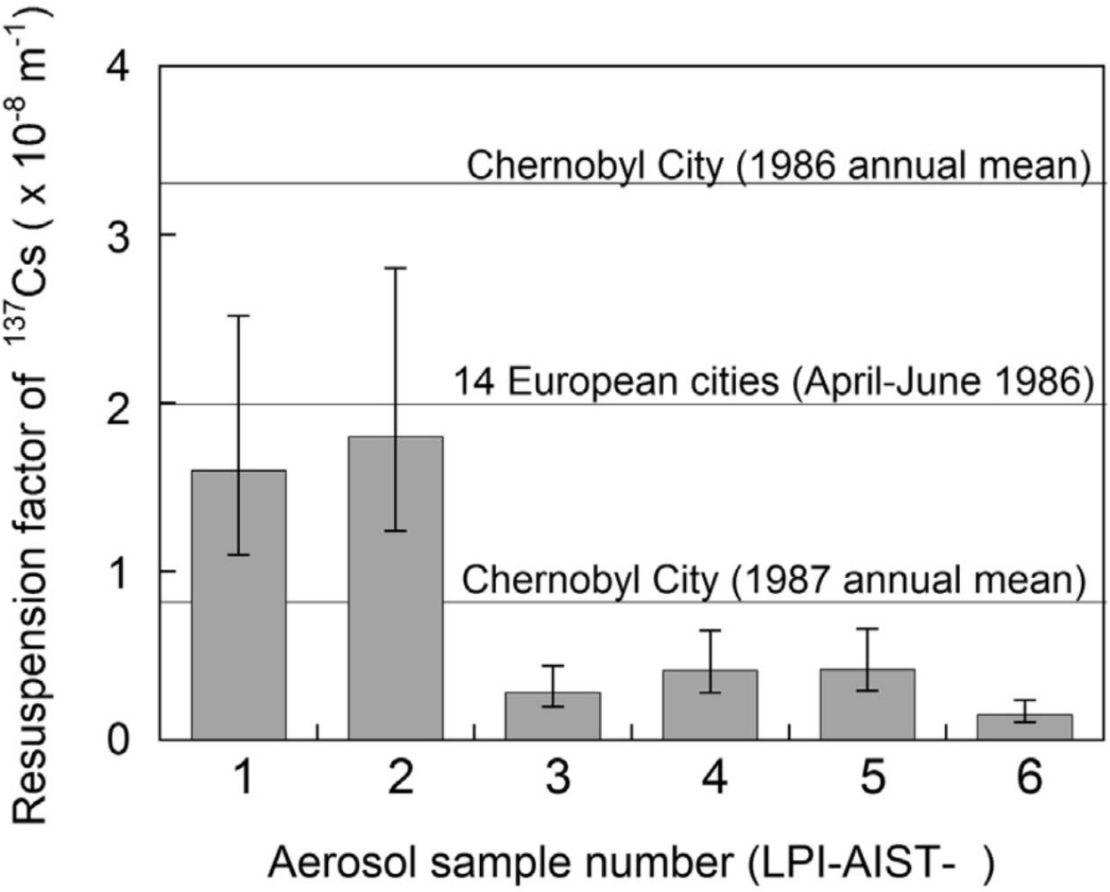

Figure 11: Resuspension factors of ^{137}Cs in aerosol samples collected during the time periods of Apr. 28-May 12 (1), May 12-May 26 (2), May 26-Jun. 9 (3), Jun 9-Jul.19 (4), Jul 19-Aug 21 (5) and Aug 21-Sept 21 (6) when 17.3 kBq m^{-2} was used as the average level of ground surface contamination with ^{137}Cs in Tsukuba. The error bars indicate the calculated maximum and minimum values when 25 and 11 kBq m^{-2}, respectively, were used as the ground surface ^{137}Cs contamination levels. The resuspension factors at Chornobyl City in 1986 (after May) and 1987 (annual mean) and averaged over 14 European cities in 1986 (April-June) are indicated by horizontal lines (Kaneyasu, 2017)

Kita et al (2020) studied the rain-induced biological resuspension of radiocaesium in two forest sites in Namie and Kawamata towns in Fukushima's exclusion zone in March 2011. The Namie site is located 30 km northwest of the F1NPP, and the Kawamata site is

approximately 6 km northwest of the Namie site. Studies showed that rain increased the radiocaesium in the air in forests due to splashes generated by rain droplets, which is the leading cause of the suspension of radiocaesium-bearing mould (Kita, 2020).

The literature review performed by Whicker (2021), showed that the measured resuspension factor found in the past ranges over nine orders of magnitudes, wind-driven resuspension factor ranges from 1×10^{-10} to 1×10^{-3} m^{-1}, and mechanical resuspension factor ranges from 1×10^{-9} to 1×10^{-1} m^{-1}. Whicker (2021) used the Equation to calculate the resuspension factor across the ecosystem, E.

$$\boldsymbol{RF_E = \frac{VMF_E}{v_d \rho_s S_d} + RF(0)e^{-\lambda t}} \qquad \textbf{(9)}$$

here, RF_E is the resuspension factor across the ecosystem, VMF_E vertical mass flux of the ecosystem, v_d is deposition velocity, ρ_s is bulk density of soil, $RF(0)$is resuspension factor at t = 0 after deposition, λ is half-time [40 days (Anspaugh, Shinn, Phelps, & Kennedy, 1975)], t is time in days.

The calculated resuspension factors across undisturbed and disturbed ecosystems based on past measurements from wind erosion research are shown in Figure 12 and Figure 13, respectively.

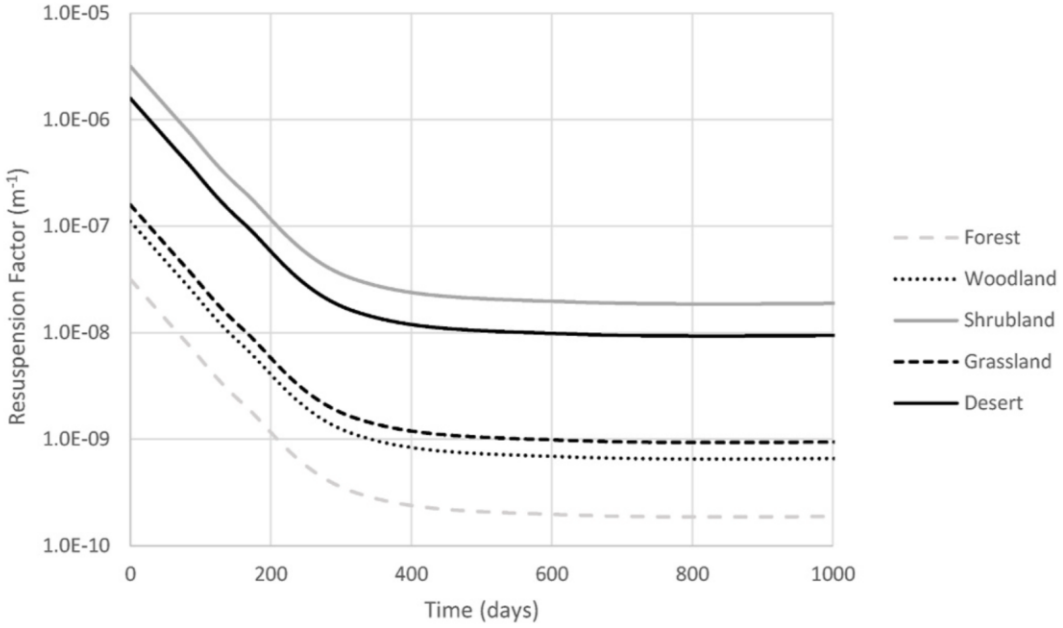

Figure 12: Resuspension factors as a function of time across an undisturbed ecosystem (Whicker, 2021)

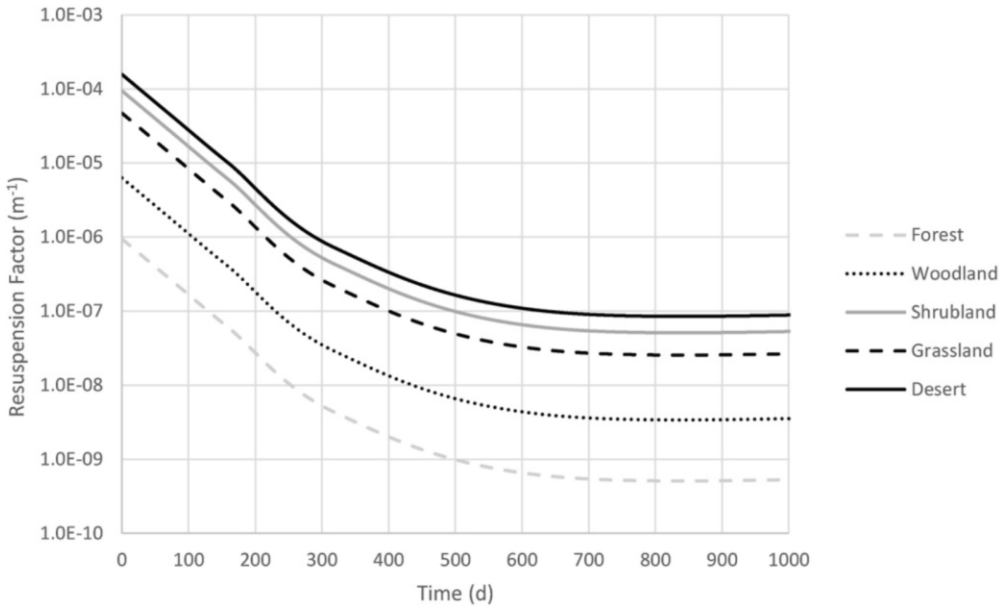

Figure 13: Resuspension factors as a function of time across disturbed ecosystems (Whicker, 2021)

Recent work performed by Tang, et al. (2022) approximately 25 km northwest of the F1NPP showed that radiocesium-bearing microparticles, composed of silicate glass, released to the atmosphere from this site continued to maintain the same annual resuspension frequency up to 2019 since the accident happened on March 2011without human interference. These samples were collected at 1.2 m above the ground onto quartz-fibre filters using 10 timer-controlled high volume (HV) air samplers at a frequency of 3 to 4 weeks samples.

2.6 Small-Scale Resuspension Studies

Small-scale resuspension studies will encompass both theoretical modelling and experimental studies (Goldasteh, Yilin, Goodarz, & Andrea, 2014). These studies were typically not motivated by large-scale direct application but rather by the necessity for a refined resuspension explanation. This microscopic approach looks at the forces acting on a particle under possible static and dynamic consequences on the particle.

The first documented literature review known to the author on small-scale particle resuspension was performed by Corn (1966). According to this review, particles in the laminar sublayer immediately re-entrain when the particle's drag force, somehow causing

particles to move upward against the adhesion forces. Instant entrainment of the particle occurs when the ratio between fluid to adhesion forces exceeds a specific threshold limit.

Since it was challenging to explain particles' kinematics during the entrainment process using quasi-static approaches, the concept of bursts became popular in studying the resuspension process; Cleaver and Yates (1973) used the idea of “turbulent bursts” or coherent boundary layer structures when deriving resuspension rate. This process involved visual observation of spatial and temporal burst distributions. According to Cleaver and Yates (1973), these bursts are the leading cause behind a fluid’s apparent random motion near its surface that will cause particles to resuspend before friction velocity reaches a specific threshold limit. Turbulent bursts will periodically and locally penetrate the laminar sublayer, causing particles to break free.

Reeks, Reed, and Hall (1988) proposed an energy-balance resuspension model in contrast to the previously proposed force-balance resuspension models. This model considers the fluctuating lift force for the turbulent energy transfer from the surrounding flow to surface particles. This model also illustrates the similarity between molecular surface desorption and turbulent flow-based particle resuspension.

Wen and Kasper (1989) have presented a kinetic particle re-entrainment model. They compared the model performance against both data from controlled experiments involving latex particles with aerodynamic diameters between 0.4 – 1 μm in high-purity industrial gas systems. This model uses a molecular desorption approach similar to that of Reeks et al. (1988) and gives similar results with regard to surface and gas concentration

decay over time. In addition, data collected in previous independent studies were also analyzed using the proposed model, and an acceptable level of model predictability was observed from the fitted models.

Another resuspension model of semi-empirical origin was developed by Fromentine (1989) to simulate the particle resuspension process for turbulent flow acting on a multi-layer deposit. This model simulates particle erosion, assuming that the resuspension occurs when the aerodynamic forces acting on the particles overcome adhesive forces. However, the concept of a single force acting on a single particle in monolayer resuspension is not realistic.

Fromentine (1989) studied the resuspension of multilayer deposits using the concept of resuspended cubes with the following assumptions:

(a) All cubes have the same arbitrarily selected size,

(b) Both aerodynamic and adhesive forces are acting on each cube,

(c) There are no interactions between cubes in the same layer.

Particles used in this experiment were made out of Fe_2O_3 and Sn. Experiments were conducted in both wet and dry conditions. The semi-empirical stochastic model developed by Fromentine (1989) simulated the behaviour of resuspension flux as a function of time for different flow velocities.

Braaten, Paw, and Shaw (1990) experimentally studied and examined surface particle resuspension solely from turbulent fluid forces by observation. Experiments were

conducted in an environmental wind chamber using thin beds of monodisperse lycopodium spores with a median count diameter of 27.8 μm. A consistent, well-developed turbulent boundary layer airflow at free-stream velocities of 6.0, 7.5, and 9.0 (m s^{-1}) was used to study the resuspension process of thin beds of lycopodium spores. Based on the studies, the threshold friction velocity concept was identified, and random resuspension was observed below threshold friction velocities. Based on experimental observations, a burst force magnitude as a function of time was suggested. Braaten, Paw, and Shaw (1990) also developed a Monte-Carlo-style model to simulate particle resuspension. This model was able to reproduce several features observed experimentally during particle resuspension.

Ziskind, Fichman, & Gutfinger (1995) presented the available theoretical models of particle resuspension, the most recent experimental investigations, dimensional analysis to compare experimental results amongst themselves and with theoretical predictions, modern view on the structure of the turbulent boundary layer, role on turbulent coherent motion on particle resuspension, adhesion of small particle to surfaces and finally analysis of hydrodynamic forces. Ziskind, Fichman, & Gutfinger (1995) divided theoretical models based on Force Balance and Energy Accumulation. Under force balance models, Cleaver and Yates (1973) presented the lift force acting on a particle experiencing an axisymmetric viscous stagnation flow due to a vortex burst near the wall by combining work done by (Goren, 1970) and (Laufer, 1975). The lift force due to turbulent burst, $F_{L,T}$, if presented as

$$\boldsymbol{F_{L,T} = 0.076\rho\nu^2 \left(\frac{d_p u_*}{\nu}\right)^3}, \qquad \textbf{(10)}$$

Cleaver and Yates (1973) assumed the lift force created by a turbulent burst is capable of lifting a neutrally buoyant sphere at least one diameter away from the wall. After the particle is lifted from the surface, the trajectory of the particle will be dictated by hydrodynamic lift and drag forces. As per Saffman (1965), (O'Neill, 1868) and (Goren, 1970), the hydrodynamic lift ($F_{L,H}$), and drag forces ($F_{D,H}$) are proportional to

$$\boldsymbol{F_{L,H} \sim \rho v^2 \left(\frac{d_p u_*}{v}\right)^3}, \qquad \textbf{(11)}$$

and

$$\boldsymbol{F_{D,H} \sim \rho v^2 \left(\frac{d_p u_*}{v}\right)^2}, \qquad \textbf{(12)}$$

As per Zimon (1982) all types of adhesive forces acting on particles are proportional to the particle diameter, and as per the observations by Zimon (1982), the drag force is larger than the lift force. Cleaver and Yates came up with the following criteria for immediate resuspension of particles:

$$\boldsymbol{\frac{lift\ force}{adhesive\ forces} \sim \frac{\rho v^2}{d_p}\left(\frac{d_p u_*}{v}\right)^3 > B'} \qquad \textbf{(13)}$$

here, the constant, B', was a function of particle shape and type of adhesion force.

The condition of removal of particles from the surface was written as,

$$\tau_w > \frac{B}{d_p^{4/3}} \qquad (14)$$

here, B is a constant for a given fluid.

Loosmore and Hunt (2000) have experimentally proven that, when abrasion is absent, a steady wind blowing on a smooth dust bed can result in a long-term steady dust flux even under the visual threshold levels of wind. These findings are similar to what Braaten, Paw, and Shaw (1990) found in their experiment using lycopodium spores. This work questions the appropriateness of predicting small fluxes that impact contaminant transport scenarios using current conceptual dust resuspension models where threshold velocity plays a significant role.

Fries (2000). introduced a generic-theoretical resuspension model akin to the one presented by Fromentine (1989), designed explicitly for multilayer aerosol deposits. This model represents the multilayer aerosol deposits as idealized lattice structures. A constant resuspension rate was observed for all surface particles dependent on flow conditions and particle diameter distribution. Also, a method utilizing constant resuspension rates for current monolayer models has been proposed to construct more complex multilayer models. However, there was no experimental evidence to validate the model. It was an attempt to deal with one of several remaining problems under the topic of monolayer vs.

multilayer. Once solved, multilayer resuspension would have a more accurate theoretical description.

Friess and Yadigaroglu (2002) considered the dependence on typical cluster behaviour and deposit structure when modelling multilayer aerosol resuspension. Unlike other proposed resuspension models, this model accounted for many unexplained experimental observations, such as removing fluffy deposits by simply blowing on them versus removing crusty structures using a knife.

Gillette, Robert, Lawson, and Thompson (2004a) attempted to model the resuspension of uniform spherical latex microspheres (2-8.1μm) using an experimental wind chamber. These microspheres were resuspended from a single ryegrass seed pod using mechanical forces arising from collisions between stationary objects and the grass as well as aerodynamic forces. It was determined that, within the wind speed range of 2-18.5 ($m\ s^{-1}$) and turbulent intensity of 0.1($m\ s^{-1}$), the mechanical impact causes a rise in resuspension particle flux leading to aerodynamic resuspension being dominated by mechanical resuspension for 2 μm sized particles. Contrarily, both mechanisms were observed to be equally effective in situations involving larger particles. The second phase of the work by Gillette et al. (2004a) involved comparing the contributions of mechanical and aerodynamic (turbulent and viscous) forces to particle resuspension. Again, the results showed that mechanical resuspension dominated 2 μm size particles in cases where mechanical impacts lead to increased resuspension particle fluxes.

Hubbard, Brockmann, Rivera, and Moore (2012) studied the impulse (mechanical) resuspension using Laser Doppler Velocimetry (LDV). Spherical polymethylmethacrylate (pmma) particles from 1.7 to 14.4 μm in diameter were dispersed into titanium dioxide and silicon dioxide wafers. These contaminated wafers were mechanically vibrated using 5 MHz piezoelectric transducers, introducing ~ 106 (m s^{-2}) acceleration, while resuspension ratios were quantified using LDV and digital microscopy.

Zhao Z. (2012) used the turbulent burst principle introduced by Cleaver and Yates (1973) to find the resuspension rate in a duct flow using the critical jump-start friction velocity.(u_c^*) as defined in Equation (15).

$$\boldsymbol{\alpha = \frac{u^{*\,2}}{u_c^{*\,2}}} \qquad \textbf{(15)}$$

here, α is a fraction of resuspended particles per turbulent burst and u^* is friction velocity. According to Zhao Z. (2012), the particle resuspension rate from a flat surface in a duct flow can be written using Equation (16).

$$\boldsymbol{R = \frac{\lambda}{\nu_f T_B^+}\frac{u^{*\,4}}{u_c^{*\,2}} exp\left(\frac{\lambda}{\nu_f T_B^+}\ \frac{u^{*\,4}}{u_c^{*\,2}} t\right)} \qquad \textbf{(16)}$$

here, λ is a fraction of the turbulent burst area compared to the typical area used to estimate the resuspension rate; please refer to Figure 14. The λ can be calculated as 0.0037and T_B^+

is equal to 75 and t is time. Figure 14 shows the particular distribution of the turbulent burst.

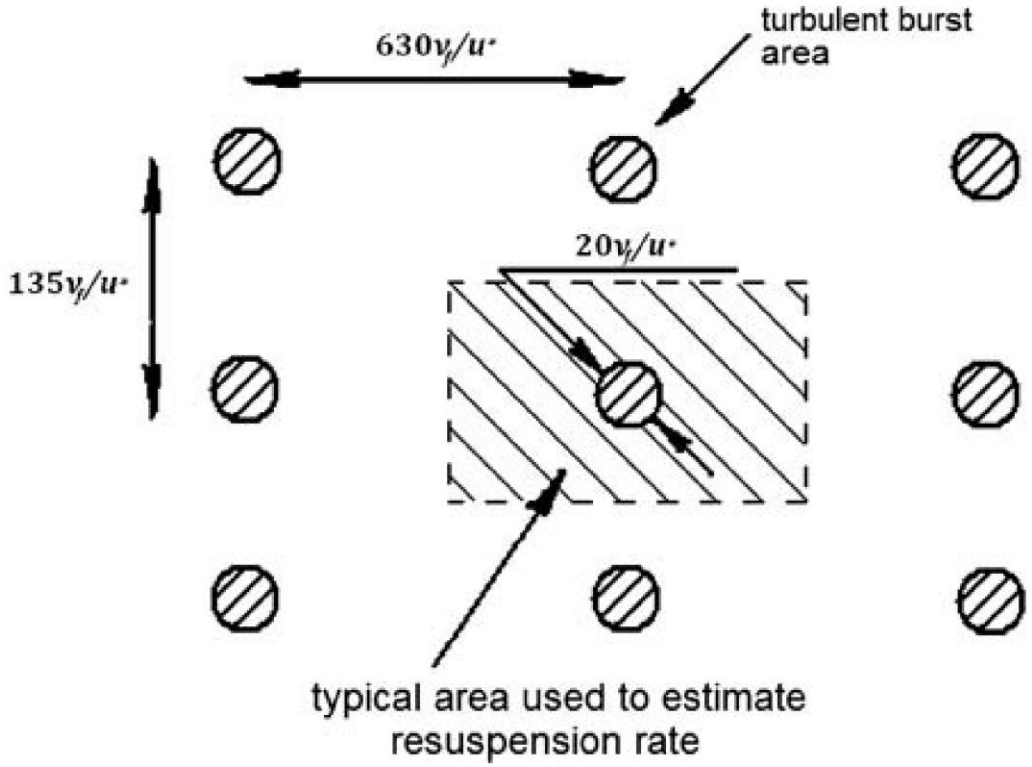

Figure 14: Schematic diagram showing the burst distribution on a ground surface used by (Zhu, Zhao, & Tan, 2012) based on Cleaver and Yates (1973). Here $\boldsymbol{\nu_f}$ is the kinematic viscosity of air and $\boldsymbol{u_*}$is friction velocity

As per Cleaver and Yates (1973), the approximate lateral and axial spacing between bursts were observed to be $\frac{135\nu_f}{u^*}$ and $\frac{630\nu_f}{u^*}$ The mean time between bursts and the mean

diameter of the burst were found to be $\frac{75\nu_f}{u^{*2}}$ and $\frac{20\nu_f}{u^*}$ respectively. Here ν_f is kinematic viscosity of air and u^* is friction velocity

2.7 Use of Computational Fluid Dynamics to model Particle Resuspension

The utilization of high computational power to simulate particle resuspension through Computational Fluid Dynamics (CFD) has significantly advanced our understanding of this complex phenomenon. In this pursuit, high-performance computers and supercomputers have been pivotal, furnishing the essential computational power to address the intricate calculations and simulations needed for comprehensive modelling of particle resuspension. CFD, in particular, offers distinct advantages over traditional experimental methods by providing a more comprehensive range of options and scenarios for studying particle resuspension, enabling researchers to explore conditions that may be impractical or impossible to replicate in a laboratory setting.

The International Standard Problem No 40: Aerosol Deposition and Resuspension by Castelo, Capito and De Santi (1999) was explicitly tailored not only to demonstrate the capabilities of currently available nuclear safety codes to predict radioactive aerosol deposition and resuspension after a severe nuclear power plant accident but also to aid in

finding weaknesses in each code and suggestions for possible improvements by comparing results found from STORM experiment conducted by Dilara, Karasenbrink, and Hummel (1998). The test section of the STORM experiment was made of a 5 m long straight pipe with an internal diameter of 63 mm. Tin oxide (SnO_2) was used as an aerosol with a particle size distribution of 0.43 μm geometric mean diameter and 1.7 geometric standard deviations. A mixture of gases was used as a carrier gas to study suspension and resuspension fractions under different velocity conditions. It was noted that the capability of reproducing experimental aerosol resuspension results using codes was greatly impeded by insufficient knowledge of each deposit's physical characteristics and the effective roughness of the pipe walls. Furthermore, the comparison of computer codes used during the International Standard Problem no. 40 showed that computer codes that were available had difficulties reproducing observed behaviour. (Castelo, Capitao, & De Santi, 1999).

Lengweiler (2000) used CFD-code TASCFflow (Ltd., 1993) to compare particle deposition onto floor, wall, and ceiling surfaces for indoor environments against experimental work. Lengweiler (2000) line fits the measured experimental resuspension rate data against turbulent kinetic energy. These line fits are given in Equations (17), (18), and (19) for the floor, wall and ceiling surfaces, respectively.

$$\boldsymbol{For\ floor \rightarrow\ \ r = 1.85\ x\ 10^{-4}\ k} \qquad \textit{(17)}$$

$$\boldsymbol{For\ walls \rightarrow\ \ r = 2.73\ x\ 10^{-4}\ k + 1.08\ x\ 10^{-4}} \qquad \textit{(18)}$$

$$\boldsymbol{For\ ceilings \rightarrow\ r = 3.94\ x\ 10^{-4}\ k + 1.47\ x\ 10^{-4}} \qquad \textit{(19)}$$

here, *r* is resuspension ate, and *k* is turbulent kinetic energy.

In (2000), Lengweiler employed continuity, Navier-Stokes equations, conservation of energy, and the *k*-ε turbulence model to obtain solutions for the converged computational domain. A comparison between the experimental results and the computational fluid dynamics (CFD) revealed a limitation in the CFD's particle deposition models, as they assumed that all particles entering the boundary cell would be deposited, rendering them incapable of accurately calculating deposition onto surfaces parallel to the mean flow.

Ziskind and Gutfinger (2002) modelled the gravity and shear effect on the particle motion in the turbulent boundary layer. The velocity flow field of the domain was formulated using unsteady 2D dimensionless Navier-Stokes equations and continuity equations. Governing equations were solved using the Runge-Kutta numerical scheme when the ceiling boundary of the computation domain was modelled using a dimensionless Equation (20), and the rest of the boundaries were introduced to produce inviscid irrotational flow fields to model a potential vortex in the plane (y-z).

$$w^* = w_0^* \sin\frac{2\pi z^*}{\lambda^*}\cos\omega^* t^* \qquad (20)$$

here, λ is the spanwise spacing of the computational domain, w_0 is the velocity parameter, and ω is the frequency. Five identical particles with a diameter of 4 μm were initially placed deep inside the viscous sublayer (one wall unit) and were released to the flow

domain with zero particle velocity and mean stream velocity in the Lagrangian frame of reference. Results showed that particles released with mean stream velocity followed the streamlines of the counter-clockwise secondary vortex, while the particles released with zero velocity moved rapidly away from the wall surface due to the effect of shear. It is noted that the shear effect on the particle due to flow is higher when the relative velocity between the particle and local velocity is higher (Ziskind & Gutfinger, 2002)

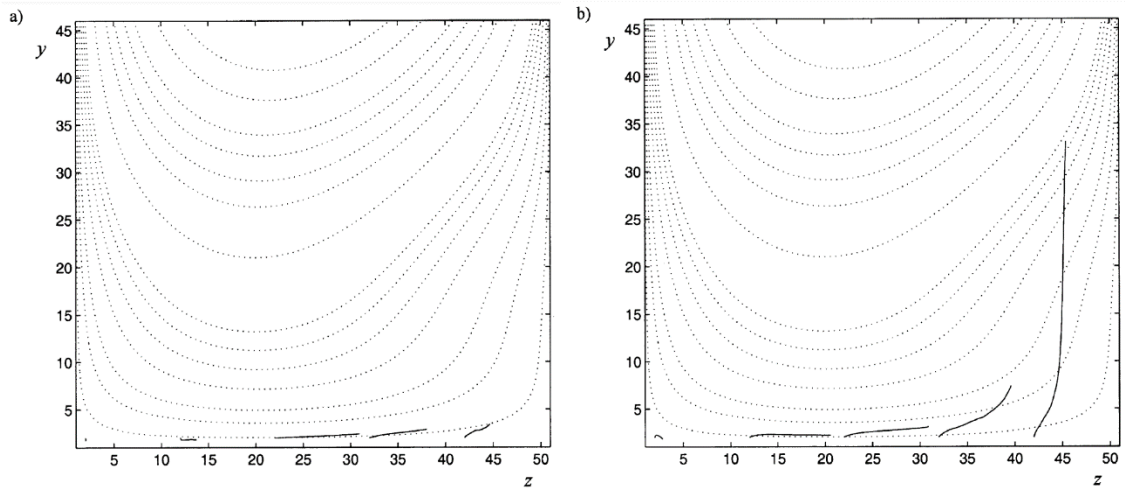

Figure 15:Particle paths of 4 μm particles that were released deep within the laminar sublayer at 5 streamwise locations (a) Particle release velocity is same as the mean stream flow velocity (b) Zero particle velocity.

Particle resuspension due to walking and vacuuming was modelled by DeGraw et al. (2006) using a standard CFD solver. A jet and a radially moving vortex were generated in CFD to model the foot movement. The particle transport model was one-way coupled

with the converged flow solutions. The wall shear along the near-wall flow structures was used to explore the particle resuspension in both cases.

Stempniewicz and Komen 2010 used the resuspension model implemented by. Stempniewicz (2009) looked into the SPECTRA thermodynamic safety analysis code to model the resuspension of radioactive graphite dust inside the primary cooling system of HTR/PBMR during LOCA. The SPECTRA code uses Equation (21) to calculate the resuspension rate when aerodynamic forces (F_{aero}) is equal for bigger than adhesive force (F_{a}) acting on the particles.

$$\boldsymbol{R_m = f_0\ exp\left[-C_1\left(\frac{F_a - C_2\ F_{aero}}{F_{aero}}\right)^{x_f}\right]} \qquad \textbf{(21)}$$

here, C_1, C_2, x_f and f_0 are user-defined coefficients.

Stempniewicz and Komen (2010) introduced two new resuspension models and Vainshtein and Rock'n Roll resuspension models into SPECTA code, and calculated resuspension factor results were compared against experimental results conducted at STORM experiment SR11under steady state and transient conditions. Stempniewicz and Komen (2010) mentioned that knowing about the adhesion force and the distribution of particles deposited onto the rough surface is vital to predicting particle resuspension successfully.

Kim, et al. (2010) developed three resuspension rate source terms that can be used to introduce resuspension at the boundaries of CFD models. The resuspension source codes were developed based on dimensional analysis, and derived model parameters were found by curve-fitting experimental resuspension data published by Ibrahim (2004) and Nicholson (1993). The table given in Figure 16 shows the dimensional variables for the resuspension rate (Λ) and dimensionless variables for dimensionless variable for $\Lambda\, d_\mathrm{p}/u_*$used in the 3 models. The $d_\mathrm{p}$is particle diameter, ρ_p is particle density, t is time, u_* is friction velocity, RH is relative humidity, z_0 is aerodynamic surface roughness length, A_{123} is Hamaker constant for Particle 1 and Surface 2 in Medium 3.

Model	Dimensional variables for Λ	Dimensionless variables for $\Lambda d_\mathrm{p}/u_*$
I	$d_\mathrm{p}, \rho_\mathrm{p}, t, u_*, \mathrm{RH}, z_0, A_{132}$	$\frac{u_* t}{d_\mathrm{p}}, \mathrm{RH}, \frac{z_0}{d_\mathrm{p}}, \frac{A_{132}}{d_\mathrm{p}^3 u_*^2 \rho_\mathrm{p}}$
II	$d_\mathrm{p}, \rho_\mathrm{p}, t, u_*, \mathrm{RH}, z_0, A_{132}, \rho_\mathrm{a}$	$\frac{\rho_\mathrm{p}}{\rho_\mathrm{a}}, \frac{u_* t}{d_\mathrm{p}}, \mathrm{RH}, \frac{z_0}{d_\mathrm{p}}, \frac{A_{132}}{d_\mathrm{p}^3 u_*^2 \rho_\mathrm{a}}$
III	$d_\mathrm{p}, \rho_\mathrm{p}, t, u_*, \mathrm{RH}, z_0, A_{132}, \rho_\mathrm{a}, \mu_\mathrm{a}$	$\frac{\rho_\mathrm{p}}{\rho_\mathrm{a}}, \frac{u_* t}{d_\mathrm{p}}, \mathrm{RH}, \frac{z_0}{d_\mathrm{p}}, \frac{A_{132}}{d_\mathrm{p}^3 u_*^2 \rho_\mathrm{a}}, \frac{\mu_\mathrm{a}}{d_\mathrm{p} u_* \rho_\mathrm{a}}$

Figure 16: Independent dimensional and dimensionless variables for the 3 resuspension rate models. The dimensionless variables were obtained using the Buckingham $\prod$ theorem (Kim, Gidwani, Wyslouzil, & Sohn, 2010)

Equation (22) shows the correlation for Model II. You can refer to the paper by Kim et al. (2010) for the rest of the correlations.

$$\frac{\Lambda\, d_p}{u_*} = 8.521 \times 10^{-3} \left(\frac{\rho_p}{\rho_a}\right)^{-0.3028} \left(\frac{u_* t}{d_p}\right)^{-1.0135} \left(\frac{z_0}{d_p}\right)^{-0.3269} \left(\frac{A_{123}}{d_p^3 u_*^2 \rho_a}\right)^{-0.3} \quad (22)$$

Gaudio, Malizia and Lupelli (2010) conducted experiments in the STARDUST facility to find the effect of geometrical features inside a vacuum chamber in a fusion reactor and determine the influence of temperature on dust resuspension. 2D FLUENT solver with a GAMBIT mesh generator was used to simulate the flow inside the STARDUST facility. CFD results for both velocity fields and resuspension rates matched with experimental results.

Bellecci et al. (2011) used a 2D FLUENT CFD finite volume code to simulate a low pressurization rate Loss of Vacuum Accident (LOVA) event inside an International Thermonuclear Experimental Reactor (ITER) vacuum vessel (VV) to find the fluid dynamics behaviour during LOVA and to justify the activated dust mobilization data using a much smaller facility, Small Tank for Aerosol Removal and Dust (STARDUST). The initial mesh of the 2D STARDUST facility had 59056 quadrilateral mesh cells. The model and the mesh were created using Gambit software. The compressible form of the continuity equation, momentum equations with gravity effect, energy equation and RNG-based *k-ε* turbulence closure models were solved until all residuals achieved convergence. The

turbulence intensity of 5% and turbulence length scale of 0.63 mm were specified at the two mass flow inlets of the STARDUST computational model. The mass flow rate of the inlet was defined by a function similar to the one found during the experiment to achieve a 300 Pa s^{-1} LOVA event. The governing equations were discretized using the MUSCL discretization scheme, and all gradients were estimated using the Green-Gauss node-based method. The AMD Phenom 9600, Quad-Core, 8GB of memory and a maximum speed of 2.26 GHz computer took 72 hours to achieve 4s transient solutions. In addition, the CFD simulation showed that velocity is one of the driving factors for particle resuspension.

According to van Hout (2013), local high-speed flow due to bursts is linked to particle resuspension events. Once the particles are resuspended, the small particles ($dp \leq 20$ μm) display a long-term suspension compared to larger particles, which undergo short-term suspension with parabolic trajectories. These saltated bigger particles will enhance resuspension due to impact with deposited clusters of particles on the surfaces, as shown in Figure 17 (Kok, Parteli, Michaels, & Karam, 2012).

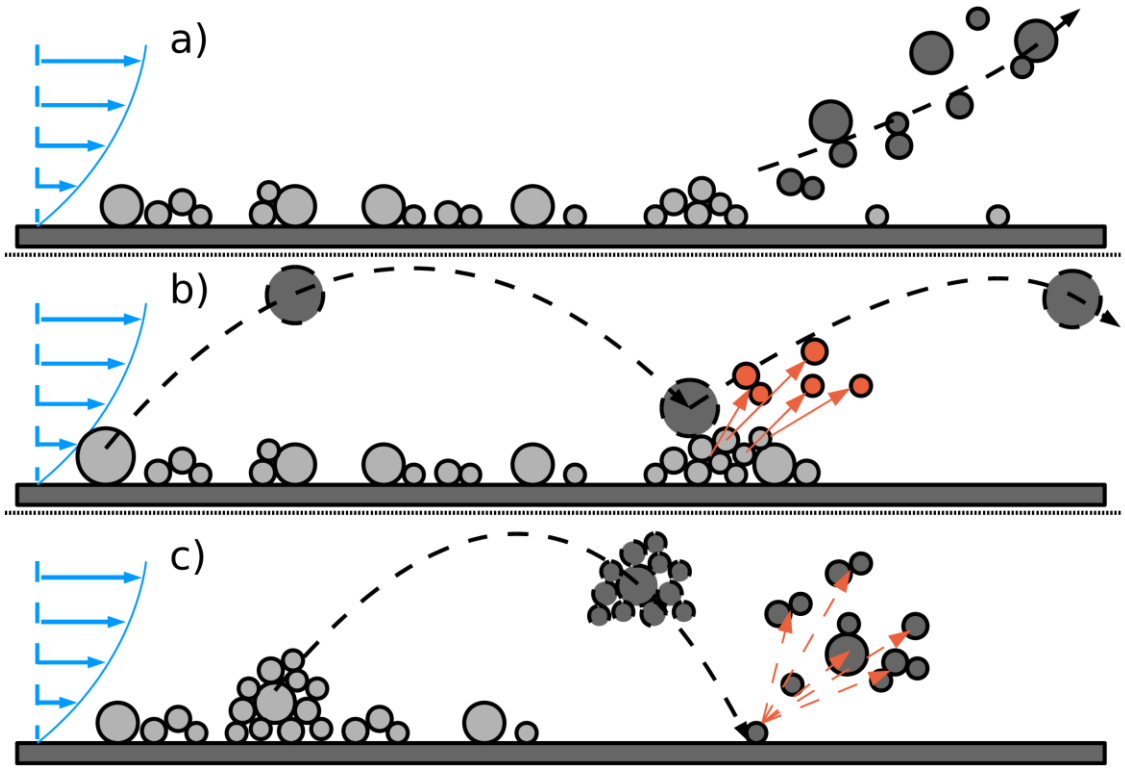

Figure 17: Illustration of the three dust emission mechanisms proposed by Kok, et al (2012) (a) aerodynamic re-entrainment, (b) resuspension following impaction of saltating particles, (c) breakage of saltating particle clusters after impaction

Peng, Zhang and Yanan Zhen (2014) used the CFD method to calculate the graphite dust resuspension in the HRT-10 steam generator. The computational domain of the axial cross-section of the heat transfer tubes inside a casing tube was built using 30,734 structure 2D mesh elements with y + less than 5. FLUENT 6.3.26 CFD code was used to solve the incompressible form of ideal gas Navier-Stokes Equation with RNG k-ε turbulence model using a finite volume method with a second-order central difference algorithm. The velocity and pressure were coupled using the SIMPLE algorithm, and the advection terms were discretized using a second-order upwind algorithm. The friction velocities along a

heat transfer tube were calculated using CFD after the solutions converged to 10^{-4} for velocity, k and ε and 10^{-6} for temperature. Peng, Zhang and Yanan Zhen (2014) found that particles less than 1 μm hardly got resuspended, while bigger particles increase the resuspension fraction as the particle size increases.

Henry and Minier (2014) conducted a thorough literature review on the progress of particle resuspension from the rough surface by turbulent flows. As per his review, Soldati and Marchioli (2009) simulated the deposition and entrainment of particles due to turbulent flow inside a fully developed gas-solid channel with 2h spacing between two non-slip walls using Direct Numerical Simulation (DNS) and complementary Large-Eddy Simulations (LES) via a pseudo-spectral approach by tracking particles in the Lagrangian reference frame. The computational domain size was $L_x \times L_y \times L_z = 4\pi h \times 2\pi h \times 2h$ in downstream, transverse and wall-normal directions. For the DNS approach, the continuity and conservation of momentum equations were solved, and for the filtered form of continuity and conservation of momentum, equations were solved with the dynamic SGS model (Germano, Piomelli, Moin, & Cabot, 1991). It was shown that the dynamics of the turbulent structure dominate the particle entrainment process closer to the wall surfaces. Figure 18 shows a snapshot of particle distribution driven by the coherent structure close to the wall surfaces. According to Soldati and Marchioli (2009), particles initially settled down into high-speed, high-shear areas ($\frac{\max \partial v'}{\partial z}$) creating brief clusters. These clusters will start splitting to the left and right of $\frac{\partial v'}{\partial z} = 0$ lines (black lines). This region is demarcated as Short-Duration Accumulatio (SDA) area in Figure 19. Then particles move in the spanwise

direction towards low-speed, low-shear stress region, forming more profound clusters that are flanking $\frac{\partial v'}{\partial z} = 0$ lines. This region is demarcated as Long-Term Accumulation (LTA) in Figure 19.

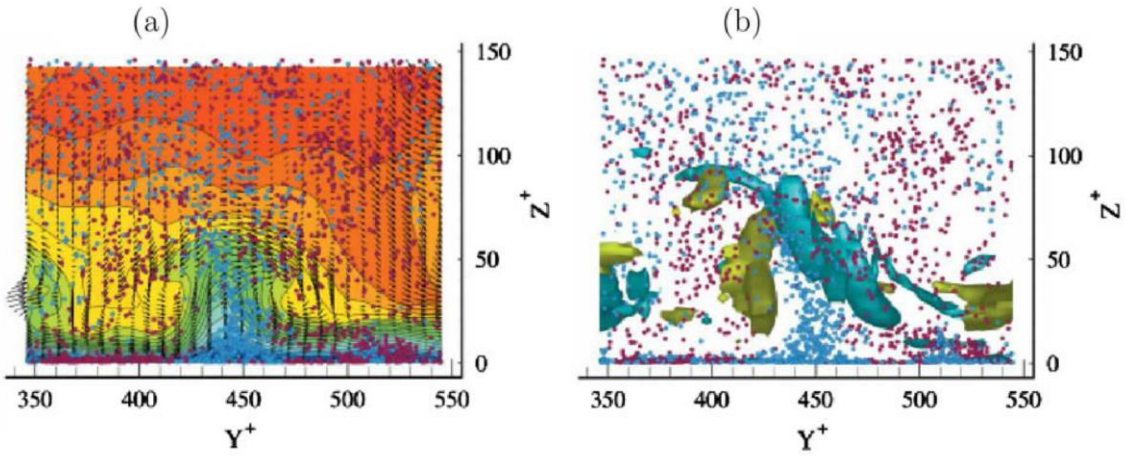

Figure 18: Cross-section of the flow field perpendicular to the streamwise direction. (a) Streamwise velocity contours and vectors and particle structure (b) Shows the clockwise (blue) and counter-clockwise (green) near wall vortex (Soldati & Marchioli, 2009)

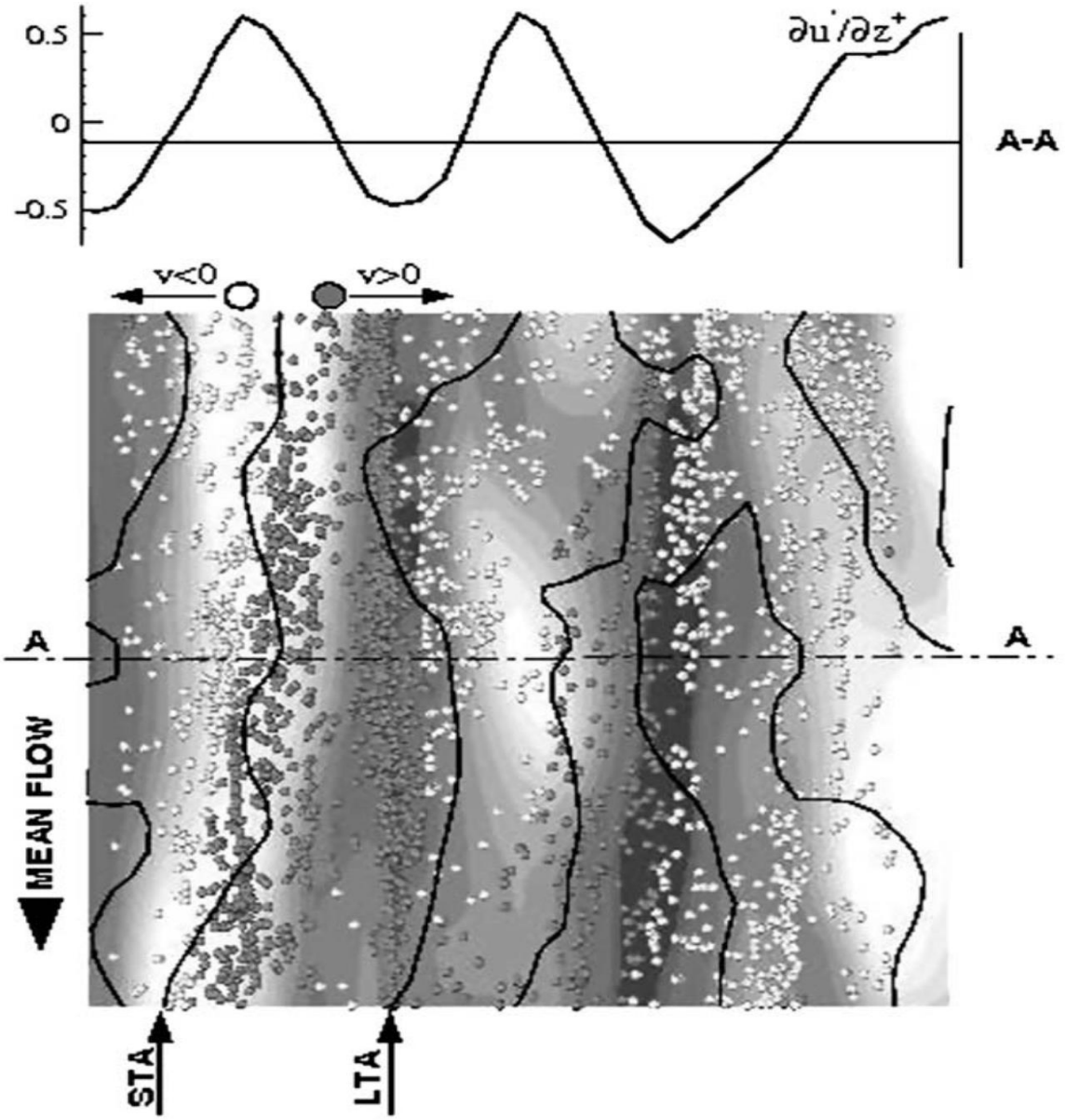

Figure 19 $L_x \times L_y \times L_z = 4\pi h \times 2\pi h \times 2h$: Instantaneous particle distribution in the viscous sublayer($0 < Z^+ < 5$). The computational window is 400 wall units long and 250 wall units wide in the (x, y) plane. The mean flow is directed top-down. The dark gray spheres represent particles with positive spanwise velocity ($v > 0$), moving from left to right and light gray spheres represent particles with negative spanwise velocity ($v < 0$), moving from right to left. Dark gray contours indicate high positive wall shear stress values, and white contours indicate low negative shear stress values. Black solid lines connect the point where wall stress is equal to zero. (Soldati & Marchioli, 2009)

Goldasteh, et al. (2014) developed an experimental setup to model the particle resuspension during walking at a speed of 0.5 steps/s in indoor settings and used the ANSYS-FLUENTTM CFD package to simulate the experimental setup. The shoe movement during the gait cycle was modelled in CFD using a dynamic mesh. A Reynolds Average Numerical Simulation (RANS) approach with RNG-*k*-ε turbulence models was used to simulate the unsteady flow under and around a shoe during a gait cycle. In the CFD model, particles with the same particle size distribution as measured were randomly distributed on the test section floor into the CFD model using a user-defined function (UDF). The particles suspend off rough surfaces due to rolling detachment from 3 contact bumps. The adhesion force at the moment of detachment is given by Equation (23) (Goldasteh, Yilin, Goodarz, & Andrea, 2014).

$$F_{P0}^{Rough} = \left(\frac{d}{n_u n_b \sqrt{N} K}\right)^2 \left[1.5\pi^2 n W_a \beta_r exp\left(-0.6/\Delta_c^2\right)\right]^3 \qquad (23)$$

here, d is particle diameter, n_u is a constant equal to 1, which corresponds to a uniform distribution of bumps, n_b= 1,2, …is the average spacing between bumps, *N* is the number of bumps, *K* is composite Young's modulus, n is the number of asperities per unit area, W_a is thermodynamic work of adhesion between particle and surface, $\beta_r = 1.485\sigma$ where σ is the root mean square of asperity height and Δ_c is a non-dimensional roughness parameter which ranges from 0.6 to 0.95. The suspended particles were tracked using the

Lagrangian approach, and the effect of instantaneous turbulent velocity fluctuations on the particle was simulated using a discrete random walk (DRW) model. The number of particles found in bins sizes 5-7 μm and 7.5-10 μm at various locations around the shoe during the gate cycle using CFD simulation were in good agreement with the experimental results (Goldasteh, Yilin, Goodarz, & Andrea, 2014).

Ali and Waller (2014) used coupled FLUENT CFD software and Monte Carlo radiation transport code, MCNP version 2.6.e, to calculate the radiation dose following a radioactive particle resuspension. The experimental setup (flow over a bluff body inside a wind chamber) was generated and meshed using Gambit software. The mesh had two million mesh nodes, and the Reynolds Average Numerical Simulation (RANS) approach with k-ε turbulence models was used to simulate the flow inside a wind chamber with a rectangular-shaped bluff body under an average wind speed of 6 m s^{-1}. ^{140}La spherical shape particles with sizes ranging from 1 to 6 μm were introduced to the converged CFD model one particle size at a time per simulation from contaminated plates on the floor just before the bluff body to simulate the particle resuspension due to the vortices generated in front of the bluff body. The suspended particles were tracked in the Lagrangian frame of reference, and particle numbers entering into virtual computational volumes were counted for each time step. Based on the particle information data file exported by FLUENT software, the volumetric activity of ^{140}La in individual spatial compartments was calculated using MATLAB code. Using MCNP software, the internal and external doses due to resuspended particles at two locations downstream of the contaminated plates were calculated (Ali & Waller, 2014)

Gélain, et al. (2015) performed a numerical simulation of ITER Tokamak during a Loss Of Vacuum Accident (LOVA) using ANSYS CFX computation fluid dynamics software to find velocity fields using a compressible unsteady solver. The Reynolds-Averaged Navier-Stokes (RANS) equations were employed to study turbulence in the vicinity of the lower region of a Tokamak. Two distinct turbulence models, namely the k-ε and k-ω SST models, were utilized in this investigation. The primary objective was to compute the friction velocities in order to assess the potential for dust particle resuspension. This assessment involved a comparison between the adhesive forces and the aerodynamic forces acting on microscopic particles, ranging in size from 0.1 to 30 μm, that had been deposited in the area. A comparison of results concluded that resuspension is possible during a LOVA. It was noted that further studies needed to be conducted to quantify the resuspension since many other factors, such as particle agglomerations, electric charge, and thermophoresis, could affect the resuspension process.

Ciparisse, Malizia and Poggi (2016) used multiphase CFD code COSMOL to understand the time evolution of two possible Chemical-Biological-Radiological-Nuclear-explosive (CBRNe) events and to model the resuspension of dust particles after a nuclear fusion plant accident in an enclosed environment. The two-phase flow governing equations: Average Density Equation, Continuity Equation, Navier-Stokes Equation, Mass Balance between the two-phase Equation, Momentum Balance between the two-phase Equation, Effective Viscosity Equation, Drag Coefficient Calculation (Schiller-Naumann Model), Particle-Based Reynolds Number, Energy Equation, Turbulent Kinetic Energy Conservation Equation, Turbulent Kinetic Energy Dissipation Rate Conservation

Equation, Turbulent Kinetic Energy Production Rate Equation, Turbulent Viscosity Equation and Perfect Gases State Equations were solved.

Assaad et al. (2020) developed a mono-layer particle resuspension model due to vibration and aerodynamic disturbances by coupling an analytical model with CFD. The CFD software ANSYS Fluent v17.2 was used to calculate the friction velocity. An unstructured, 3D dynamic mesh with 340,883 mesh elements with a moving floor plate at the center of the floor domain was used to model a rectilinear flow domain. The inlet of the flow domain and the air jets were selected as "velocity inlet" boundaries with constant velocities of 0.0135 m s^{-1} and 1.5 ms^{-1}, respectively. The chamber outlet was modelled as a "pressure outlet" boundary at 10 Pa gauge pressure, and the remaining boundaries of the computational domain were modelled as "wall" boundaries. The velocity of the Imping jets hitting the floor was 1.5 m s^{-1}, and the vibration acceleration and frequency of the sample plate on the middle of the floor were between 0%-20% g and 4-20 Hz, respectively. The time step size of 0.001s was selected to ensure the time step is smaller than the period of turbulent burst events and period of vibration. The governing equations were discretized using the second-order upwind scheme and pressure using the PRESTO scheme. The model was used to calculate the resuspension fractions (RF) due to aerodynamic forces and vibration on different surfaces; the RF increased by 48.4%, 60.5% and 63% for glass, marble and linoleum, respectively. It was shown that a decrease in surface roughness would increase adhesive forces and stiffness, hence reducing resuspension due to vibration.

Kottapali, et al (2023) established a relationship between shear stress and particle exposure time due to pulsated impinging jet on the explosive residual particle resuspension.

The shear stress acting on the particles was calculated using CFD methods, and the particle removal was observed using an optical analysis method. Kottapali, et al (2023) performed CFD simulations using ANSYS FLUENT 17. The Favre-averaged Navier Stokes equations and k-ω SST turbulence closure model were discretized using the QUICK scheme. Results showed that critical wall shear stress required to remove 25% and 50% of Royal Demolition Explosive (RDX) particles on a glass slide by an impinging jet decreases from 5 -10 µm equivalent diameter of particles and increases from equivalent diameters from 13 – 26 µm. It was also found that the rate of removal of RDX particles is inversely proportional to jet exposure time, especially for lower wall share stress. The RDX particles were exposed to shear stresses between 2 to 250 Pa during these experiments.

After a thorough literature review of past work in radiological particle resuspension and modelling methods, it has become evident that CFD will provide the tools to model the particle resuspension process successfully with the required accuracy and repeatability. In the context of resuspension studies following a dirty bomb event, computational fluid dynamics (CFD) has hardly been used to model large-scale resuspension studies in the past. With the advent of new computer technology, CFD can be used as a safe and convenient tool to model the flow fields in large and small-scale particle resuspension after an RDD event.

The following section under this chapter looks into the factors affecting particles exposed to wind from a microscopic perspective.

2.8 The journey of Resuspended Particles from the wall surface to Average Human Breathing Height

Based on the literature review performed on large-scale and small-scale radioactive particle resuspension studies, the journey of resuspended radioactive microscopic particles up to the human breathing level can be divided into three main stages (Perera, 2015):

Stage 1 – Wall region, where the movements of microscopic particles due to wind or mechanical shear are affected by the roughness elements of the wall (small-scale resuspension)

Stage 2 – Turbulent region, where the movements of the particles are affected by the free surface (small-scale resuspension)

Stage 3 - The region where the movement of the particles is affected by the atmospheric boundary layer and the canopy formed by the buildings, trees and other structures that will control the free stream airflow (large-scale resuspension)

Figure 20 shows the layout of three stages and microscopic particles sitting on a surface with a roughness of k.

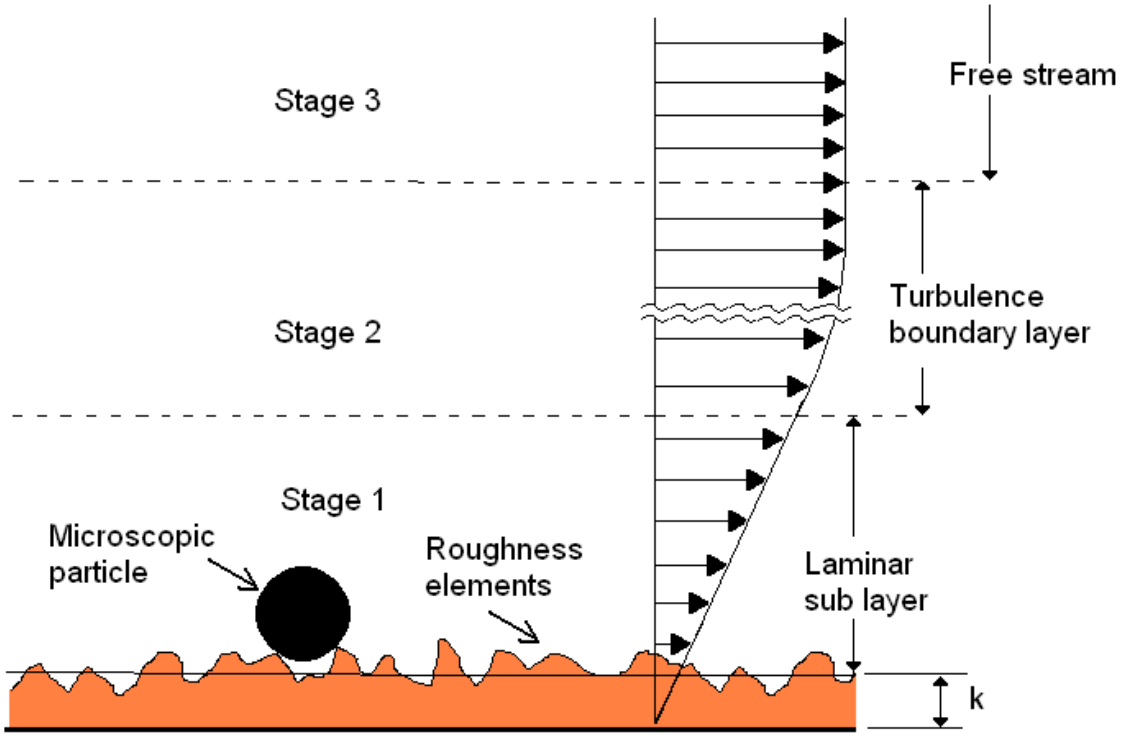

Figure 20: Velocity profile of the boundary layer (k- average surface roughness) and three stages of the resuspension process

2.9 tage 1: Wall Region

Due to aerodynamic forces, the initial resuspension of microscopic particles happens in the wall region. As depicted in Figure 21, freshly fallen microscopic particles can undergo suspension, saltation, creep, or a combination of these mechanisms.

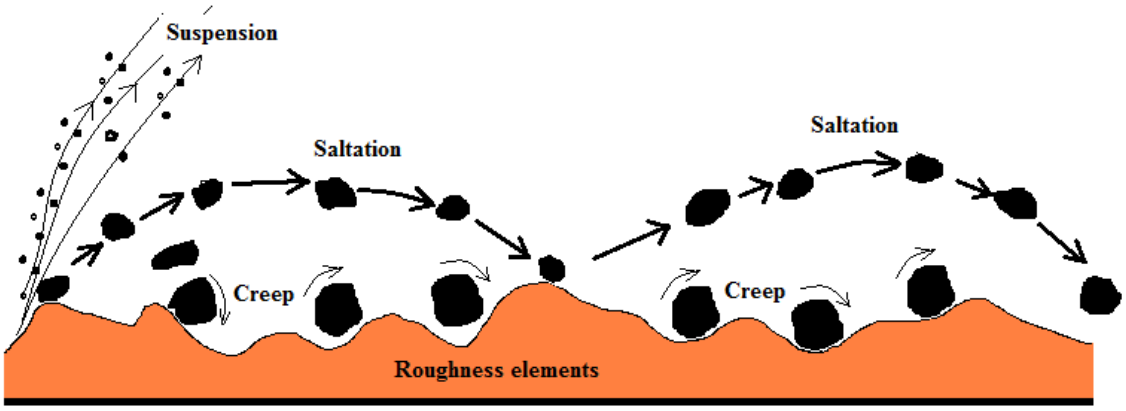

Figure 21: Different mechanisms of particle movement in Stage 1-wall region

The Stage 1 region can either be fully embedded in the laminar sub-layer or shared with the turbulent boundary layer's buffer region based on the heights of roughness elements (k) of the wall surfaces, particle sizes, and laminar sub-layer thickness.

The aerodynamic drag forces acting on microscopic particles depend on the flow velocity, particle shape, and particle size. The air velocity at the point of interest in Stage 1 can be found either using the velocity profile of the laminar sub-layer or by the velocity

profile of the turbulent boundary layer when roughness elements are protruding into the turbulent boundary layer.

2.9.1 Laminar Sub-Layer

The laminar sub-layer is the linear velocity profile found very close to the wall surface. The velocity profile of the laminar sub-layer can be written using Equation (24).

$$\left(\frac{\partial U}{\partial y}\right)_{l.s.l} = constant \qquad (24)$$

The constant in Equation (24) can be found simply by dividing the velocity at the edge of the laminar sub-layer by the laminar sub-layer thickness. The thickness of the laminar sublayer is usually found experimentally, but with computer power available today, CFD techniques can be used to calculate the thickness.

Freshly fallen radioactive particles after an RDD event will settle down over surface roughness elements on wall surfaces. Figure 22 shows the thickness of the laminar sublayer (δ') compared to the roughness element height (*k*).

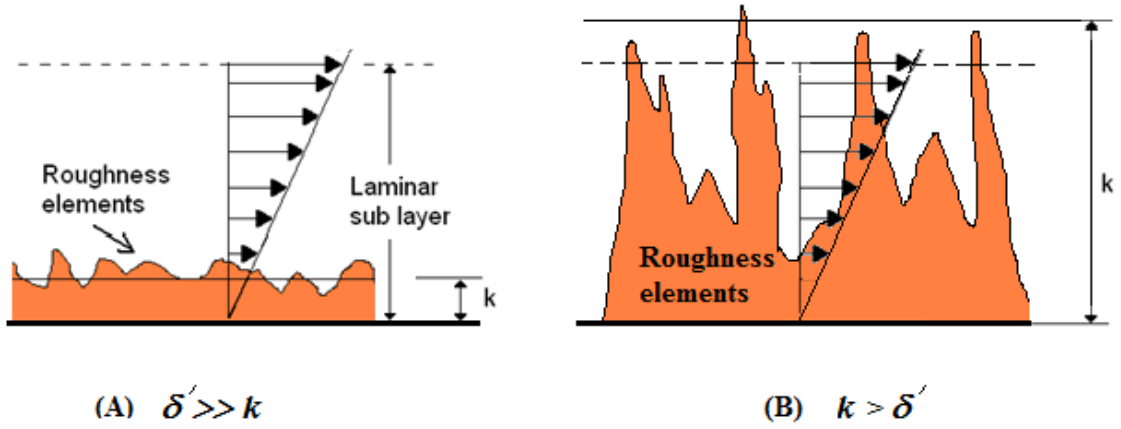

Figure 22: Extent of the laminar sub-layer: (A) when $k << \delta'$, (B) when $k > \delta'$, here δ' is the thickness of the laminar sub-layer and k is the height of the roughness elements.

Kim (1971) visually observed the turbulent flow close to the wall surfaces in an open surface water channel by releasing hydrogen bubbles inside a boundary layer in Transverse and Floor Normal directions. Kim (1971) found the mean values and temporal distribution of turbulent bursts, as shown in Figure 23.

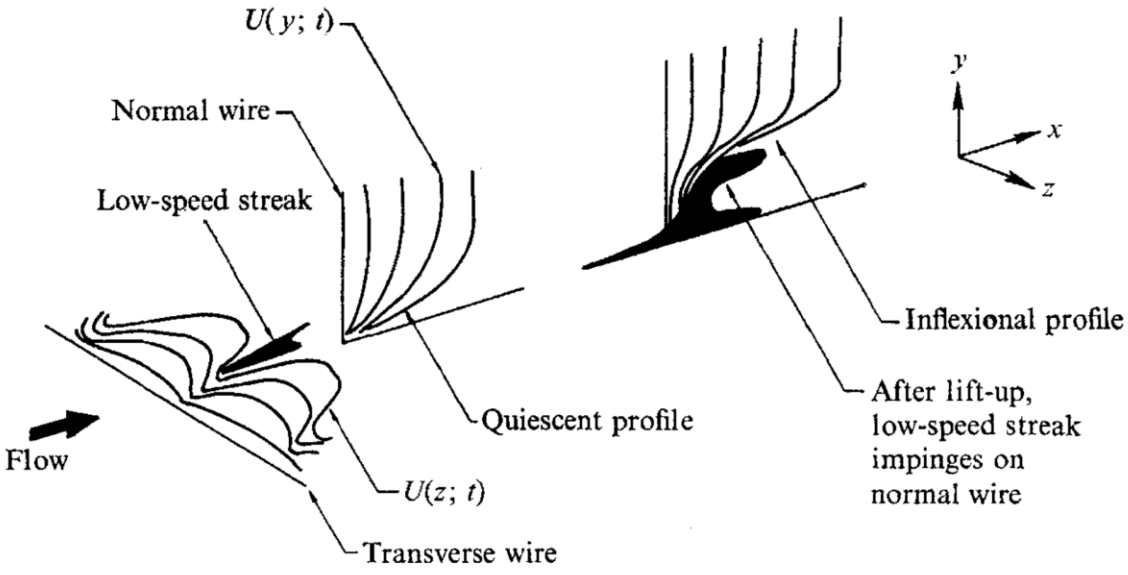

Figure 23:Typical lift-up stage of a low-speed streak during the bursting process according to Kim (1971).

Figure 24 shows the conceptual model of the turbulences near the wall during a cyclic process presented (Hinze, 1975). Hinze aimed to capture various ideas and experimental results regarding the boundary layer in this model.

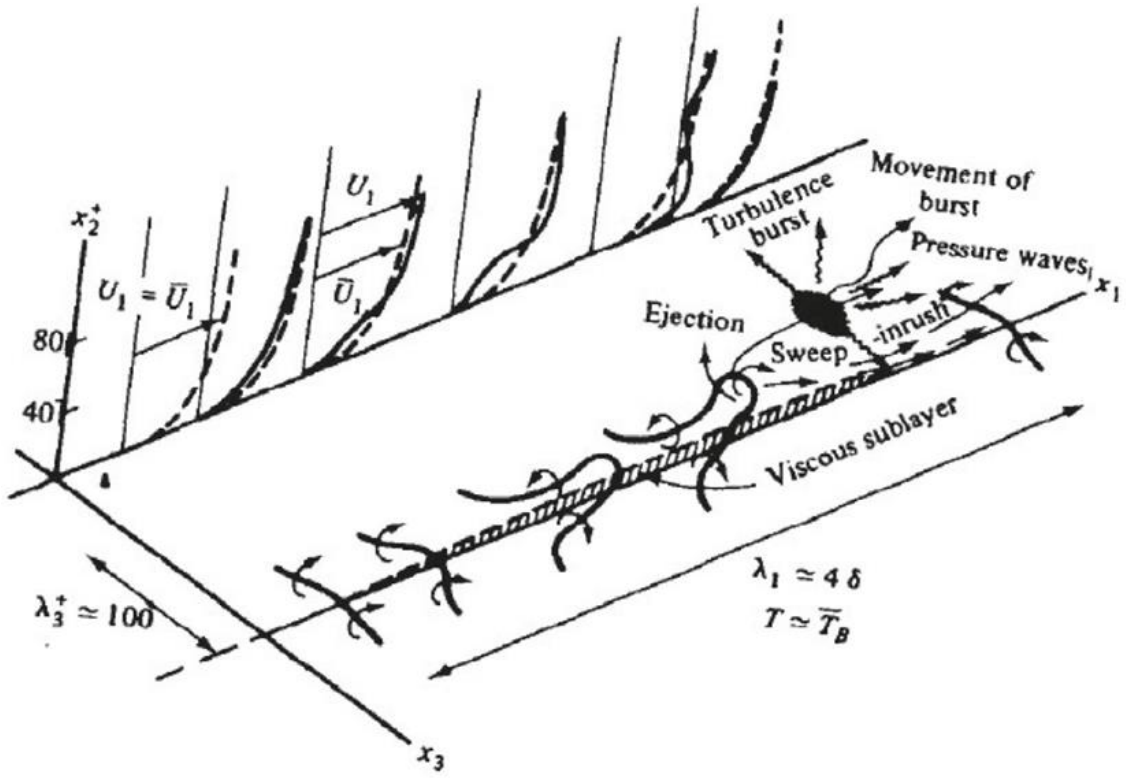

Figure 24: "Conceptual model of the turbulences near the wall" (Dennis, 1987), (from (Hinze, 1975))

Parameters x_1 and x_3 in Figure 24 are streamwise and spanwise distances, respectively, δ is the thickness of the boundary layer, λ_1 is the streamwise distance a vortex will travel from its birth to burst, $\lambda_3^+ = {\lambda_3 u_*}/{\nu}$ is the nondimensional spanwise distance between two vortex sheets, $x_2^+ = {x_2 u_*}/{\nu}$ is the wall-normal nondimensional distance, $\bar{U}_1$ is the velocity at the edge of the laminar boundary layer and U_1 is the instantaneous velocity of the boundary layer.

According to Hinze, 1975 a cylindrical shape vortex is formed very close to the wall surfaces due to large-scale disturbances from the wall region's outer part. This cylindrical vortex will eventually change its shape into a horseshoe vortex. The tip of the horseshoe vortex will start moving away from the wall due to self-induction and entering into an increasing velocity region (Dennis, 1987). This process will move low-momentum fluid away from the wall surfaces, creating a positive contribution to the horizontal shear layer at around $5 < x_2^+ < 30$, and it can be seen as an inflectional dent in the instantaneous velocity profile (Dennis, 1987). The inflectional instability in the instantaneous velocity will break down the vortex, causing a Turbulence burst. The pressure wave generated due to turbulence burst will create a sweep/inrush flow towards the wall. The horizontal sweep is retarded by the wall and will contribute to the birth of another vortex.

For smooth wall surfaces ($k << \delta'$), Ibrahim, Dunn & and Qazi (2008) developed Equation (25) to find the thickness of the laminar sublayer.

$$s' = 11.5\upsilon \left[\frac{\tau_0}{\rho}\right]^{\frac{1}{2}} \qquad (25)$$

here, υ is the kinematic viscosity of the air, and τ_0 is the shear stress of the wall surface and ρ is the density of continuous flow.

The burst and sweep action will bring particles away from the wall surfaces, as shown in Figure 25.

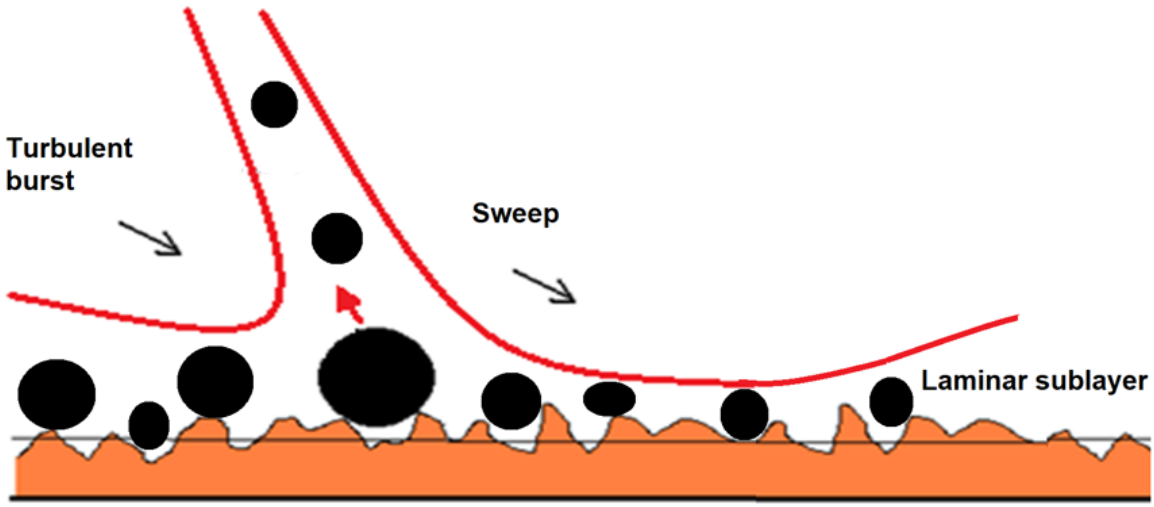

Figure 25:Entrainment of microscopic particles away from wall surfaces due to turbulent sweep and burst actions (Cleaver & Yates, 1973)

Figure 26 shows streamwise velocity vector plots of a turbulent channel flow close to a wall surface measured using a PIV system by Christensen and Adrain (2001) for the Reynolds number of 547.

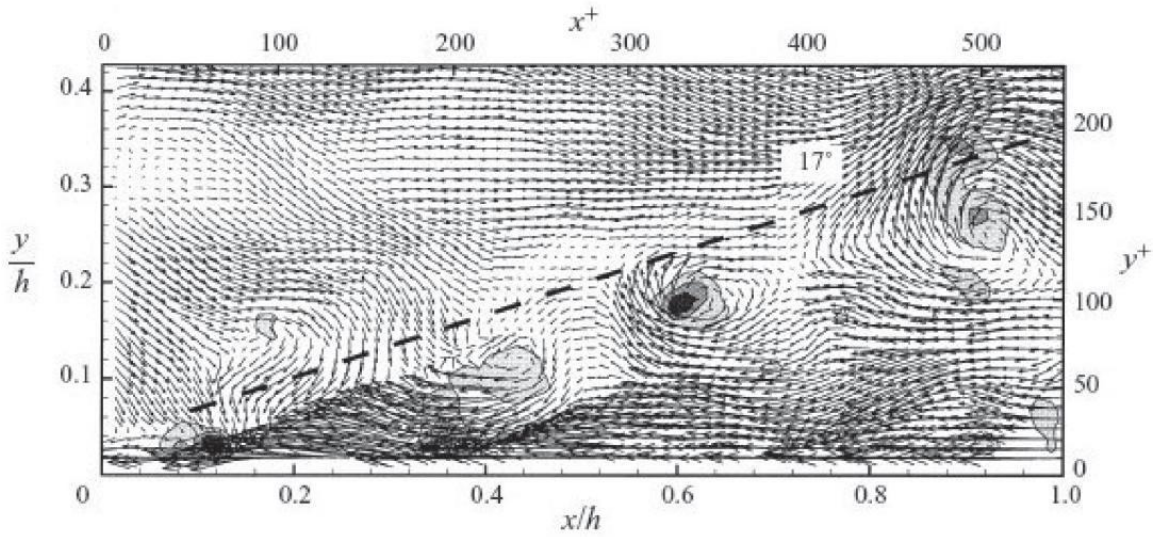

Figure 26: Instantaneous velocity vector plots in a turbulent channel flow at Re=547, with a constant convection velocity removed (flow moves from left to right) (Christensen & Adrian, 2001)

According to Figure 26, a vortex is formed very close to the floor surfaces and starts moving downstream at an angle of 17° with respect to the floor.

As discussed earlier, particles on rough surfaces can get directly lifted off, slide or roll due to external forces. The particles within the laminar sublayer detach from the surfaces mainly due to rolling (Brambilla, Speckart, & Brown, 2017), (Ibrahim, Dunn, & Qazi, 2008). Peillon, et al. (2022) presented the condition for rolling considering linear velocity gradient in the laminar sublayer.

$$F_{adh} > \left(\frac{1.4R_p}{a}\right) F_D + F_L \qquad \textbf{(26),}$$

here, $F_{adh}$is adhesion force, $R_p$is the radius of the particle, a is the horizontal distance between asperities/contact points, F_D and F_L are drag and lift forces acting on the particles.

$$\boldsymbol{F_L = (56.9 \pm 1.1) v^2 \rho \left(\frac{Re_p}{2}\right)^{1.87 \pm 0.04}} \qquad \textbf{(27),}$$

here, v is the kinematic viscosity of the fluid, ρ is the density of the fluid, Re_p is the Reynolds number of the particles.

For hard particles on a hard, rough surface, the adhesion force can be written as (Peillon, et al., 2022).

$$\boldsymbol{F_{adh} = \frac{ARe_p}{6z_0^2}\left[\frac{1}{1 + 58\frac{rmsR_p}{2\lambda_s^2}} + \frac{1}{\left(1 + 1.82\frac{rmsR_p}{z_0}\right)^2}\right]} \qquad \textbf{(28),}$$

here, A is the Hamaker constant, rms is the root mean square roughness, z_0 minimal distance, $\lambda_s$is the wavelength of surface roughness.

2.10 Stage 2: Turbulent Boundary Layer

The second stage of the resuspended particles is to entrain from the end of the laminar sub-layer (for smooth surfaces) or the lower part of the turbulent boundary layer (for rough surfaces) to the end of the turbulent boundary layer ($0.99U_x$, where U_x is the free stream velocity).

The Reynolds number of the flow at the location of interest will indicate the nature of the flow within the boundary layer, whether the flow is laminar, in the transition from laminar to turbulent or fully turbulent. The Reynolds number based on distance ($\mathbf{Re}_x$) along a flat plate is defined by Equation (29).

$$\boldsymbol{Re_x = \frac{\rho U_x x}{\mu} = \frac{U_x x}{\nu}} \qquad \textbf{(29)}$$

here, ρ is the density of air, U_x is the free stream velocity at the location x downstream and μ and ν are dynamic and kinematic viscosity of the air, respectively.

Figure 27 shows the top-view and side-view of developing flow over a flat plate presented by Schlichting, et al. (1996) and Cengel and Cimbala (2006). The boundary layer was tripped using a rectangular tripwire

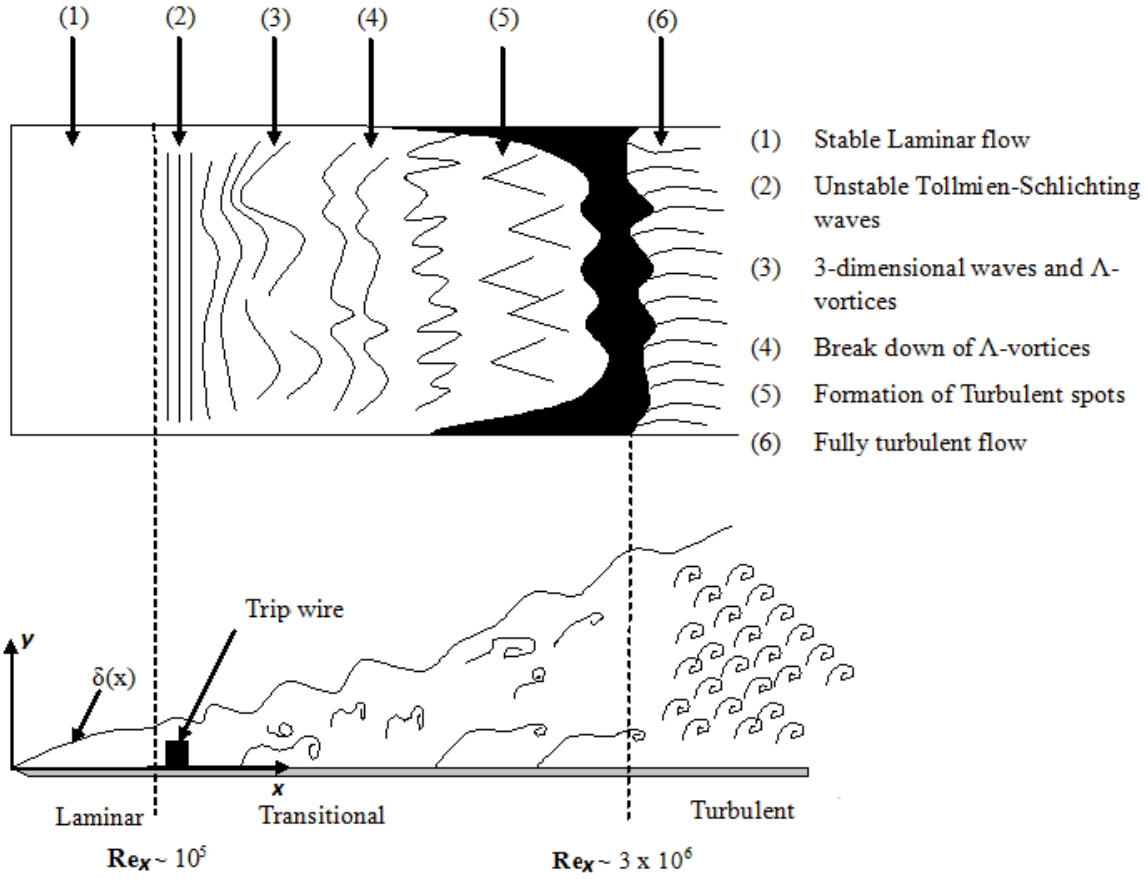

Figure 27: Top and side views of the boundary layer over a flat plate (not to scale). (Schlichting, et al., 1996) (Cengel & Cimbala, 2006)

The Reynolds number increases as the flow advances downstream from the tip of the flat plate. The boundary layer starts laminar at the beginning and turns turbulent as it grows. When the Rex of the flow over a smooth flat plate is less than the critical Reynolds number (Rex~105), the boundary layer is called the laminar boundary layer, and when the flow Reynolds number is higher than the critical Reynolds number (Rex ~ 3×10^6) the boundary layer is called the turbulent boundary layer. The boundary layer between these two Reynolds numbers is the transitional boundary layer (Cengel & Cimbala, 2006).

A semi-empirical log law relationship can be used for the turbulent boundary layer to find the velocity distribution (Muralidhar & Biswas, 1999). The horizontal velocity profile of the turbulent boundary layer can be written as Equation (30)

$$\frac{U}{U_*} = \frac{1}{\kappa} log\left(\frac{U_* y}{\upsilon}\right) + B \qquad (30)$$

here, U is the horizontal velocity component, U_* is the friction velocity as defined by Equation (31), κ is von Kármán constant [0.41], and B = 5.0 to 5.5, ν is the kinematic viscosity of the air, and y is wall-normal distance.

$$U_* = \left(\frac{\tau_0}{\rho}\right)^{\frac{1}{2}} \qquad (31)$$

The log law deviates from experimental values close to the wall since log[0] is undefined. On the other hand, Spalding's law of the wall given by Equation (32) is a creative expression to find the velocity distribution all the way to the wall surfaces (Cengel & Cimbala, 2006); one equation can be used to map the velocity profile from the edge of the laminar sub-layer to the free stream velocity.

$$\frac{yU_*}{\nu} = \frac{U}{U_*} + e^{-\kappa B}\left[e^{\kappa\left(\frac{U}{U_*}\right)} - 1 - \kappa\left(\frac{U}{U_*}\right) - \frac{\left[\kappa\left(\frac{U}{U_*}\right)\right]^2}{2} - \frac{\left[\kappa\left(\frac{U}{U_*}\right)\right]^3}{6}\right] \qquad (32)$$

here, U is the horizontal velocity component U_* is the friction velocity as defined by Equation (31), κ is von Kármán constant [0.41], and B = 5.0 to 5.5, ν is the kinematic viscosity of the air, and y is wall-normal distance.

2.11 Stage 3: Free Stream

The third stage of the resuspension process brings particles from the edge of the boundary layer to target average human breathing height (h) at a distance (d) downstream from the initial fall out, as illustrated by Figure 28.

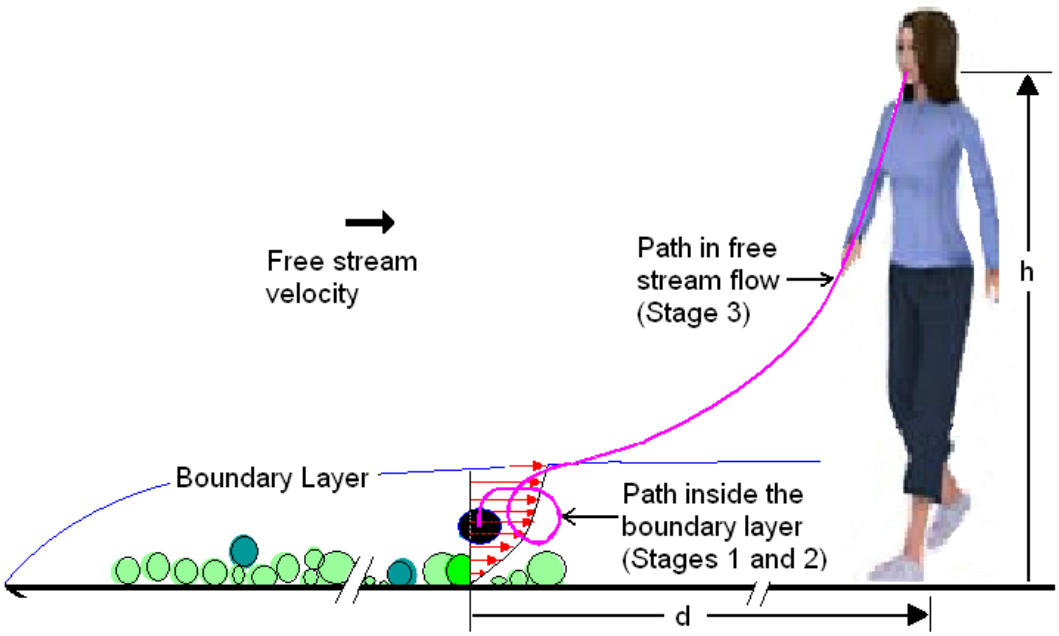

Figure 28: Particle path up to an average human breathing height (*h*)

In Stage 3 of the resuspension process, respirable range particles follow the streamlines' path inside the atmospheric boundary layer.

2.11.1 Atmospheric Boundary Layer

The Atmospheric Boundary Layer (ABL) is often turbulent. However, according to Troen and Peterson (1989), the velocity profile of the ABL at neutral conditions (negligible thermal effects) can be defined by Equation (33).

$$\frac{U(Z)}{U_*} = \frac{1}{\kappa} ln\left[\frac{Z}{Z_0}\right] \qquad (33)$$

here, Z_0 is the elevation measured in meters, Z_0 is the roughness length representing different terrains as given in Table 3, U_* is the friction velocity, and κ is the von Kármán constant [0.41].

Table 3: Classification of terrains by their roughness length, adapted from the European wind atlas (Troen & Petersen, 1989) (Crasto, 2007)

Class	**Terrains**	***Zo* (m)**
I	Muddy terrains, wetlands, icepacks	$10 \times 10^{-6} – 30 \times 10^{-6}$
	Water areas	$30 \times 10^{-6} – 200 \times 10^{-6}$
II	Sand	$200 \times 10^{-6} – 1 \times 10^{-3}$
III	Airport runway areas, mown grass	$1 \times 10^{-3} – 1 \times 10^{-2}$
IV	Farmland/Airports with very few trees, buildings, etc.	$1 \times 10^{-2} – 4 \times 10^{-2}$
V	Many trees and /or bushes	$4 \times 10^{-2} – 100 \times 10$-2
VI	Forests, suburbs	$100 \times 10^{-2} – 1$
VII	Cities	1 – 4

The ABL can be subdivided into three layers: the canopy layer, the surface layer, the Ekman layer, and the free atmosphere, where frictional forces are negligible (Crasto, 2007). Figure 29 shows the layout of the ABL.

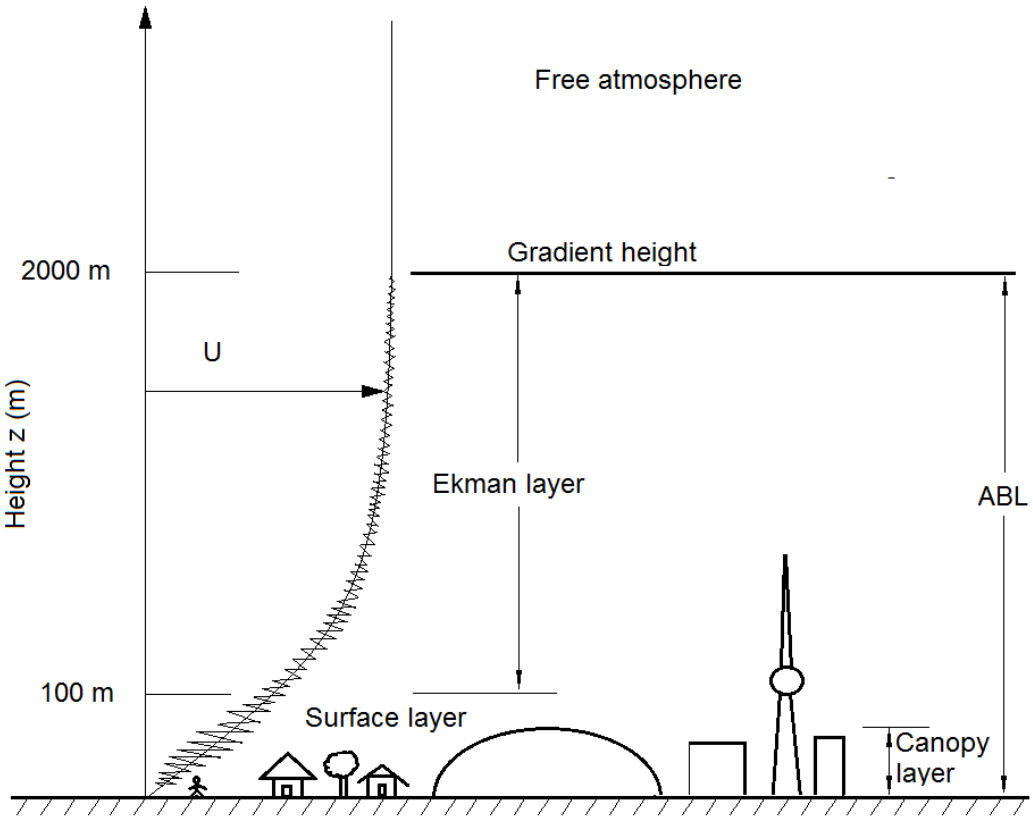

Figure 29: Subdivision of the ABL, adapted from (Crasto, 2007)

As shown in Figure 29, the boundary layer is formed by the obstacles attached to the ground called the canopy layer, where most of the local resuspension process takes place due to turbulences (Crasto, 2007). The flow field inside the canopy layer can be very

complex and governed by the layout and shapes of the obstacles. In urban settings, these obstacles can be buildings, vehicles, trees, etc, varying in size from a few centimetres to a few hundred meters.

The boundary layer above the canopy layer is called a surface layer and usually extends up to one-tenth of ABL's elevation. The outer layer of ABL is called the Ekman layer, which is affected by the earth's rotation utilizing Coriolis forces (Crasto, 2007).

Particles that were moved from Stage 2 of the resuspension process to the canopy layer can be inhaled by humans inside this layer or moved into the surface layer or to the Ekman layer by vortices generated by the obstacles in the canopy layer. Particles transported to the surface layer or the Ekman layer will travel long distances before they fall back onto the ground, imposing a health hazard to people living far away from the initial fallout.

2.12 Forces Acting on Particles during the Resuspension Process

Forces imposed on particles due to mechanical or wind disturbances may have the ability to overcome the particle’s bonding forces (capillary, van der Waal’s or electrostatic) and forces due to gravity, resulting in immediate suspension, saltation or creep of the particles. The most common models that examine particle resuspension at the microscopic

level are the Rock'n'Roll model, the Force Balance Model and the Energy-Accumulation Model (Reeks & Hall, 2001), (Cleaver & Yates, 1973) (Reeks, Reed, & Hall, 1988).

2.12.1 Force Balance Model

The particle removal rate in the Force Balance Model is measured based on visual observations of the spatial distribution and the frequency of turbulent ejections near the particle's deposited surface (Cleaver & Yates, 1973)

According to the force balance method, particles in the laminar sublayer region can immediately re-entrain when the ratio between the resulting aerodynamic lift force and adhesive force exceeds a threshold value. The threshold value (B'), which is a function of particle shape and type of adhesion force, is shown in Equation (34) (Van Hout, 2013) (Ziskind, Fichman, & Gutfinger, 1995).

$$\frac{\boldsymbol{lift\ force}}{\boldsymbol{adhesive\ forces}} \sim \frac{\boldsymbol{\rho\, v^2}}{\boldsymbol{d_p}}\left(\frac{\boldsymbol{d_p u_*}}{\boldsymbol{\nu}}\right)^{\boldsymbol{3}} > \boldsymbol{B'} \qquad \textbf{\textit{(34)}}$$

here, ρ is the particle density, d_p is particle diameter, ν is the kinematic viscosity, u_* is friction velocity and B' is a function of the type of adhesion force, particle shape and adhesion force distribution (Reeks, Reed, & Hall, 1988), (Wen & Kasper, 1989).

2.12.2 The Rock'n'Roll (R'n'R) model

The Rock'n'Roll (R'n'R) model is based on the aerodynamic forces acting on a particle located in the boundary layer. The energy spectrum of a particle's fluctuating lift and drag forces can be measured using experimental methods. Figure 30 illustrates the forces acting on a particle according to the Rock 'n' Roll model (Reeks & Hall, 2001).

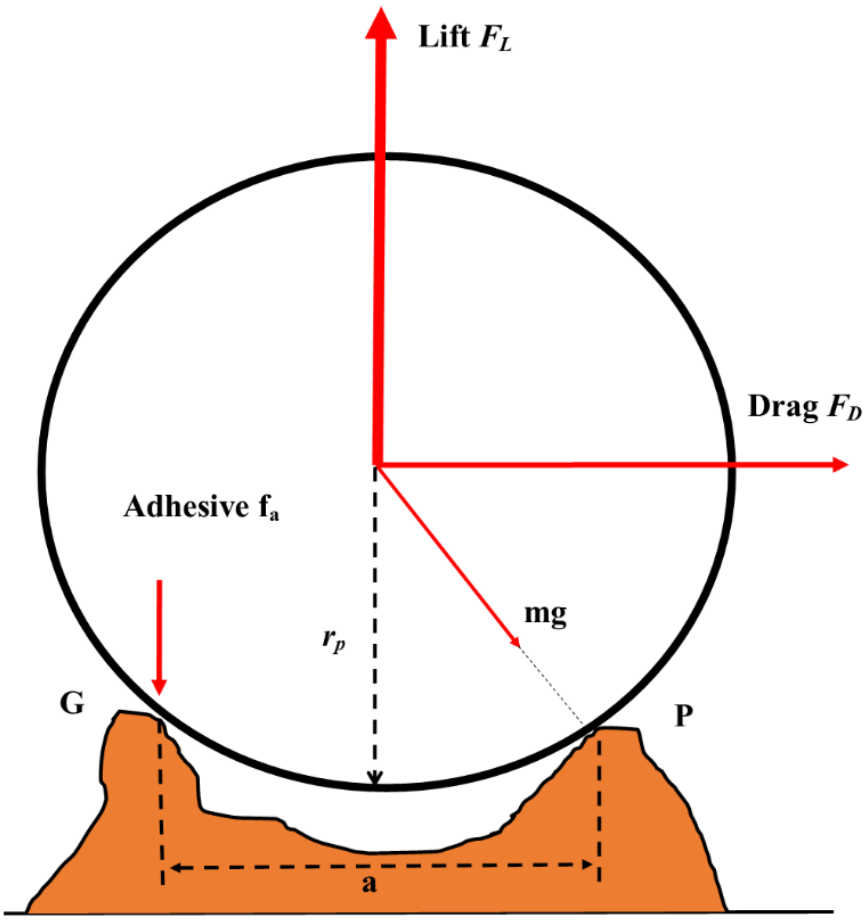

Figure 30: Forces acting on a particle according to the Rock 'n' Roll model (Reeks & Hall, 2001)

According to the Rock 'n' Roll model, particles will move from their deposited location when the resulting moment acts on the particle with respect to location P due to lifting force (F_L) and drag force (F_D) exceeds the moment due to adhesive force. This model is represented in Equation (35):

$$\frac{a}{2}F_L + r_p F_D > a f_a \qquad (35)$$

here, a is the distance between locations where the particle touches the ground, and r_p is the particle radius.

According to the correlations developed by Biasi, De Los Reyes, Reeks, & De Santi (2001), the geometric normalized adhesive force ($\overline{f_a} = {F_{adh}}/{F_a}$) and standard deviation of the distribution of this adhesive force (σ_a) acting on particles deposited in irregular surfaces can be written as in Equations (36) and (37), respectively. Here $F_{adh}$is the adhesive force, F_a is the adhesive force for perfect smooth contact. Here $F_a = 4\pi\gamma r$, where γ is adhesive surface energy and r is the radius of the spherical particle.

$$\overline{f_a} = 0.016 - 0.0023(r^p)^{0.545} \qquad (36)$$

here, $r^p$is the radius of the spherical particle measured in micrometres.

As per Reeks and Hall (2001), adhesive forces have a log-normal distribution due to the interaction between the particles and rough surface with a standard deviation of σ_a given by Equation (37). The adhesive forces between surface and particle are small when particles sit on top of the asperities, and adhesive forces are high when particles or particles' roughness elements are inside the surface roughness elements.

$$\sigma_a = 1.8 - 0.136(r^p)^{1.4} \qquad (37)$$

Reeks and Hall (2001) presented the mean drag force, $\langle F_D \rangle$, and mean lift force, $\langle F_L \rangle$, for a spherical particle of radius r as

$$\langle \boldsymbol{F_D} \rangle = \mathbf{32}\boldsymbol{\rho_f \nu_f^2}\left[\frac{\boldsymbol{ru_*}}{\boldsymbol{\nu_f}}\right]^{\mathbf{2}} \quad \textit{(38)}$$

and,

$$\langle \boldsymbol{F_L} \rangle = \mathbf{20.9}\boldsymbol{\rho_f \nu_f^2}\left[\frac{\boldsymbol{ru_*}}{\boldsymbol{\nu_f}}\right]^{\mathbf{2.31}} \quad \textit{(39)}$$

where, ρ_f is the fluid density, ν_f is the fluid kinematic viscosity and u_* is friction velocity.

2.12.3 Energy-Accumulation Model

With the Energy-Accumulation Model, a particle is resuspended when it has absorbed enough vibrational energy to overcome the adhesive surface barrier/potential well at the point of detachment (Reeks, Reed, & Hall, 1988). The shape and the height of the potential well are modified by the energy transferred by the fluctuating lift component. The equations of motion of the particle under the fluctuation lift force are given below (Reeks, Reed, & Hall, 1988).

$$\frac{du}{dt} + \beta u + \omega^2 y = m^{-1} f_L(t) \,, \qquad \frac{dy}{dt} = u \qquad (40)$$

here, u is velocity, t is time, β is the damping term, ω is natural frequency, m is the mass of the particle, and f_L is fluctuating lift component. Typically, ω is around 107 Hz for a 10 µm spherical particle on a flat plate (Ziskind, Fichman, & Gutfinger, 1995).

According to Reeks, Reed and Hall (1988) the probability of particle release per unit time is given by Equation (68).

$$p = \frac{\omega_0}{2\pi} exp\left(-\frac{Q}{2\langle PE\rangle}\right), \qquad (41)$$

here, ω_0 is the typical frequency of vibration, Q is the height of the potential well, and $\langle PE\rangle$ is some average potential energy.

According to Wang (1990) particles can lift off, slide or roll when the following conditions are achieved.

$$F_L > F_A + F_G \qquad direct\ liftoff \qquad (42)$$

$$F_D > k(F_A + F_G - F_L) \qquad sliding \qquad (43)$$

$$F_D\, d_p/2 + (F_L - F_G)\, a/2 > F_A\, a \qquad rolling \tag{44}$$

here, F_{L} is lift force, F_A is adhesive force, F_G is the force due to gravity, d_p is particle diameter, k is the friction coefficient, and a is the horizontal distance between two asperities as shown in Figure 32.

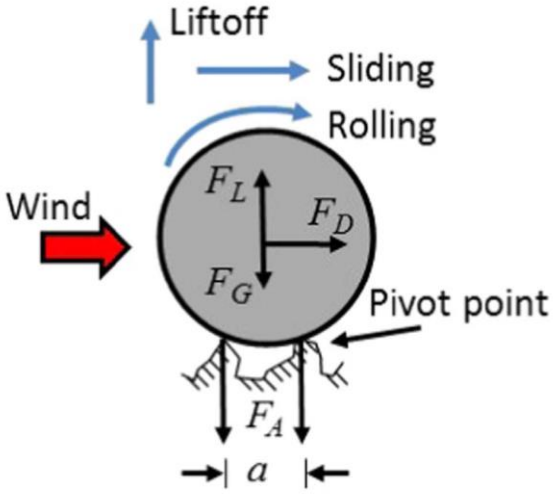

Figure 31: Forces acting on a spherical particle on two asperities on a rough surface (Brambilla, Speckart, & Brown, 2017)

Henry and Minier (2014) developed a Lagrangian stochastic model to predict particle resuspension from rough surfaces and compared their results against the experiments conducted by Reeks and Hall (2001). Figure 31 shows the motion, roll/slide and rocking over particles. According to Henry and Minier (2014), the particles detach from the surface while rolling over bigger asperities when the kinetic energy gained by the particle during rolling/sliding overcomes the adhesion force moment.

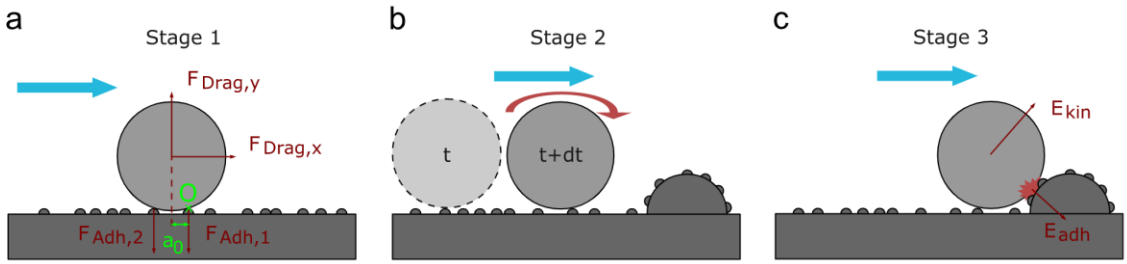

Figure 32: 3 Stage resuspension model proposed by Henry and Minier (2014) (a) Set into motion (b) rolling or sliding (c) rocking

According to Brambilla, Speckart and Brown (2017), Equation (45) can be used to find Adhesive force (F_A) acting on a spherical particle with diameter d_p on a nono-scale and micro-scale roughness surface as shown in Figure 33.

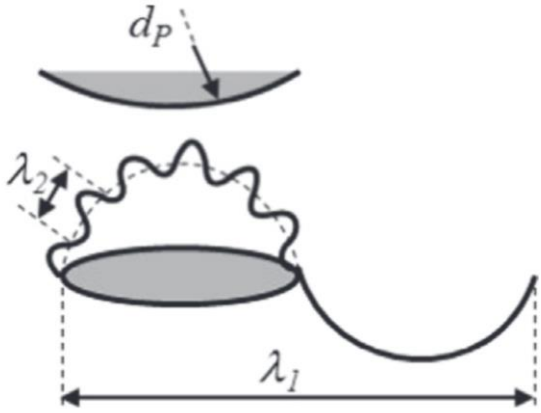

Figure 33: Nano-scale and micro-scale roughness elements (Brambilla, Speckart, & Brown, 2017) (Brambilla, Speckart, & Brown, 2017)

The equation below is used to find the Adhesive force (F_A) acting on a spherical particle with a diameter d_p.

$$F_A = \frac{Hd_p}{12s^2}\left[\frac{1}{1+\frac{58d_p\,rms_2}{2\lambda_2^2}} + \frac{1}{\left(1+\frac{58d_p\,rms_1}{2\lambda_1^2}\right)\left(1+\frac{1.82\,rms_2}{s}\right)^2}\right] \quad (45)$$

here, H is Hamaker constant (~ 10–19 J for air), s is the separation distance between surface and particle, λ is the distance between asperities as shown in Figure 33, rms is the root-mean-square of the surface roughness, and subscripts 1 and 2 identify the micro-scale and nanoscale roughness elements (Brambilla, Speckart, & Brown, 2017).

2.13 Forces Acting on a Suspended Spherical Particle

Figure 34 shows the free-body diagram of a spherical particle with unit mass exposed to a laminar stream of air.

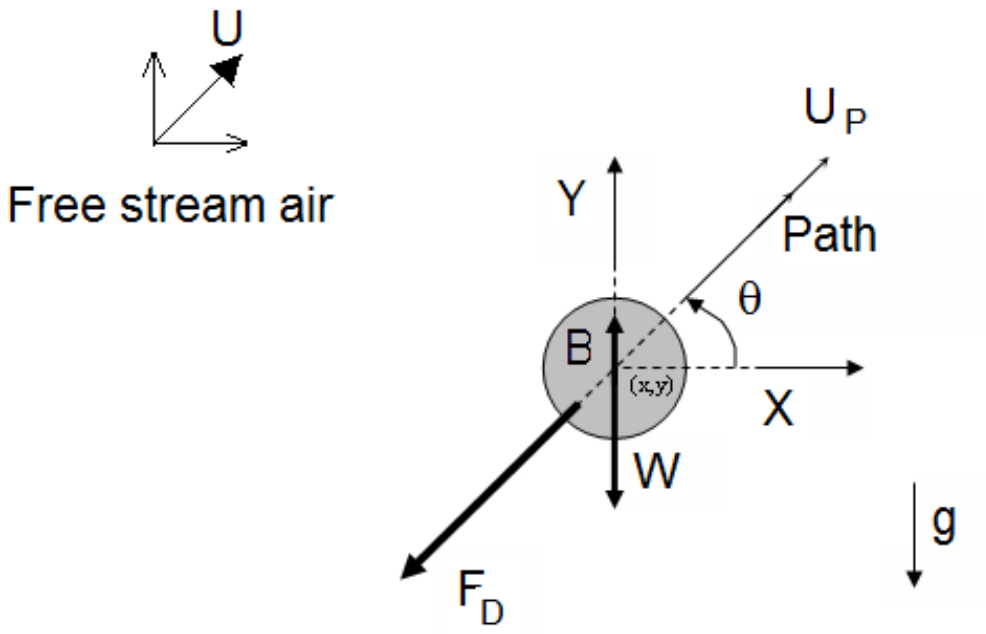

Figure 34: Free body diagram of the forces acting on a spherical particle in laminar air

As per Figure 34, the force due to gravity per unit mass (W) acts in the negative y-direction, and the force due to buoyancy per unit mass (B) acts in the positive y-direction. The drag force per unit mass (FD) acts exactly opposite to the direction of the particle path. The instantaneous velocity of the particle at time t has a magnitude of UP in the direction of the angle θ with regards to the positive X-axis at the location (x, y). Here, g represents the acceleration due to gravity acting in the negative Y-direction.

The acceleration of this unit mass spherical particle due to forces acting on it can be derived, as discussed in the next section.

2.13.1 Particle Trajectory in the X-direction

Using Newton's second law of motion, the rate change of velocity for a unit mass particle in the X-direction when the drag force, gravity, buoyancy, and other forces acting on it can be written using Equation (46).

$$\frac{dU_P}{dt} + F_D(U - U_P) + g_X\left(\frac{\rho_P - \rho}{\rho_P}\right) + F_X = 0 \qquad (46)$$

here, F_X represents the acceleration due to other forces, such as the Saffman lift force. The Saffman (1965) lift force is the subsequent drift force acting on a particle across streamlines due to Brownian motion. Here ρ is the density of continuous flow (free stream air) and ρ_P is the particle density. Here F_D can be derived using Equation (47).

$$F_D = \frac{18\mu}{\rho_P d_P^2}\frac{C_d Re}{24} \qquad (47)$$

where, μ is the continuous flow dynamic viscosity, C_d is the coefficient of drag of the particle found using Equation (49) or (50), d_p is particle size (diameter), and **Re** is the Reynolds number of the spherical particle found using Equation (48).

$$\boldsymbol{Re = \frac{\rho d_P |U_P - U|}{\mu}} \qquad \textit{(48)}$$

here, U_P is particle velocity, and U is free stream velocity.

The relationship given in Equation (50) is valid for a full range of **Re**, but for **Re** < 1, one can use the simple Stokes relationship given in Equation (49) to find the coefficient of drag.

$$\boldsymbol{C_d = \frac{24}{Re}} \qquad \textit{(49)}$$

CFD software FLUENT uses Equation (50) to calculate the drag coefficient for the full spectrum of Reynolds numbers when a spherical particle moves through the continuous flow (Moris & Alexander, 1772).

$$\boldsymbol{C_d = \frac{24}{Re}\left(1 + b_1 Re^{b_2}\right) + \frac{b_3 Re}{b_4 + Re}} \qquad \textit{(50)}$$

where, b1, b2, b3, and b4 are constants that depend on the shape factor (ϕ) of microscopic particles, and they are given by Equation (51).

$$\begin{aligned} b_1 &= exp(2.3288 - 6.4581\phi + 2.4486\phi^2) \\ b_2 &= 0.0964 + 0.5565\phi \\ b_3 &= exp(4.9050 - 13.8944\phi + 18.4222\phi^2 - 10.2599\phi^3) \\ b_4 &= exp(1.4681 + 12.2584\phi - 20.7322\phi^2 + 15.8855\phi^3) \end{aligned} \qquad (51)$$

The Reynolds number, **Re** used in Equations (49) and (50), is computed with the diameter of a sphere having the same volume as the particle under consideration. Here ϕ is the shape factor of the particle that is defined by Equation (52) (Haider & Levenspiel, 1989).

$$\phi = \frac{A_{sph}}{A_P} \qquad (52)$$

here, $A_{sph}$is the surface area of a sphere having the same volume as the particle, and A_P is the actual surface area of the particle. For resuspension factor calculations, the particles are considered as spheres having shape factors of 1.

2.13.2 Respiratory Deposition

Resuspended particles travel within the canopy layer or travel a long distance in the Surface or Ekman layers and can be inhaled by humans when they fall back into human breathing height. The hazards caused by inhaled particles depend on their chemical composition and where they will deposit in the human respiratory system (Hinds, 1999). The deposition of particles within the respiratory system is similar to particle deposition onto a filter in an air sampler. However, the geometry and the flow rate of the human respiratory system are continuously changing compared to a stationary continuous flow rate filtering system.

Due to the complexity of geometry and the flow properties of the human respiratory system, most of the available respiratory deposition models are either experimental or empirical. In empirical models, the respiratory system is considered as a series of anatomical compartments through which the aerosol passes during breathing. Each compartment is seen as a filter and models the complex human respiratory system as a stationary filtering process (Mitsakou, Helmis, & Housiadas, 2005). The human face acts as a pre-separator, allowing only the respirable range particles (< 10 μm) to enter the human breathing system.

The human respiratory system can be divided into three main regions based on its structure, airflow patterns, functions, particle retention time, and sensitivity to deposited particles. The first region is the head airways region, consisting of the nose, mouth,

pharynx, and larynx. The second is the tracheobronchial region, which includes airways from the trachea to the terminal bronchioles. The third region is the alveolar region, where gas exchange occurs in the lungs (Hinds, 1999). Figure 35 shows the parts of the human respiratory system and three central regions.

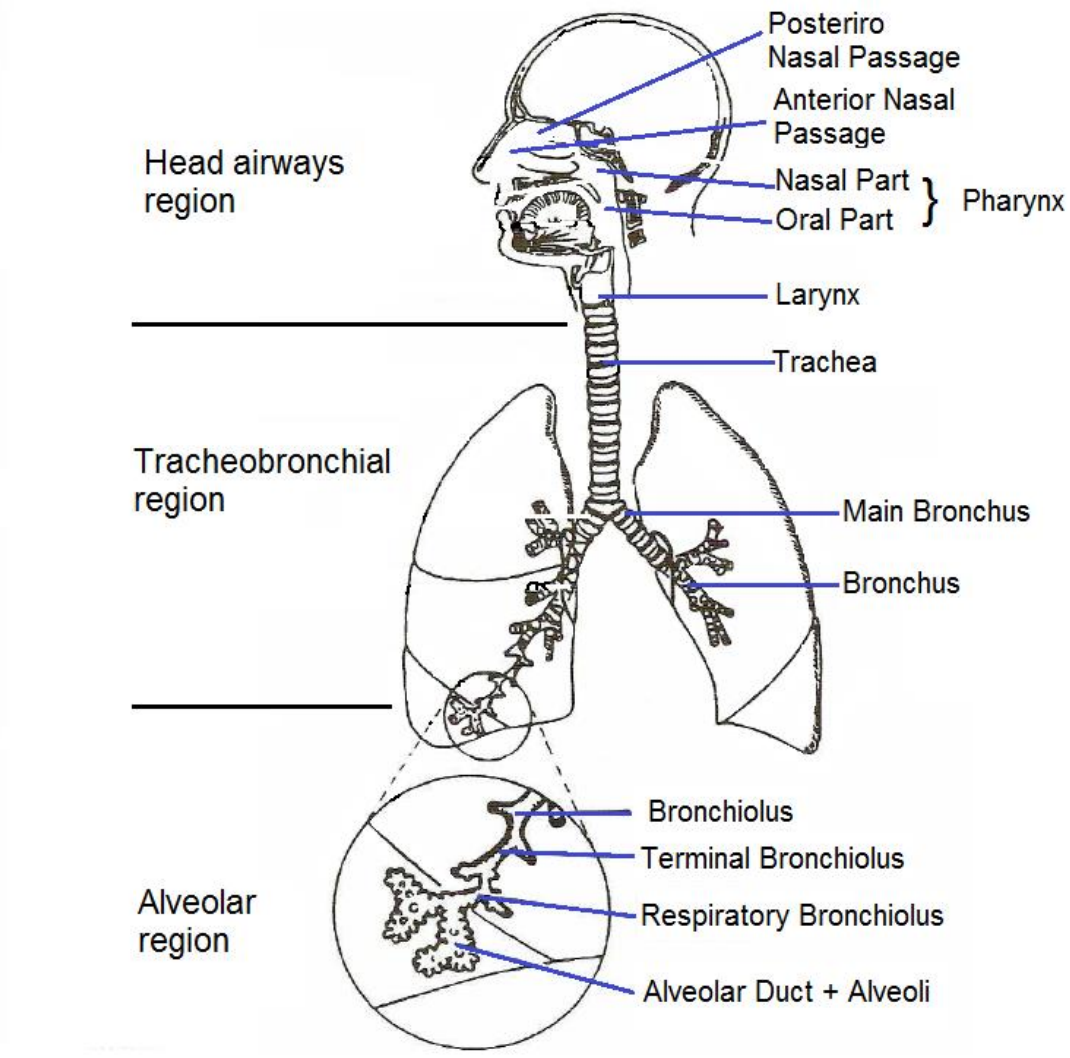

Figure 35: Three main regions and the parts of the human respiratory system (Hinds, 1999)

Hinds (1999) curve fit the International Commission on Radiological Protection (ICRP) 1994 respiratory track data into models with ±0.03% accuracy over the size range of 0.001 to 100 μm (ICRP, 1994).

The deposition fraction for the head airways (DF_{HA}) can be written as in Equation (53).

$$\boldsymbol{DF_{HA} = IF\left[\frac{1}{1 + exp(6.84 + 1.183\, ln(d_P)} + \frac{1}{1 + exp(0.924 - 1.885\, ln(d_P)}\right]} \qquad \textbf{(53)}$$

here, IF is the inhalable fraction as used by the ICRP model given by Equation (54), and d_P is the physical diameter of a monodispersed particle measured in μm.

$$\boldsymbol{IF = 1 - 0.5\left[1 - \frac{1}{1 + 0.00076 d_P^{2.8}}\right]} \qquad \textbf{(54)}$$

The deposition fraction for the tracheobronchial region (DF_{TB}) and alveolar (DF_{AL}) regions are given by Equations (55) and (56), respectively.

$$\boldsymbol{DF_{TB} = \left(\frac{0.00352}{d_P}\right)\left[\begin{matrix} exp(-0.234(ln(d_P) + 3.40)^2) + \\ 63.9\, exp(-0.819(ln(d_P) - 1.61)^2) \end{matrix}\right]} \qquad \textbf{(55)}$$

$$DF_{AL} = \left(\frac{0.0155}{d_P}\right)\left[\begin{matrix} exp(-0.416(ln(d_P) + 2.84)^2) + \\ 19.11\, exp(-0.482(ln(d_P) - 1.362)^2) \end{matrix}\right] \qquad (56)$$

The total deposition in the respiratory system (DF) is the sum of all regional deposition and can be written as in Equation (57).

$$DF = IF\left[\begin{matrix} 0.0587 + \dfrac{0.911}{1 + exp(4.77 + 1.485\, ln(d_P)} + \\ \dfrac{0.943}{1 + exp(0.508 - 2.58\, ln(d_P)} \end{matrix}\right] \qquad (57)$$

Equations (53) to (57) are graphed in Figure 36 for 0.001 to 100 μm physical diameter particles.

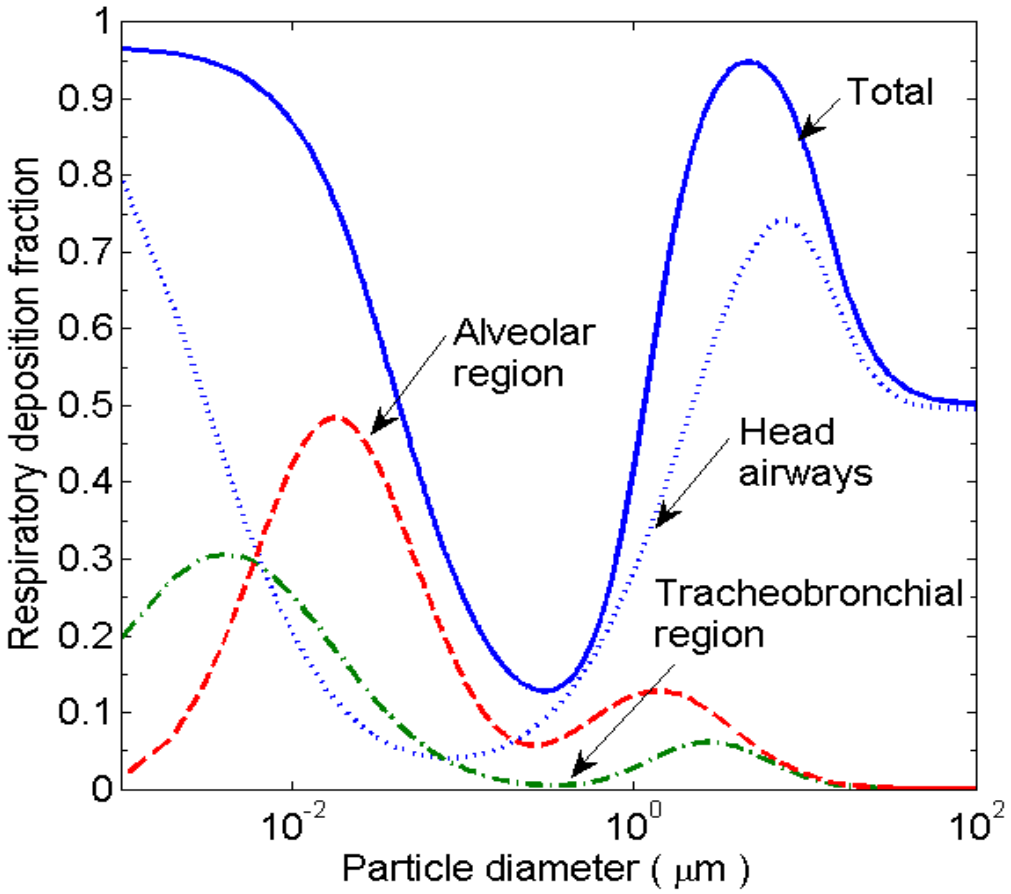

Figure 36: in the human respiratory Deposition of particles tract when breathing through a nose (light exercise) based on the ICRP deposition model. Average data for males and females (Hinds, 1999)

The head airways region removes the largest particles due to impaction on the nasal hairs and at the bends in the posterior nasal passage. These particles are cleared to the pharynx and swallowed, where they can become an ingestion hazard. According to Hinds (1999), approximately 72% of the 10 μm particles and 28% of 1 μm particles are deposited before inhaled air reaches the larynx.

In the tracheobronchial region, during light exercise conditions, most of the bigger particles larger than 3 μm settle down due to impaction and particles less than 3 μm are deposited by settling mechanisms.

In general, particle sizes 10 μm and higher do not enter the alveolar region (Hinds, 1999). According to Hinds (1999), approximately 48% of 0.02 μm are deposited in the alveolar area due to settling.

In collaboration with the resuspension models presented in this thesis, respiratory tract deposition models offer a valuable tool for estimating the proportion of particles deposited in the lungs compared to the initial fallout on the ground following an RDD event. This comprehension of the complete trajectories of particles during the resuspension and respiratory tract deposition processes post-RDD event will facilitate the effective administration of drugs to those affected, benefiting both the medical community and field commanders.

3 RESUSPENSION EXPERIMENTS

Resuspension experiments were conducted in a 10 m long, open-ended wind chamber built exclusively for radioactive particle resuspension experiments. This wind chamber was set up inside the Wehrwissenschaftliches Institut für Schutztechnologien (WIS) facility in Munster, Germany. The WIS facility is equipped with an appropriate ventilation system to handle live agent radioactive materials experiments. Figure 37 shows the picture of the WIS facility wind chamber used for radioactive particle resuspension experiments, and Figure 38 shows the layout of the experimental setup.

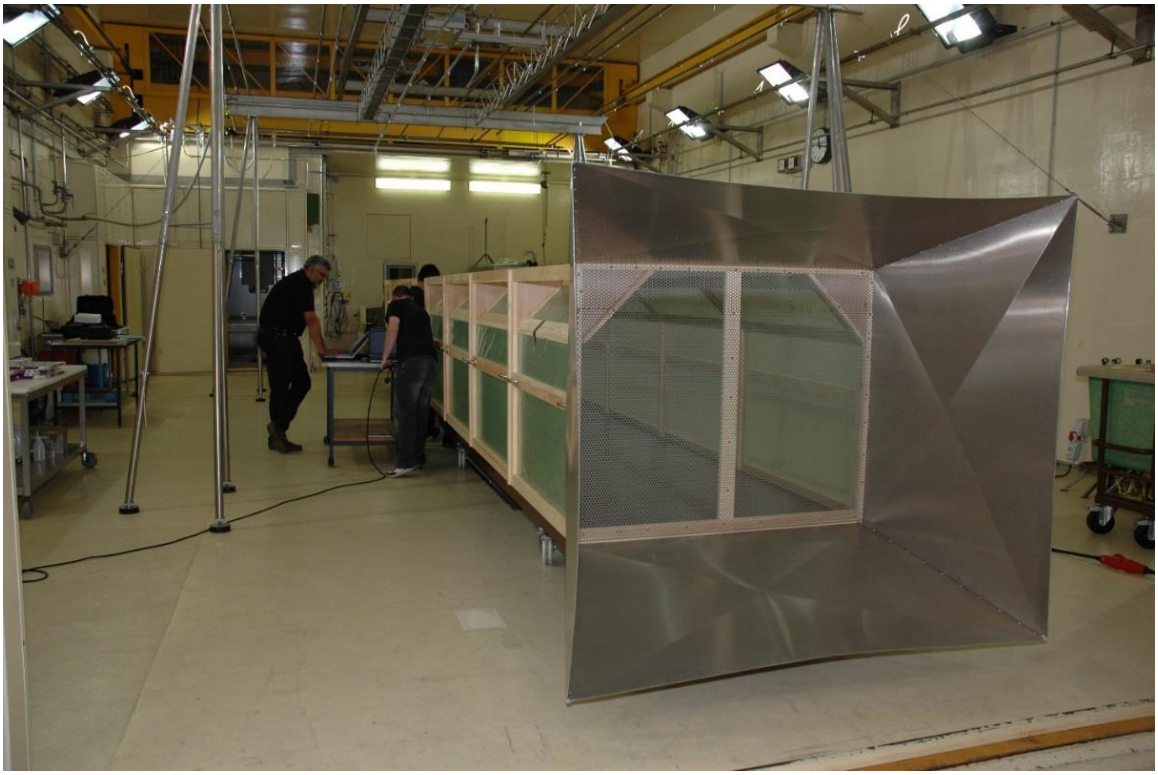

Figure 37: WIS Facility Wind Chamber

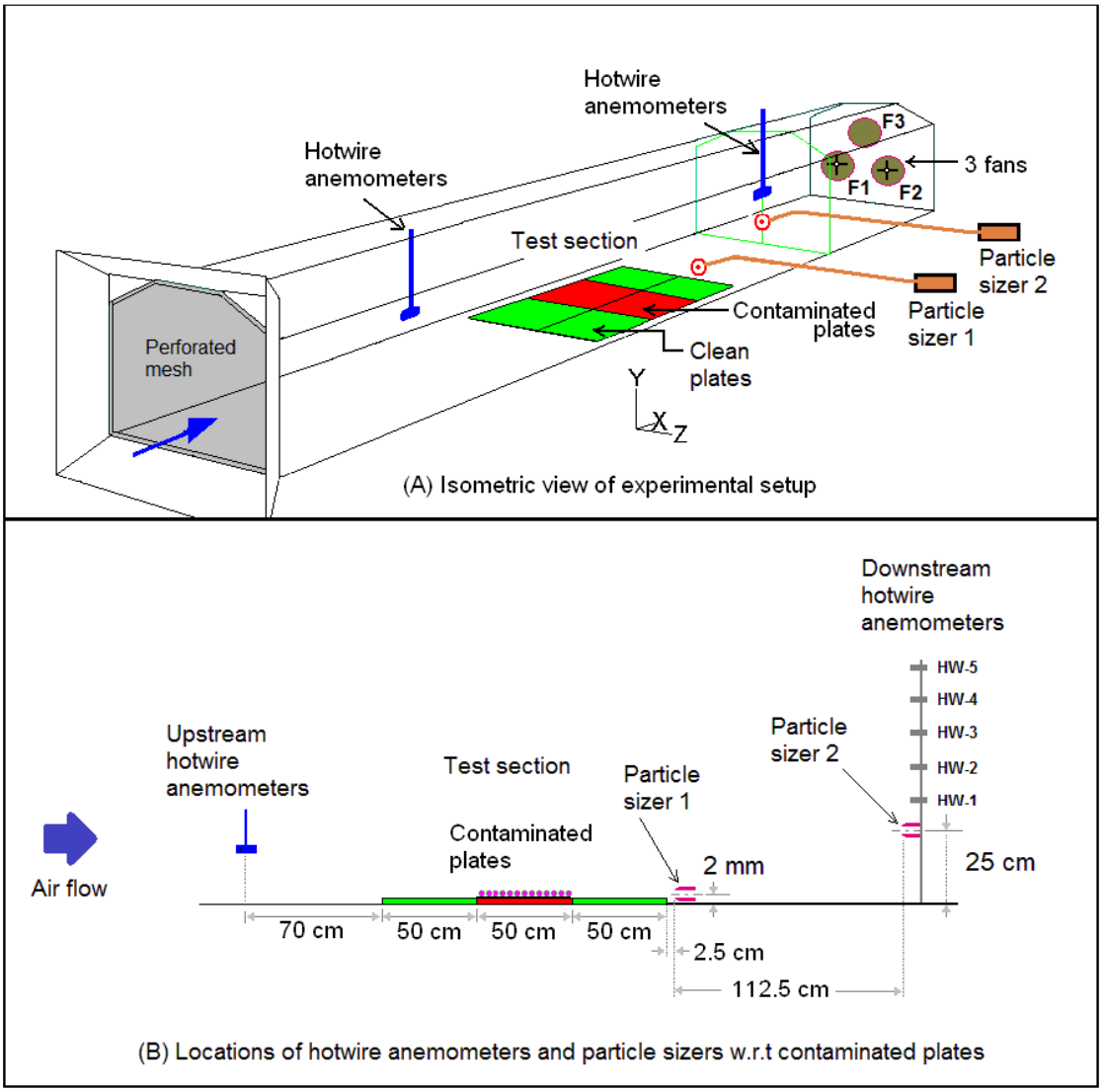

Figure 38: Layout of the experimental setup at the WIS facility test chamber showing the locations of Hotwire anemometers (HW), contaminated plates and Particle Sizers.

The wind chamber could generate speeds up to 6.7 m s^{-1} at the center of the test section using three fans, each moving 10,000 m^3 of air per hour. Fans F1 and F2 were axial propeller fans, and fan F3 was a ducted vent connected to a fan located 2 m downstream of

the wind chamber. Each fan was 40 cm in diameter and mounted onto the back of the 10 m long wind chamber.

The front view of the wind chamber back panel and the locations of the fans are shown in Figure 39.

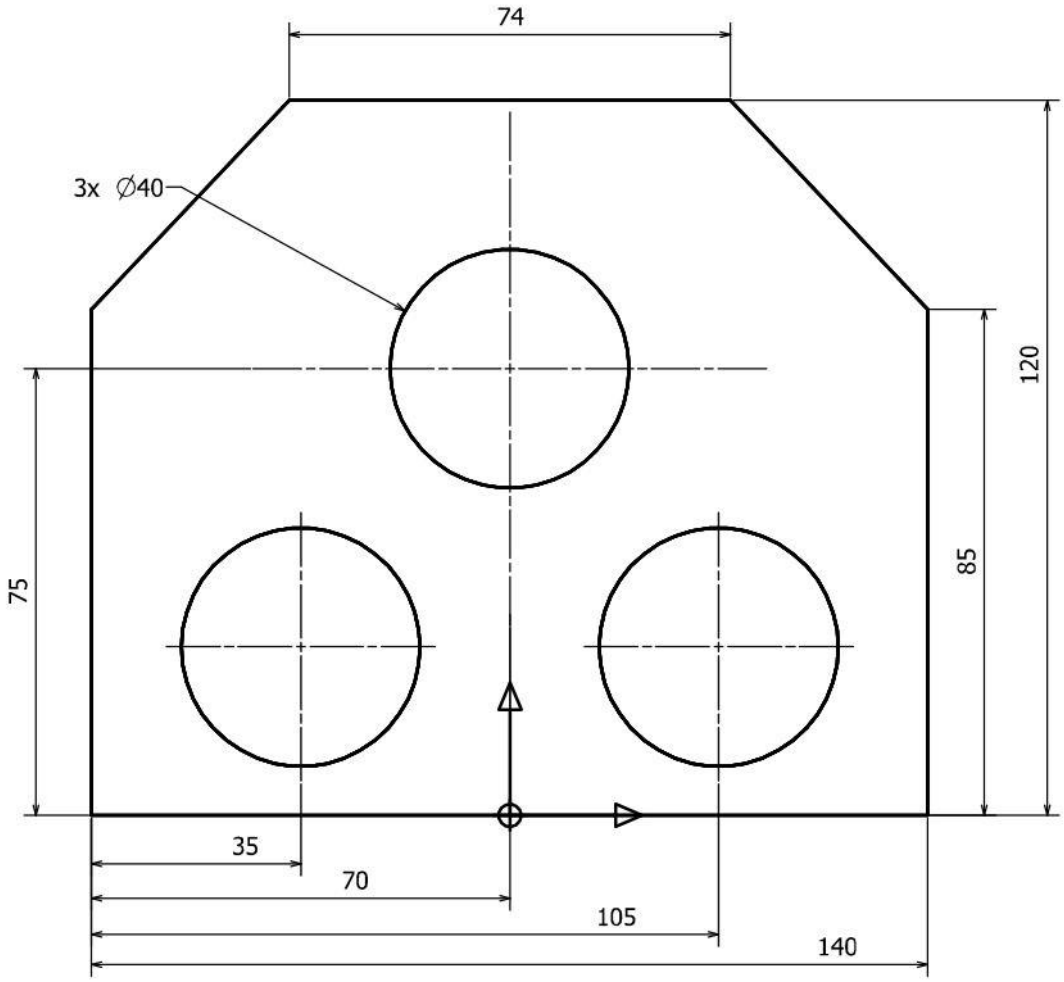

Figure 39: Front view of the back panel of the wind chamber and the locations of fans (Note: All dimensions are in cm)

The hydraulic diameter, D_h of the test section was calculated to be 130.3 × (1 ± 1.93%) cm using Equation (58).

$$\boldsymbol{D_h = \frac{4A}{P}} \qquad \textbf{(58)}$$

here, A is the cross-sectional area 15645 × (1 ± 1.51%) cm^2, and P is the perimeter of the test section 480.2 × (1± 0.42%) cm.

The boundary layer of the wind chamber was tripped from laminar to turbulent using 10 cm × 10 cm rectangular turbulators. The turbulator board was placed on the floor of the wind chamber after a perforated mesh. The perforated mesh was used to reduce the turbulent intensities of the free stream flow. A commercially available 1 mm thick, 1 cm diameter perforated membrane with a circular hole density of 5776 per square meter was used as a mesh in this wind chamber.

Turbulent flow near the wind chamber floor was visually observed by injecting liquid nitrogen condensation clouds prior to resuspension experiments.

3.1 Mapping the Wind Chamber and Sample Preparation

The WIS wind chamber was located inside an environmentally controlled facility with 32.5 × (1± 3.4%) %RH humidity and 24 × (1± 7.4%) oC temperature during the entire time of experiments. This facility was also equipped with a ventilation system capable of scrubbing the contaminated air to minimize the recirculation of resuspended particles.

3.1.1 Temperature Measurements

The temperature inside the wind chamber at two locations of the hotwire anemometers were measured using K-type thermocouples with 0.1℃ resolution and (±2% + 0.5) ℃ accuracy. The average temperature of the wind chamber during the active resuspension experiments was calculated to be 24 × (1 ± 7.4%) ℃ using 719 data points with statistical uncertainty (2σ) of ±0.8 ℃.

3.1.2 Velocity Mapping of the Wind Chamber Before Active Trials

The velocity distribution inside the wind chamber was mapped before the resuspension experiments. Two sets of hotwire anemometers were used to measure velocity upstream and downstream of the wind chamber with respect to the location of contaminated sampling plates. The upstream hotwire anemometers were mounted off the ceiling along the symmetry plane of the wind chamber at (40 ± 0.5) cm above the floor. The downstream hotwire anemometers were placed in a vertical grid to map the vertical velocity distribution from the floor to the ceiling of the wind chamber. The tips of the hotwire anemometers were placed (15 ± 0.5) cm, (33 ± 0.5) cm, (51 ± 0.5) cm, (68 ± 0.5) cm and (82 ± 0.5) cm above the floor and offset to the left (towards the fan F1) by (16 ± 0.5) cm from the symmetric plane to avoid interferences from the upstream hotwires. These downstream hotwire anemometers were numbered HW-1, HW-2, HW-3, HW-4, and HW-5, respectively, starting from the floor of the wind chamber. Figure 40 shows instantaneous velocity measurements of HW-3 recorded for 107 minutes.

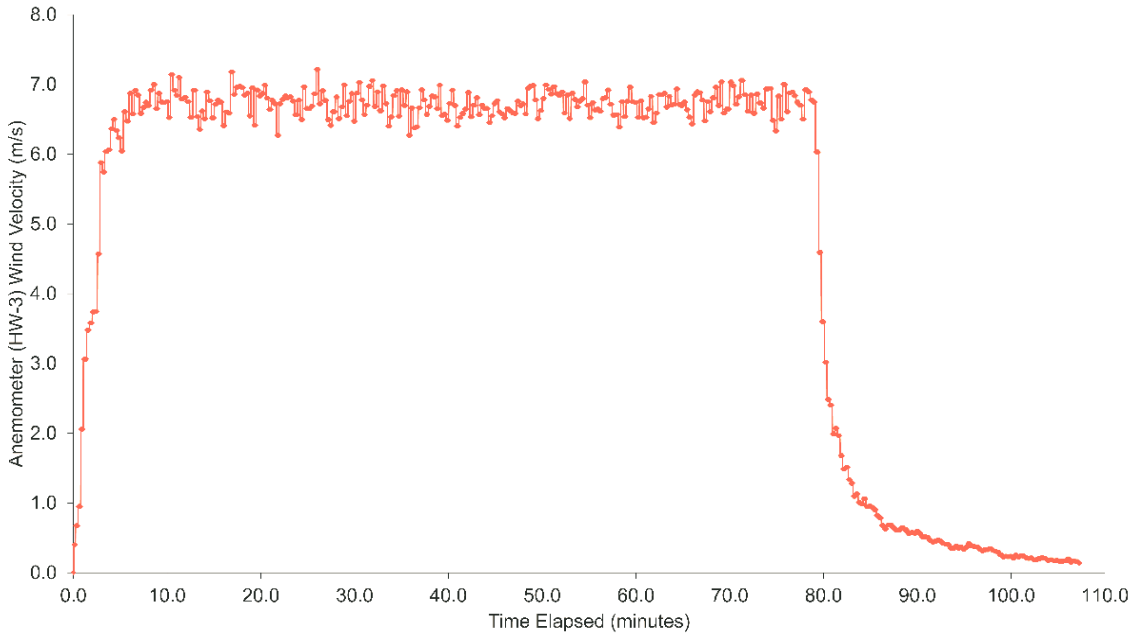

Figure 40: Instantaneous velocity measurements of the hotwire anemometer (HW-3)

There are three distinct velocity regions in Figure 40: the startup region, where instantaneous velocity increases from 0 m s^{-1} to a mean velocity of 6.7 × (1 ± 7.5%) m s^{-1}; the steady-state region; and the shutdown region, where instantaneous velocity decays down to 0 m s^{-1}.

According to Figure 40, the instantaneous velocity measurements in the steady-state region fluctuate between 6.3 and 7.2 m s^{-1}. Therefore, the time-averaged velocity of the steady-state area has two main velocity components: the mean velocity and the time-average fluctuating velocity.

3.1.2.1 Mean velocity component

The mean velocity component ($\bar{U}$) was calculated using Equation (59) by taking the arithmetic average of instantaneous velocity values (U_i) in the steady-state region.

$$\bar{U} = \frac{1}{N}\sum_{i=1}^{N} U_i \qquad (59)$$

where, N is the total number of data points (2745) measured in the steady-state region.

3.1.2.2 Time-averaged fluctuating velocity component

The time-averaged fluctuating velocity component $\bar{U}'$ was calculated by taking the sample standard deviation of instantaneous velocities using Equation (60).

$$\bar{U}' = \sqrt{\frac{\sum_{i=1}^{N}(U_i - \bar{U})^2}{(N-1)}} \qquad (60)$$

Table 4 shows the values and calculated average velocity readings of all downstream hotwire anemometers with corresponding uncertainties. The total uncertainty represents both statistical (2σ) and accuracy of the hotwire anemometer as per manufacture specifications (±1%+least significant digit of the reading).

Table 4: Velocity readings of the downstream hotwire anemometers located on the hotwire grid at 700 cm down steam from the front of the wind chamber (165 cm from the contaminated plate)

Hotwire anemometer	**HW-1**	**HW-2**	**HW-3**	**HW-4**	**HW-5**
$\bar{U}'$ (m s^{-1})	0.17	0.14	0.15	0.17	0.14
$\bar{U}$ (m s^{-1})	6.51±0.51	6.61±0.45	6.74±0.47	6.74±0.51	6.03±0.42

The boundary layer was not characterized during the WIS facility experiment. As a result, the flow parameters close to floor surfaces, such as friction velocity, turbulent kinetic energy and turbulent dissipation rates, were determined by simulating the WIS facility wind chamber using a full-scale 3D CFD model, ensuring that the CFD model can match the measured velocities at HW-1, 2, 3,4 and 5 locations.

3.2 Preparation of Radioactive Lanthanum Oxide Powder

Radioactive $^{140}La_2O_3$ powder was selected as a surrogate for the material used in the experiments for several reasons: it can be easily produced, is easily detectable thanks

to its distinctive high-energy beta and gamma radiation peaks, and its radioactive contamination levels persist for a relatively short duration, lasting only 17 days (equivalent to 10 half-lives) due to its short half-life (Erhardt, Quayle, & Noel, Full-Scale RDD Experiments and Models, 2013) However, it's important to note that ^{140}La salts can potentially be acquired in bulk by individuals with malicious intentions, who may attempt to submit forged radioisotope licenses. Moreover, La_2O_3 powder can be readily prepared into the necessary particle size distributions using grinding or milling techniques that are generally accessible, raising concerns about its availability to individuals who may seek to use it for unauthorized purposes (Waller E. , 2003).

Radioactive La_2O_3 powder was produced in a research reactor facility near Hamburg, Germany, by irradiating $1.000 \times (1 \pm 0.05\%)$ g of non-radioactive microscopic La_2O_3 power in a high-flux thermal neutron field. Upon receiving the 2.Ci of ^{140}La from the supplier, the La_2O_3 powder was mixed inside a hot cell with inactive La_2O_3 powder to get the total starting mass of $30.000 \times (1 \pm 0.002\%)$ g.

For the active trial, a 20 g of La_2O_3 powder vial with 1GBq (27 mCi) of ^{140}La was prepared by mixing 2.9 g of a previously prepared mixture of La_2O_3 powder with inactive La_2O_3 powder inside the Hot Cell until homogeneous mixing was achieved. The vial was carefully brought into the contamination chamber and emptied into the dispersion pod placed at the center of the contaminated chamber.

3.3 Preparation of Contaminated sampling plates Before WIS Experiment

The active and inactive La_2O_3 powder mixture was dispersed inside an environmentally controlled 32.5 × (1 ± 3.4%) % RH humidity and 24 × (1 ± 7.4%) ^oC temperature contamination chamber at the WIS facility, simulating a high-energy dispersion by an RDD event using a pressurized pneumatic system.

The procedure involved transferring the vial containing the La_2O_3 powder blend from the measurement stand to the contamination chamber. Subsequently, the contents were emptied into a cylindrical container known as a "puff pod," positioned atop a table within the contamination chamber. This puff pod is intricately linked to a pressurized air reservoir situated outside the contamination chamber via a high-speed valve designed to supply compressed air to the dispersion system. Moreover, an air inlet was thoughtfully positioned tangentially to the contamination plate located inside the puff pod.

Figure 41 shows a view into the contamination chamber through a lead-glass shielding window.

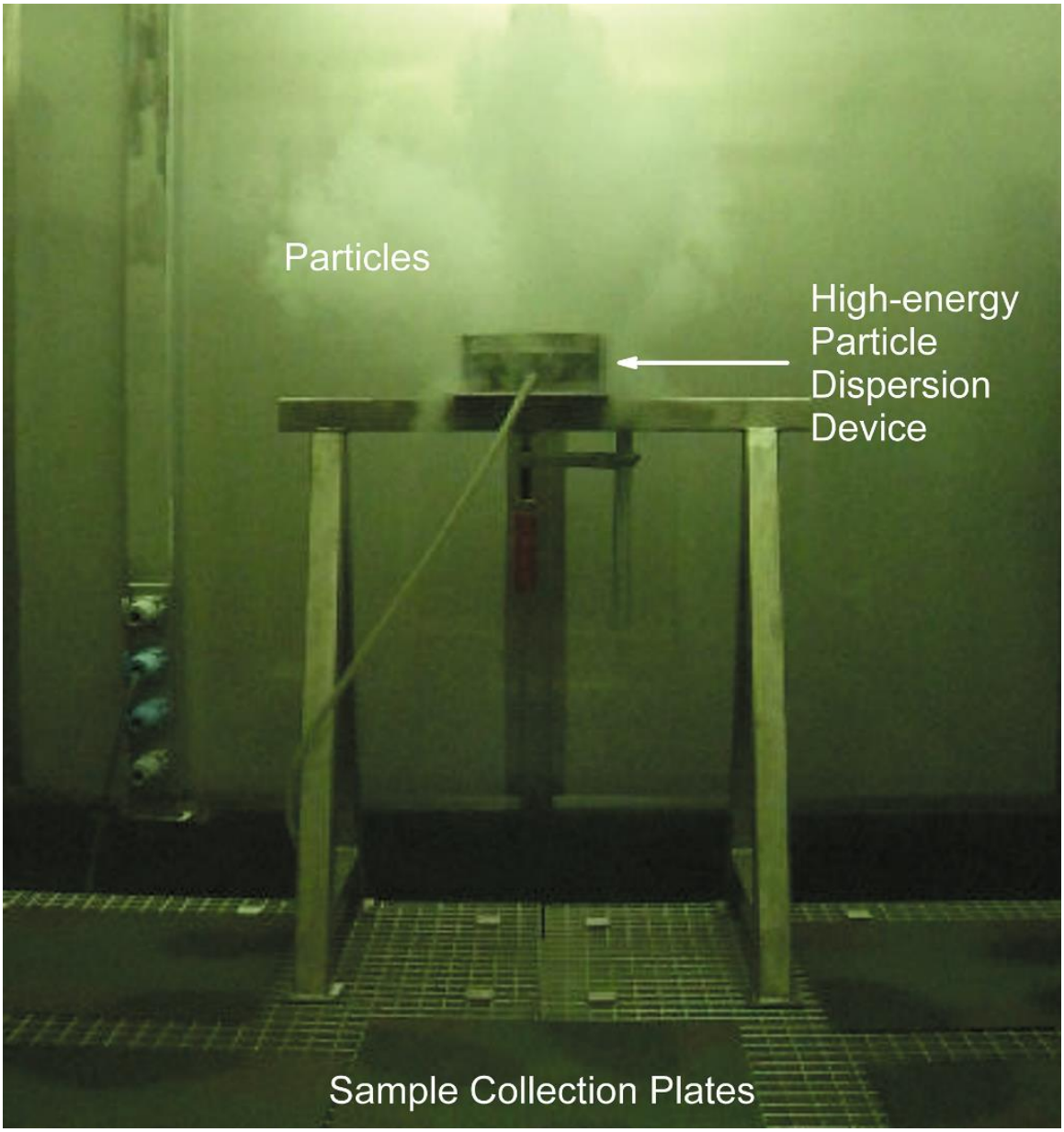

Figure 41: View into the contamination chamber (through a lead-glass shielding window) after a few seconds of high-energy release.

The powder was collected onto (2 ± 0.5) mm thick, (50 ± 0.5) cm × (50 ± 0.5) cm square sample plates over 8 hrs. of gravitational settling. Before entering the contamination

chamber to retrieve the contaminated plates, the air inside was drawn out of the chamber via the facility's ventilation system to remove any leftover airborne radioactive particles.

After the contamination process, contaminated plates were carefully carried by hand to a multi-probe radiation measuring system built out of 9 contamination probes connected to SVG2 radiation monitoring systems via telescopic handles, as shown in Figure 42.

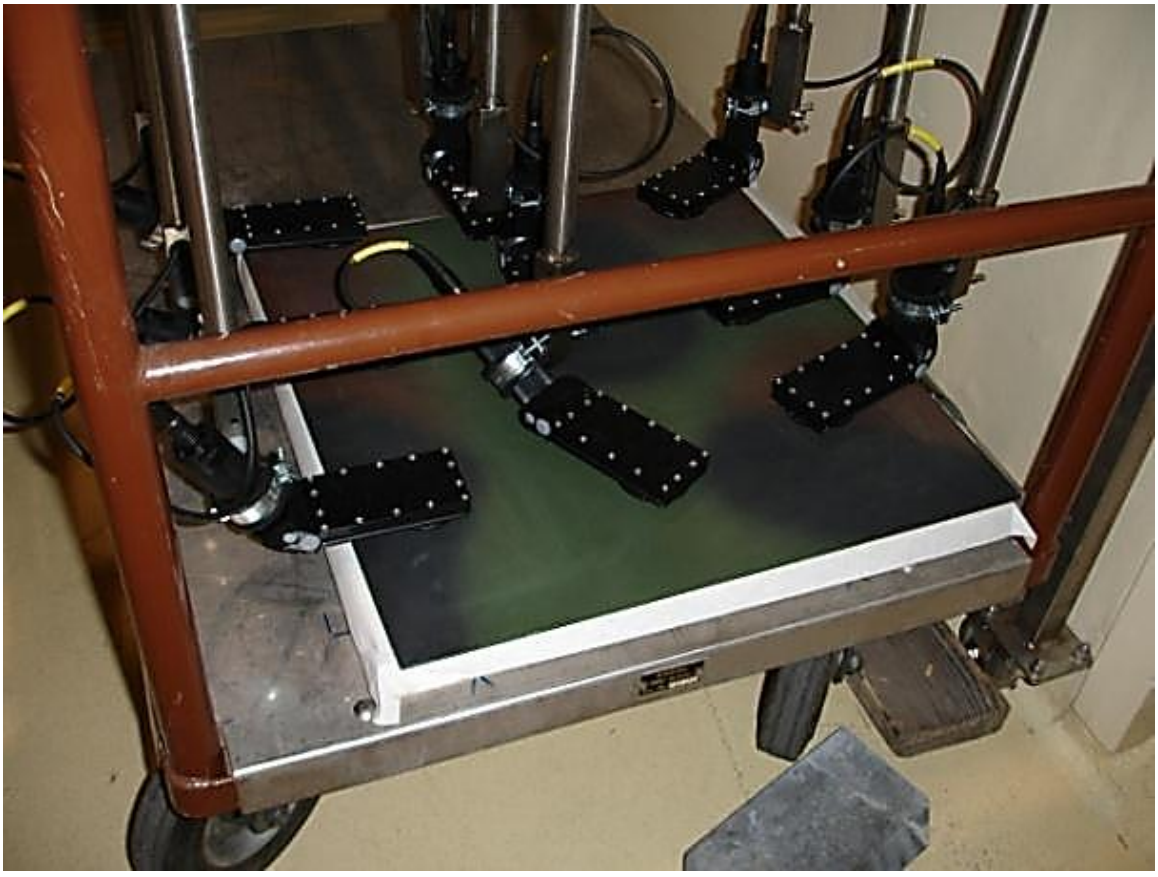

Figure 42: Multi-probe radiation measuring system built out of 9 Alpha-Beta-Gamma (□BG) probes connected to SVG2 radiation monitoring systems via long telescopic handles to measure activity distribution of contaminated sampling plates.

Contamination probes were placed at (10 ± 0.5) cm above the contaminated sampling plates. In addition, the detector probe was shielded above and around to improve the directional detection efficiency. The efficiency of the SVG2 detector with ABG probe for ^{140}La is 0.3 ± 0.05 cps/Bq (Erhardt, et al., 2016).

3.4 Activity Distribution on the Contaminated sampling plates

Sample plates were contaminated with a homogeneous mixture of La_2O_3 powder consisting of radioactive ^{140}La and stable ^{139}La. Radioactive ^{140}La emits both beta and gamma radiation during its decay process. Initially, it emits 100% beta radiation. Some of the ^{140}La will reach stable ^{140}Ce via direct beta decay, and the rest will decay by numerous gamma-rays to reach stable 140Ce, as shown in Equation (61)

$$^{139}\mathrm{La}(n,\gamma)^{140}\mathrm{La} \xrightarrow[40.27h]{\beta^-} {}^{140}\mathrm{Ce} \qquad \textbf{(61)}$$

Figure 43 shows the decay chain of ^{140}La. The light green arrow shows the decay of ^{140}La to stable ^{140}Ce, the dark green arrows represent the decay of ^{140}La to various

excited states, and the blue arrows represent the decay of different excited states to stable ^{140}Ce (Stosch, 2016).

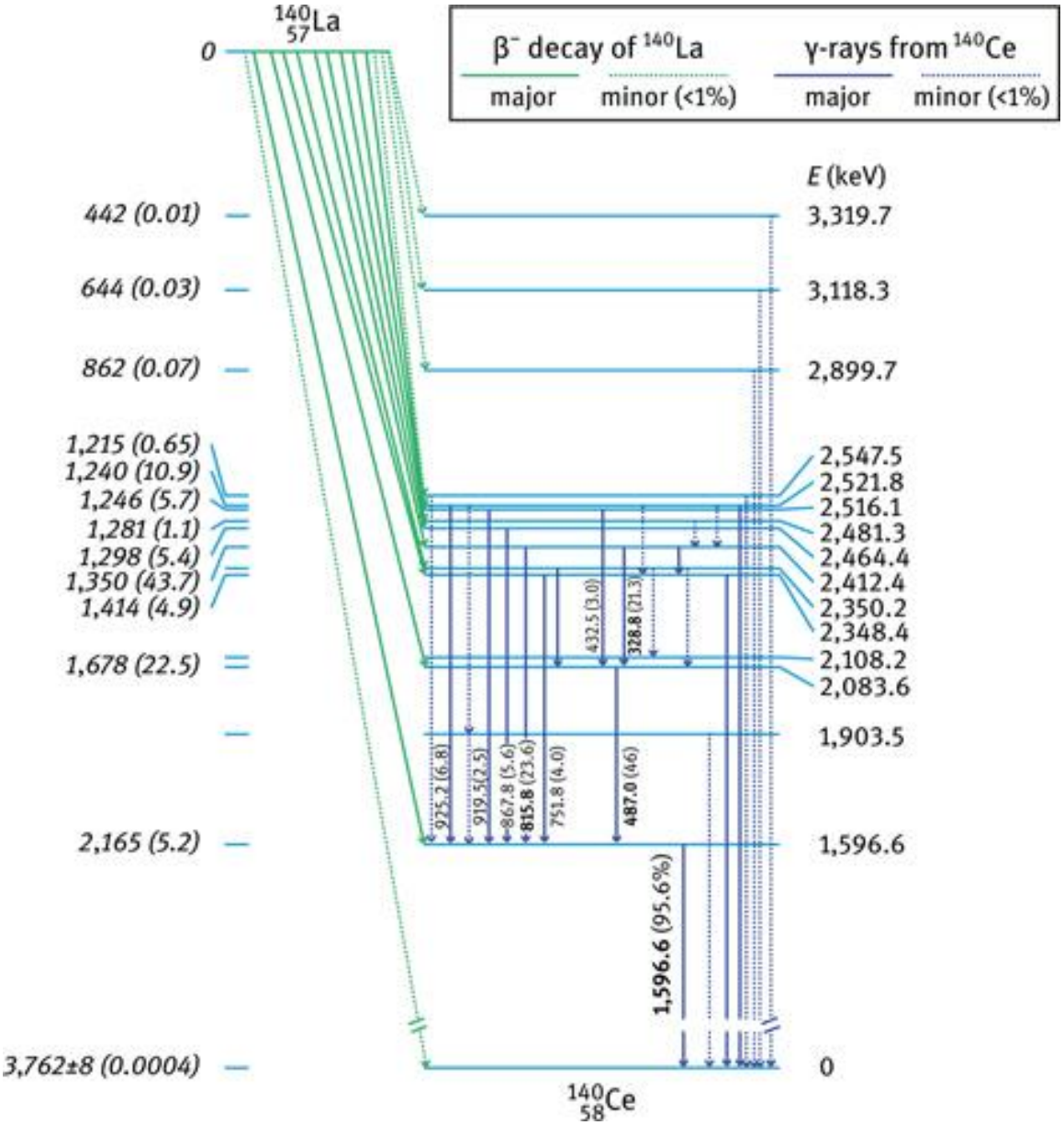

Figure 43: Decay chain of 140 La (Stosch, 2016)

Since the sample plates were contaminated only with La_2O_3 powder, the SVG2 detector with Alpha-Beta-Gamma (ABG) probe was used to calculate the cps/cm^2 of beta radiation emitted by the decay of ^{140}La on the contaminated sampling plates. The ABG probe has three photodiodes, each with an active area of 1 cm^2, and a suitable combination of the detector signals allowed the count rates of α, β, and γ radiation to be captured separately (Bottcher, 2003)

Table 5 shows the measured β radiation count rate from contaminated sampling plates before and after the resuspension experiment. With respect to the downstream direction of the wind chamber, the Contaminated sampling plate-1 was placed on the left side, and the contaminated sampling plate-6 was placed on the right side.

Table 5: Discriminated beta radiation reading from the 9-probe radiation measuring system before and after contaminated sampling plates were exposed to wind (before the wind –BW, and after wind – AW)

Contaminated sampling plates (cps/cm2)	**BW or AW**	**Probe location**								
		1	**2**	**3**	**4**	**5**	**6**	**7**	**8**	**9**
1	BW	183 ±0.8	271 ±0.9	315 ±1.0	167 ±0.7	245 ±0.9	278 ±1.0	146 ±0.7	200 ±0.8	167 ±0.7
	AW	178 ±0.8	243 ±0.9	277 ±1.0	163 ±0.7	223 ±0.9	247 ±0.9	141 ±0.7	186 ±0.8	147 ±0.7
2	BW	406 ±1.2	340 ±1.1	326 ±1.0	333 ±1.1	345 ±1.1	314 ±1.0	266 ±0.9	292 ±1.0	205 ±0.8
	AW	283 ±1.0	301 ±1.0	305 ±1.0	257 ±0.9	307 ±1.0	298 ±1.0	216 ±0.8	282 ±1.0	233 ±0.9
3	BW	523 ±1.3	493 ±1.3	429 ±1.2	1196 ±2.0	759 ±1.6	530 ±1.3	1457 ±2.2	920 ±1.8	447 ±1.2
	AW	242 ±0.9	320 ±1.0	334 ±1.1	393 ±1.1	484 ±1.3	411 ±1.2	382 ±1.1	504 ±1.3	332 ±1.1
4	BW	194 ±0.8	232 ±0.9	227 ±0.9	257 ±0.9	281 ±1.0	255 ±0.9	224 ±0.9	238 ±0.9	177 ±0.8
	AW	134 ±0.7	172 ±0.8	181 ±0.8	206 ±0.8	239 ±0.9	221 ±0.9	185 ±0.8	234 ±0.9	182 ±0.8
5	BW	135 ±0.7	175 ±0.8	239 ±0.9	214 ±0.8	307 ±1.0	312 ±1.0	221 ±0.9	369 ±1.1	398 ±1.2
	AW	96 ±0.6	139 ±0.7	192 ±0.8	158 ±0.7	238 ±0.9	247 ±0.9	173 ±0.8	289 ±1.0	270 ±0.9
6	BW	145 ±0.7	170 ±0.8	181 ±0.8	222 ±0.9	223 ±0.9	208 ±0.8	284 ±1.0	270 ±0.9	198 ±0.8
	AW	135 ±0.7	171 ±0.8	189 ±0.8	206 ±0.8	219 ±0.9	205 ±0.8	249 ±0.9	263 ±0.9	194 ±0.8

After wind (AW) measurements given in Table 5 were decay corrected using Equation (62).

$$N_0 = N_t exp\left(\left(\frac{ln(2)}{t_{\frac{1}{2}}}\right)t\right) \qquad (62)$$

where, N_0 is the decay corrected cps, N_t is the measured cps, t is elapsed time, and $t_{\frac{1}{2}}$ is half-life of ^{140}La (1.679 × (1 ± 0.01%) days) (Kellett, M. A.; Bersillon, O.; Mills, R. W., 2009)).

3.4.1 The Total Activity of the Contaminated sampling plates

The 9-ABC probe detector array was placed (10 ± 0.5) cm above the contaminated sampling plates to provide a safe gap to insert the contamination sample plates without damaging the detectors and to avoid cross-contamination to improve the efficacy of measurement.

Since the 9-ABC probe detector array was not placed very close to the contaminated sampling plates, individual probe readings did not represent the contamination of the area directly underneath the detector. Instead, the detector reading resulted from the contributions of all the contaminated areas on the sample plate. Hence, the relationship between SVG2 detector reading and activity distribution over the contaminated sampling plates was calculated using a system of equations, as shown in Equations (63) and (64).

$$\frac{\mu_\beta}{4\pi}\left[\frac{1}{d_{ij}^{\,2}}\right]\left[Ac_j\right] = \left[R_i\right] \qquad (63)$$

where, μ_β is the efficiency of the SVG2 detector, R_i is the area-averaged beta radiation count rate (cps cm^{-2}).

As shown in Figure 44, these contaminated sampling plates were divided into 9 equal squares for calculation purposes; d_{ij} is the distance from the center of square i to the center of detector j (where i =1..9 and j=1..9). Ac_j is the total area activity in the square area of A_j, concentrated to a point source at location j. Here, detectors and sources were modelled as point detectors and point sources.

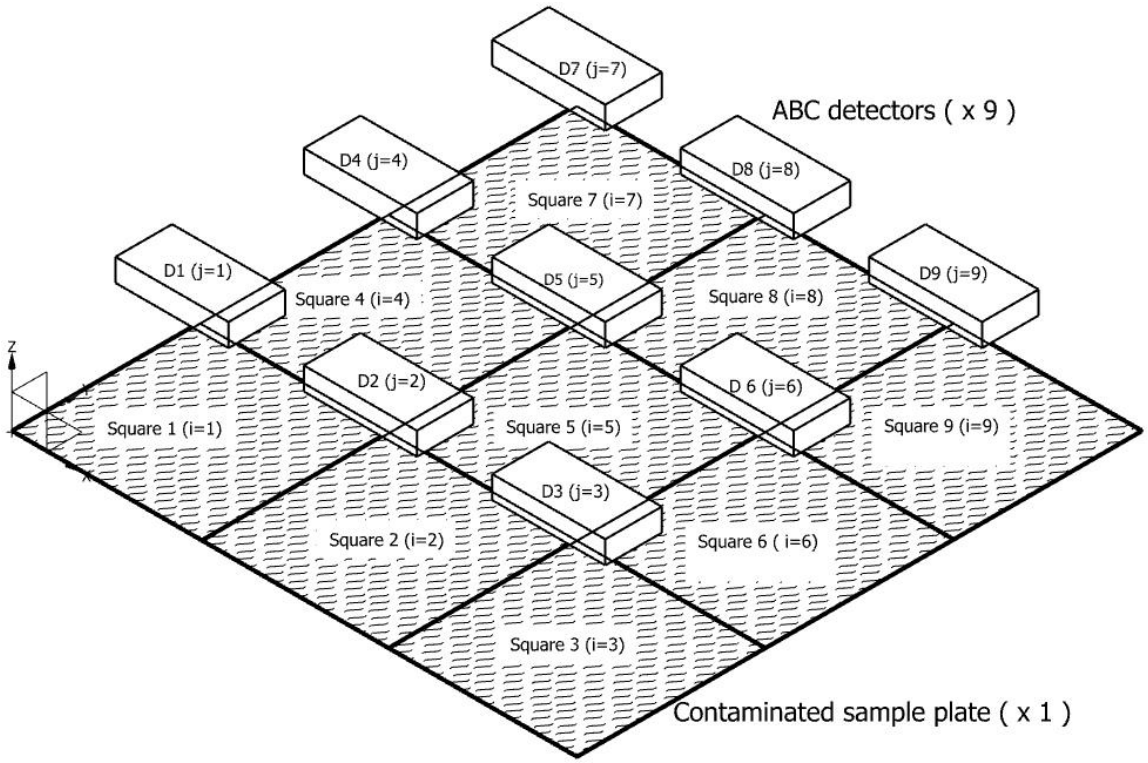

Figure 44: Location of ABC detectors (× 9) with respect to imaginary equal squares on the contaminated sampling plates (×9)

The expanded version of the corresponding system of equations for the 9-ABC probe detector array is given by Equation (64).

$$\frac{\mu_B}{4\pi}\begin{bmatrix}
\frac{1}{d_{11}^2} & \frac{1}{d_{12}^2} & \frac{1}{d_{13}^2} & \frac{1}{d_{14}^2} & \frac{1}{d_{15}^2} & \frac{1}{d_{16}^2} & \frac{1}{d_{17}^2} & \frac{1}{d_{18}^2} & \frac{1}{d_{19}^2} \\
\frac{1}{d_{21}^2} & \frac{1}{d_{22}^2} & \frac{1}{d_{23}^2} & \frac{1}{d_{24}^2} & \frac{1}{d_{25}^2} & \frac{1}{d_{26}^2} & \frac{1}{d_{27}^2} & \frac{1}{d_{28}^2} & \frac{1}{d_{29}^2} \\
\frac{1}{d_{31}^2} & \frac{1}{d_{32}^2} & \frac{1}{d_{33}^2} & \frac{1}{d_{34}^2} & \frac{1}{d_{35}^2} & \frac{1}{d_{36}^2} & \frac{1}{d_{37}^2} & \frac{1}{d_{38}^2} & \frac{1}{d_{39}^2} \\
\frac{1}{d_{41}^2} & \frac{1}{d_{42}^2} & \frac{1}{d_{43}^2} & \frac{1}{d_{44}^2} & \frac{1}{d_{45}^2} & \frac{1}{d_{46}^2} & \frac{1}{d_{47}^2} & \frac{1}{d_{48}^2} & \frac{1}{d_{49}^2} \\
\frac{1}{d_{51}^2} & \frac{1}{d_{52}^2} & \frac{1}{d_{53}^2} & \frac{1}{d_{54}^2} & \frac{1}{d_{55}^2} & \frac{1}{d_{56}^2} & \frac{1}{d_{57}^2} & \frac{1}{d_{58}^2} & \frac{1}{d_{59}^2} \\
\frac{1}{d_{61}^2} & \frac{1}{d_{62}^2} & \frac{1}{d_{63}^2} & \frac{1}{d_{64}^2} & \frac{1}{d_{65}^2} & \frac{1}{d_{66}^2} & \frac{1}{d_{67}^2} & \frac{1}{d_{68}^2} & \frac{1}{d_{69}^2} \\
\frac{1}{d_{71}^2} & \frac{1}{d_{72}^2} & \frac{1}{d_{73}^2} & \frac{1}{d_{74}^2} & \frac{1}{d_{75}^2} & \frac{1}{d_{76}^2} & \frac{1}{d_{77}^2} & \frac{1}{d_{78}^2} & \frac{1}{d_{79}^2} \\
\frac{1}{d_{81}^2} & \frac{1}{d_{82}^2} & \frac{1}{d_{83}^2} & \frac{1}{d_{84}^2} & \frac{1}{d_{85}^2} & \frac{1}{d_{86}^2} & \frac{1}{d_{87}^2} & \frac{1}{d_{88}^2} & \frac{1}{d_{89}^2} \\
\frac{1}{d_{91}^2} & \frac{1}{d_{92}^2} & \frac{1}{d_{93}^2} & \frac{1}{d_{94}^2} & \frac{1}{d_{95}^2} & \frac{1}{d_{96}^2} & \frac{1}{d_{97}^2} & \frac{1}{d_{98}^2} & \frac{1}{d_{99}^2}
\end{bmatrix}\begin{bmatrix} Ac_1 \\ Ac_2 \\ Ac_3 \\ Ac_4 \\ Ac_5 \\ Ac_6 \\ Ac_7 \\ Ac_8 \\ Ac_9 \end{bmatrix} = \begin{bmatrix} R_1 \\ R_2 \\ R_3 \\ R_4 \\ R_5 \\ R_6 \\ R_7 \\ R_8 \\ R_9 \end{bmatrix} \qquad \textbf{(64)}$$

Table 6 provides the measured distances from each probe to the centroid of the selected square area.

Table 6: Distances from probes to locations (loc.). All distances are measured in cm, and the uncertainty of measured values is ±0.5 cm.

Distance (cm)	loc 1	loc 2	loc 3	loc 4	loc 5	loc 6	loc 7	loc 8	loc 9
Probe- 1	10.0	19.5	34.8	19.5	25.6	38.6	34.8	38.6	48.1
Probe- 2	19.5	10.0	19.5	25.6	19.5	25.6	38.6	34.8	38.6
Probe-3	34.8	19.5	10.0	38.6	25.6	19.5	48.1	38.6	34.8
Probe- 4	19.5	25.6	38.6	10.0	19.5	34.8	19.5	25.6	38.6
Probe- 5	25.6	19.5	25.6	19.5	10.0	19.5	25.6	19.5	25.6
Probe- 6	38.6	25.6	19.5	34.8	19.5	10.0	38.6	25.6	19.5
Probe- 7	34.8	38.6	48.1	19.5	25.6	38.6	10.0	19.5	34.8
Probe- 8	38.6	34.8	38.6	25.6	19.5	25.6	19.5	10.0	19.5
Probe- 9	48.1	38.6	34.8	38.6	25.6	19.5	34.8	19.5	10.0

Figure 45 shows the contour plots of decay corrected activity distribution on the contaminated sampling plates 1 and 6 measured in MBq, just after the contamination process [before the wind (BW)] and after the resuspension experiment [after the wind (AW)] found by solving the system of equations given in Equation (64).

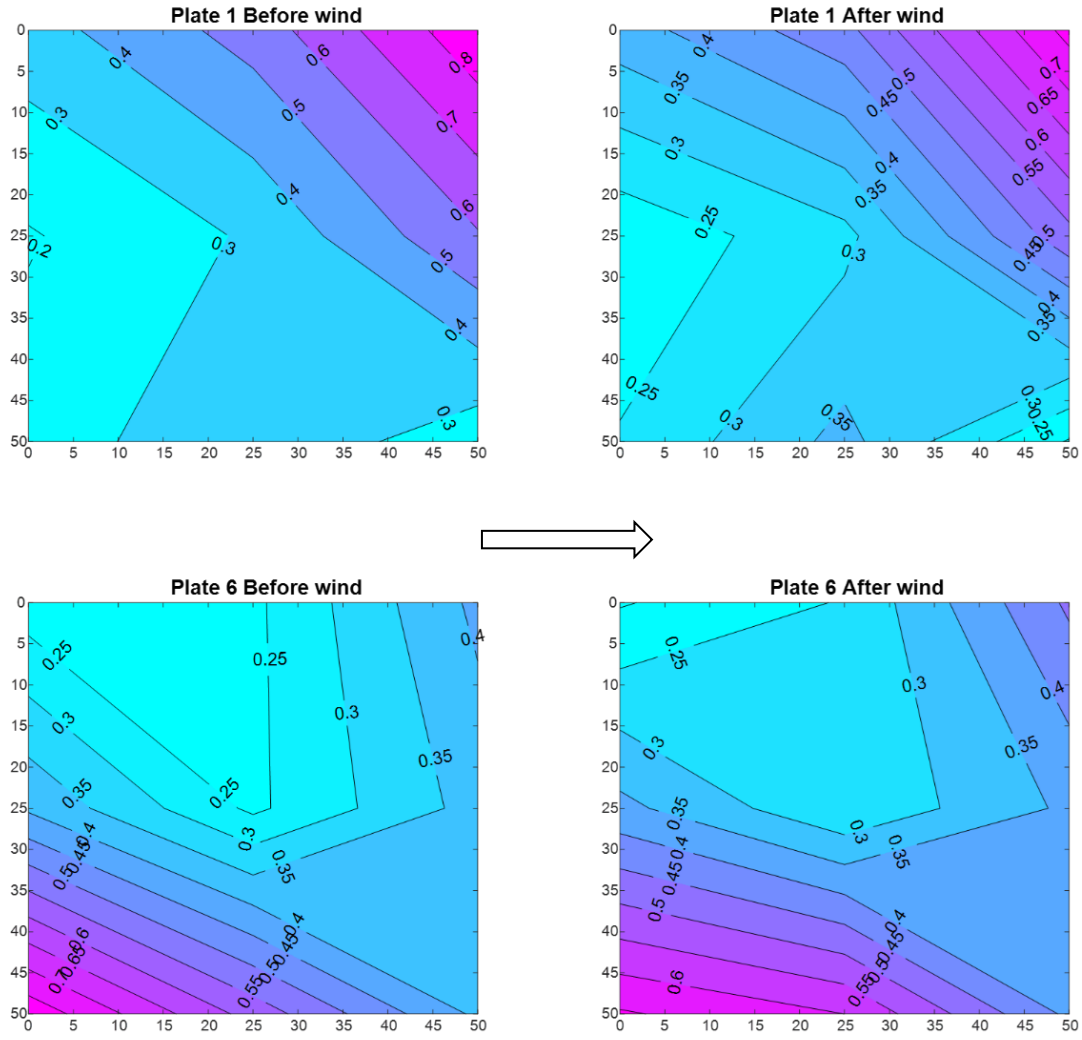

Figure 45: Contour plots of decay corrected activity of ^{140}La off 50 cm × 50 cm rectangular contaminated sampling plates measured in MBq before and after they were exposed to the wind during the resuspension experiment (wind blows from left to right).

The contour plots of activity (MBq) on the contaminated sampling plates before the wind clearly show a circular distribution of gravitationally deposited $^{140}La_2O_3$ power. Circular distributions were expected since particles were dispersed at the center of the

contamination chamber, simulating a high-energy dispersion by an RDD event without the effect of any external disturbances such as crosswind.

The decay corrected (at the beginning of before wind SVG2 measurements) activity of the sampling plate 1 before and after were calculated to be 3.73 × (1 ± 8.1%) MBq and 3.48 × (1 ± 8.1%) MBq, respectively, and for sampling plate 6 they were 3.63 × (1 ± 8.0%) MBq and 3.53 × (1 ± 8.0%) MBq, respectively. The decay corrected average contamination distribution on plates 1 and 6 before winds were 1.47 × (1 ± 8.1%) kBq cm^{-2} and 1.40× (1 ± 8.0%) kBq cm^{-2} respectively.

3.5 Experimental Resuspension Fraction from Plates (FR)

Hill (2007) proposed resuspension fraction as an alternative expression for resuspension. It is defined as the fraction of a given material on a given surface resuspended due to a given disturbance.

$$\boldsymbol{RF_A = \frac{S_{before} - S_{after}}{S_{before}} = \frac{\Delta S\ (Bq\ m^{-2})}{S_{before}(Bq\ m^{-2})}} \qquad \textbf{(65)}$$

here, RF_R is activity-based resuspension fraction, S_{before} is the activity on a surface before disturbance, $S_{after}$is the activity on the same surface after the disturbance, and ΔS is the difference in activity concentration on the surface before and after the disturbance.

The average percent removal of material, resuspension fraction, due to wind was calculated to be 4.79% based on 9 SVG2 detector array readings of 1472.62 Bq cm-2 before wind and 1402.14 Bq cm-2 after wind surface concentrations. The corresponding average activity-based resuspension factor (K_A) was calculated to be 6.21E-6 × (1 ± 16.1%) m^{-1} using Equation (66).

$$K_A = \frac{\textbf{Activity added to air per unit volume}}{\textbf{Activity lost from ground per unit area}} = \frac{\left(\frac{\Delta S\, A}{\dot{V}_{CF}\, t_W}\right)}{S_{before}} = \frac{RF_A\, A}{\dot{V}_{CF}\, t_{DW}} \quad (66)$$

here, ΔS is the difference in activity concentration before and after wind, A is the area of the contamination plate (0.5 m2) , $\dot{V}_{CF}$ is the average volume flow rate of the wind chamber (8.3 $m^3 s^{-1}$), t_W is the accumulated duration when the fans were on (465 seconds), and RF_R is an activity-based resuspension fraction found using Equation (65).

3.6 Calculating Lanthanum Oxide Mass on Contaminated Sampling Plates Using Decay Corrected SVG2 Detector Readings.

Since the ratio between activity and mass of La_2O_3 at the time of final mixing was known, the calculated total activity of the contaminated sampling plates was decay

corrected to the time of final mixing [(1387 ± 0.02) minutes for plate 1 and (1399 ± 0.02) minutes for plate 6]. The decay corrected overall activity at the time of mixing before wind-contaminated sampling plates 1 and sample plate 6 were calculated to be 5.56 × (1 ± 8.1%) MBq and 5.42 × (1 ± 8.0%) MBq, respectively. The average decay-corrected activity of a sample plate was 0.5% of the dispersed powder activity (1 GBq). Around 2.2% of the powder dispersed was deposited onto four contamination plates inside the contamination chamber, and the rest was deposited onto other surfaces inside the chamber, including the table holding the dispersion chamber. Please refer to Figure 41.

At the time of final mixing, the activity of 1GBq was achieved after mixing a measured amount of active powder with inactive La_2O_3 powder to get the final starting mass of 20.000 × (1 ± 0.002%) g. Therefore, based on the known mass-to-activity ratio, the total masses of La_2O_3 on the contaminated sampling plates-1 and contaminated sampling plates-6 were calculated to be 111.1 × (1 ± 8.1%) mg and 108.4 ×(1 ± 8.0%) mg, respectively.

3.7 Particle Concentration Measurements during the WIS Experiment

Grimm Portable Aerosol Spectrometers (Grimm Particle Sizer 1 and Grimm Particle Sizer 2) were used during the wind chamber resuspension experiments to measure

the resuspended particle number concentrations and particle mass concentrations at the selected downstream locations.

Figure 46-(A) shows the typical layout of a Grimm Particle Sizer, and Figure 46-(B) depicts its operating principle.

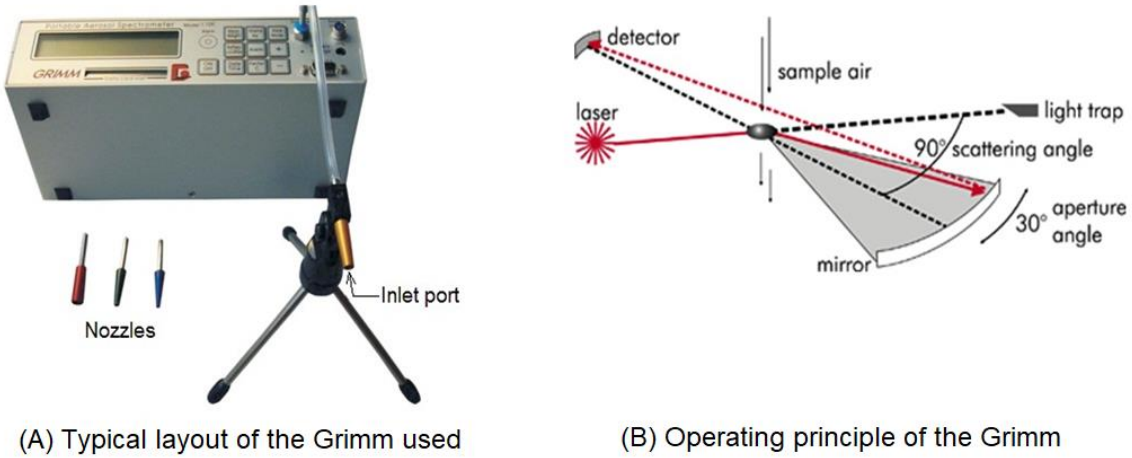

(A) Typical layout of the Grimm used (B) Operating principle of the Grimm

Figure 46: Grimm Particle Sizer (Grimm Aerosol Technik GbH & Co. KG, 2010).

Inlet ports of the Grimm Particle Sizer nozzles were positioned inside the wind chamber at (2.5 ± 0.5) cm and (115 ± 0.5) cm downstream from the ends of the last two clean sample plates and (2 ± 0.5) mm and (25 ± 0.5) cm above the floor of the wind chamber respectively. The Grimm Particle Sizer (model 1.109) was capable of counting particles using 31 channels under bins that have cutoff values of 0.25, 0.28, 0.30, 0.35, 0.40, 0.45, 0.50, 0.58, 0.65, 0.70, 0.80, 1.00, 1.30, 1.60, 2.00, 2.50, 3.00, 3.50, 4.00, 5.00, 6.50, 7.50,

8.50, 10.00, 12.50, 15.00, 17.50, 20.00, 25.00, 30.00 and 32.00 µm. It could also measure particle number concentrations from 1 to 2E6 particles/litre and particle mass ranging from 0.1 to 1E5 µg m^{-3}. The Grimm Particle Sizer has reproducibility within ± 3% over the whole measuring range.

The Grimm Particle Sizer nozzles used for the active experiments were made of 4 mm OD and 3 mm ID stainless steel tubes and connected to the spectrometer via flexible tubing. As shown in Figure 46-(A), Grimm Particle Sizer nozzles come with four different shapes to provide an iso-kinetic sampling. The red nozzle is for still air to 0.5 ms^{-1}, the golden nozzle is for 0.5 to 1.0 ms^{-1}, the green nozzle is for 1.0 to 2.0 ms^{-1}, and the blue nozzle is for 2.0 to 4.0 ms^{-1} speed of emerging air. The iso-kinetic sampling was performed during all stages of resuspension experiments based on the measured velocity readings prior to active experiments.

During the active resuspension experiment, the air contaminated with La_2O_3powder was drawn into the spectrometer via the nozzle at a volume flow rate of 1.2 × (1 ± 5%) l min^{-1} by a volume-controlled pump.

In the measurement chamber of the Grimm spectrometer, particles were drawn across a thin, collimated laser curtain. As particles hit the laser, the laser beam scatters in all directions. Particle size was determined by the amount of scattered light detected by the photodiode located perpendicular to the beam path.

In one counting cycle (6 seconds), bigger particles (2.5 □m and above) are counted for 1 s, and smaller particles (0.25 to 2.5 µm) are counted for the next 5 s with higher

intensity laser light compared to the one used to detect bigger particles. Finally, particles were collected onto a 47-mm Polytetrafluoroethylene (PTFE) filter for gravimetrical analysis. Grimm manufacturer recommends using a microbalance with a 10 µg resolution and collecting at least 1 mg of powder material onto the filter to perform gravimetric measurements to keep weighing error negligible (Grimm Aerosol Technik GbH & Co. KG, 2010).

Before the WIS facility experiments, the initial calibrations of the Grimm Particle Sizers were performed by the manufacturer in Germany (Grimm Particle Sizer Aerosol Technik) using NIST-traceable mono-disperse Polystyrene Latex Spheres (PLS).

3.8 Particle Size Distribution of Lanthanum Oxide Powder Used During WIS Experiment

Two different systems were used to measure the mass fractional size distribution of non-radioactive La_2O_3 powder: Malvern Spraytec laser diffraction particle sizing system and a 31-channel Grimm aerosol spectrometer (model 1.109).

3.8.1 Particle distribution using Malvern Spraytec laser diffraction particle sizing system

The Malvern Spraytec Laser Diffraction system can measure particles from 0.1 to 2000 µm diameters. The Spraytec system has accuracy better than ±1% on the Dv(50) and Dv(90) for NIST-traceable latex standards (Malvern Spraytec, 2013).

Figure 47 shows a typical layout of the Spraytec system and its operating principle (Malvern Spraytec, 2013).

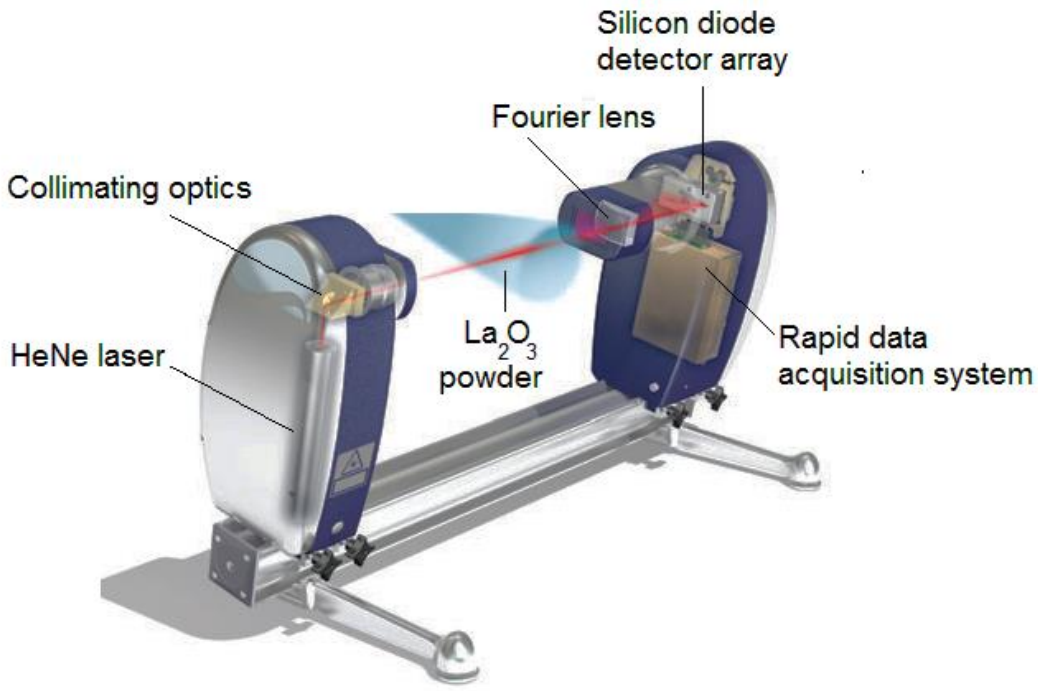

Figure 47: Malvern Spraytec laser diffraction particle sizing system (Malvern Spraytec, 2013)

Particles were sprayed across a 632.8 nm, 2 mW helium-neon laser beam using an in-house-built particle dispersion system. The diffracted laser beam from the La_2O_3 enters a Fourier lens and reaches 36 elements log-spaced silicon diode detector array. Using optical models and third-party software, the Spraytec system converts the signals from silicon diodes into corresponding particle size distributions (Malvern Spraytec, 2013).

Figure 48 shows the particle size distribution of inactive La_2O_3 powder measured from the Spraytec system.

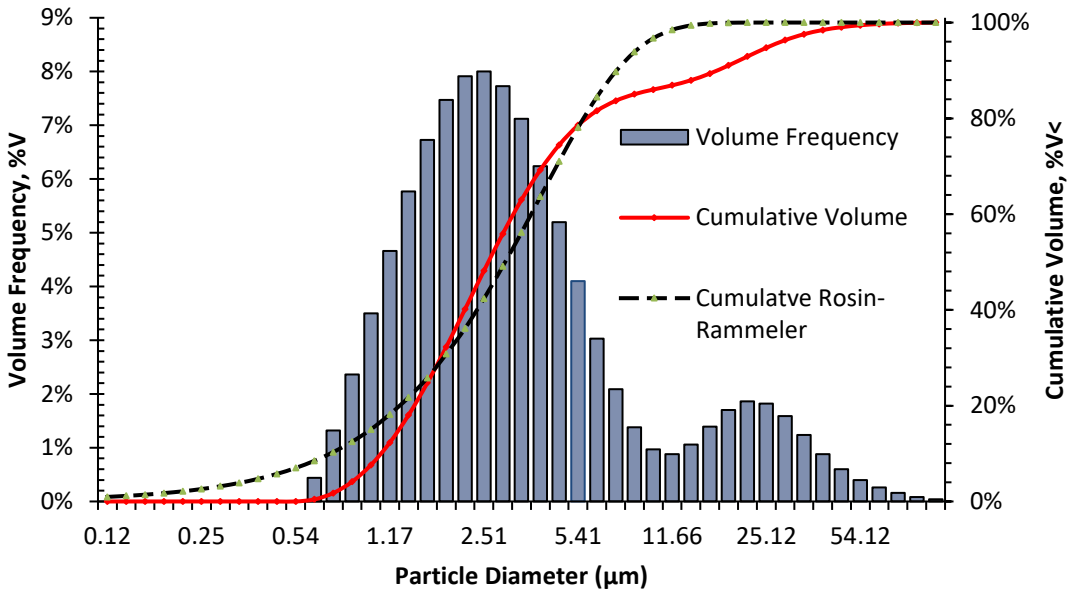

Figure 48: Volume-based particle size distribution of Lanthanum Oxide powder measured by the Malvern Spraytec laser diffraction system and

In Figure 48, the bar graph shows the volume frequency in percent volume vs. particle bin center diameter. This distribution is a bi-model with the highest volume frequency of 8% at 2.51 µm for the first mode and 1.86% at 21.54 µm for the second mode. The solid red line graph shows the cumulative volume percentage vs. Di, and the dotted line shows the Cumulative Rosin-Rammler distribution of the particles.

Powders generated by grinding or milling operations usually fit into the well-known Rosin-Rammler distribution (Ahmed & Ahmed, 2008). Equation (67) shows the cumulative Rosin-Rammler distribution function (Vesilind, 1980).

$$\boldsymbol{R_{CVF} = 1 - exp\left[-\left(\frac{D_i}{D}\right)^N\right]} \qquad \textbf{(67)}$$

here, D is the mean particle diameter, R_{CVF} is the cumulative volume fraction of particles with a diameter greater than the particle diameter D_i, and N is a measure of the spread of particle sizes. Since La_2O_3 powder was produced using a milling and grinding process, particle size distribution results were fitted into the cumulative Rosin-Rammler function. Based on Malvern Spraytec measurements, corresponding D and N values of La_2O_3 powder were calculated to be 3.95 and 1.32, respectively. The Rosin-Rammler fit provided for the cumulative volume fraction of particles measured using Malvern Spratec has an R^2 of 0.8552.

3.8.2 Particle Distribution Using Grimm Particle Sizer

A specified mass of 0.1 grams of La_2O_3 powder was dispersed into an in-house built high-energy particle dispersion system to find the particle size distribution of La_2O_3 powder. Figure 49 shows the schematic of the sampling section of the closed-loop channel used to measure the particle size distribution. The arrows in Figure 49 indicate the particle path and how they move through the iso-kinetic probe connected to the Grimm Particle Sizer.

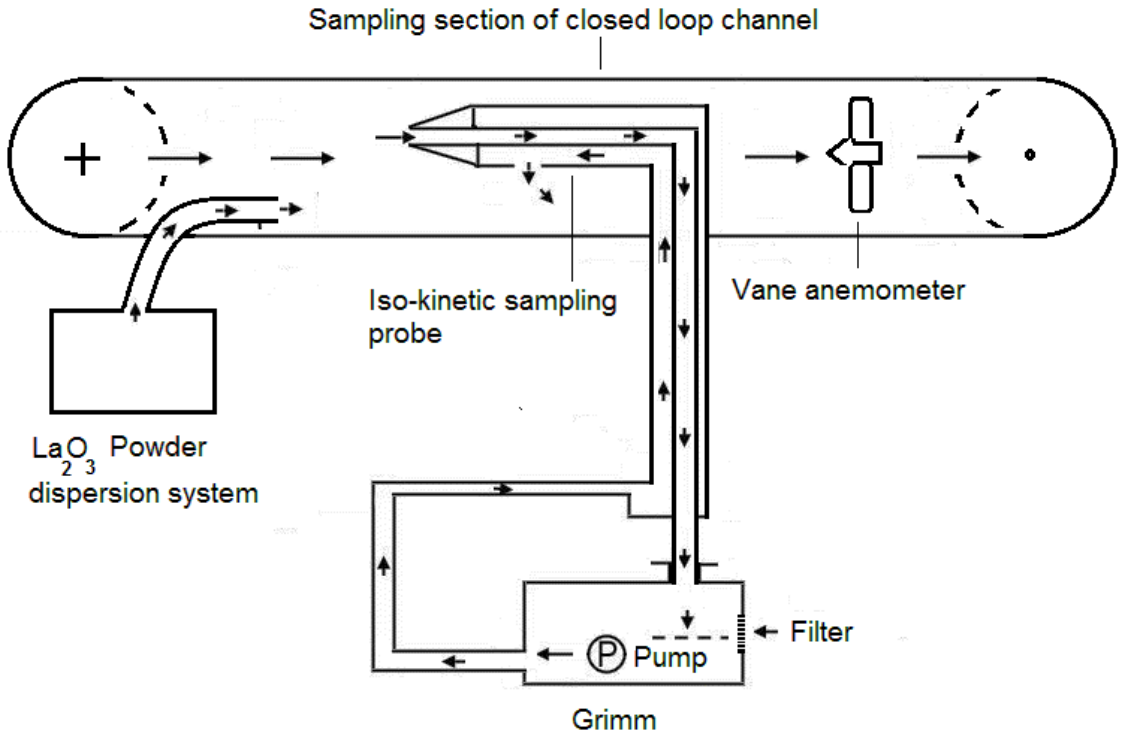

Figure 49: Schematic of the sampling section of the closed-loop channel and operating principle of the isokinetic sampling probe

The particle size distribution of suspended La_2O_3 powder inside a 1-inch internal diameter closed-loop channel was measured using 31 channel Grimm Particle Sizer (model 1.109). An iso-kinetic probe capable of re-feeding sample air back to the close loop channel was used to draw the particles into the Grimm Particle Sizer. The iso-kinetic probe used here differs from the probe used during radioactive resuspension experiments conducted at the WIS facility.

A factory-calibrated vane anemometer was used to measure the velocity inside the closed-loop chamber since vane-type anemometers are more robust and appropriate for a highly contaminated environment than hotwire anemometers used to measure the particle size distribution inside the WIS facility wind chamber before resuspension experiments. A suitable nozzle for the iso-kinetic sampling probe was selected according to the velocity reading of the vane anemometer as per the recommendations by the Grimm aerosol spectrometer-operating manual.

Figure 50 shows the particle size distribution of inactive La_2O_3 powder measured using the Grimm Particle Sizer.

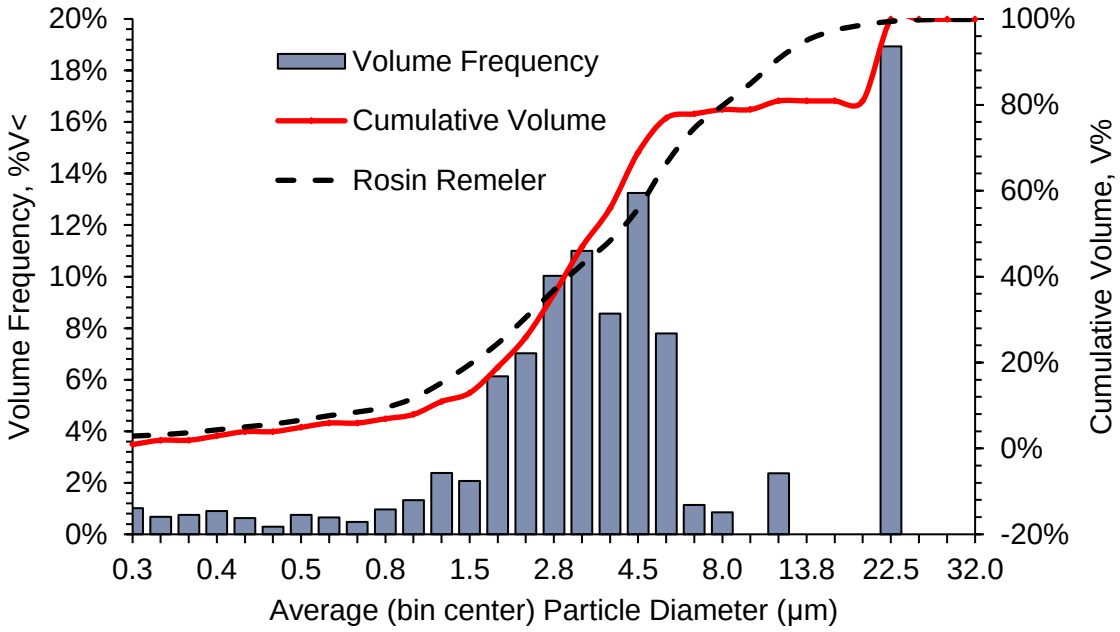

Figure 50: Volume-based particle size distribution of Lanthanum Oxide powder measured by Grimm Particle Sizer

In Figure 50, the bar graph shows the volume frequency in percentage vs. particle bin center diameter (Di). The solid red line graph shows the cumulative volume percentage vs. Di, and the dotted line shows the Rosin-Rammler distribution of the particles.

Based on Grimm Particle Sizer measurements, corresponding D and N values of La_2O_3 powder were calculated to be 5.34 and 1.17and corresponding D and N values of

La_2O_3 powder using Malve Spraytech were calculated to be 3.95 and 1.32, respectively. The Rosin-Rammler fit provided for the cumulative volume fraction of particles measured using Grimm Particle Sizer has an R^2 of 0.8558.

3.9 Comparison of Particle Size Distributions Found Using the Malvern Spraytec Laser Diffraction System and Grimm Particle Sizer

Malvern Spraytec and Grimm Particle Sizer results for volume frequency percentage vs. particle diameter have similar trends. However, the corresponding mean particle diameter (*D*) and *N* (a measure of the spread of the particle sizes) measured using Grimm Particle Sizer are 35% higher and 11% less than values calculated based on Spraytech measurements.

Table 7 compares the volume-based size of particles (Dv). Here, Dv(10) is the size of the particle below which 10% of the volume of La_2O_3 powder lies. Similarly, Dv(50) and Dv(90) correspond to particle sizes of material below which 50% and 90% of the volume of the material lie (Grimm Aerosol Technik GbH & Co. KG, 2010).

Table 7: Comparison of volume-based particle sizes of Lanthanum Oxide powder measured using Malvern Spraytec systems compared to Grimm Particle Sizer.

	Dv(10)	**Dv(50)**	**Dv(90)**
Grimm Particle Sizer (□m)	1.0 × (1± 3.8%)	3.4 × (1 ± 4.4%)	20.5 × (1 ±20.4%)
Malvern Spraytec (□m)	1.1 × (1±5.4%)	2.6 × (1±8.2%)	16.8 × (1±30.1%)
% difference	-10%	-23.5%	18.1%

A comparison of the Grimm Particle Sizer and Malvern Spraytec results shows that the calculated Dv(10) particle size using Malvern Spraytec is higher by 10% than the Grimm Particle Sizer. For Dv(50) and Dv(90) sizes, Grimm Particle Sizer values were calculated to be higher by 23.5% and 18.1%, respectively, compared to Malvern Spraytec values.

The surface weighted mean diameter ($d_{3,2}$), which some literature calls the Sauter mean diameter of La_2O_3 on the contaminated sampling plates, was calculated using Equation (68).

$$\boldsymbol{d_{3,2} = \frac{\sum n_i d_i^3}{\sum n_i d_i^2}} \qquad \textit{(68)}$$

here, $d_{3,2}$ is the Sauter diameter, n_i is the number of particles in bin i, and d_i is the bin center diameter. Since $d_{3,2}$ gives the diameter of a sphere with an equal volume-to-surface area ratio, the Sauter diameter is mainly used as particle diameter in powder research to study particles' aerodynamic properties (Nicholson K. W., 1988). Therefore, corresponding

values for Sauter diameters were calculated to be 2.3 µm using the Grimm Particle Sizer and 2.2 µm using the Malvern Spraytec system.

3.10 Online Radiation Measurement During Resuspension Experiment

The main objective of the online radiation monitoring system was to provide instantaneous radiation field measurements inside the wind chamber during the particle resuspension process without disturbing the airflow and to calculate the mass loading of La_2O_3 powder at detector locations before and after wind. During the resuspension experiments, the radioactivity of La_2O_3 powder on the sample plates was changing continuously due to the resuspension process and radioactive decay.

Figure 51-(A) shows the decay chain of ^{140}La and the energies of the most prominent gamma rays emitted during this process. Figure 51-(B) shows the gamma energy spectrum of ^{140}La generated using a Mobile Microspecs spectroscopic system with NaI(Tl) detector. As discussed earlier, ^{140}La emits both beta and gamma radiation during its decay process. Initially, it emits 100% beta; less than 1% of the ^{140}La will reach stable 140Ce via direct beta decay, and the rest of the daughter products will reach stable ^{140}Ce by releasing gamma rays (Stosch, 2016).

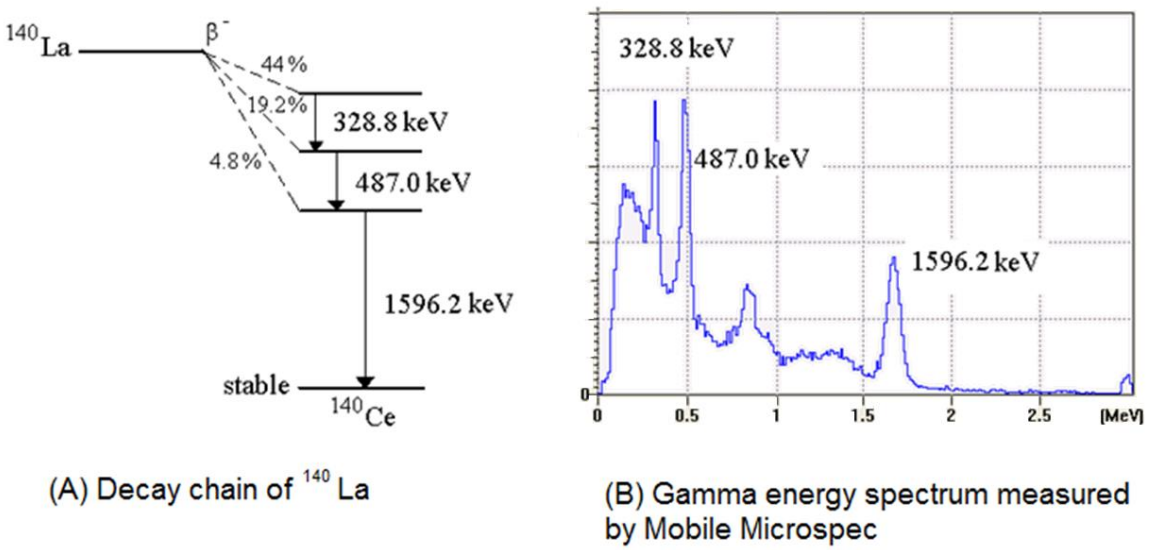

(A) Decay chain of ^{140}La

(B) Gamma energy spectrum measured by Mobile Microspec

Figure 51: Gamma radiation decay chain of ^{140}La and the gamma energy spectrum of prominent peaks measured using the Mobile Microspec spectroscopic system.

The beta count rate could have been measured using a large area contamination monitor as a marker for the number of radioactive atoms in the La_2O_3 powder mixer. However, having an area contamination monitor inside the wind chamber above the contaminated sampling plates would have disturbed the aerodynamic properties of the test chamber. Hence, sensitive gamma detectors were placed under the wind chamber to measure penetrating gamma radiation as a marker for the sample plate contamination level (Rambousky, 2008).

Figure 52 shows the location of the NaI (Tl) detector used with the Mobile Microscopy spectroscopic system during active agent resuspension experiments.

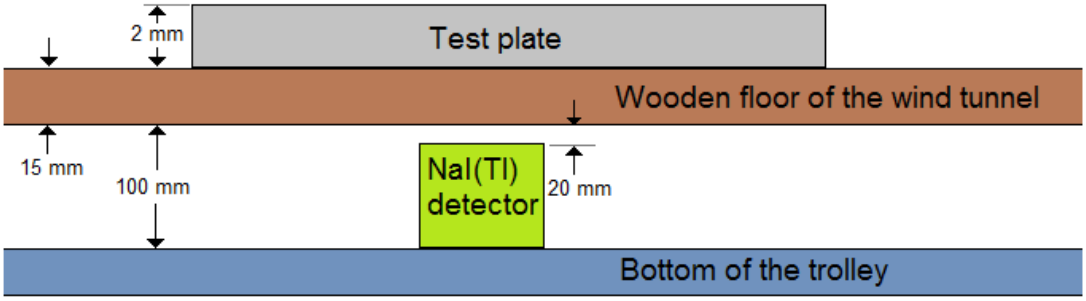

Figure 52: Microspec detector setup for time-dependent dose measurements (Note: all dimensions are in mm, and the length of the Test plate is 50 cm (Rambousky, 2008).

Figure 53 shows a picture of the Mobile Microscopy spectroscopic system with a 3″×3″ NaI(Tl) probe used during the WIS facility online radiation measurements.

Figure 53: BTI MOBILE MICROSPECTM system with 3″×3″ NaI(Tl) probe (Industries, Bubble Technology)

The Mobile Microspec spectroscopic system manufactured by Bubble Technology Industries (BTI) was used to monitor the penetrating gamma radiation from stationary and resuspended La_2O_3 powder during the wind chamber operation due to its proven capabilities of detecting moving radioactive sources. According to engineers from Bubble Technologies Industries Inc, the Mobile Microspec system with 4″ × 4″ × 16″ NaI probe was successfully used to detect moving radioactive sources. For example, this system could count 1000 cps from a 16 μCi ^{137}Cs source located at 3 m away and travelling at 5 mph (2.2 m s^{-1}) velocity with an uncertainty of 7.5% cps.

The geometric efficiency of the detector and the fluence rate before the wind configuration were calculated using MicroShield® and MCNP software. During this modelling process, it was assumed that radioactive La_2O_3 powder was homogenously distributed over the contaminated sampling plates with an average contamination distribution of 300 Bq cm-2 (Rambousky, 2008), (Waller E. , 2007) and (Hill J. D., 2007).

The photon fluence rate at the top surface of the NaI(Tl) detector was calculated by considering that one disintegration of ^{140}La will produce statistically 2.12 photons (Rambousky, 2008). The top surface of the detector was placed 20 mm below the 15 mm thick wooden floor of the wind chamber. Using MicroShield® and MCNP software, the fluence rates at the top surface of the detector were calculated to be 332 $cm^{-2}s^{-1}$ and 326 $cm^{-2}s^{-1}$, respectively (Rambousky, 2008).

Using MCNPX, the geometric efficiency for the NaI(Tl) probe was calculated to be 3.2% (cps/Bq) with a 5% relative error (Shultis & Faw, 2011). The corresponding intrinsic efficiency for NaI(Tl) probe with BTI Mobile Microspec detector was found to be 18-80% from the published data for the energies between 1.5-0.3 MeV, respectively (Green & Finn, 1964).

Four NaI(Tl) detectors (Mic.1, Mic.2, Mic.3 and Mic.4) were used during the active resuspension experiments to measure the radioactivity of ^{140}La powder at selected locations. They were placed under the floor of the wind chamber between lead bricks, as shown in Figure 54.

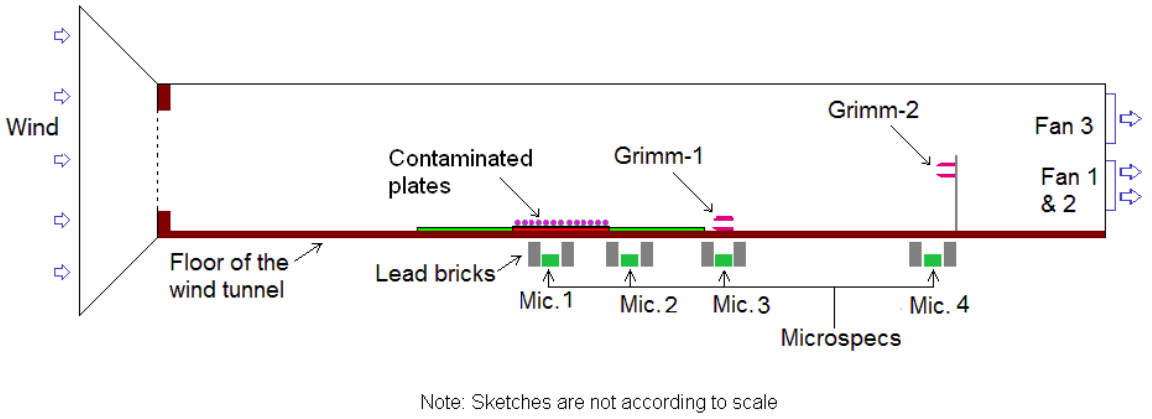

Figure 54: General locations of NaI(Tl) detectors used with the Microspecs System during the active-agents resuspension experiments.

NaI (Tl) detectors (Mic. 1 to Mic. 4) locations under the wind chamber were selected so that one can compare the resuspension factor measurements calculated using

the Mobile Microspec system against Grimm Particle Sizers results. Mic.1 was placed underneath the contaminated sampling plates; Mic. 2 was placed underneath the clean sample plates located downstream of the contaminated sampling plates; Mic. 3 and Mic.4 were placed underneath the Grimm Particle Sizer 1 (Grimm-1) and 2 (Grimm -2) locations respectively.

Table 8 summarizes the net count rate measured using Mic.1, Mic.2, Mic.3 and Mic.4 at different stages of the active-agent resuspension experiment.

Table 8: Summary of net count rate measured using Mic. 1, Mic. 2, Mic. 3, and Mic. 4 NaI(Tl) detectors in cps mode during different stages of active-agent resuspension experiment. Note: BKG corresponds to the background.

Location	Comment	Net peak rate cps	Absolute count rate (Net peak cps – BKG)
Mic. 1	15 min BKG	0	0
Mic. 2	15 min BKG	0	0
Mic. 3	15 min BKG	0	0
Mic. 4	15 min BKG	0	0
Mic. 1	5 min BKG	0	0
Mic. 2	5 min BKG	0	0
Mic. 3	5 min BKG	0	0
Mic. 4	5 min BKG	0	0
Mic. 1	before wind	695338	695338
Mic. 2	before wind	28313	28313
Mic. 3	before wind	0	0
Mic. 4	before wind	43	43
Mic. 1	wind	682757	682757
Mic. 2	wind	35057	35057
Mic. 3	wind	433	433
Mic. 4	wind	93	93
Mic. 1	after wind	676915	676915
Mic. 2	after wind	35641	35641
Mic. 3	after wind	524	524
Mic. 4	after wind	164	164

At the beginning of the day, background measurements were taken for 15 minutes using all four Mobile Microspec systems and for another 5 minutes before every run. Then, contaminated sampling plates were brought into the wind chamber after mapping the contamination distribution using a 9 SVG2 detector array.

After contaminated sampling plates were brought inside the wind chamber, radiation measurements were taken for another 5 minutes (before the wind) to calculate the starting activity of the contaminated sampling plates before the wind chamber was started. Two more sets of radiation measurements were taken for 4 minutes each duration: during the steady-state operation of the wind chamber (wind) and after the wind chamber fans had come to a complete stop (after wind)

The detection limit (DL) of the NaI(Tl) detector was calculated to be 0. 0.009 cps using Equation (69) (Designing and Implementing a Radiobioassay Program, 2008).

$$\boldsymbol{DL(cps) = \frac{2.71 + 4.65\sqrt{BKG(cps) \times CT(s)}}{CT(s)}} \qquad \textbf{(69)}$$

here, BKG is the background reading in cps, and CT counts time in seconds.

The cps readings of NaI(Tl) detectors were decay corrected to the final mixing time. The calculated corresponding Before Wind (BW) and After Wind (AW) Mass loading on the wind chamber surface above Mic. 1 to Mic. 4 detector locations are presented in Table 9.

Table 9: Mass loading at detector locations calculated based on decay Mobile Microspec readings. Note: elapsed time was measured up to the last second.

	Before Wind (BW)		**After Wind (AW)**	
	Mass loading (mg cm-2)		**Mass loading (mg cm-2)**	
Mic.1	6.03E-02	9.18%	5.89E-02	9.18%
Mic.2	2.46E-03	9.18%	3.10E-03	9.18%
Mic.3	0	-	4.56E-05	9.27%
Mic.4	3.72E-06	9.27%	1.43E-05	9.27%

The corresponding activity of ^{140}La on the contaminated sampling plates at the time of mixing was calculated by dividing the decay corrected cps of Mic.1 before wind measurements by the absolute efficiency of Mic. 1 and gamma intensity. The average activity of a contaminated plate Before Wind using a Mic.1 detector was calculated to be $7.5 \times (1 \pm 8.7\%)$ MBq. The calculated average mass of La_2O_3 on a contaminated sampling plate, prior to the influence of wind, was determined to be $150.83 \times (1 \pm 8.8\%)$ mg, in contrast to the $111.1\times (1 \pm 8.1\%)$ mg obtained using the SVG2 detector array.

3.11 Bin-by-bin Resuspension Factors Based on Particle Number

The bin-by-bin resuspension factor around the breathing space of a reference human will provide the size distribution of contaminated particles present due to the

resuspension process. Since different sizes of particles are deposited in different regions of the human respiratory tract, one can find the ratio of deposited particles at respective areas of the lungs versus what was initially deposited on the ground after an RDD event.

3.12 Online Particle Concentration Reading from Grimm Particle Sizers

The time history graphs measured using Grimm Particle Sizers provide particle number concentration (number of particles in 1 litre of air) against the elapsed time. The Grimm Particle Sizer calculates particle concentration readings for all 31 channels at every 6-second interval for the total duration of the experiment.

Combinations of Figure 55, Figure 56 and Figure 56 depict the time history of particle concentration for Grimm Particle Sizer 1. The WIS facility's fans initiated operation at the 726-second mark, remained on until the 1074-second mark, and then gradually ramped down until the 1524-second mark. The fan operation was held constant between the 744 and 1074-second marks.

The wind chamber was running at steady state conditions under the mean velocity of $6.7 \times (1 \pm 7.5\%)$ m s^{-1}, the humidity of $32.5 \times (1 \pm 3.4\%)$ %RH and temperature of $24 \times (1 \pm 7.4\%)$℃.

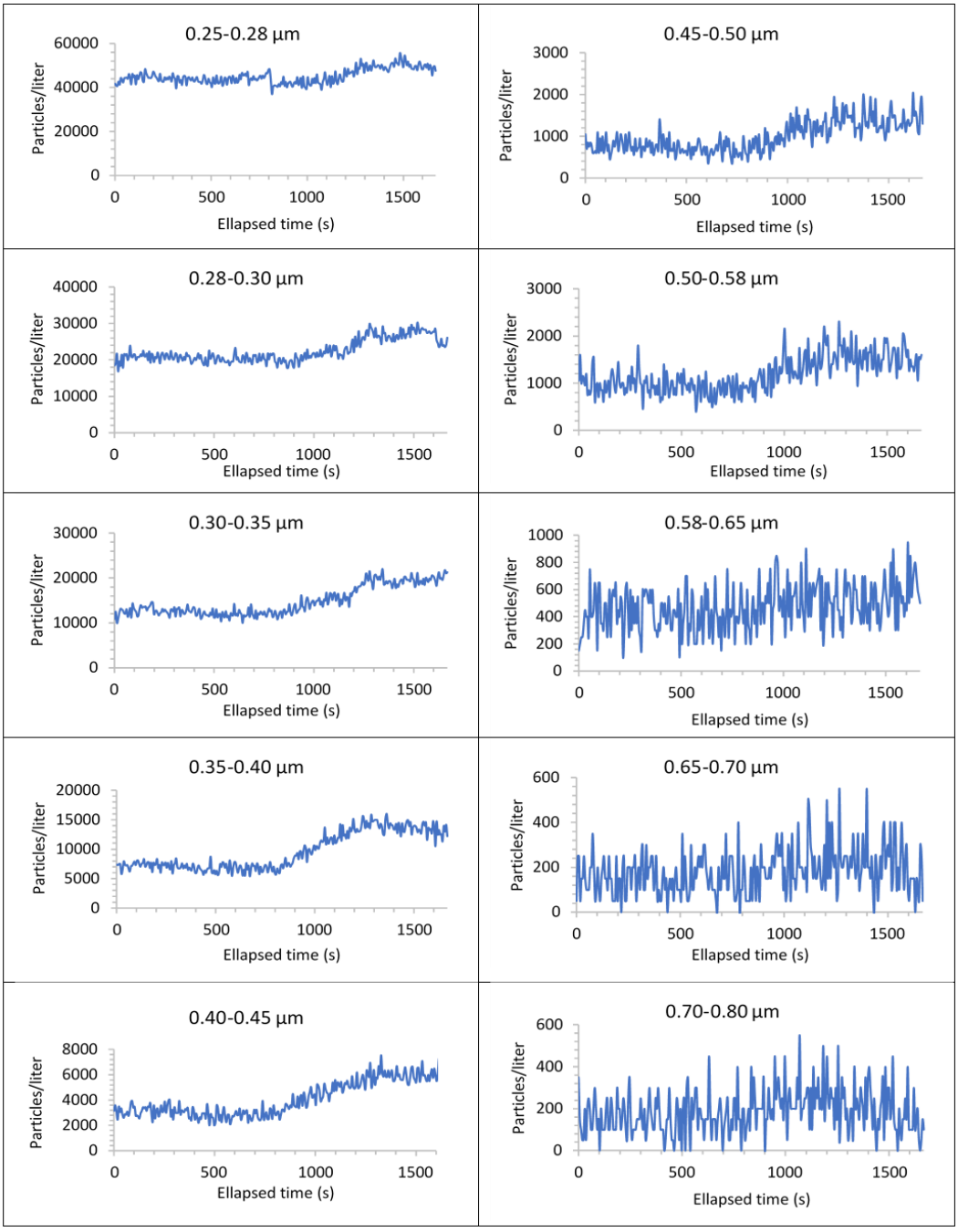

Figure 55: Grimm Particle Sizer 1 time history from particle sizes 0.25 to 0.80 µm. The Y-axis shows the particle number, and the X-axis shows the elapsed time in seconds.

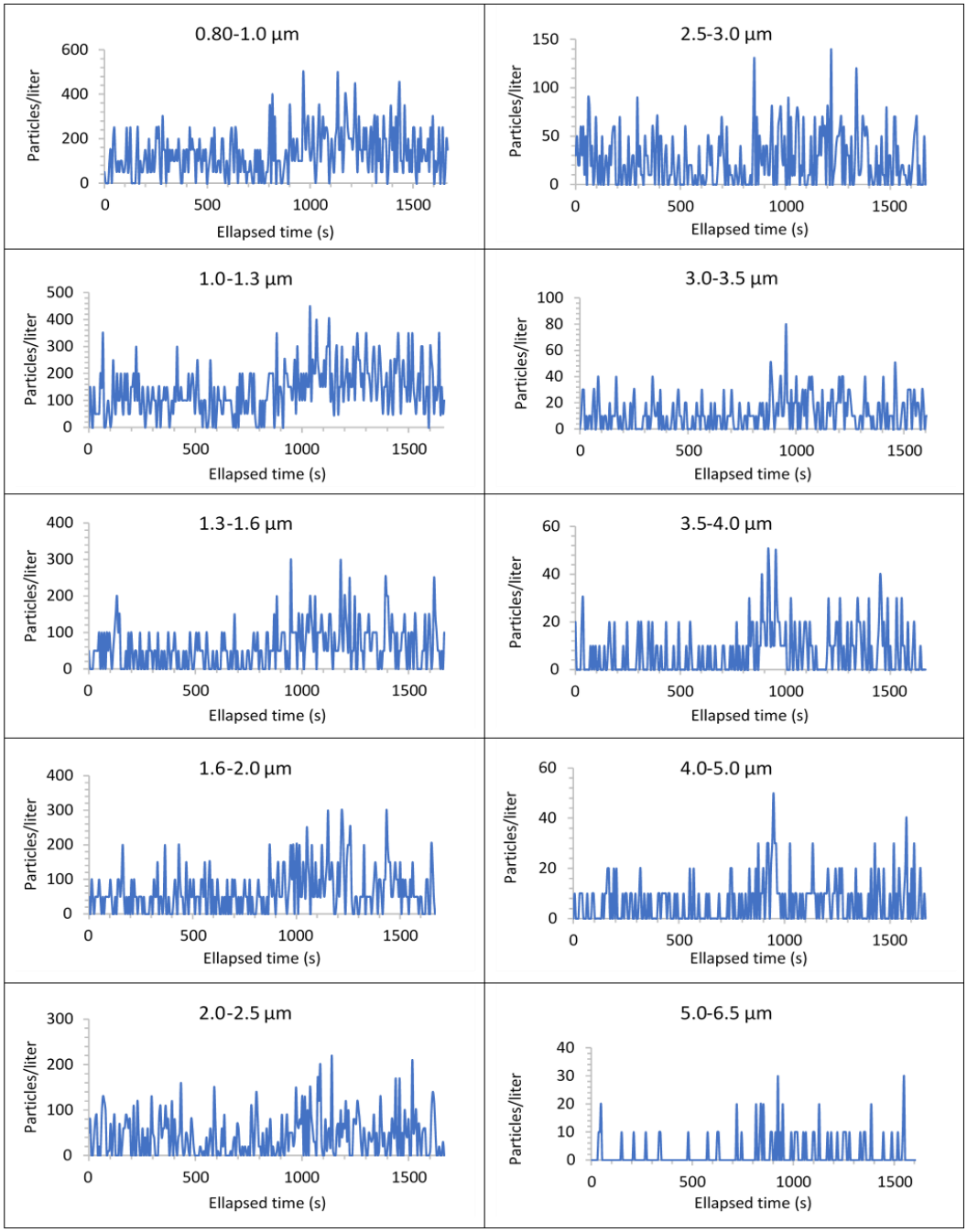

Figure 56: Grimm Particle Sizer 1 time history 1.0 to 6.5 µm. The Y-axis shows the particle number, and the X-axis shows the elapsed time in seconds.

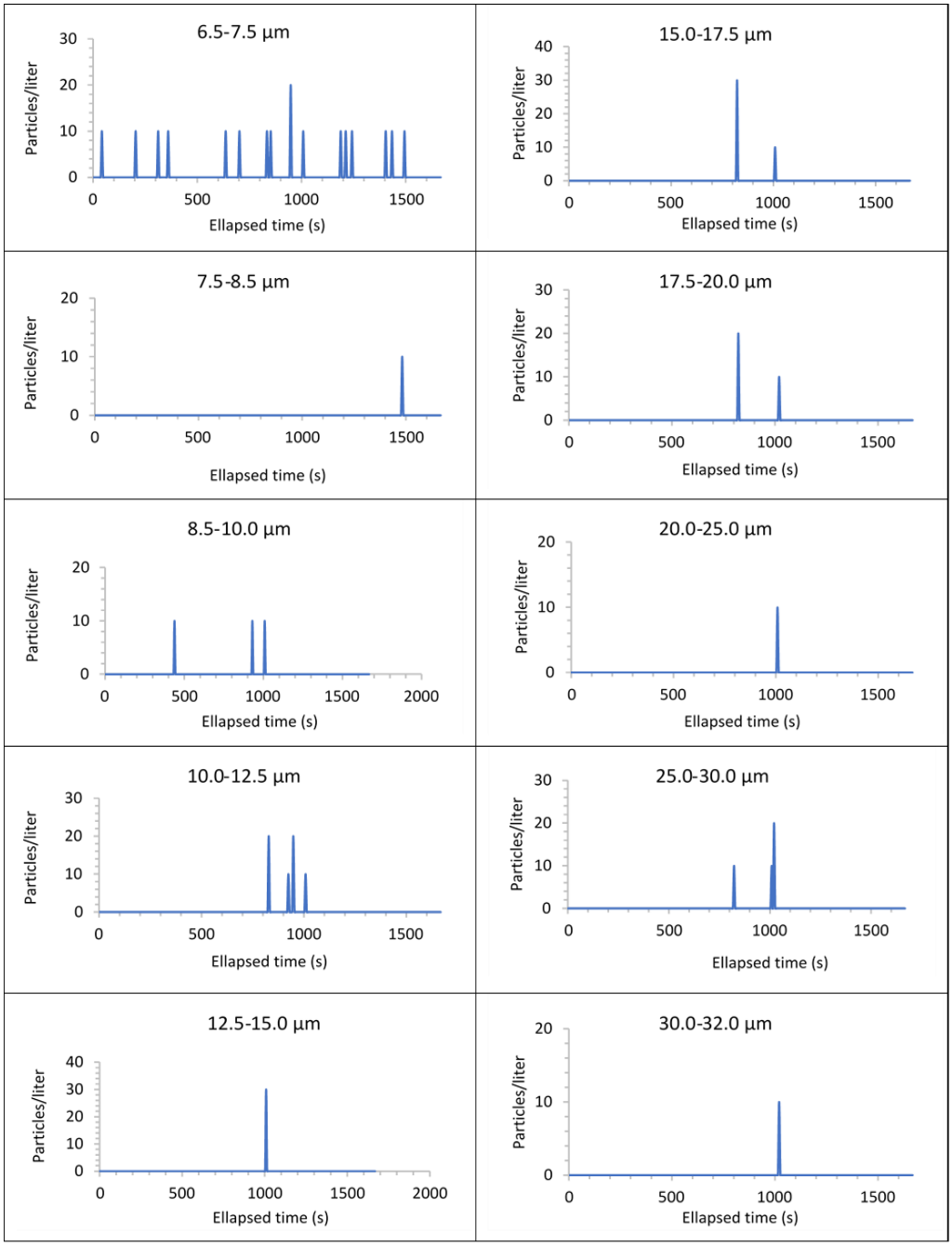

Figure 57: Grimm Particle Sizer 1 time history 6.5 to 32 µm. The Y-axis shows the particle number, and the X-axis shows the elapsed time in seconds.

Careful examination of Figure 55, Figure 56 and Figure 56 shows that particle number concentrations of some bins increase significantly from time to time compared to their average concentrations due to resuspension by immediate lift-off due to turbulent bursts. (Reeks, Reed, & Hall, 1988).

3.13 Summary of critical Steps followed during the WIS facility experiment

Following are the critical steps followed during the critical path of the experiment to calculate the bin-by-bin particle resuspension factor:

3.13.1 Critical steps used in the WIS facility experiment

Step 1: Prepared a La_2O_3 power vial of 20 g with 27 mCi (1 GBq) activity.

Step 2: Contaminated six plates with the powder prepared under gravitational deposition for 8 hours. Note: Particles were dispersed using pressurized air released into a dispersion pod, and a plate has a surface area of 50 cm × 50 cm.

Steps 3 and 4: Measured plate contamination distribution using 9 SVG2 detectors.

Steps 5, 6 and 7: Turned on the Grimms and NaI detectors to measure the background measurements. After taking the initial background reading, contaminated plates were brought inside the wind chamber, and the final background readings were taken with contaminated plates inside the wind chamber for a few minutes before starting the wind chamber. After that, the wind chamber was turned on, and velocity was slowly increased up to steady-state conditions. After a few minutes of running the wind tunnel at a steady state, fans were turned off and ramped down while continuing to take measurements using the Grimm Particle Sizer and NaI detectors.

Steps 8 and 9: Contaminated plates 1 and 6 exposed to wind were brought back to the 9 SVG2 detector array to measure the contamination distribution after the wind.

Step 10: Knowing the decay corrected (to the time of final mixing) activity of the before wind plates measured from the 9 SVG2 probe and the mass (20 g) to activity (1 GBq) ratio, calculate the mass of La_2O_3 on the before wind plates.

Figure 58 shows the experimental activities (steps 1 to 10) in sequential order. You can also see how these activities are connected to the analysis part of the resuspension studies.

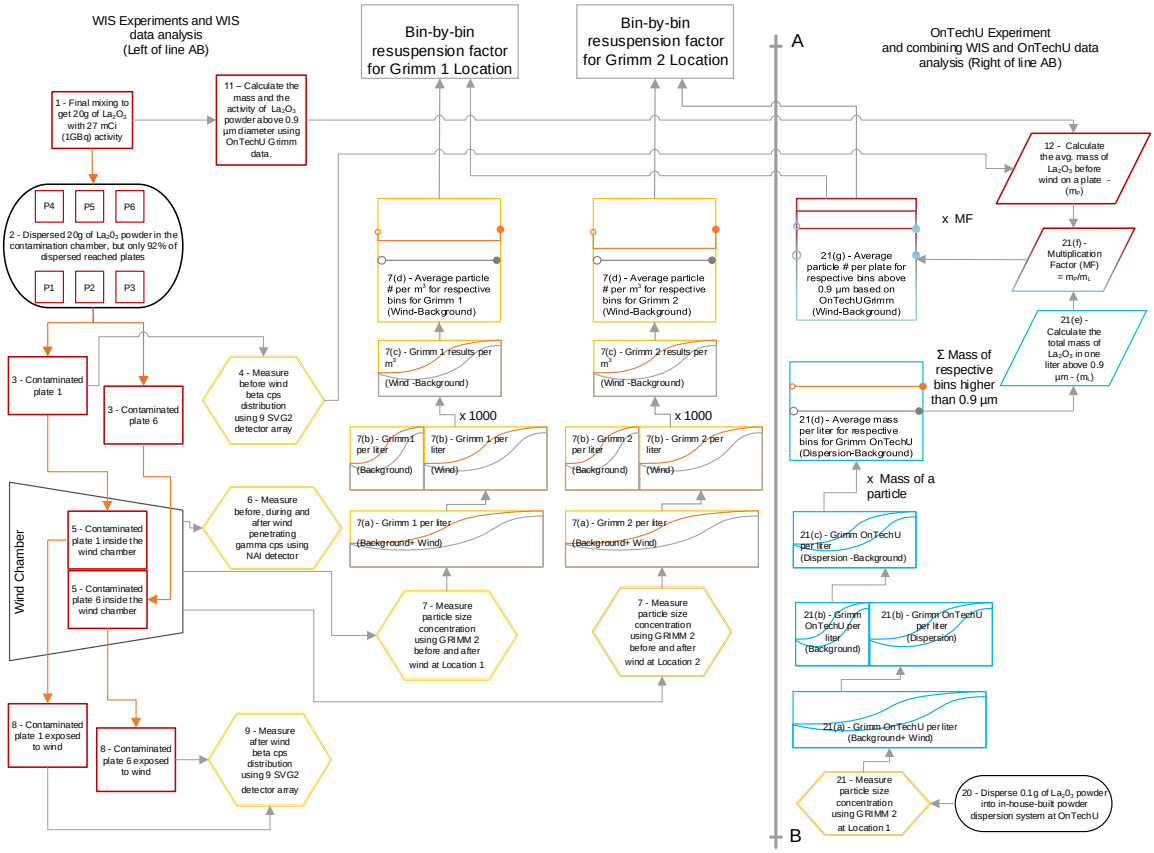

Figure 58: WIS facility resuspension experiment [steps 1 to 9], WIS experiment Grimm results analysis [steps 7. (a to d)], OnTechU Grimm measurements to find particle size distribution [steps 20 to 21. (3)] and finally, the steps that were combined [steps 21(f and g)]

3.13.2 WIS facility experimental data analysis based on Grimm and 6 SVG2 detector array data

The Grimm measurements before and after the wind were further analyzed as described in steps 7(a) to 7(d):

Step 7(a): Grimm 1 and 2 were started well before the plates were brought into the wind chamber; hence, Grimm data will have combined Background and during-wind data.

Step 7(b): Background and during-wind data of Grimm 1 and 2 were separated.

Step 7(c): The Background data of Grimms 1 and 2 were subtracted from respective during-wind data.

Step 7(d): The background subtracted Grimm 1 and 2 data, which were multiplied by 1000 to convert the number of particles of respective bins in 1 litre to $1m^3$ of air at the locations of the Grimms.

3.13.3 OnTechU experimental step

The bin-by-bin particle numbers on the contaminated plates were calculated by combining WIS facility and OnTechU results.

Step 20: 0.1g of La_20_3 powder was dispersed inside an in-house-built powder dispersion system

Step 21: Powder concentration per litre was measured using OnTechU Grimm.

3.13.4 OnTechU experimental data analysis based on OnTechU Grimm data

Steps 21(a) to 21(e) were followed to analyze the Grimm OnTechU data collected at OnTechU at a later time under the same environmental conditions as the WIS facility contamination chamber.

Step 21(a): Grimm OnTechU was started well before the La_2O_3 power was dispersed into the in-house-built dispersion chamber.

Step 21(b): Background and during Dispersion Grimm data were separated.

Step 21(c): The Background data was subtracted from respective Dispersion data.

Step 21(d): The background subtracted an average number of particles in a respective bin per litre and was multiplied by the mass corresponding to the bin center diameter. Note: the density of the La_2O_3 was used as 6.51 g cm^{-3} (LTS Research Laboratories, Inc, 2015)

Step 21(e): Calculate the total mass of La_2O_3 powder in a litre of air by summing all the masses for respective bins.

3.13.5 Combining the WIS facility and OnTecU data

Steps 21(f) and 21(g) were used to combine the WIS facility and OnTechU data.

Step 21(f): Calculated the Multiplication Fraction (MF) by dividing the total mass of La_2O_3 powder on a contaminated plate found from WIS facility data (step 11) by the total mass of La_2O_3 powder in a litre of air calculated using OnTechU Grimm data (step 21(e)).

Step 21(g): Calculated the average number of particles on the contaminated plate for the respective particle bin size used at the WIS facility by multiplying the average number of particles measured using OnTechU Grimm for the respective MF.

Note: Particles were deposited for 8 hrs. onto the contamination plate under gravity. Figure 59 shows the particle deposition time found using CFD modelling of WIS facility contamination chamber particle deposition during the contamination process.

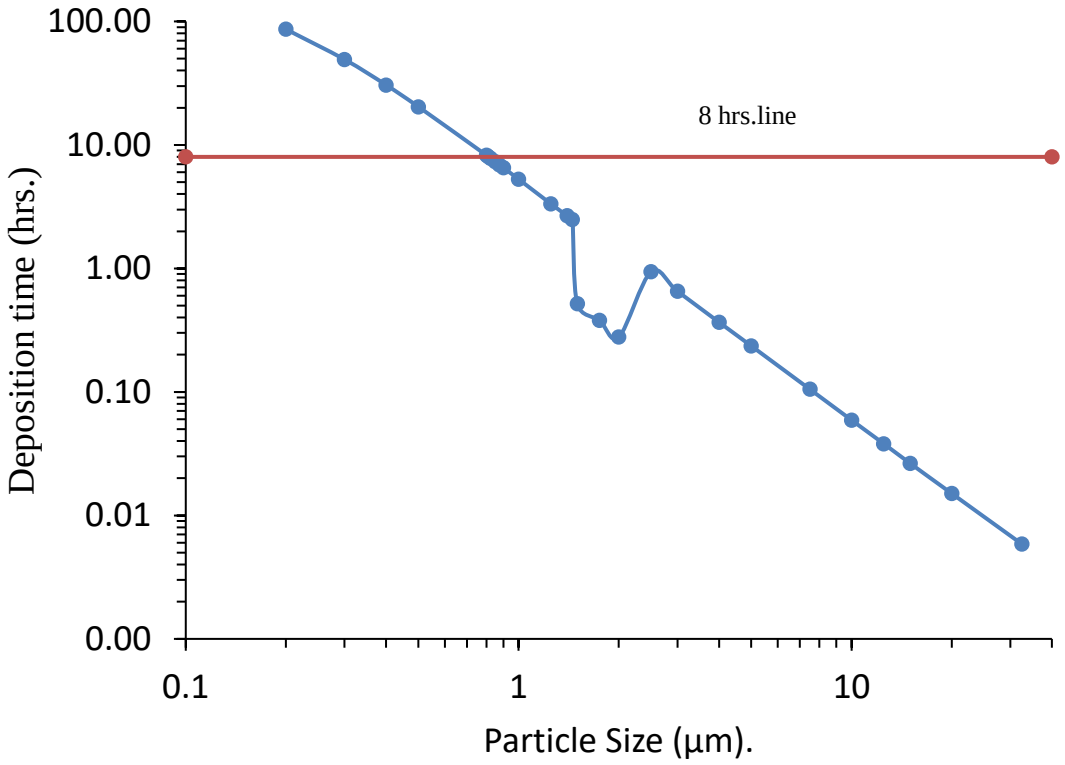

Figure 59: Particle deposition time during the contamination process

CFD results show that particles less than 0.82 µm would take longer than 8 hours to reach the contamination plates. As per OnTechU Grimm results, the cumulative volume fraction corresponding to particle size 0.9 µm is 8%. During the contamination plate preparation process, 20 g of La_2O_3 powder with 27 mCi (1GBq) was dispersed inside the chamber, but only 92% of the powder was deposited onto plates. Hence, 18.4 g of La_2O_3 powder with decay corrected activity of 24.8 mCi (919 MBq) with particle sizes larger than 0.9 µm will reach the plate. This activity-to-mass ratio will be used to calculate the corresponding Multiplication Factor (MF) required to calculate the number of particles on

a plate by combining the OnTechU Grimm results for the particle sizes higher than 0.9 µm. As per this analysis, it is only possible to calculate the bin-by-bin resuspension factor for particle sizes larger than 0.9 µm using the experiment setup conducted at the WIS facility.

3.14 Calculating bin-by-bin experimental resuspension factor data

The definition of the bin-by-bin resuspension factor used in the thesis is given by

$$\boldsymbol{K_i = \frac{n_{a,i}}{n_{cp,i}}} \qquad \textit{(70)}$$

here, K_i is the resuspension factor under particle size bin i, $n_{a,i}$ is the arithmetic average of background reduced particle concentration values in 1 m^3 of air in bin i calculated from the steady-state Grimm Particle Sizer readings $n_{cp,i}$ is the calculated average number of particles on the $1m^2$ area of contaminated sampling plates in particle size bin i prior to the resuspension experiment. The value of $n_{cp,i}$ was calculated using Equation (71).

$$\boldsymbol{n_{cp,i} = n_{p,i}\, MF} \qquad \textit{(71)}$$

here, $n_{p,i}$ is the number of particles measured in bin i using OntrioTechU Grimm at a later time, and MF is the Multiplication factor

3.14.1 Experimental Bin-by-bin Resuspension Factors

Figure 60 shows the background reduced particle concentrations at Grimm 1 and 2 particle sizer locations per m^3 during the steady winds and particle concentration on the contamination plate per m^2 before the wind for particle sizes between 0.9 and 31 µm.

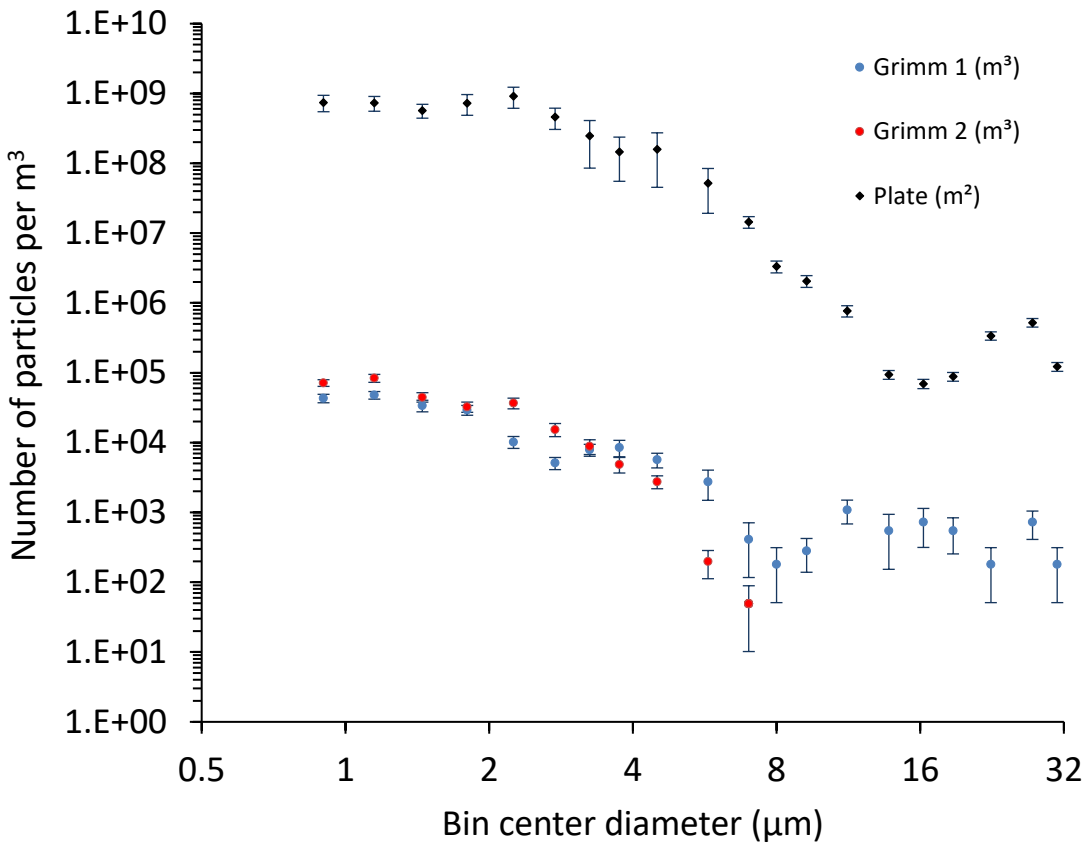

Figure 60: Number of particles calculated on an average contaminated plate per m²(black diamonds), average particle concentration per m³ at Grimm Particle Sizer 1 (blue circles) and Grimm Particle Sizer 2 (red circles) locations.

As per Figure 60, particles beyond 6.75 µm in bin-center diameter did not reach the Grimm Particle Sizer 2 location.

Figure 61 shows the resuspension factors at the Grimm Particle Sizer 1 location for particle sizes between 0.9 and 6.5 µm.

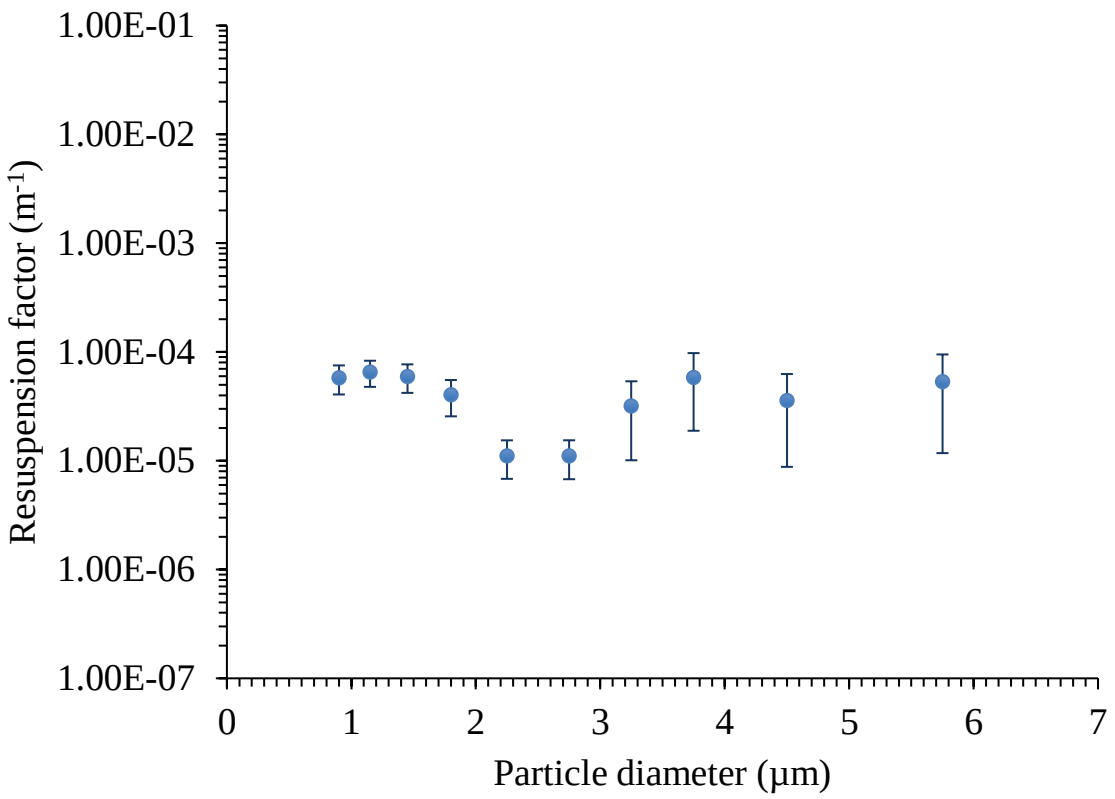

Figure 61: Background reduced average bin-by-bin resuspension factor for Lanthanum Oxide power at Grimm Particle Sizer 1 location for particle sizes between 0.9 and 6.5 µm particle size range. Note: The resuspension factors found beyond particle size 6.5 µm were statistically insignificant.

The bin-by-bin resuspension factors at Grimm Particle Sizer 1 location have an average value of 4.12E-05 × (1 ± 46.8%) m^{-1} for the particle sizes between 0.9 to 6.5 µm.

Figure 62 depicts the bib-by-bin resuspension factors for Grimm Particle Sizer 2 location for particle sizes between 0.9 and 6.5 µm.

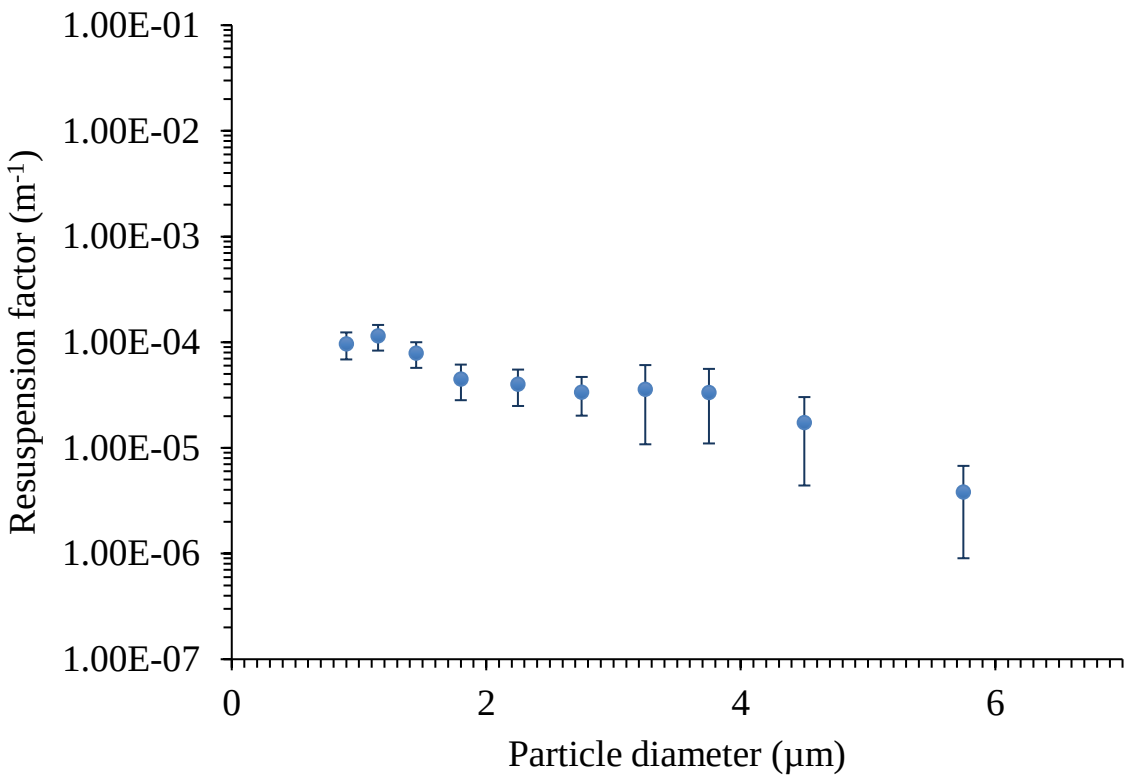

Figure 62 Background reduced average bin-by-bin resuspension factor for Lanthanum Oxide power at Grimm Particle Sizer 2 location for particle sizes between 0.9 and 6.5 µm particle size range. Note: The resuspension factors found beyond particle size 6.5 µm were statistically insignificant.

The average bin-by-bin resuspension factor at Grimm Particle Sizer 2 location has an average value of 4.56E-05 × (1 ± 79.5%) m^{-1} for the particle sizes between 0.9 to 6.5 µm. The average bin-by-bin resuspension factor at Grimm Particle Sizer 2 location reduces from 9.63E-05 at 0.9 µm to 3.83E-6 at 6.5 µm, following the equation: $K_i = 0.0002e^{-0.588\Phi_i}$ (R2 =0.8975), where K_i is the average bin-by-bin resuspension factor and $\Phi_i$is bin-center diameter.

Respiratory deposition fractions of resuspended particles

Figure 63 shows respiratory deposition fractions (RDF) curves for three central anatomical regions that Hinds (1999) generated for particles from 0.9 to 6.5 µm physical diameters.

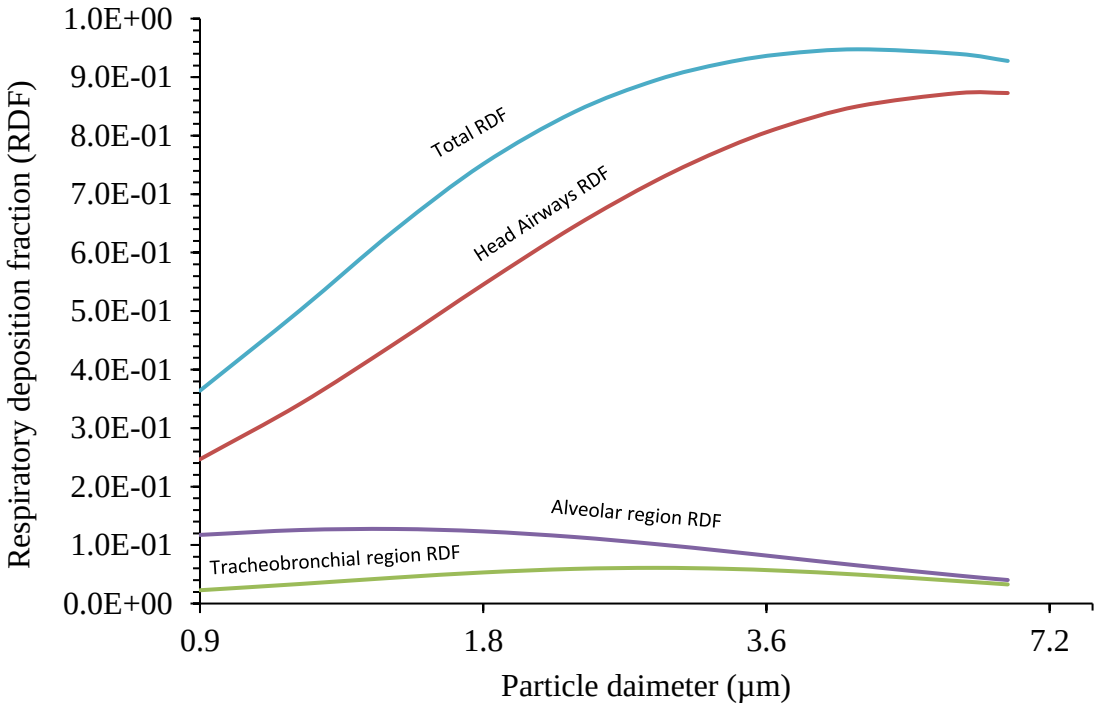

Figure 63: Deposition of particle sizes between 0.9 and 6.5 µm in the human respiratory tract when a person breathes through a nose (light exercise) based on the ICRP deposition model. Average data for males and females (Hinds 1999).

The RDF for the Head Airways (HA) region increases from 2.47E-01 at 0.9 μm to 8.73E-01 at 6.5 μm. The RDF for the Alveolar (AL) region increases from 1.17E-01 at 0.9 μm to 1.27E at 1.45 μm and reduces to 4.02E-2 at 6.5 μm particle size. The RDF for the Tracheobronchial (TB) region increases from 2.28E-2 at 0.9 μm to 6.10E-2 at 2.75 μm and reduces to 3.27E-2 at 6.5 μm. The total RDF increases from 3.64E-1 at 0.9 μm to 9.48E-2 at 4.5 μm and reduces to 9.28E-1 at 6.5 μm.

3.14.2 Deposition Fraction of Resuspended particles (DFR)

Figure 36 shows that respiratory deposition fraction at different anatomical regions of the respiratory tract depends on particle size. Therefore, one can find the deposition fraction of the particles that were resuspended due to a dirty bomb event by multiplying the respiratory deposition fraction (RDP) with the corresponding bin-by-bin particle resuspension factor (K_i). Here, we used the bin-by-bin resuspension factor to find the deposition fraction for the worst-case scenario.

$$\boldsymbol{DFR_i = RDF_i \times K_i} \qquad \textbf{(72)}$$

where, DFR_i (m^{-1}) is the deposition fraction of resuspended particles for bin i, RDF_i is the respiratory deposition fraction for bin i, and K_i. (m^{-1}) is the average bin-by-bin resuspension factor for bin i.

Figure 64 shows the DFR_i and K_i for particle sizes from 0.9 to 6.5 µm generated using the bin-by-bin resuspension factor values calculated at the Grimm Particle Sizer 2 location.

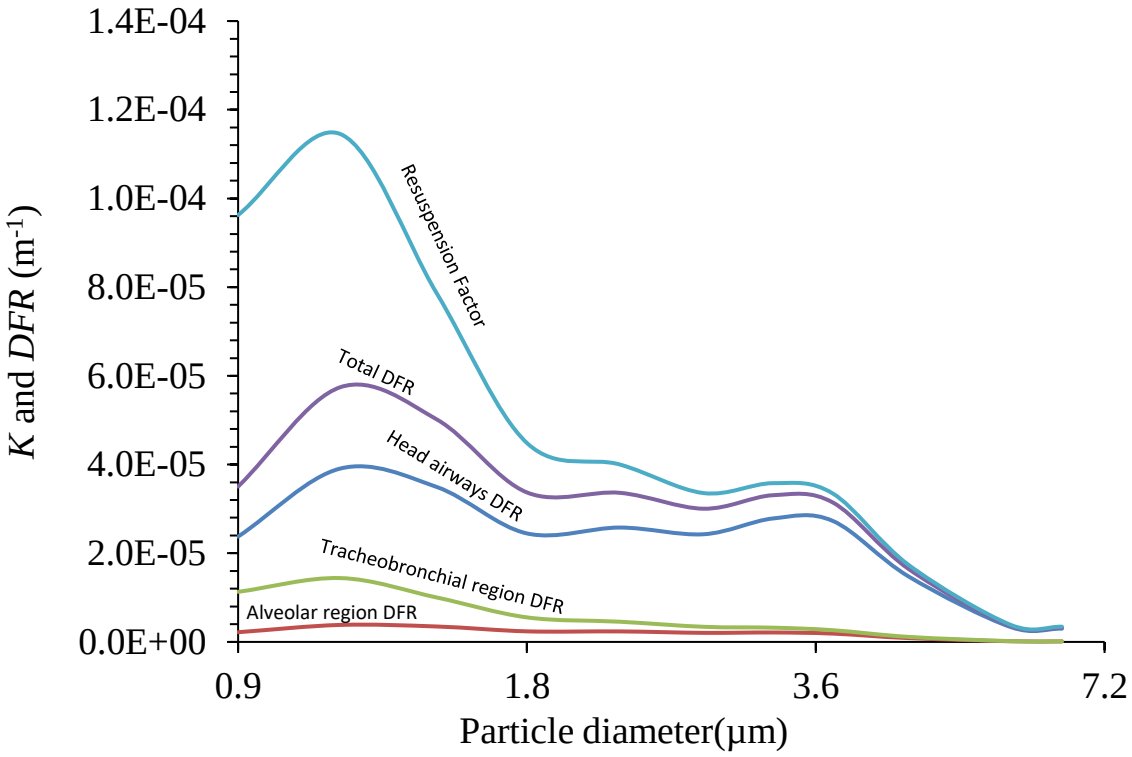

Figure 64: DFR for Head Airway (HA), Tracheobronchial (TB) and Alveolar (AL) regions, and bin-by-bi resuspension factor against Particle sizes between 0.9 and 6.5 µm.

The DFR value for the Head Airway (HA) region increases from 2.37E-5 at 0.9 µm to 3.91E-5 at 1.15 µm and reduces to 2.45E-5 at 1.8 µm. Beyond this point, the DFR value for HA stays around 2.59E-5 ± 11.61E-6 up to 3.75 µm and reduces to 2.98E-6 at 7 µm. A similar trend is observed for the DFR in the Tracheobronchial (TB) and Alveolar (AL) regions. The DFR for the TB region increases from 2.19E- at 0.9 µm and up to 3.83E-6 at 1.15 µm and then reduces to 1.00E-7 at 7 µm. Similarly, DFR for the AL region increases from 1.13E-5 at 0.9 µm to 1.44E-5 at 1.15 µm and reduces down to 1.23E-7 at 7 µm.

It is also observed that the shapes of DFR for the HA, AL and TB curves are similar to the Resuspension factor curve.

3.15 Summary

Radionuclide particle resuspension after an energetic release from a dirty bomb event was successfully modelled using a specially built 10 m long wind chamber that was capable of producing winds up to 6.7 × (1 ± 7.5%) m s-1.

The average bin-by-bin resuspension factors (*K*) for particle sizes between 0.9 µm to .5 µm at Grimm Particle Sizer 1 and 2 locations, 52.5 cm and 165 cm downstream from the initial fallout, were calculated to be 4.12E-05 × (1 ± 46.9%) m^{-1} and 4.98E-05 × (1 ± 79.5%) m^{-1} respectively. Table 10 summarizes the experimental resuspension data.

Table 10: Summary of average Resuspension factor data

	Grimm 1 location	**Grimm 2 location**
Particle Size Range (µm)	0.9-6.5	0.9 -6.5
Average *K* (m^{-1})	4.12E-05	4.56E-05
Std. Dev of *K* (m^{-1})	1.99E-05	3.53E-05

The resuspension factor values calculated in the experiment match very well with the improved Anspaugh et al. modified relationship capable of predicting resuspension data down to 0.01 days. The modified Anspaugh correlations were derived by curve-fitting resuspension data collected across three continents (Maxwell & Anspaugh, 2011). Figure 10 shows how the derived average bin-by-bin experimental resuspension factor results for particle sizes 0.9 µm to 6.5 µm would fit into the previously collected experimental resuspension data summarized by Anspaugh.

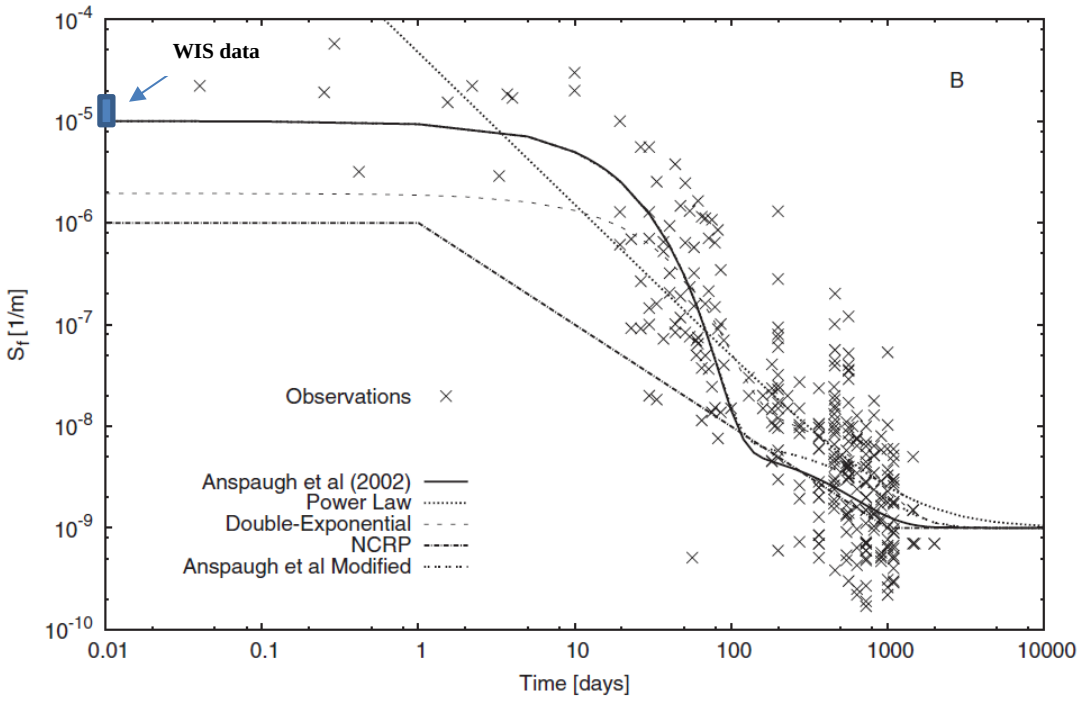

Figure 65: Plot of Sf vs. time for previously observed data and five resuspension models, Anspaugh et al. (2002), Power Law, Double-Exponential, Anspaugh modified, and NCRP. (Maxwell & Anspaugh, 2011)

As per the modified Anspaugh correlation, the upper-bound resuspension factor value at $time = 0.01$ days is 4.2E-5 m^{-1}. The average bin-by-bin center resuspension factor values calculated during the experiment at Grimm Particle Sizer 1 and 2 are 1.1% and 18.6% higher compared to the lower bound value of the modified Anspaugh correlation.

Most large-scale resuspension studies were conducted via observations or experiments conducted using aged atomic bomb sites and past nuclear accidents. Parameters, such as initial resuspension factors at time=0, were calculated using mathematical models.

In this chapter, the research delves into a comprehensive examination of resuspension factors for particles spanning 31 different sizes, ranging from 0.25 to 32 μm in diameter. Notably, the concept of average bin-by-bin resuspension factors (Ki) has received limited attention within the existing literature pertaining to resuspension studies. The methodology employed in this chapter underscores the necessity of simultaneously assessing both the initial fallout's radioactivity and the particle size distributions to derive these bin-by-bin particle resuspension factors.

The significance of calculating the average bin-by-bin resuspension factor lies in its potential application in assessing the health risks to the human respiratory system following a dirty bomb event. Since particles of varying sizes tend to deposit in distinct regions of the respiratory tract, this data becomes invaluable for understanding the associated health hazards, as previously discussed by Hinds (1999).

Furthermore, the subsequent chapter will delve into a detailed exploration of the resuspension process using Computational Fluid Dynamic (CFD) methods. This will encompass CFD modelling of the experimental setup and a comprehensive examination of the resuspension process.

4 CFD MODELING OF THE WIS FACILITY RESUSPENSION EXPERIMENT

The goal of the CFD modelling of the thesis is to simulate the particle resuspension due to aerodynamic forces acting on the particles due to wind shear generated by the air inside the WIS facility wind chamber using computer resources that will be available to an average analyst who will be helping first responders attending a dirty bomb event.

The length scales of the CFD model of the WIS facility wind chamber to model the particle resuspension process can vary from meters to micrometres. The wall adjacent cell size of the WIS facility wind chamber must be at least less than the smallest particle size (0.25 μm) to capture aerodynamic forces acting on individual particles during initial particle resuspension. The resultant 3D WIS facility wind chamber computational domain mesh that can capture the resuspension of the particles on the wind chamber floor as a result of the mean flow generated by the fans will have close to 2.25 billion mesh elements. According to ANSYS and Cray, one of the most extensive external aerodynamics simulations performed by Ansys FLUENT software to model an entire peloton of 121 cyclists utilizing Reynolds-averaged Navier-Stokes (RANS) equations and the Transition k-ω SST closure model had close to 3 billion mesh elements, and it took 108 supercomputing hours across 13,824 parallel processes to solve. The wall adjacent cell size of the mesh next to the cyclist used in the peloton of 121 cyclist model was 20 μm (Blocken, et al., 2018).

Solving the WIS facility computation model using a supercomputer is possible. However, the time it takes will not be quick enough for the incident commanders or the first responders to make evacuation plans following the release of radioactive material into the atmosphere as a result of a dirty bomb. Also, one cannot guarantee that the analyst can have access to a supercomputer in a reasonable time frame. Hence, the computational domain will be divided into global and local models to find the solutions within a reasonable time frame using a high-end personnel computer. A similar problem is usually faced when modelling metrological events. The mesh sizes of a global metrological model can have length scales from 300 km to 5 km. However, the local weather phenomena occur on a much smaller scale, and one should use a fine mesh, in the orders of meters, to predict global weather conditions. The boundary conditions of the regional model are usually found in the converged global model (Warner, 2010).

4.1 The Global and Regional models' concepts

Figure 66 shows the Global and Regional model concept used for the 3D WIS facility CFD model.

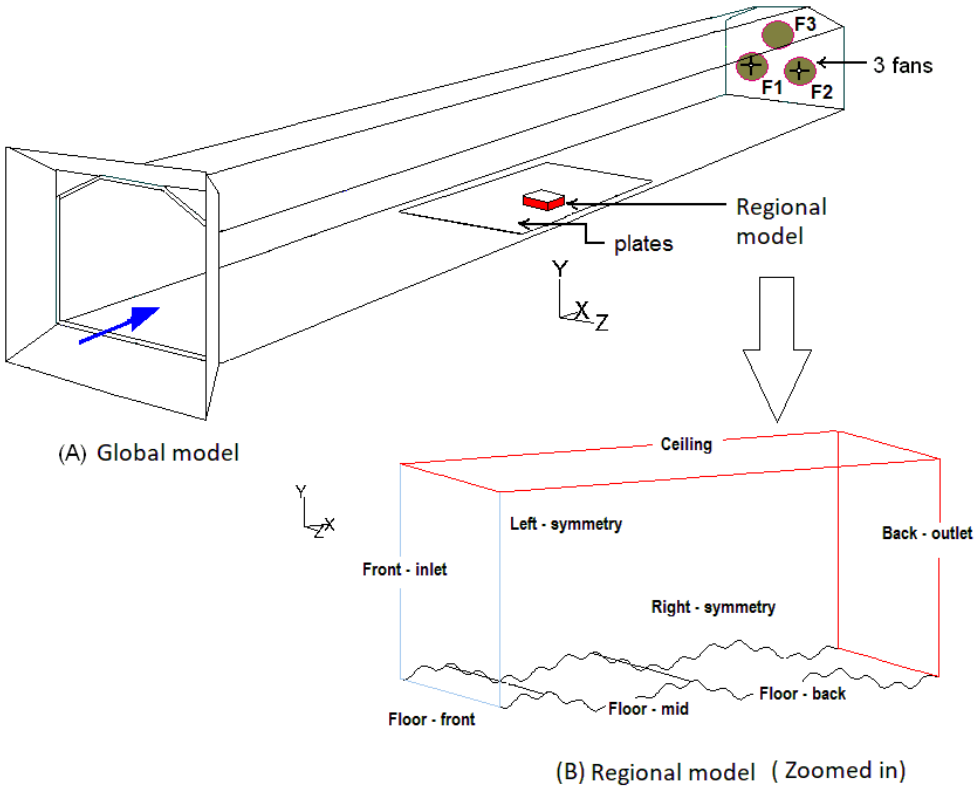

Figure 66:Concept of the Global and Regional model. Note: Figures are not according to scale. The Regional model is 414 μm x 106 μm x 100 μm, in downstream, floor normal and transverse directions, respectively, and the downstream length of the Global model is 10m.

The size of the Global model, which represents the whole wind chamber, was 24,155 times bigger than the Regional model. The Global model was 10 m long, and the size of the Regional model was 414 μm × 106 μm × 100 μm in x, y, and z directions, respectively.

In order to find the resuspension factor using computational fluid dynamics within a reasonable time frame, the experimental setup conducted at the WIS facility in Germany was modelled using Large Eddy Simulations (LES). In the LES model, the large eddies are resolved directly while the smaller eddies are simulated, reducing the computational cost compared to Direct Numerical Simulations (DNS), where eddies from the large scale to the smallest scale (Kolmogorov scale) are resolved (Fluent Inc., 2006). Given the current state of technology, high-performance computers can only handle the direct numerical simulation (DNS) of simple low Reynolds number flows (Crasto, 2007).

First, the computational domains were solved using the Reynolds-Averaged Naiver-Stokes (RANS) approach, and turbulences were modelled using the Shear Stress Transport k-ω SST closure model to find realistic initial conditions (U, k, ε profiles) required to solve the problem using LES approach (Fluent Inc., 2006). The k-ω SST closure model was used due to its superior capability of modelling the velocity and turbulent parameters close to the floor surfaces where initial particle resuspension would take place. Please refer to Appendix B, section 8.2, to see the initial work done by the author to select the best closure model available in FLUENT 6.3.26 software for particle resuspension studies and the theoretical background behind the k-ω SST turbulence model.

Mesh generations of the models were performed using Gambit 2.4.6 software, solving governing equations, and the post-processing of results was done using FLUENT 6.3.26 double-precision solver. Governing equations were integrated into the individual control volumes (mesh elements) to construct a set of linear algebraic equations consisting of discrete dependent variables such as velocities, pressure, and turbulence parameters (Fluent Inc., 2006). Solutions for a linear set of algebraic equations provided updated values of dependent variables. The best practice guidelines in CFD modelling were followed to ensure grid independence and the use of higher-order numerical schemes (Kaiser, 2019)

The Global CFD model of the WIS facility wind chamber included all physical features except the surface roughness elements of the walls and detectors used during the experiments. The computational domain of the Global CFD model, with wall adjacent cell size of 0.1 μm, has close to 16 million mesh nodes. Utilizing the LES approach, the Fluent software's 3D double-precision version, running on an Intel(R) Core(TM) i7-4930K computer equipped with 6 cores and 12 threads, required nearly a month to attain converged solutions down to a convergence level of 1E-6.

The time it took to solve just the Global model is much longer than the total available time for the analyst since the evacuation plans need to be prepared within the first 100 minutes following the dirty bomb (US Homeland Security, 2017). Hence, we expect the analyst to have access to a database of Global CFD solutions handy for the vulnerable cities where terrorists may explode dirty bombs.

The analyst will build the Regional CFD computational model following the process provided in the thesis. The computational domain mesh of the Regional model will be developed using the measured surface roughness properties of the Hot Zone and the precalculated interface boundary data between the Global and Regional models under weather conditions similar to the day of the dirty bomb.

The measured particle size distribution of the radioactive particles fallen to the Hot Zone provided by the first responders will be used to calculate the bin-bin-bin resuspension factor by releasing particles with known particle size distribution into converged Regional and Global CFD models.

4.2 The summary of the CFD process used to calculate the particle resuspension using CFD

The CFD modelling sequence of the dirty bomb scenario can be divided into two main parts: Part 1: The CFD modelling of the Global model prior to the dirty bomb event and Part 2: the CFD modelling of the Regional model after the dirty bomb event as summarized below:

4.2.1 Part 1: Global model (pre-dirty bomb)

Step 1: Mesh generation of the Global model of the vulnerable cities (For thesis: WIS facility wind chamber used during the experiment)

Step 2: Solving appropriate governing equations related to the Global model

a. First, solve the Global computation domain using the Shear Stress Transport k-ω SST closure model to find realistic inlet conditions (U, k, ε profiles) (Fluent Inc., 2006).
b. Second, solve the Global computational domain using the LES method

Step 3: Post-processing of results of the Global model

a) Calculate the time-averaged mean inlet ceiling boundary conditions for the Regional model.

Step 4: Calculate the bin-by-bin Global CFD transfer factors at the receptor location (For thesis: at the Grimm detector locations) of the computational domain using the converged Global model when particles with measured size distributions were released from the ceiling location of the Regional model.

4.2.2 Part 2: Regional model (post dirty bomb)

Step 1: Mesh generation of the Regional model using the surface roughness information of the Hot Zone provided by the first responders to the analyst (For thesis: The author

measured the surface roughness profile of the contaminated plates used during the WIS facility experiment)

Step 2: Solving appropriate governing equations related to the Regional model

a. First, solve the Regional computation domain using the Shear Stress Transport k-ω SST closure model to find realistic inlet conditions (U, k, ε profiles) using the mean boundary conditions found from the Global model.
b. Second, solve the Regional computational domain using the LES method using the boundary conditions calculated from the Global model.

Step3: Post-processing of results of the Regional models

3.1 Calculate the bin-by-bin resuspension Regional CFD resuspension fractions at the ceiling of the computational domain when particles with measured size distributions were released from the floor of the Regional model. Note: The first responders will measure the particle size distribution of the particles settling into the Hot Zone and provide that information to the analyst performing the CFD analysis.

4.2.3 Part 3: Combining Regional and Global Models

Step 1: Finally, multiply the bin-by-bin Global CFD transfer factor values by the corresponding Regional CFD resuspension fraction to find the CFD resuspension factor.

Step 2: The analyst will pass bin-by-bin CFD resuspension factors to incident commanders or can continue finding the Deposition Fraction of Resuspended particles into human lungs due to a dirty bomb event by multiplying the bin-by-bin CFD resuspension factors values by the respective curve fit of ICRP deposition fraction (DP) data given by Hinds (1999).

4.3 CFD modelling of the 3D WIS facility Wind Chamber

The 3D WIS facility wind chamber was modelled in two stages. In stage 1, the Global CFD model was solved to find the boundary conditions for the Regional CFD model. In stage 2, the solutions for the Global CFD model were found by applying the boundary conditions found in the Regional model.

4.3.1 The Global CFD model

The Global CFD model represents all the WIS facility wind chamber's geometric features except the surface roughness and detectors used inside the wind chamber. The fans used to draw the air through the wind chamber were modelled using appropriate boundary conditions available in FLUENT software.

4.3.1.1 Mesh Generation of the Global CFD Model

The Global 3D computational domain (WIS facility wind chamber) mesh was generated using hexahedral and edge elements (Hex/Wedge mesh). Like the 2D mesh of the WIS facility shown in Appendix B, a fine mesh was developed close to wall surfaces to ensure an adequate number of nodes in the region dominated by the fluid's viscosity to accurately model turbulent boundary layer properties.

Figure 67 shows the boundaries and mesh of the 3D WIS facility wind chamber.

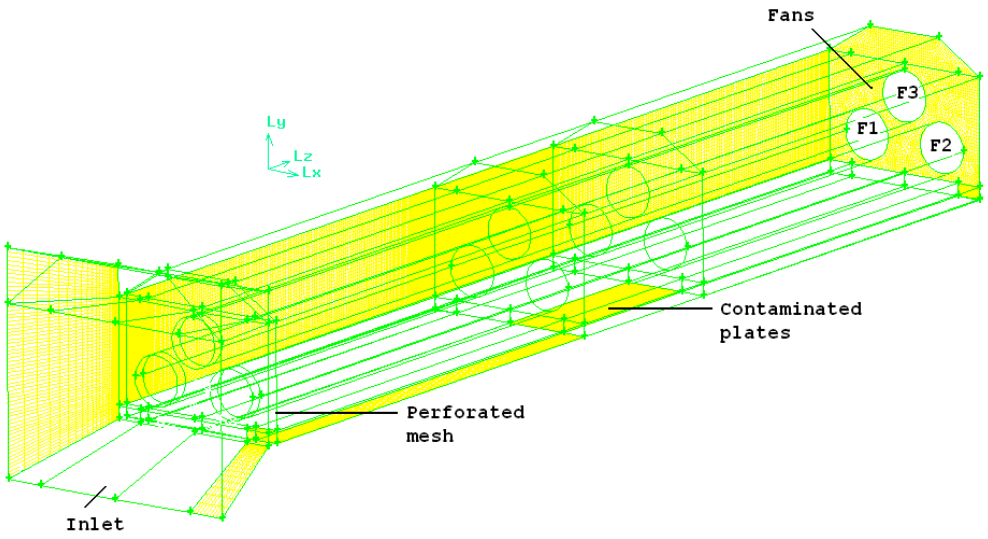

Figure 67: Boundaries and 3D mesh of selected areas of the WIS facility computational domain

The Inlet of the 3D wind chamber was modelled as a pressure-inlet boundary condition with a hydraulic diameter of 2.2 m and a turbulent intensity of 1%. Fans F1 and

F2 were modelled as exhaust-fan boundary conditions with a mass flow rate of 2.61 kg s^{-1} each and a turbulent intensity of 20% with a length scale of 0.04 m. Fan F3 was also modelled as an exhaust fan, with a mass flow rate of 2.61 kg s^{-1}, a turbulent intensity of 10%, a hydraulic diameter of 40 cm, and a backflow gauge pressure of 37 Pa. All walls of the wind chamber were modelled as non-slip boundary conditions with smooth wall surfaces. The reasoning for selecting appropriate turbulent intensities and length scales for Fan boundary conditions under 2D CFD modelling of the Wind Chamber can be found in Appendix B, section 8.2.

4.3.1.2 Grid convergence study for the Global Model

As a part of mesh convergence studies, five hybrid meshes with 1,131,635, 2,235,231, 3,705,824, 4,925,014 and 9,693,494 cells were generated. The first three meshes, with 1,131,635, 2,235,231, and 3,705,824 cells, were generated using 4 cm, 3 cm and 2 cm mesh elements using Gambit software, respectively. The last two meshes with cell numbers 4,925,014 and 9,693,494 were generated by refining 3,705,824 mesh using the y+ adoption algorithm available in FLUENT software.

The primary requirement of all meshes was to match the velocities at the Hotwire locations 1 to 5. The secondary requirement was to have the required y^+ (< 5), especially on the floor of the wind chamber, so one can accurately find the velocity at 100 μm above the contaminated plate using *k*-ω SST viscous turbulence model. The tertiary requirement

was to develop a mesh that could be solved using computer power available to the user within a reasonable time frame.

Table 14 shows the converged solutions (up to 1E-4 convergence) of velocity magnitude and intensities at Hotwire (HW) 1 to 5 locations for different sizes of meshes.

Table 11: Velocity magnitudes and % Intensities calculated at HW1, HH2, HW3, HW4 and HW5 locations by solving the computational domains with meshes with cell numbers 1,131,635, 2,235,231, 3,705,824, 4,925,014 and 9,693,494.

	HW1		**HW2**		**HW3**		**HW 4**		**HW5**	
Number of cells	**V (ms^{-1})**	**I%**	**V (ms^{-1})**	**I%**	**V (ms^{-1})**	**I%**	**V (ms^{-1})**	**I%**	**V (ms^{-1})**	**I%**
1131635	5.2978	54.3438	5.6654	59.9822	5.8626	60.2589	5.9266	58.9735	5.8859	57.0631
2235231	5.2891	54.2892	5.6849	60.5356	5.8493	60.7560	5.9092	59.3362	5.8656	57.1540
3705824	5.2781	55.5558	5.6522	61.3312	5.8523	61.3352	5.9134	59.9260	5.8772	57.5795
4925014	5.2659	55.6006	5.6667	61.0449	5.8754	60.8119	5.9347	59.3976	5.8940	57.3492
9693494	5.2736	54.6559	5.6683	60.1803	5.8707	60.1775	5.9272	58.9544	5.8866	56.9858

Figure 68 shows the velocity magnitudes measured at five hotwire locations (HW1, HW2, HW3, HW4 and HW5) found using five meshes in the grid convergence studies.

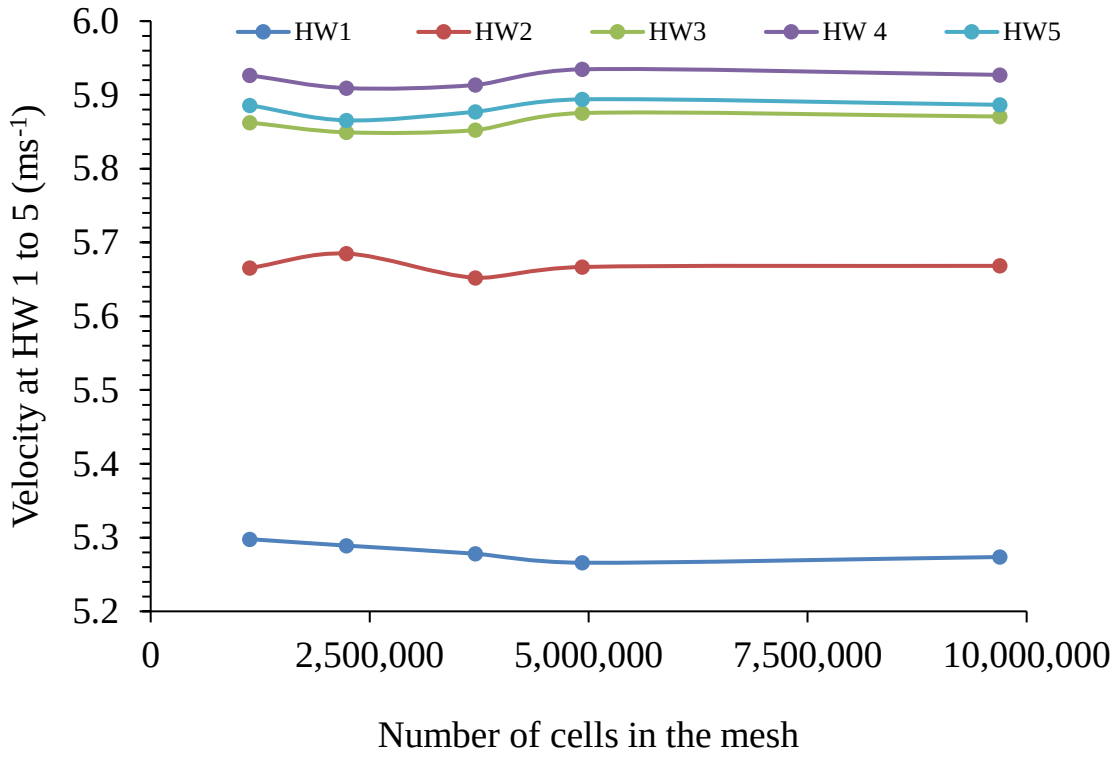

Figure 68:Velocity magnitude calculated at HW1, HH2, HW3, HW4 and HW5 locations by solving the computational domains with meshes will cell numbers 1,131,635, 2,235,231, 3,705,824, 4,925,014 and 9,693,494.

As per Figure 68, the velocity magnitude results at Hotwire 1 to 5 locations with respect to mesh sizes started producing the same results independent of mesh size beyond 4,925,014 mesh size under *k-ω* SST viscous models with an operating pressure of 101325 Pa, acceleration of gravity of 9.817 m s^{-2} and the boundary conditions used in the Global CFD model. Later, this mesh was refined using the y^+ adaptation algorithm available in the FLUENT software until the y^+ of all floor surfaces, including contaminated plates, were less than 2.5. The final 3D mesh had 16,289,581 mesh nodes. Special attention was paid during the mesh generation process to the area where the small Regional model is located

to ensure there are enough mesh elements to capture the time average U, k, ε values required to solve the Regional model at a later time.

4.3.1.3 CFD modelling of the Global 3D WIS Facility Wind Chamber Flow Fields

Initially, a pressure-based, double-precision, unsteady, implicit segregated solver was used to find solutions for continuity, momentum equations, and the k-ω SST turbulence model to find the initial U, k, ε profiles of the Global 3D WIS facility Wind Chamber. The best practice guidelines in CFD modelling were followed to ensure grid independence and the use of higher-order schemes until the 1E-7 convergence criterion was achieved.

Later, k-ω SST turbulence model was changed to Large Eddy Simulation (LES) to accurately model the boundary conditions required for the CFD modelling of the Regional model.

4.3.1.4 Large Eddy Simulation (LES)

Eddies characterize turbulent flows inside the 3D WIS facility wind chamber. As seen during the WIS facility experiment, these eddies can have a wide range of length and time scales during the wind chamber operation. For example, the length scales of turbulent eddies inside the wind chamber can vary from micron sizes to a few meters.

In the wind chamber, momentum and mass are mainly transported by large eddies, which are unique for the wind chamber setup and boundary conditions of the flow (Fluent Inc., 2006). In the LES model, bigger eddies are resolved directly using a filtered version of the Navier-Stokes equations and eddies smaller than the filter size (grid spacing) were modelled using the Smagorinsky-Lilly sub-grid-scale model (Fluent Inc., 2006).

Filtered continuity and Navier-Stokes equations are given by Equations (73) and (74), respectively.

$$\frac{\partial \rho}{\partial t} + \frac{\partial}{\partial x_i}(\rho \bar{u}_i) = 0 \qquad (73)$$

and,

$$\frac{\partial}{\partial t}(\rho\bar{u}_i) + \frac{\partial}{\partial x_j}(\rho\bar{u}_i\bar{u}_j) = \frac{\partial}{\partial x_j}\left(\mu\frac{\partial\sigma_{ij}}{\partial x_j}\right) - \frac{\partial\overline{p}}{\partial x_i} - \frac{\partial\tau_{ij}}{\partial x_j} \quad (74)$$

here, subscripts i and j are free indices that can take 1, 2 and 3 $\bar{u}_i$ represent ith component of filtered velocities and $\overline{p}$ represent filtered static pressure at position x_i and time *t*. The density and kinematic viscosity of the fluid passing at this location are denoted by ρ and μ respectively. The stress tensor (σ_{ij}) due to molecular viscosity is defined by

$$\sigma_{ij} \equiv \left[\mu\left(\frac{\partial\bar{u}_i}{\partial x_j} + \frac{\partial\bar{u}_j}{\partial x_i}\right) - \frac{2}{3}\mu\frac{\partial\bar{u}_i}{\partial x_j}\delta_{ij}\right] \quad (75)$$

and, the subgrid-scale stress is defined by Equation (76).

$$\tau_{ij} \equiv R_{ij} = \rho\overline{u_i u_j} - \rho\bar{u}_i\bar{u}_j \quad (76)$$

The subgrid-scale stresses resulting from the filtering operation are modelled in FLUENT using the Boussinesq hypothesis given in Equation (77).

$$\boldsymbol{\tau_{ij} - \frac{1}{3}\tau_{kk}\delta_{ij} = -2\mu_t \bar{S}_{ij}} \quad \textit{(77)}$$

here

$$\boldsymbol{\bar{S}_{ij} = \frac{1}{2}\left(\frac{\partial \bar{u}_i}{\partial x_j} + \frac{\partial \bar{u}_j}{\partial x_i}\right)} \quad \textit{(78)}$$

In the Smagorinsky-Lilly model, the eddy-viscosity (μ_t) is found using Equation (79).

$$\boldsymbol{\mu_t = \rho L_s^2 |\bar{S}|} \quad \textit{(79)}$$

where

$$\boldsymbol{|\bar{S}| \equiv \sqrt{2\bar{S}_{ij}\bar{S}_{ij}}} \quad \textit{(80)}$$

and

$$\boldsymbol{L_s = min\left(\kappa d C_s V^{\frac{1}{3}}\right)} \quad \textit{(81),}$$

here, κ is the von Kármán constant, d is the distance to the closest wall, C_s is the Smagorinsky constant (0.1 to 0.2), and V is the volume of the mesh element. For the Global and Regional CFD models of the WIS facility C_s=0.2 was used.

4.3.2 CFD Results of Global CFD Model

Figure 69 shows the velocity profile across a plane running through the center of the wind chamber at 0.35 sec flow time.

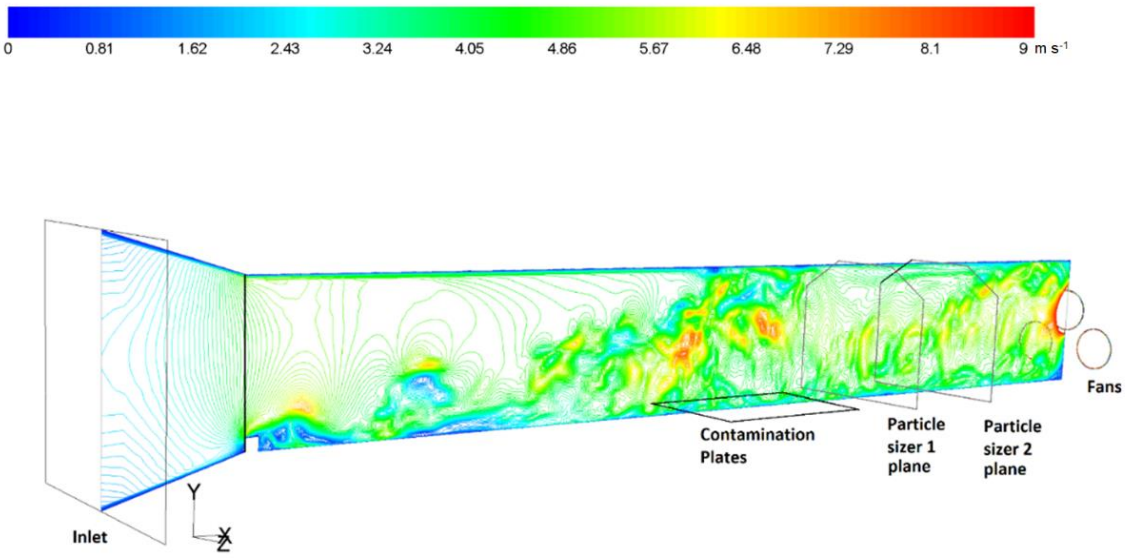

Figure 69: Velocity contours (capped at 9 m s^{-1}) of a 2D plane running through the center of the wind chamber, 3d, dp, pbns, LES, unsteady, 1E-7 convergence at flow time = 0.35 sec. (**Re**$_L$ = 5.6E5 at WIS facility operating conditions)

As shown in Figure 69, the LES model captured the spatially developed turbulent boundary layer and the vortices generated by the rectangular-shaped bluff body located just after the converging section of the wind chamber. The domain's velocity profile was capped at 9 m s^{-1} to visualize the flow, especially in the regions of the Contamination plates, Particles Sizer 1 and Particle Sizer 2 locations.

Figure 70 shows a screen capture of FLUENT software Residual Monitors between 118,000 and 122,700 iterations. The average time step size was 1E-7 sec. The maximum iterations per time step of 40 were set up during the pressure-based unsteady Large Eddy Simulation (LES) run with the Smagorinsky-Lilly subgrid-scale model.

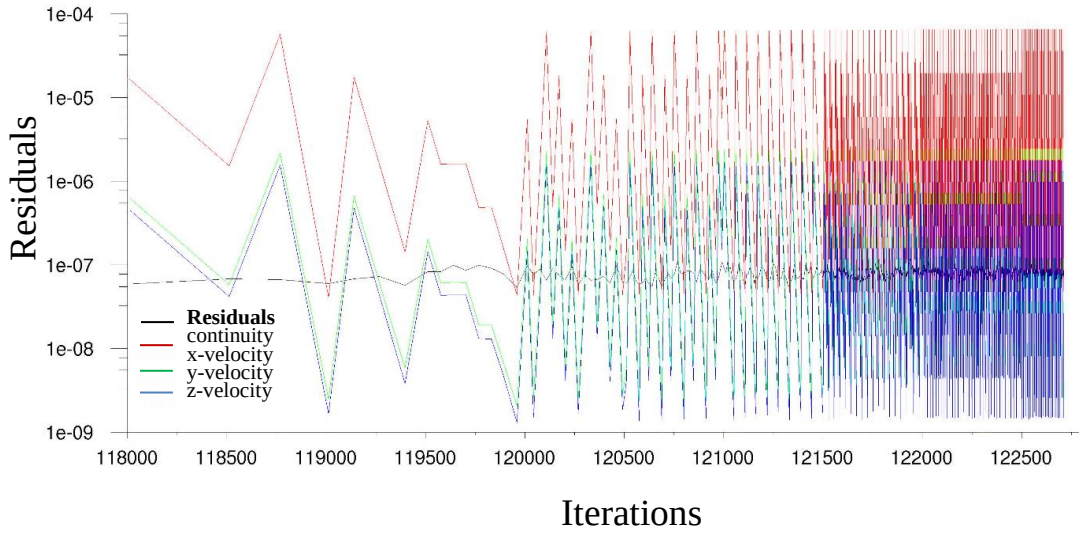

Figure 70: Residuals of continuity, x-velocity, y-velocity, and z-velocity with respect to Iterations between 118,000 and 122,700. The residuals were captured at 3.627E-1 sec. flow time.

As per Figure 70, all conserved variables such as continuity, x-velocity, y-velocity and z-velocity were converged down to 1E-7 at the end of every time step.

Figure 71 shows the velocity time history at Hotwire 1 to 5 locations between 10,801 and 50,000 time steps. The time step size used during this part of the CFD simulation was 1E-7 seconds.

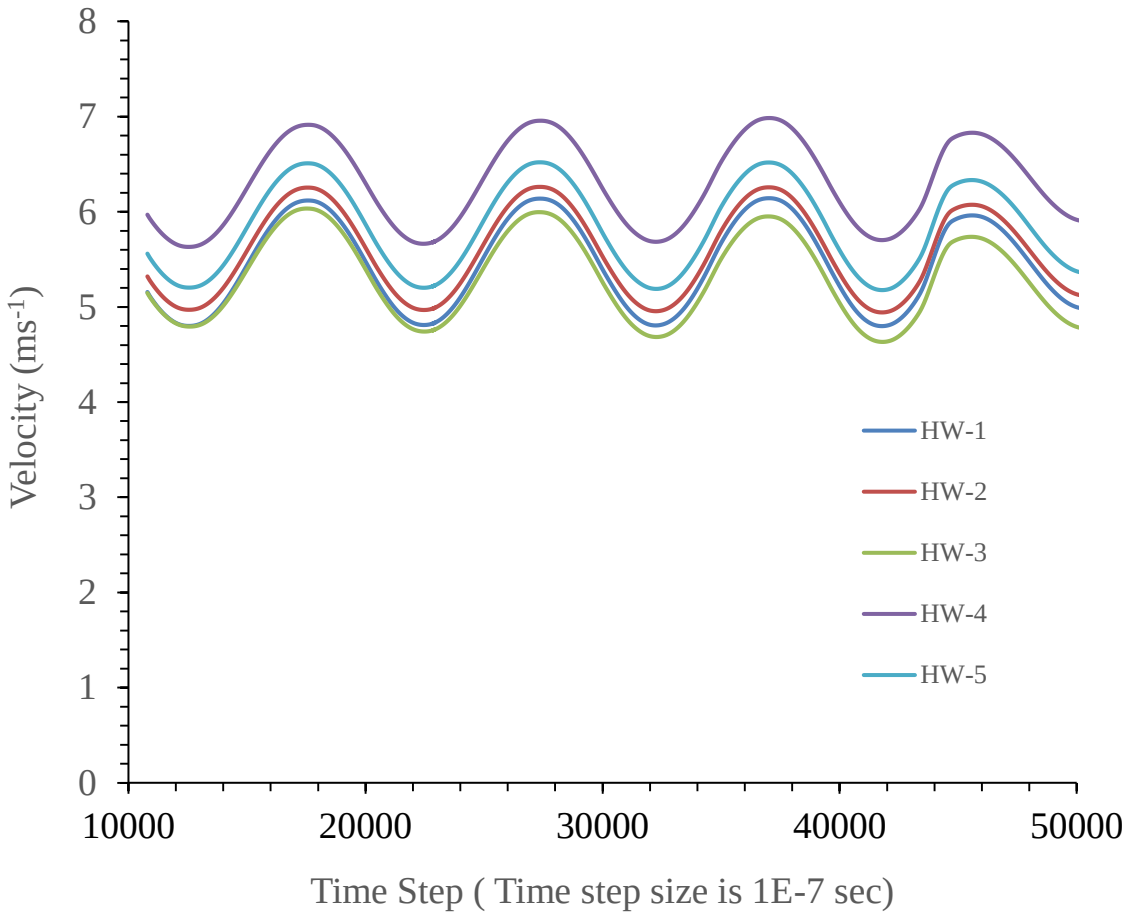

Figure 71: Time history of velocity at Hotwire locations 1 to 5.

The time history graph shows the velocities at HW 1 to 5 locations oscillate with a period of 0.935 × (1 ± 7.4%) msec. The average values of velocity magnitudes at HW 1 to 5 locations are provided in Table 12, and Figure 71 shows how the vortices that are being shed by the turbulator located at the front of the wind tunnel are affecting the velocity at HW 1 to 5 locations as the vortices are moving downstream the wind tunnel with respect to flow time. Figure 72 shows the velocity contour plots at time steps 22500, 25200 and 27900, corresponding to the lowest, mid and highest velocity profiles measured at Hotwire 1 to 5 locations and a comparison of velocity magnitude along the vertical line running at HW 1 to 5 locations.

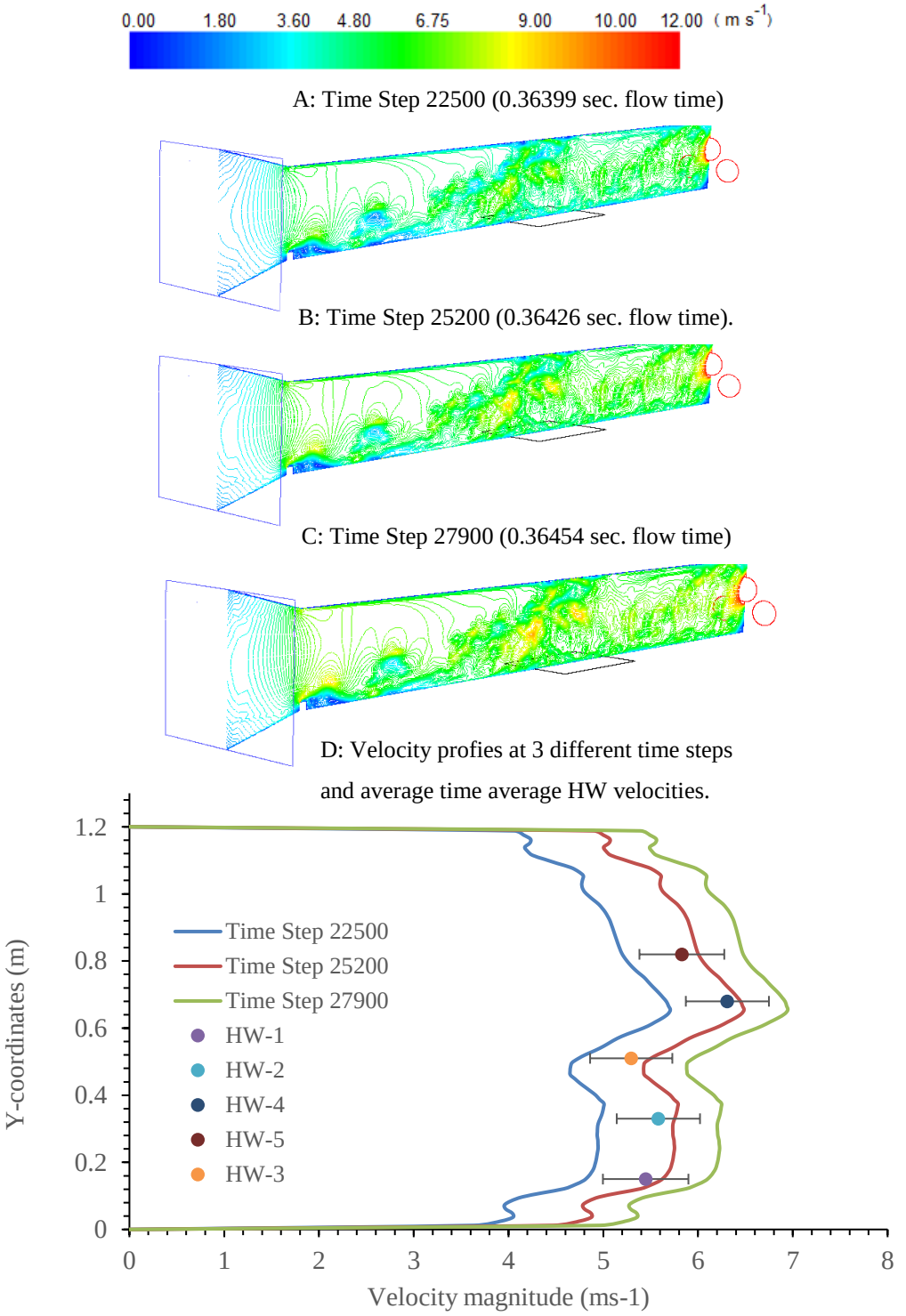

Figure 72: A, B and C – Contour plot of velocity magnitude (ms^{-1}) across the vertical symmetry plane and D- velocity profiles along a vertical line running at the tips of Hotwires at 22500, 25200 and 27900 time steps and Time Average velocity at Hotwires.

Based on the results presented in Figure 70, Figure 71 and Figure 72, one can confirm that flow has reached oscillatory convergence since residuals converge below 1E-7 and time history velocity profiles at Hotwire 1 to 5 locations maintain steady oscillatory values.

Figure 73 shows instantaneous velocity at the vertical plane running through the hotwire anemometer array placed down steam the Contamination plates (Particle Sizer 2 plane).

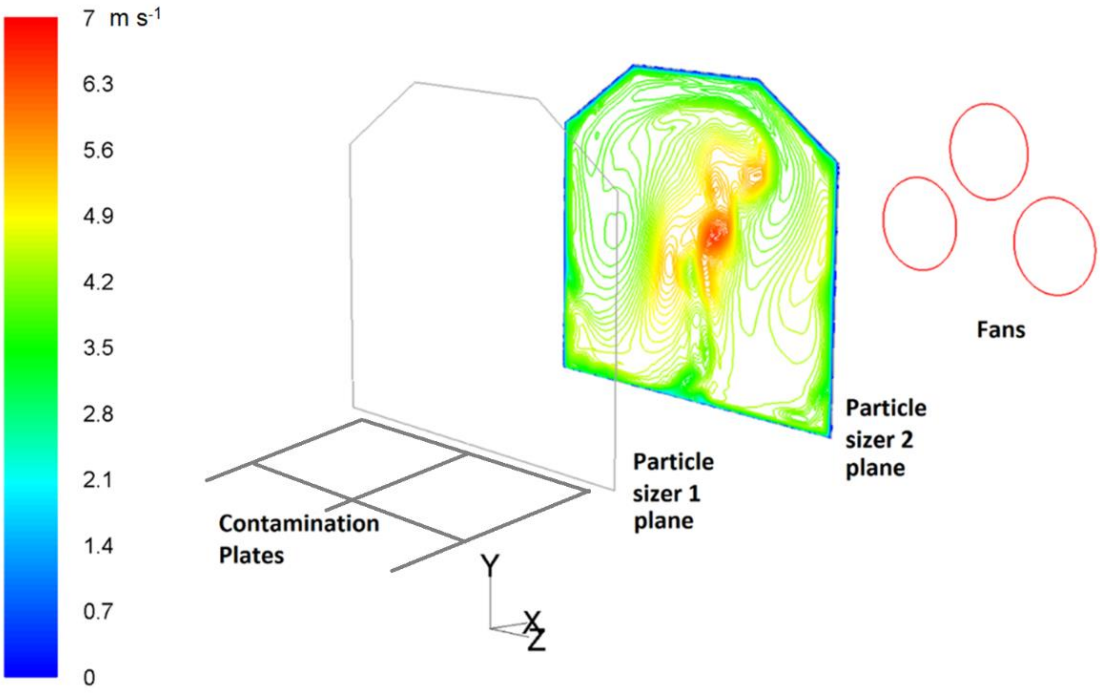

Figure 73: Velocity profile of Particle Sizer 2 plane ($\mathbf{Re}_L$ = 5.6E5 at SAC)

Figure 73 shows that the flow in the Particle Sizer 2 plane is 3D in nature. Velocity at the plane's center is much higher than the walls, and this region has two apparent vortices.

The time average velocity readings found at hotwire anemometer array locations with respective experimental results are shown in Table 12.

Table 12: Comparison of velocity results of CFD model with Experiment readings at respective hotwire locations of the WIS facility

Hotwire (HW)	**Time average CFD velocity ($m\ s^{-1}$) readings between 10,801 and 50,000 time steps using the LES model**	**Experimental velocity reading ($m\ s^{-1}$)**
HW-1	5.45±0.45	6.51±0.51
HW-2	5.58±0.43	6.61±0.45
HW-3	5.29±0.43	6.74±0.47
HW-4	6.31±0.43	6.74±0.51
HW-5	5.83±0.45	6.03±0.42

A comparison of velocity readings calculated using the 3D Global CFD LES model and measured experimental values at the exact locations on the hotwire array shows that velocity readings of the converged 3D WIS facility CFD model were well within the experimental results for Hotwire locations 1 to 5.

4.3.2.1 Velocity and Pressure drop at 100 µm above the contaminated plate

The Ceiling boundary of the Regional computation domain was located at 100 µm above the contaminated plate. The time average and facet average velocity, turbulent kinetic energy, turbulent dissipation rate, and pressure gradient at the Ceiling boundary were calculated from the converged Global WIS facility CFD models to introduce the boundary condition of the Ceiling boundary of the Regional CFD model.

Utilizing the results from the converged Global CFD model, we calculated the time-averaged and facet-averaged stream-wise (V_x), wall-normal (V_y), and span-wise (V_z) velocity components at the height of 100 µm above the contaminated plates. These values were found to be 8.93E-01 m s^{-1}, -4.52E-06 m s^{-1}, and 1.35E-02 m s^{-1}, respectively. The facet average turbulent kinetic energy and turbulent dissipation rate were found to be 9.91E-01 m^2 s^{-2}, and 4.62E+03 m^2 s^{-3}, respectively. These turbulent properties were found from the converged Global CFD WIS facility RANS model. Furthermore, the time-averaged facet pressure drop at the same elevation was determined to be 5.31 Pa m^{-1}.

For visual reference, snapshots of contour plots displaying velocity and pressure at the 100 µm height above the contaminated plate are provided in Appendix B.

4.4 The Regional CFD model

The Regional CFD model includes the laminar sublayer region and surface roughness elements on the contamination plates. The laminar sublayer region lies close to the floor, and a very complicated non-linear relationship exists between fluid and particles on the floor. Therefore, as discussed in the literature review section of the thesis, it is essential to model the surface roughness features on the floor to simulate the combined effect of the flow and the geometry during the resuspension process (Guingo & Minier, 2008) (Castelo, Capitao, & De Santi, 1999).

The Regional 3D computational domain's floor profile was modelled to match the measured steam-wise equivalent roughness profile of the contaminated plates used in the WIS facility resuspension experiment.

4.4.1 Floor profile of the Regional CFD model

The surface roughness of the contamination plates was measured using TR200 surface roughness profilometer. The TR200 measures surface roughness based on the amount of inductive current generated by the sensor as a built-in sharp probe slides along a measurement surface (Innovatest Europe BV, 2021).

Figure 74 shows the sample roughness profile (out of 20 measured profiles) of the uncontaminated plate measured using TR200 between 1 mm and 3 mm demarcation points downstream of the plate.

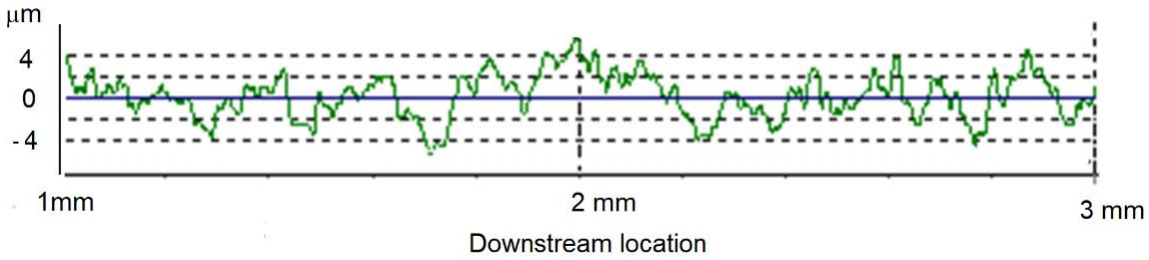

Figure 74: Sample roughness profile of the contamination plate used at the WIS facility resuspension experiment using TR200 surface roughness profilometer

The average measurements for Ra, Rz, and Rsm were recorded as follows: Ra was 1.663 µm (with a tolerance of ±17%), Rz was 9.174 µm (with a tolerance of ±16.1%), and Rsm was 137.9 µm (with a tolerance of ±10.5%).

4.4.2 Surface profile of the contamination plate used in the 3D Regional computational domain

The roughness profile at a specific location on the uncontaminated plates used at the WIS facility experiment would differ from locations on the same plate. Therefore, the

surface roughness pattern of the computational domain floor was modelled based on measured averaged surface roughness parameters. Laurent et al. (2018) used the sum of two sinusoidal functions perpendicular to each other in a plane to model the landscapes to study the sensitivity of cell migration due to curvature variation of the topology. Brambilla, Speckart and Brown (2017) used two sinusoidal curves to represent the surface roughness of the flow when calculating the adhesive force between a rough surface and particles. Similarly, we will be using double sinusoidal curves in the same plane to model the topological features of the uncontaminated plate. The equation used to model the surface topology in the 2D plane is given by Equation (83).

Figure 75 shows the simplified surface profile of the floor used in the Regional 3D computational domain generated based on 20 sample measurements conducted at various locations of the contamination plate; the calculated averaged R_a was 1.663 × (1 ± 17%) µm, R_Z was 9.174 × (1 ± 16.1%) µm and R_{sm}, was 137.9 × (1 ± 10.5%) µm.

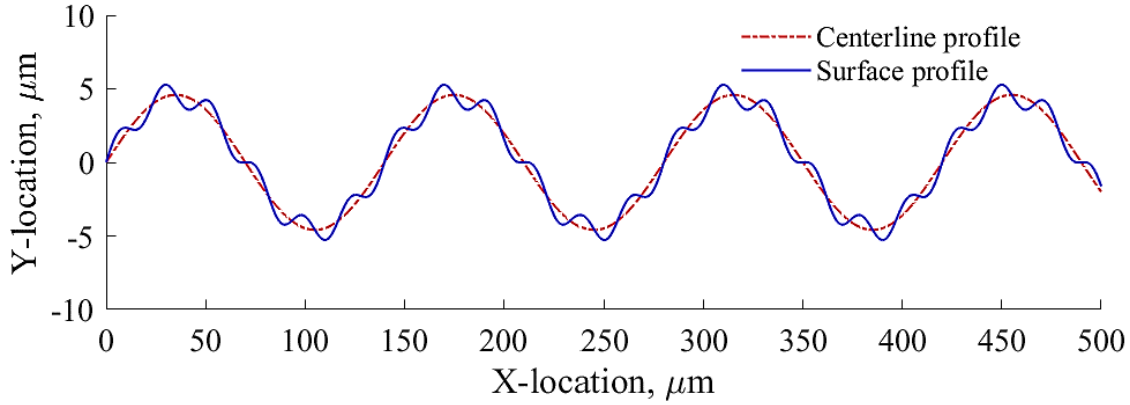

Figure 75: Equivalent roughness profile based on measured average R_a, R_{sm}, and R_Z

Figure 75 shows the equivalent 2D surface roughness profile and the centerline profiles of the contamination plate generated based on the measured R_a, R_{sm}, and R_Z results. Equations (82) and (83) show the centerline and surface roughness profiles, respectively.

$$y = \frac{R_Z}{2} sin\left(\frac{6x}{R_{sm}}\right), \quad (82)$$

and,

$$y = \frac{R_Z}{2} sin\left(\frac{6x}{R_{sm}}\right) + \frac{R_a}{2} sin\left(\frac{36x}{R_{sm}}\right), \quad (83)$$

here, x and y are the coordinates in streamwise and wall-normal directions, R_Z is the maximum peak-to-valley height surface roughness, R_{sm}, is the mean spacing of irregularities, and R_a is the average arithmetic mean surface roughness.

4.4.2.1 Mesh Generation of Regional CFD Model

The initial 3D mesh of the Regional computational domain had 64,350 hexahedral structured mesh cells, and the final mesh after mesh independence studies ended up with 397,900 hexahedral structured mesh cells. The size of the computational domain was 414 μm, 106 μm and 100 μm in X (downstream), Y (wall-normal) and Z (transverse) directions, respectively. The floor close to the wall surfaces was meshed using boundary layer mesh options available in GAMBIT software. The boundary layer mesh is shown in red colour in Figure 76.

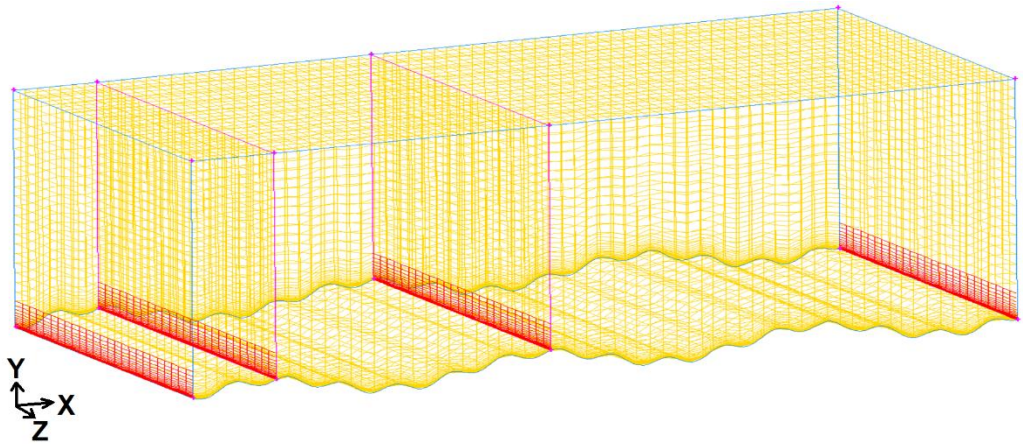

Figure 76: Regional domain mesh. The boundary layer mesh is shown in red colour. The size of the computational domain was 414 μm, 106 μm and 100 μm in X (downstream), Y (wall-normal) and Z (transverse) directions, respectively.

In the initial 3D mesh, the thickness of the boundary layer mesh was 11.68 μm, and it had ten rows. The first-row height of the boundary layer was 0.45 μm), with a growth factor (the thickness ratio between the row above and the current row) of 1.2. The first-row height was selected as 0.45 μm to ensure at least two mesh rows are available within the space that the smallest particle (0.9 μm) will occupy during the discrete phase modelling. The corresponding Knudsen number ($\mathbf{K}_n$) of the mesh was calculated to be 0.15 using the Equation (84) (Oosthuizen, 1997).

$$K_n = \frac{\lambda}{L}, \qquad (84)$$

here, λ is the mean free path, and L is the physical length scale. In our case, L will be the space between the floor and the first mesh node away from the floor (0.45 μm). The mean free path of air at the operating temperature of the wind chamber was calculated to be 66.5 nm, resulting in a corresponding $\mathbf{K}_n$ value of 0.1478. Given that $\mathbf{K}_n$ exceeds 0.1, the flow is no longer within the slip region. Consequently, the shear conditions of the floors of the Regional model can be prescribed as no-slip.

Figure 77 shows boundary conditions and the mesh close to the floor surfaces of the Regional 3D computational domain.

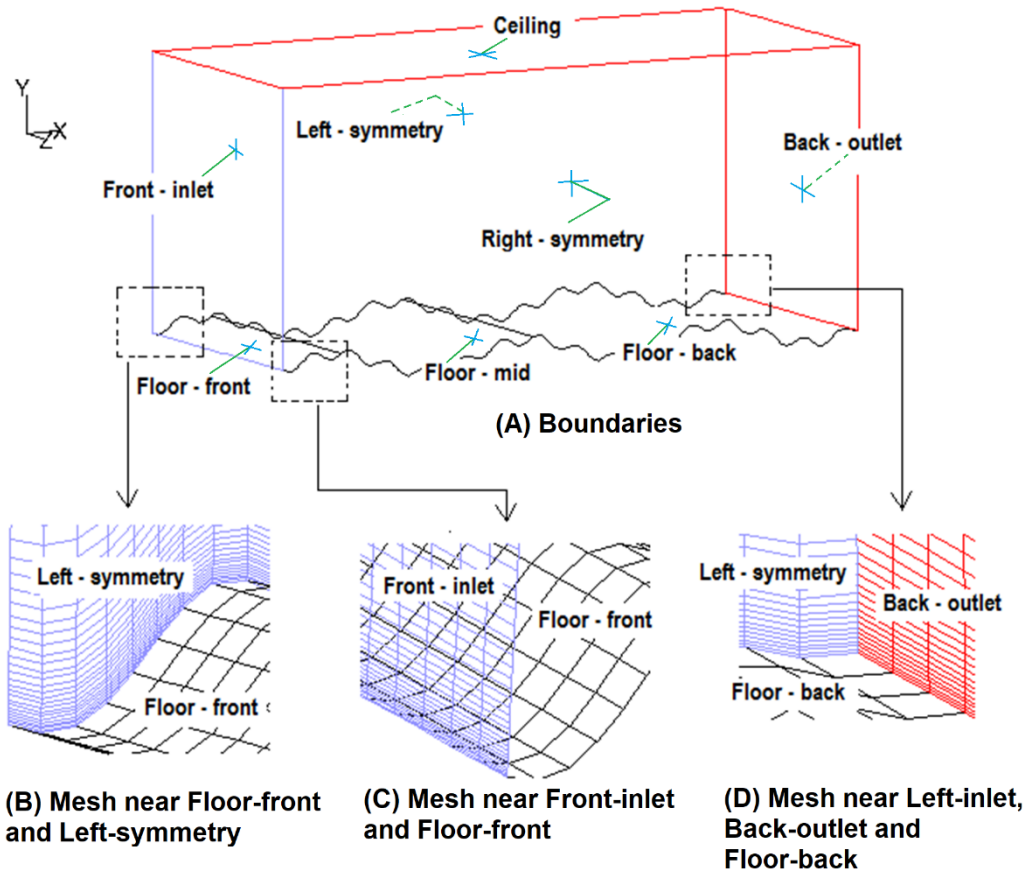

Figure 77: Boundaries and 3D mesh of the selected areas of the Regional computational model (Dimensions: 424 μm, 106 μm and 100 μm in X, Y, and Z directions, respectively)

Figure 77-(A) shows boundaries used in the computational domain. For the purpose of regulating the locations from which particles are released, the computational domain floor was partitioned into three distinct wall surfaces: the floor-front, floor-mid, and floor-

back regions. Figure 77-(B) shows the zoomed-in 3D mesh close to the Floor-front and Left-symmetry; Figure 77-(C) shows the zoomed-in 3D mesh close to the Front-inlet and Floor-front; Figure 77-(D) shows the zoomed-in 3D mesh close to the Left-inlet, Floor-back, and Back-outlet.

4.4.2.2 Boundary conditions of the Regional CFD model

Boundary conditions of the Regional CFD model are dictated by the edge boundaries of the Global 3D WIS facility wind chamber CFD model. All wall boundaries: Floor-front, Floor-mid, and Floor-back were modelled as non-slip stationary steel walls with a surface roughness of zero since surface roughness features were physically modelled into the computational domain.

4.4.2.2.1 Ceiling

The ceiling boundary of the 3D Regional CFD domain was modelled as a velocity inlet. The facet average velocity calculated 100 μm above the floor in the test section of

the Global 3D WIS facility wind chamber model was applied at the ceiling boundary of the Regional CFD model. The facet averaged velocity of the ceiling was given by Equation (85).

$$\begin{aligned} V_x &= 8.93 \times 10^{-1}\ ms^{-1}, \\ V_y &= -4.52 \times 10^{-6}\ ms^{-1}, \\ V_z &= 1.35 \times 10^{-2}\ ms^{-1}. \end{aligned} \qquad (85)$$

As discussed in the literature review section, turbulent eddies in the wall region ($y^+ < 50$) of the turbulent boundary layer have a coherent structure – retain their character over a substantial downstream transport distance (Laufer, 1975) (Cantwell, 1981). A vorticial structure was observed in the viscous sublayer region, where the turbulent boundary layer in the transition from laminar to turbulent (Kline, Reynolds, Schraub, & Runstadler, 1967) and (Grass, 1971). According to (Allen, 1985), this vortical structure starts as a cylindrical vortex in the laminar sublayer region and slowly starts lifting to form a horseshoe-shaped vortex. This horseshoe-shaped vortex bursts at a maximum height of around eight sublayer thicknesses (Allen, 1985), transferring momentum and particles from the laminar sublayer region to the lower part of the logarithmic turbulent boundary layer.

The coherent structure of the Regional domain was simulated by introducing fluctuating velocity algorithms available in Fluent software under Large Eddy Simulation (LES). FLUENT uses the Spectral Synthesizer algorithm proposed by Kraichan (1970) and Smirnov et al. (2001) to generate fluctuating velocity components by synthesizing

divergence-free velocity-vector field representing turbulent velocity fluctuations by summation of 100 Fourier harmonics (Fluent Inc., 2006) The Spectral Synthesiser algorithm has been validated in the cases of boundary layer and flat plate floors (Smirnov, Shi, & Celik, 2001).

The facet average turbulent kinetic energy, k = 9.91E-1 m^2 s^{-2}, and turbulent dissipation rate, ε = 4.62E+03 m^2 s^{-3} found from the converged Global CFD WIS facility RANS model were used at the Ceiling inlet boundary of the Regional model.

4.4.2.2.2 The Left inlet, Right inlet, Front inlet, and Back outlet

The left-symmetrical and the Right-symmetry boundaries were modelled as symmetry boundary conditions.

The Front inlet and Back outlet boundary conditions were modelled as periodic transitional boundaries with a pressure gradient of -5.31 Pa m^{-1} towards the +x direction (downstream). The pressure gradient was calculated based on the wind chamber's converged Global CFD model results.

4.4.2.3 Mesh independence studies for the Regional CFD model

Initial particle resuspension occurs close to the floor surfaces. Therefore, it is essential to achieve stable solutions for maximum y^+ (< 1), floor shear stress and velocity fields close to the floor surfaces independent of the Regional computational domain's mesh size.

The work presented by Cleaver and Yates (1973) by combining work done by (Goren, 1970), (Laufer, 1975), (Goren, 1970), (O'Neill, 1868) and (Saffman, 1965) showed that initial lift force acting on particles on the surfaces due to vortex bursting near the wall and the Lift force and Drag force after initial lift-off is proportional to $\rho v^2 \left(\frac{d_p u_*}{v}\right)^3$ where, ρ, and v are density and kinematic viscosity of the flow, d_p is the particle diameter and u_* is the friction velocity. Here all parameters are constants for a given fluid and particle except u_* which is a function of wall shear stress, τ_w, and fluid density. Cleaver and Yates (1973) also mentioned that particle will be removed from the wall surfaces when $\tau_w > B/{d_p}^{4/3}$, where B is a constant for a given fluid. Wang (1990) showed that Lift, Drag and Adhesive force between surface and particle directly affect the detachment of particle from the surface by direct liftoff, sliding or rolling. Previous research conducted by numerous investigators indicates that the primary factor influencing particle detachment from wall surfaces is wall shear stress, mainly when the particles are situated in the viscous sublayer region. For the particles that are outside the viscous sublayer, the lift force and drag force

are affected by the local velocity. So, we will use the wall shear stress and velocity as essential parameters to conduct the mesh convergence studies.

As a part of grid convergence studies, the facet average y^+ of all floor surfaces, the facet average shear stress of all floor surfaces, vertex average velocity values at four selected locations close to the floor just above the second valley located at the symmetry plane, and vertex average velocity values of four selected locations close to the floor just above the second peak located at the symmetry plane were monitored.

Table 13 shows the coordinates of the high and low points in the Regional computational domain.

Table 13: Locations of the high and low points [Computational domain extents (µm): X_{min} = 0, X_{max} = 456, Y_{min} = -5.74, Y_{max} = 100, Z_{min} = 100 and Z_{max} =200]

Low Locations	X coordinate (µm)	Y coordinate (µm)	High Locations	X coordinate (µm)	Y coordinate (µm)
L1	100	-2.5	**H1**	198	7.75
L2	100	0	**H2**	198	10.25
L3	100	2.5	**H3**	198	12.45
L4	100	5.0	**H4**	198	14.65

The goal of the mesh independence studies was to come up with the best mesh for the 3D Regional model that can simulate the particle resuspension with reasonable mesh size, ensuring that there are enough mesh elements to study the smallest particle resuspension from the floor surfaces and to accurately model the fates of the particles inside the Regional model. The wall-normal boundary layer mesh profile was kept the same for

all meshes to ensure at least 2 mesh rows were available within the space that the smallest particles (0.9 μm) will occupy during the discrete phase modelling process.

Four structured meshes were generated for mesh independence studies. The first mesh had 64, 354 rectilinear mesh cells. The mesh spacing along the downstream direction of the first mesh was 4 μm and had 50 equally spaced mesh spacing in the transverse direction within 100 μm depth. The second mesh had 129,195 rectilinear mesh cells. The mesh spacing along the downstream direction of the second mesh was 3 μm, and the mesh spacings in transverse and wall-normal directions were similar to the first mesh. The third mesh had 379,900 rectilinear mesh cells with 2 μm mesh spacing in the downstream direction and similar mesh spacing as the first mesh in the other two directions. The fourth mesh had 730,800 rectilinear mesh cells and had the same mesh spacing in the downstream direction as the third mesh, but it had 70 nodes in the transverse direction and similar mesh spacing as the other three meshes in the wall-normal direction. All four meshes had 40 mesh intervals in the wall-normal direction, with the boundary layer mesh attached to the floor surfaces.

Table 14 shows the converged solutions (up to 1E-6 convergence) and respective average y+, face average shear stress of all floor surfaces and average velocity values of Low Points and High Points as defined in Table 13.

Table 14: Facet average shear stress and velocities at selected locations for the different mesh cell numbers for LES viscous models.

Number of cells	Viscous model	Average y+	Low points vertex avg. velocity (ms-1)	High points vertex avg. velocity (ms-1)
64350	LES	4.9369E-03	3.2114E-02	7.1050E-02
129195	LES	4.9141E-03	3.1167E-02	7.2372E-02
379900	LES	4.8895E-03	3.0439E-02	7.3688E-02
730800	LES	4.8875E-03	3.0412E-02	7.3688E-02

Figure 78 shows the facet average y+ of all floor surfaces and vertex average velocities of the Regional computer domain just above the second valley and the peak locations.

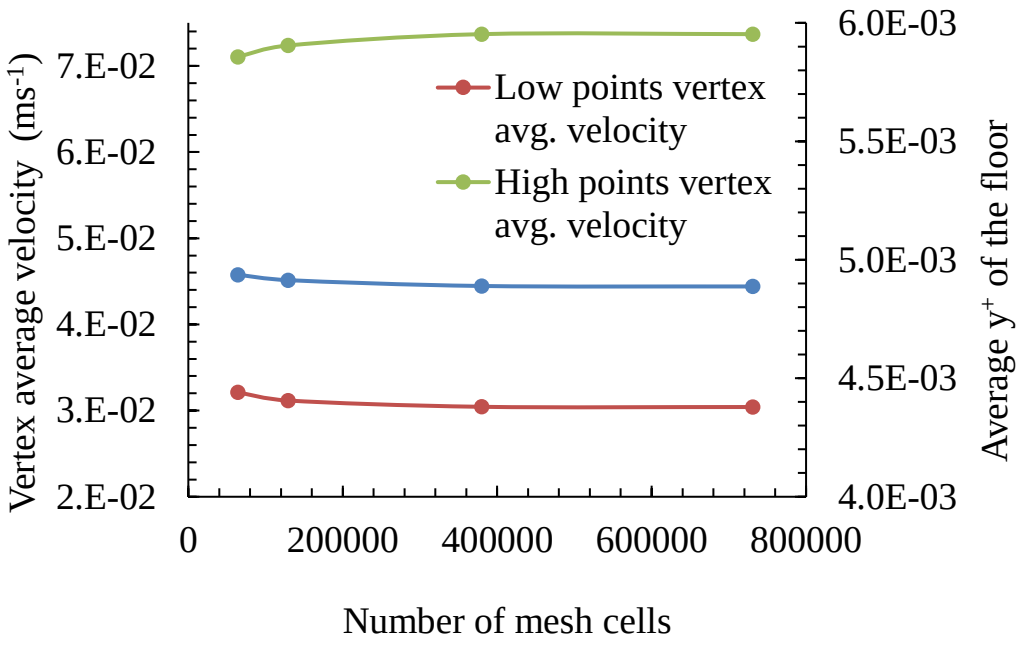

Figure 78: Facet Average y^+, Vertex Average Velocity located vertically above each other at the second Valley (L), and Vertex Average Velocity located vertically above each other at the second Peak (H) found using LES viscous models

As per Figure 78, the facet average y^+ of all floor surfaces and node average velocities of the Regional computer domain just above the second valley and the peak locations with respect to mesh sizes started producing the same results independent of mesh size beyond 379,900 mesh size under Large Eddy Simulation (LES) viscous models with an operating pressure of 101325 pa, acceleration of gravity of 9.817 m s^{-2} and The ceiling of the Regional computation domain was modelled as a velocity inlet with fixed velocity as defined by the Equations (85) without any perturbation at the ceiling.

4.4.2.4 Uncertainty due to discretization

Uncertainty due to discretization was calculated following published ASME guidelines (ASME, 2008). ASME guidelines use the Richardson extrapolation (RE) method, which has been evaluated for many types of CFD problems (Roache, 1993).

The RE method can be used to find the respective numerical errors when performing CFD work to predict the flow fields close to the ground surface since experimental results were not available for comparison.

The representative mesh size h was calculated using Equation (86) for the Regional CFD model.

$$\boldsymbol{h = \left[\frac{1}{N}\sum_{i=1}^{N}(\Delta V_i)\right]^{1/3}} \qquad \textbf{(86)}$$

here, N is the total number of cells in the Regional computational domain and ΔV_i is the volume of the ith cell.

The grid refinement factor r for the selected computational domains was calculated using Equation (87).

$$\boldsymbol{r = h_{coarse}/h_{fine}} \qquad \textbf{(87)}$$

For the Regional computational model, the grid refinement was done systematically by doubling the mesh nodes in the windward direction first and doubling the mesh in the transverse direction second using a structured mesh scheme. The starting mesh size was similar to the mesh size used for the Grid Independence study, with 73,172 cells. The second mesh had 233,142 cells, and the third mesh had 732,783 cells.

The local order of accuracy p was calculated using Equation (88).

$$p = \frac{1}{ln(r_{21})} |ln|\varepsilon_{32}/\varepsilon_{21}| + q(p)| \quad (88)$$

where,

$$q(p) = ln\left(\frac{r_{21}^{p} - s}{r_{32}^{p} - s}\right) \quad (89)$$

here,

$$s = 1 \cdot sgn(\varepsilon_{32}/\varepsilon_{21}) \quad (90)$$

here,

$$\varepsilon_{32} = \emptyset_3 - \emptyset_2 \quad (91)$$

and,

$$\varepsilon_{21} = \emptyset_2 - \emptyset_1 \quad (92)$$

here, the variable $\emptyset$ is the reported values such as y+, shear stress, and velocity at selected locations. The negative values of $\varepsilon_{32}/\varepsilon_{21}$ and $\varepsilon_{32}/\varepsilon_{21} < 0$ values are indications of oscillatory convergence.

The extrapolated values of the variable $\emptyset$ were calculated using Equations (93).

$$\emptyset_{ext}^{21} = \left(r_{21}^{p}\emptyset_1 - \emptyset_2\right)/\left(r_{21}^{p} - 1\right) \quad (93)$$

The approximate relative errors of the variable ∅ were calculated using Equation (94).

$$e_a^{21} = \left| \frac{\emptyset_1 - \emptyset_2}{\emptyset_1} \right| \tag{94}$$

The approximate relative errors of the extrapolated variables were calculated using Equation (95).

$$e_{ext}^{21} = \left| \frac{\emptyset_{ext}^{21} - \emptyset_1}{\emptyset_{ext}^{21}} \right| \tag{95}$$

Finally, the grid convergence indexes were calculated using equation (96).

$$GCI_{fine}^{21} = \frac{1.25 e_a^{21}}{r_{21}^p - 1} \tag{96}$$

Table 15 and Table 16 show the discretization errors for velocities measured at locations L1 to L4 and H1 to H4.

Table 15: Discretization error table for velocities measured in m s^{-1} at locations L1 to L5

	Velocity at L1, (p<1) (m s^{-1})	**Velocity at L2 (m s^{-1})**	**Velocity at L3 (m s^{-1})**	**Velocity at L4 (m s^{-1})**
N1	379,900	379,900	379,900	379,900
N2	129,195	129,195	129,195	129,195
N3	64,350	64,350	64,350	64,350
r21	1.43265	1.43265	1.43265	1.43265
r32	1.26153	1.26153	1.26153	1.26153
ϕ1	0.00901	0.02161	0.03685	0.05387
ϕ2	0.00927	0.02241	0.03792	0.05502
ϕ3	0.01026	0.02354	0.03900	0.05597
p	6.35613	2.69356	1.53662	0.80336
$\boldsymbol{\phi_{ext}^{21}}$	0.008982	0.021114	0.035399	0.050407
$\boldsymbol{e_a^{21}}$	2.91%	3.73%	2.91%	2.15%
$\boldsymbol{\phi_{ext}^{21}}$	0.33%	2.34%	4.10%	6.86%
$\boldsymbol{GCI_{fine}^{21}}$	0.41%	2.85%	4.92%	8.03%

Table 16: Discretization error table for velocities measured in m/s at locations H1 to H4

	Velocity at H1, (Os. Conv) ($m\ s^{-1}$)	**Velocity at H2, (Os. Conv) ($m\ s^{-1}$)**	**Velocity at H3, (Os. Conv) ($m\ s^{-1}$)**	**Velocity at H4, (Os. Conv) ($m\ s^{-1}$)**
N1	379,900	379,900	379,900	379,900
N2	129,195	129,195	129,195	129,195
N3	64,350	64,350	64,350	64,350
r21	1.43265	1.43265	1.43265	1.43265
r32	1.26153	1.26153	1.26153	1.26153
ϕ1	0.03370	0.06288	0.08700	0.11024
ϕ2	0.03282	0.06169	0.08581	0.10909
ϕ3	0.03206	0.06044	0.08423	0.10731
p	1.01420	1.67716	2.51318	3.02737
$\boldsymbol{\phi_{ext}^{21}}$	0.0357	0.0643	0.0878	0.1108
$\boldsymbol{e_a^{21}}$	2.61%	1.89%	1.36%	1.05%
$\boldsymbol{\phi_{ext}^{21}}$	5.59%	2.23%	0.92%	0.53%
$\boldsymbol{GCI_{fine}^{21}}$	7.41%	2.85%	1.16%	0.67%

As per Table 16, the local order of accuracy *p*. ranges between 1.0142 and 3.02737, with an average value of 2.05798. The fine mesh yields a maximum numerical error of 7.41% at the H1 location.

Referring to Table 15, the local order of accuracy *p* spans from 0.80336 to 6.35613, with an average value of 2.84742. The fine mesh results in a maximum numerical error of 8.03% at the L4 location.

4.4.3 CFD Results of the Regional CFD Model

The LES method was used to explicitly resolve the turbulent fluctuations (Smirnov, Shi, & Celik, 2001) of the Regional CFD model, and the Subgrid-Scale was solved using the Smagorinsky-Lilly model with $C_s = 0.2$ (Comte-Bellot & Corrsin, 1971). Pressure and velocity were coupled using the Simplec algorithm. The pressure was discretized using a second-order scheme, and momentum was discretized using the default Bounded Central Differencing scheme.

Figure 79 shows the time history data of vertex average velocities of high location points (H), low location points (L), and facet average y^+ values of the floor surfaces for 1000 time steps. The time step size was 1E-6 seconds, and the maximum time step size per iteration was 200. The time stepping was started from a converged reference solution.

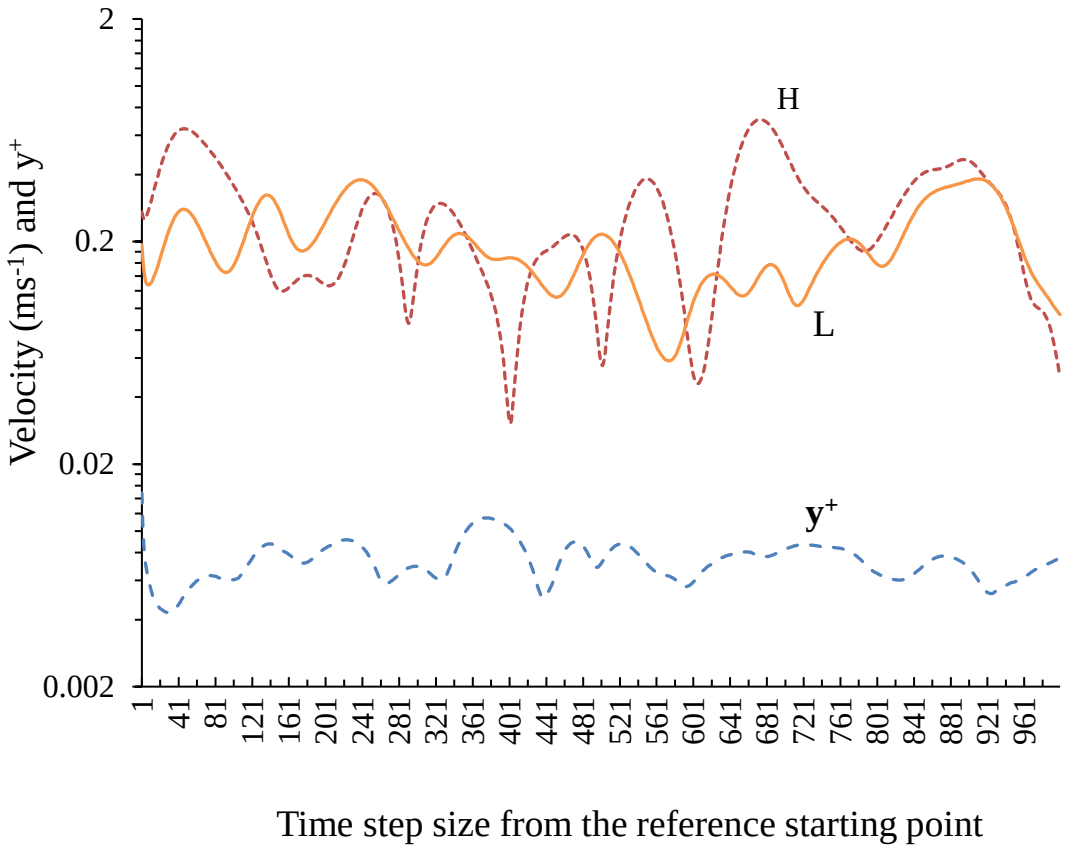

Figure 79: Time history data of vertex average velocity at High location points (H) and Low location points (L) and facet average y^+ of the floor of the computational domain.

The time average vertex velocities of H and L locations were 1.354E-01 × (1 ± 56%) ms^{-1} and 7.028E-02 × (1 ± 48%) ms-1, respectively, and facet average y+ of the floor surfaces was 4.3461E-03 × (1 ± 20%).

The vertex average velocities at the H and L positions, as well as the facet average y^+ values on the floor, determined during the mesh convergence study, when the ceiling was simulated with fixed velocity components and no perturbations, exhibited lower values compared to the time-averaged values obtained in this study with the introduction of perturbations using the Spectral Synthesizer fluctuating velocity algorithm.

Figure 80 shows velocity vectors coloured as per total pressure (Pa) of the streamwise vertical plane (Z = 50 μm) and particle traces emanating from the same streamwise vertical plane for three different time steps.

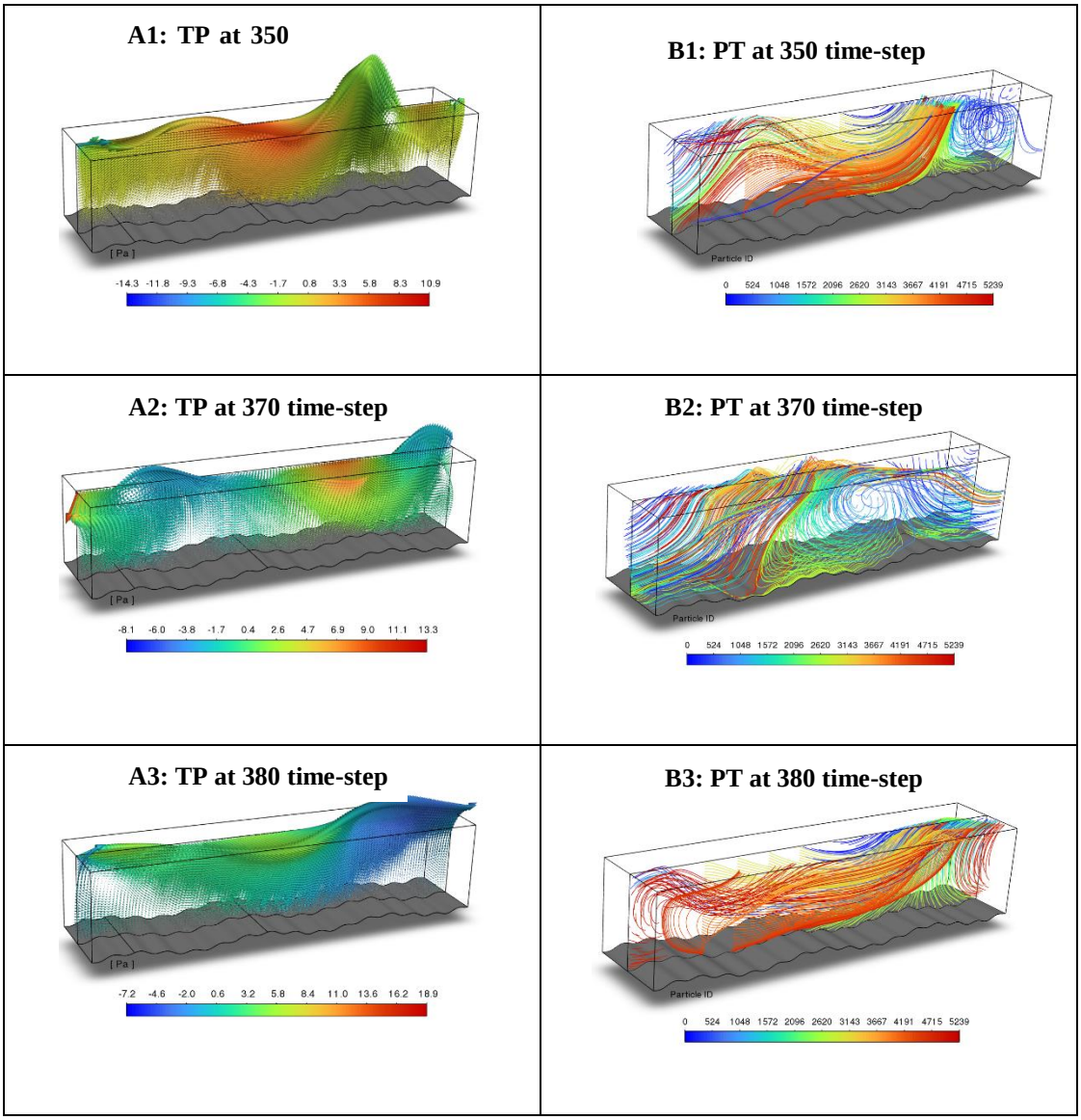

Figure 80: Figures on the left show the velocity vectors on the vertical plane running at the center of the Regional computational domain coloured as per the Total Pressure (TP) measured in pascals, and figures on the right show the Particle Traces (PT) emanating from the same vertical plane for the time steps 350, 370 and 380.

Figure 80-A1 shows a significant lift (around -0.86 Pa total pressure) at the halfway of the floor-back due to high vertical velocity. In this region, the velocity directions change from 42˚. to -42˚. and again from -42˚. to +42˚. The attached flow up to halfway of the floor-back will push and roll the particles into the lift region, where particles will get immediately suspended. The pathlines in Figure 80-B1 also show that particles on the floor at halfway through the floor-back can immediately suspend and reach the ceiling.

Figure 80-A2 shows a lift (around - 0.19 Pa total pressure) in the floor-front and floor-middle regions. Just before the halfway of the floor-middle, the flow velocity direction changes from -108 ˚ to 108 ˚. The pathlines in Figure 80-B2 show that leaping particles arriving in the central region of the floor-middle will get entrained into the ceiling, but no particle will immediately resuspend off the floor since the magnitude of the negative total pressure is low compared to the situation found at 350 time-step.

Figure 85-A3 shows a significant lift (around negative 1.8 Pa total pressure) in the floor-back region. At the beginning of the floor-back region, the velocity directions change from -110˚. to 110˚. The attached flow up to the beginning of the floor-back will push and roll the particles into the lift region, where particles will get immediately suspended. The pathlines in Figure 80-B3 also show that particles on the floor-back can immediately suspend and reach the ceiling.

5 PARTICLE TRACKING AND RESUSPENSION RESULTS

Spherical La_2O_3 power with a density of 6510 kg m^{-3} was released into the computation domains from the floor of the converged Regional model and 100 µm above the contamination floor for the converged Global model. These particles were divided into 21 bins with bin center diameters of 0.9, 1.15, 1.45, 1.8, 2.25, 2.75, 3.25, 3.75, 4.5, 5.75, 7, 8, 9.25, 11.25, 13.75, 16.25, 18.75, 22.5, 27.5, 31 and 32 µm.

The respective particle-releasing surface locations, velocities, and locations of measurement planes are given in Table 17.

Table 17: Initial particle releasing location and particle velocity for CFD Global and Regional models

Model	**Particle releasing surface**	**Number of particles released**	**Particle released velocity (m s-1)**	**Measurement plane**
Global 3D WIS facility CFD model	100 µm above the contamination plate. X:[4.5: 5.0] m Y:[100:100] µm Z:[-0.5:0.5] m	5000 particles per bin. Note: There were 21 particle sizes	$V_x = 8.93 \times 10^{-1}$ $V_y = -4.52 \times 10^{-6}$ $V_z = 1.35 \times 10^{-2}$	Particle Sizer 1 and 2 planes
Regional 3D model	From the whole floor	6550 particles per bin. Note: There were 21 particle sizes.	$V_x = 0$ $V_y = 0$ $V_z = 0$	Ceiling boundary plane

5.1 Particle Tracking

The Discrete Phase Model (DPM) available in the FLUENT software was used to calculate the trajectories of particles in a Lagrangian frame of reference. In the Lagrangian frame of reference, the observer follows the moving particles through the computational domain.

The FLUENT software calculates particle trajectories using Equation (97).

$$\frac{\boldsymbol{du_i^p}}{\boldsymbol{dt}} = \boldsymbol{F_D}\left(\boldsymbol{u_i} - \boldsymbol{u_i^p}\right) + \frac{\boldsymbol{g_i}\left(\boldsymbol{\rho_p} - \boldsymbol{\rho}\right)}{\boldsymbol{\rho_p}} + \frac{\boldsymbol{F_i}}{\boldsymbol{\rho_p}} \qquad \textbf{(97)}$$

The first term on the right-hand side of Equation (97), $F_D\left(u_i - u_i^p\right)$, is the drag force acting on a particle due to the relative velocity of the particle with respect to the computational domain; the second term $\frac{g_i(\rho_p - \rho)}{\rho_p}$ is the force acting on the particle due to gravity and buoyancy, and the third term, F_i/ρ_p, is the resultant force acting on a particle due to additional forces such as pressure gradient, forces due to Brownian motion and Saffman lift forces (Fluent Inc., 2006). The Brownian force acts on a sub-micron particle due to the fluid's absolute temperature. Therefore, one has to enable the energy equation in

FLUENT to add the effect of Brownian motion into the DPM model. The energy equation was not included in the WIS facility wind chamber's CFD modelling because all resuspension experiments were conducted at constant room temperature.

The fluid phase and the particle phase were coupled in one way since the fluid phase influences the particles via drag force and turbulence, and there is no influence on the fluid phase due to the particle phase since the particles are considered inert. Also, the volume fraction of the particle phase is less than 10% of the overall volume of the computational domain; otherwise, one has to use multiphase modelling techniques available in FLUENT to solve the trajectories of the particles (Fluent Inc., 2006).

5.1.1.1 Particle interaction with boundaries

Particles that were released into the converged computational domain from surfaces were tracked by FLUENT software until they escaped the computational domain or until the maximum allowed number of time steps of the discrete phase was reached, which was usually defined by the software user.

Table 18 shows particles' fates as particles approached the boundaries of the computational domains used in this report.

Table 18: CFD Boundary conditions and particle fates

Boundary types used in FLUENT	**FLUENT particle-phase boundary condition**
Pressure-inlet	Escape
Pressure-outlet	Escape
Porous-jump	Escape
Velocity-inlet	Escape
Velocity-outlet	Escape
Exhaust-fan	Escape
Wall	Reflect
Symmetry	Reflect
Periodic	Periodic

Particles that will reach Pressure-inlet, Pressure-outlet, Porous-jump, Velocity-inlet, Velocity-outlet, and Exhaust-fan boundaries will escape the computational domain. A particle's trajectory is terminated when it reaches an “Escape” boundary, as shown in Figure 81.

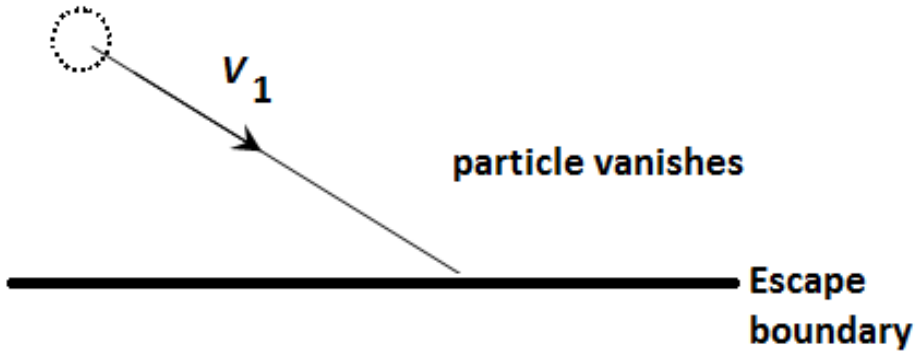

Figure 81: Particle fate after it reaches escape boundary condition

Particles that reach Wall and Symmetry boundaries will be reflected, as shown in Figure 82, and FLUENT will continue to track the particles.

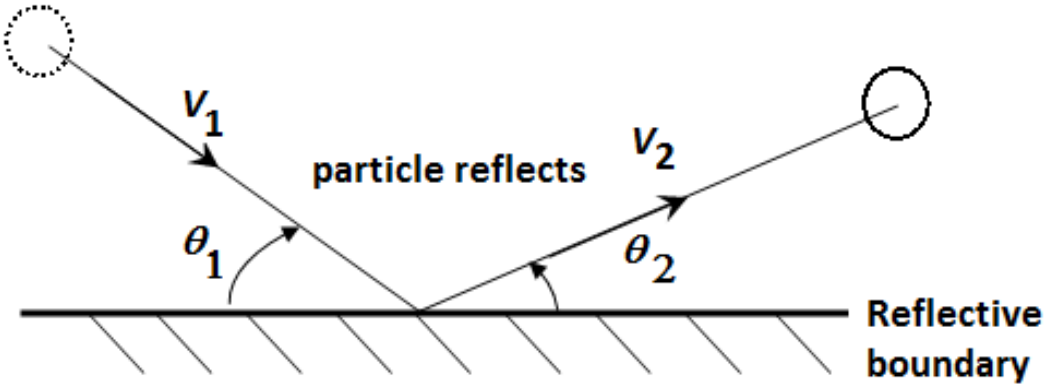

Figure 82: Particle fate after it collided with a reflecting boundary condition

At reflective boundary conditions, the particle's normal and tangential velocity components after the impact are calculated according to the coefficient of restitution of the wall surface.

The normal coefficient of restitution defines the momentum a particle retains in the direction normal to the surface after it collides against a surface, as shown in Equation (98).

$$\boldsymbol{e_n = \frac{v_{2,n}}{v_{1,n}}} \qquad \textbf{(98)}$$

here, e_n is the normal coefficient of restitution, v_n is the normal velocity component, and subscripts 1 and 2 refer to before and after conditions. Similarly, the tangential coefficient of restitution will define the tangential momentum the particle retains after colliding against the 'Reflect' boundary.

Particles that reach a periodic boundary condition will appear with the same velocity at the linked periodic boundary. For example, the particle leaving the Back-outlet periodic boundary condition in the 3D Regional CFD model will appear in the Front-inlet periodic boundary with the same velocity magnitude and direction.

5.1.1.2 Body forces acting on still particles from the wall surfaces

A user-defined function (UDF) was used to calculate the adhesion force acting on the spherical particle when a particle distance to a nearby wall is higher than a minimum threshold distance (1.0E-10 m). The adhesive force (F_{adh}) was calculated using Equation (99) (Biasi, De Los Reyes, Reeks, & De Santi, 2001).

$$\boldsymbol{F_{adh} = 4\pi\gamma r\left(0.016 - 0.0023(r^p)^{0.545}\right)} \qquad \textbf{(99)}$$

here, γ is the adhesive surface energy between particle and substrate. In the UDF, we will be using $\gamma = 0.56\text{N}m^{-2}$ (Hall, 1988). Here, r is the radius of the spherical particle measured in meters and r^p is the radius of the particle measured in micro-meters.

The UDFs responsible for determining adhesive forces based on the distance between particles and walls can consume substantial computational memory since they require storing the distance between each particle and all wall surfaces during each time integration step. Instead of relying on distance alone to decide whether a particle is close enough to the wall to compute adhesive forces, an alternative approach can be used to determine particle velocity as a criterion. Adhesive forces can be calculated when the particle velocity reaches zero. This method minimizes the computational memory footprint and accelerates the particle tracking process. However, caution must be exercised to ensure that particle velocities within the computational domain are not in still air or, particles are

not in static equilibrium, where net forces acting on particles are zero, or in specific flow regions where particle velocity can naturally drop to zero.

The distance-based and velocity-based UDFs to calculate the adhesive forces can be found in Appendix C.

5.2 CFD Particle Resuspension Results

This section will explore the outcomes and findings related to the computational fluid dynamics (CFD) analysis of particle resuspension.

The bin-by-bin CFD particle resuspension factor values were calculated by multiplying the bin-by-bin CFD resuspension fraction results of the Regional CFD model by respective Global bin-by-bin CFD transfer factor results found from the Global CFD model.

5.2.1 Regional CFD Particle Resuspension Fraction Results

For the Regional CFD model, particles were introduced to the converged computational domain from the floor of the Regional Model. Particles were introduced at the beginning of unsteady CFD simulation and tracked at the end of each time step. The initial particle velocity x, y and z directions were zero. Throughout the CFD simulation, adhesion forces were applied to all still particles on the floor using a User Defined Function (UDF). Then, particles were tracked by FLUENT software for 5000 steps or until they reached the Ceiling boundary. Once the particles hit the Ceiling boundary, which has the boundary type of Velocity inlet, particles will disappear, and FLUENT software will save the particle information such as location (x, y and z coordinates), velocity components (u,v and w), diameter, temperature, time of flight and mass flow into a text file.

In the Regional CFD model, both front-inlet and Back-outlet boundaries were modelled as Periodic boundaries. Any particle reaching a Periodic boundary would appear on the opposite side linked to the Periodic boundary with the same velocity and travel through the continuous flow domain until particles reach the Ceiling boundary or the maximum number of tracking steps defined by the user. Using this Periodic boundary type, one can drastically reduce the computational demand and simulate a longer repeating computational domain.

Figure 83 shows the particle locations at selected time steps. Time stepping was started from a converged solution.

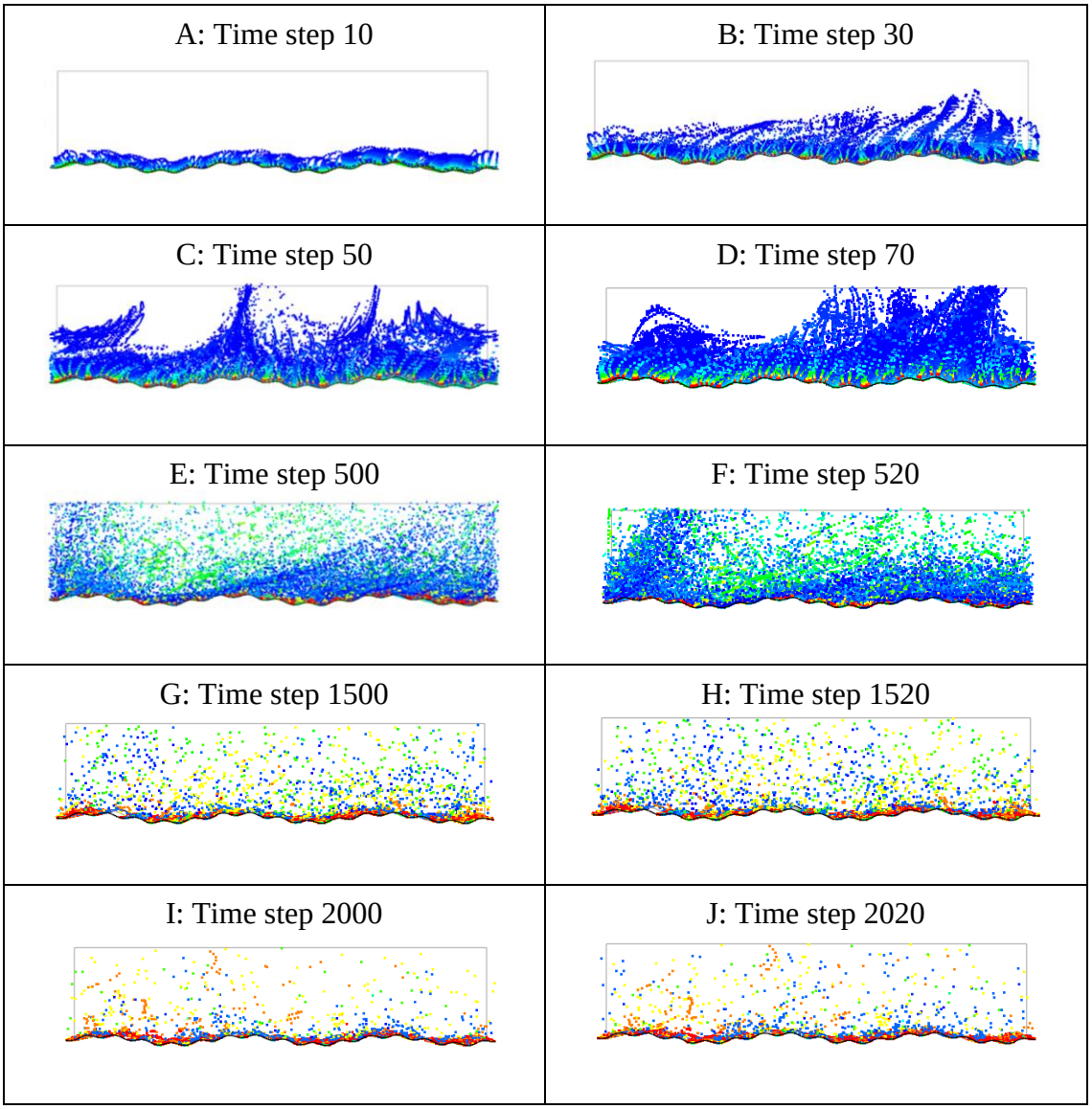

Figure 83: Particle locations in the Regional domain at selected times steps.

Figure 83 A- D shows the particle locations at the beginning of the particle resuspension process. Small particles mostly started resuspending during these time steps. As time progressed, medium size particles started resuspending with small particles. As time progressed further, small particle concentrations started decreasing as they left the ceiling boundary, and bigger particles started resuspending, as shown in Figures 90 G to J.

5.2.2 The behaviour of resuspended particles in the Regional CFD model

Figure 84 shows the overlay of velocity vectors coloured by total pressure (Pa), and some particle tracks of particles released from a line where the symmetry plane met the floor when the particles were injected to the floor to a converged Regional CFD model at 380 time step.

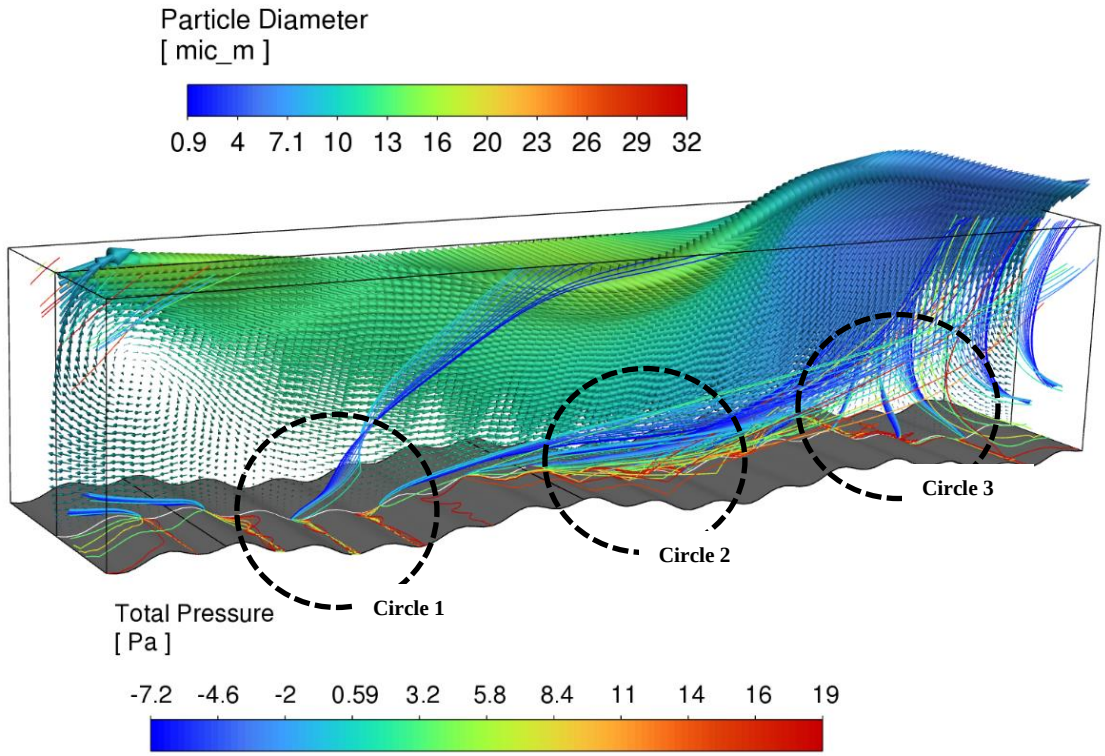

Figure 84:Particle Traces coloured by Particle Diameter (µm) and velocity vectors colored by total pressure (pa) at 380 time step.

Figure 85, Figure 86 and Figure 87 show zoomed-in pictures corresponding to circles 1, 2 and 3 in Figure 84.

Figure 85 shows how small particles (<10 um) lift off from the floor surfaces while bigger particles roll along the surfaces in the transverse direction. These bigger particles will travel up the valleys and come back down again when gravity takes over the momentum of particles and travel in a transverse direction along the valleys.

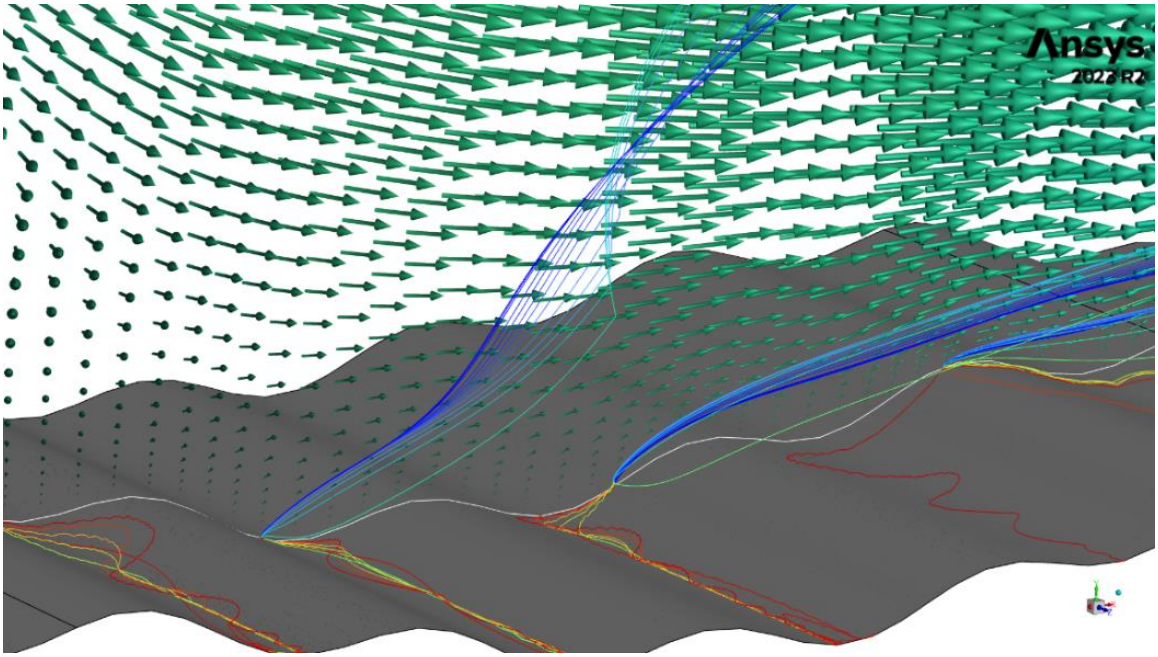

Figure 85: Zoomed-in region of circle 1 in Figure 84

Figure 86 shows how bigger particles with enough momentum will overcome the gravitation force well of the valleys. These particles will take off from the floor as they roll over the peaks and eventually start leaping along the surfaces toward the streetwise direction. The velocity vectors show that the flow in this region is attached and has no adverse pressure gradient.

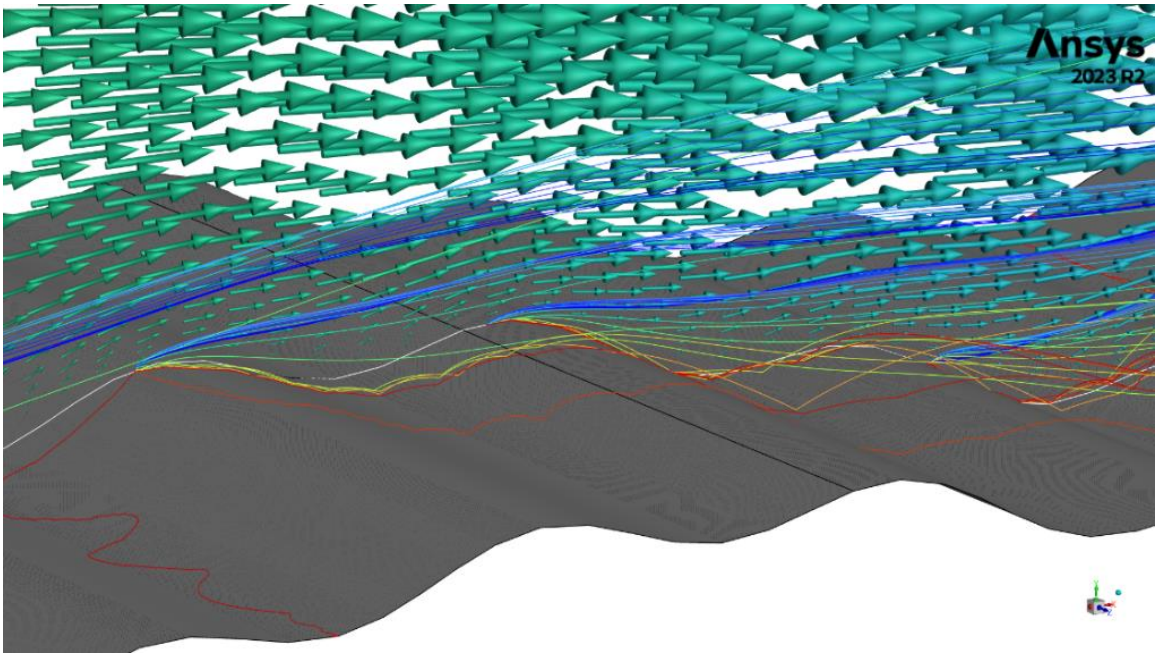

Figure 86: Zoomed-in region of circle 2 in Figure 84

Figure 87 shows how smaller particles are immediately lifted off the floor in the adverse pressure gradient region. Also, the bigger particles that have reached enough elevation due to leaping motion along the attached flow will start travelling towards the ceiling due to strong negative pressure in this region.

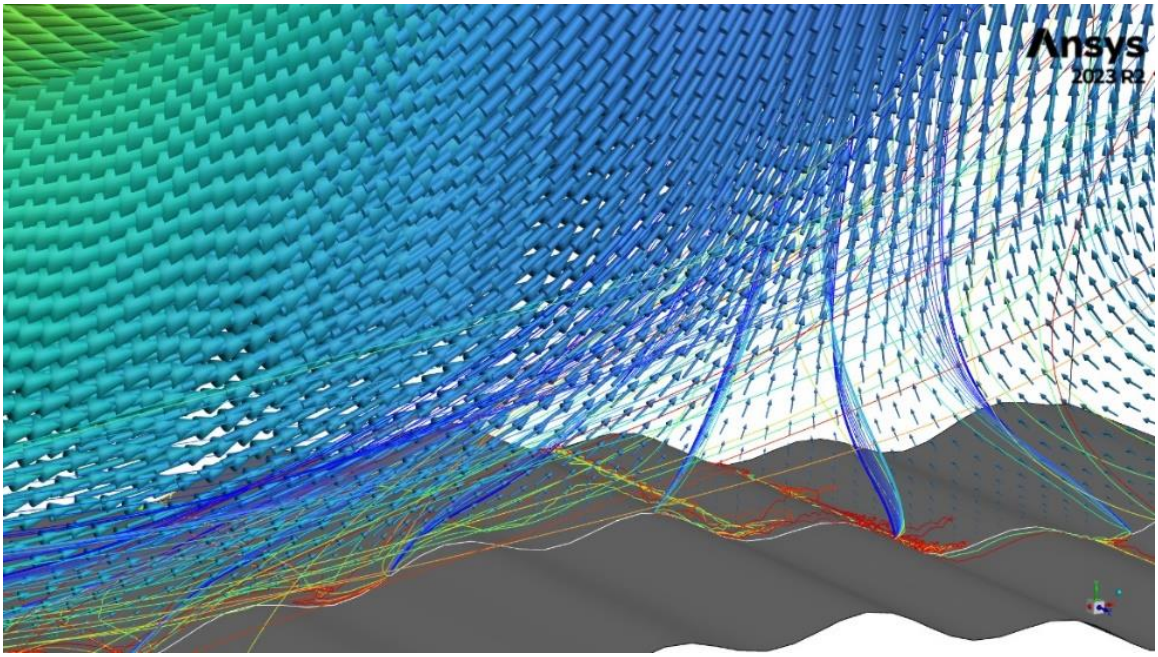

Figure 87: Zoomed-in region of circle 3 in Figure 84

5.2.2.1 Regional Resuspension fraction

The Regional CFD particle resuspension faction ($RFr_{CFD,REGIONAL}$) defined by Equation (100) is used to calculate the number of particles that will reach the Ceiling boundary.

$$RFr_{CFD,REGIONAL} = \frac{Number\ of\ particles\ crossing\ the\ Ceiling\ boundary}{Number\ of\ particles\ released\ from\ the\ ground} \qquad (100)$$

Figure 88 shows the Regional CFD resuspension fractions calculated using Equation (112).

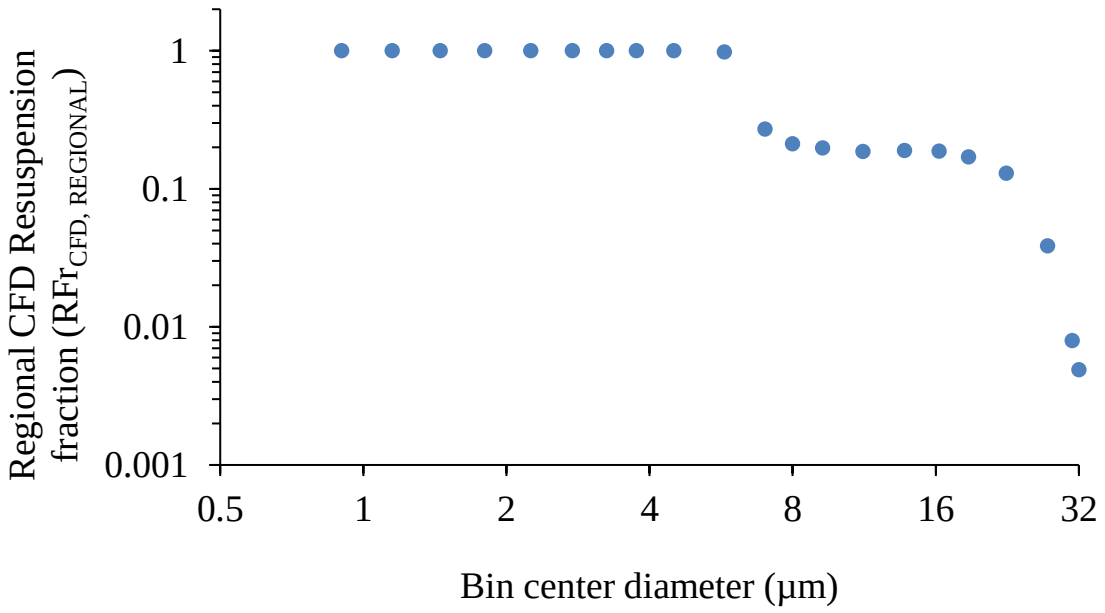

Figure 88: Resuspension fraction values found for the Regional 3D CFD model

According to Figure 88, particles with diameters between 0.9 and 4.5 μm had a resuspension fraction of 1. Then, the particle resuspension fraction reduces as per the equation: $RFr_{CFD} = -1.5710 \ln \emptyset + 3.4756$ $(R^2 = 0.8238)$ down to 2.125E-01 at particle size 8 μm. Beyond 8 μm particle size, the resuspension fraction reduces down to 4.89E-03 at 32 μm particle size following the equation $RFr_{CFD} = -0.0004\emptyset^2 + 0.0053\emptyset + 0.1842$ $(R^2 = 0.9797)$.

5.2.3 Global CFD Transfer Factor Results

Nine thousand six hundred particles were introduced to the converged CFD domains from a 0.24 m^2 surface area located 100 μm above the center of the contamination plate. These particles were tracked for 323 seconds to match the time when particle sizers (Grimms) were switched on during the active resuspension experiment at the WIS facility.

Figure 89 shows the particles released to the converged 3D computation domain from a plane located 100 μm above the contaminated plate and the measurement planes' locations (Particle Sizer 1 and 2 planes). Figure 89 shows only 10% of the released particles; all other particles and wall surfaces were intentionally erased for clarity.

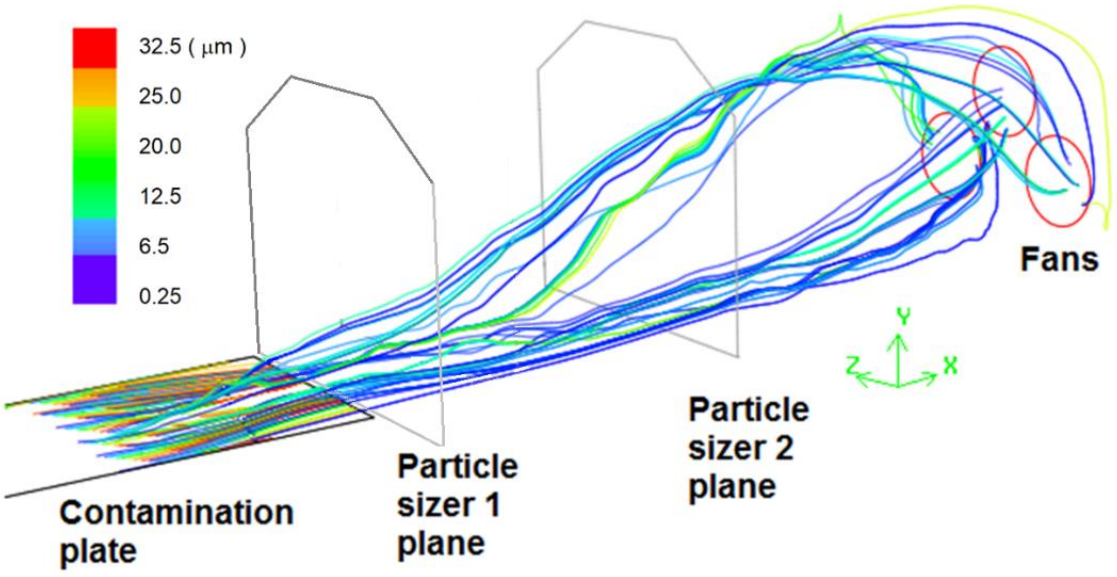

Figure 89: Sample particle tracks of Global 3D WIS facility during the resuspension process; particles are coloured according to their diameter (µm), and only 10% of the particles are shown for clarity.

The 3D Global CFD results show that there are two distinct horseshoe vortices in the region after the test section due to the asymmetric nature of the fans across the horizontal plane. The bifurcation of the particle tracks shown in this figure is mainly due to these two big vortices and the little vortices that are formed at the aft of the wind chamber due to flow stagnation.

For the Global CFD model, particles were released from a surface 100 µm above the contamination plate with velocities given in Table 17. Most of the bigger (heavier) particles fall back to the ground due to gravity. The particles that have fallen back to the

ground will bounce and leap along the floor due to viscous forces acting on them in the Laminar Sub Layer region. The larger particles will not be able to achieve enough energy to bounce out of the potential well, but some of the medium-sized particles will pick up enough energy along the way to move into the fast-moving free-stream air. These medium-sized particles will move downstream by the convecting free steam air or be removed from the wind chamber through the fans.

During the experiment, Particle Sizer-1 was placed at the same level as the contamination plate and 2.5 cm downstream from the edge of the contamination plate, and Particle Sizer-2 was placed 25 cm above the contamination plate and 112.5 cm downstream from the edge of the contamination plate. There is a higher possibility of finding bigger particles bouncing and leaping off the contamination plate at the Particle Sizer-1 location compared to Particle Sizer-2. During the experiment, resuspended particles with diameters 0.9 to 32 μm were found at Particle Sizer-1 and 0.9 to 7 μm particles at Particle Sizer-2 location. The particle tracks that we see in Global CFD results are consistent with the results found in the experiment.

5.2.3.1 Global CFD transfer factors

The definition of the CFD transfer factor used in this section of the thesis is similar to the definition of the resuspension factor defined by Stewart (1967). The only difference is the location of the particles that were released into the air. Here, particles were released into the air from the transfer plane located at 100 µm above the contamination plate. The definition of the Global CFD transfer factor is given by Equation (101).

$$\boldsymbol{RTF_{CFD,GLOBAL} = \frac{C}{S}} \qquad \textbf{(101)}$$

here, C is the number of particles hitting the detector plane per unit volume of air passing through the detector plane, and S is the number of particles released to air from the transfer surface.

The value of C used in Equation (101). can be found using Equation (102).

$$\boldsymbol{C = \frac{N_A}{V_{WT}}} \qquad \textbf{(102)}$$

here, N_A is the number of particles hitting the detector and V_{WT} is the volume of air moving through the detector plane for the duration of measurements.

The value of S used in Equation (101). was calculated using Equation (103).

$$\boldsymbol{S = \frac{N_{TS}}{A_{TS}}} \qquad \textbf{(103)}$$

here, N_{TS} is the number of particles released to air from the transfer surface and A_{TS} is the area of the transfer surface where particles were introduced into the Global computational domain.

The volume of air travelling through the detector plane was calculated using Equation (104).

$$\boldsymbol{V_{WT} = \dot{V}_{CF}\, t_{effective}} \qquad \textbf{(104)}$$

here, $\dot{V}_{CF}$ is the volume flow rate of the continuous flow (8.3 m^3s^{-1}) at the location of the resuspension factor being calculated and $t_{effective}$is the time corresponding to 99% of the Pareto graph of the number of particles hitting the detector plane versus the time of flight of particles to the detector plane. The corresponding Pareto graph is shown below.

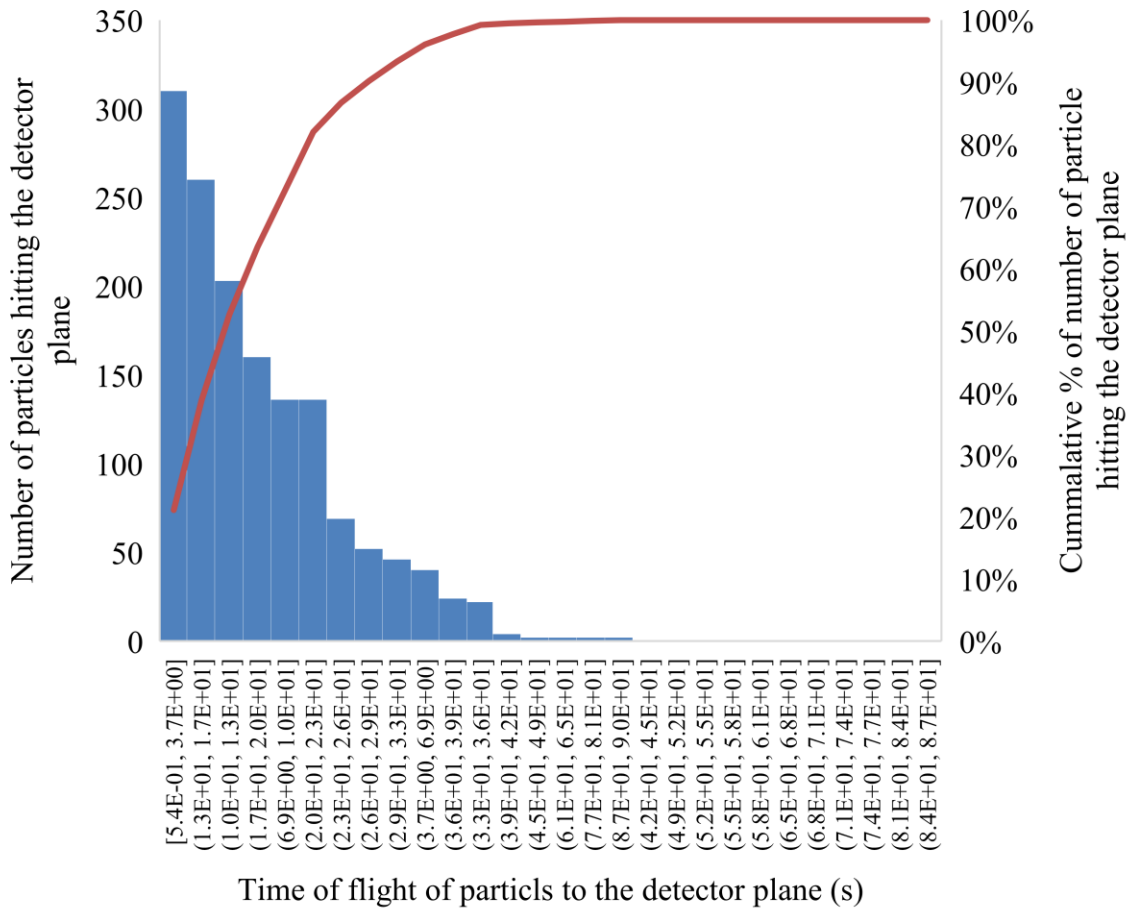

Figure 90: The bar graph shows the number of particles hitting the detector plane corresponding to Grimm particle sizer 2 location versus the time of flight of particles to the detector, and the line graph shows the corresponding Pareto chart.

The goal of counting was set up to 99% to remove the 1% of particles that would take longer to reach the detector. The time corresponding to 99% of the Pareto chart for the Grimm 2 particle sizer was 65.74 s and 11.10 s for the Particle sizer 1 particle sizer location. The time corresponding to Particle sizer 2 was used as $t_{effective}$ since both Grimms need to be on during the counting period.

Figure 91 shows Global CFD transfer factors calculated using Equation (102). at Particle Sizer (PS) 1 and 2 locations.

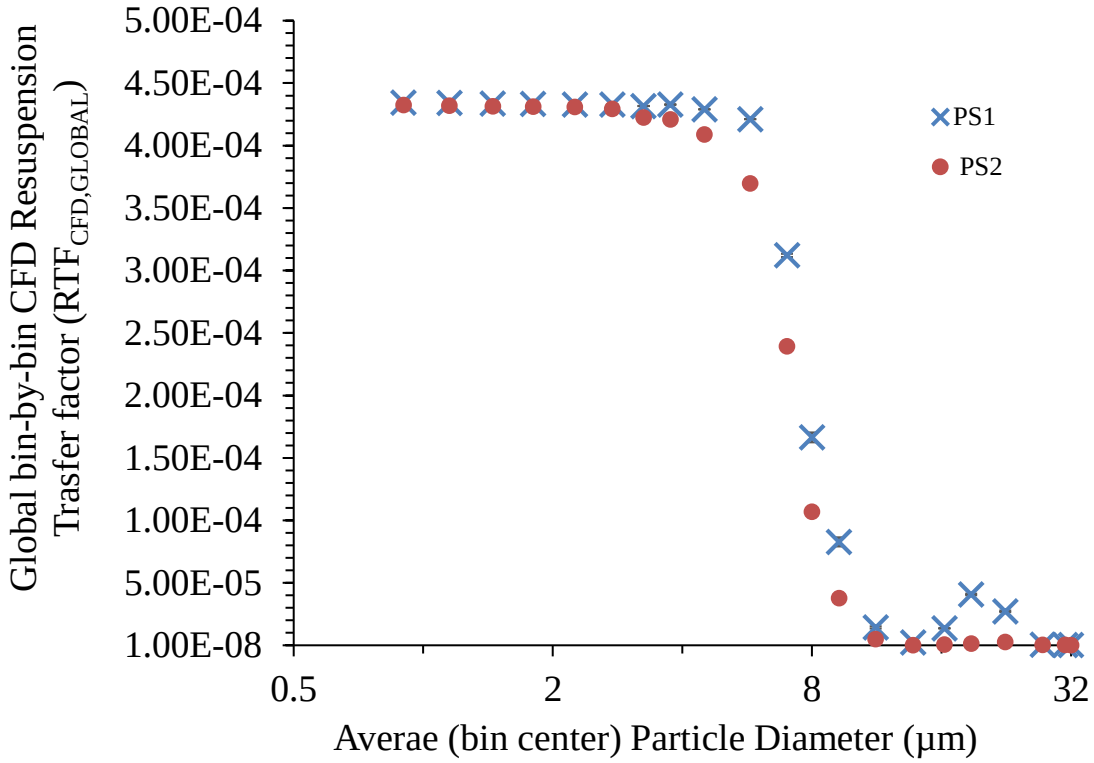

Figure 91: Global CFD transfer factors for the Particle Sizer 1 and 2 locations

The Global CFD transfer factors for Particle Sizer 1 and 2 locations have similar trends up to particle size 13.75 µm. According to Figure 91 there are three distinct regions. In region 1: particle size from 0.9 to 5.75 µm, the Global CFD transfer factors have an average value of 4.26E-04 × (1 ± 1.5%) m^{-1}. In region 2: particle sizes from 5.75 to 13.25 µm, the Global CFD transfer factors reduce from 3.95E-04 to 1.24E-06 m^{-1} following the second order polynomial: $RTF_{CFD,GLOBAL} = 1E-05E\emptyset^2 - 0.0002\emptyset + 0.0015$ ($R^2 =$

0.9884). Here, $RTF_{CFD,GLOBAL}$ is the Global CFD transfer factors and ϕ is bin center diameter. In region 3, particle size from 13.75 to 32 μm, the Global CFD transfer factors have an average value of 6.48E-06 × (1 ± 171%) m^{-1}. This region's minimum and maximum values are 2.43E-07 and 7.07E-06 m^{-1}, respectively.

5.2.4 CFD Particle Resuspension Factor

The CFD particle resuspension factor was calculated by multiplying the Regional resuspension fraction by the Global CFD transfer factors, as shown in Equation (105).

$$\boldsymbol{K_{CFD} = RFr_{CFD,REGIONAL} \times RTF_{CFD,GLOBAL}} \qquad \textbf{(105)}$$

here, K_{CFD} is the 3D, CFD resuspension factor, $RFr_{CFD,REGIONAL}$ is the Regional CFD resuspension fraction, and $RTF_{CFD,GLOBAL}$ is the Global CFD transfer factor.

Figure 91 shows the CFD resuspension factor results for Particle Sizers 1 and 2.

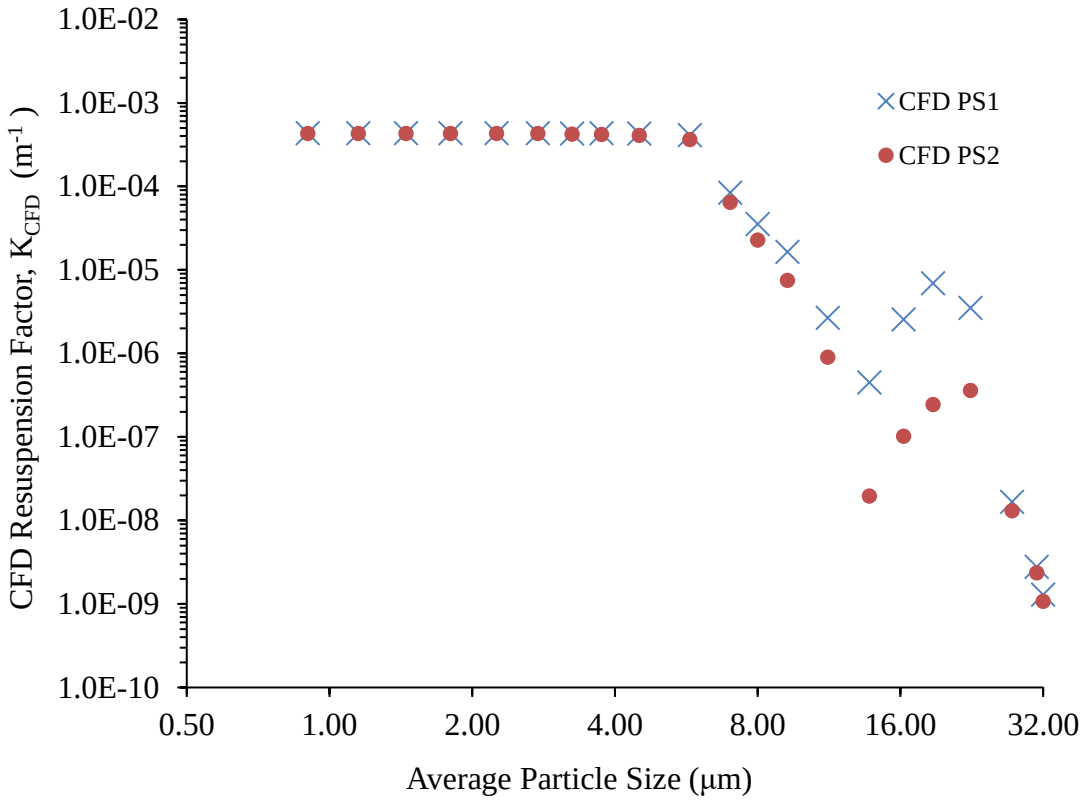

Figure 92: CFD resuspension factor for Particle Sizers (PS) 1 and 2

According to Figure 91 the CFD resuspension factor for Particle Sizer 1 and 2 have similar trends. The CFD resuspension factors can be fitted into three distinct regions. In Region 1, particle sizes from 0.9 to 6.75 μm, the average CFD resuspension factor is 4.14E-04 × (1 ± 13.3%) m^{-1} for Particle Sizer 1 and 4.01E-04 × (1 ± 16.3%) m^{-1} for Particle Sizer 2. In region 2, particle sizes from 6.75 to 13.75 μm, the average CFD resuspension factor reduces as per curves: $RF_{CFD} = 0.0342\exp(-0.83\emptyset)$ $(R^2 = 0.9911)$ for Particle Sizer 1 and $RF_{CFD} = 0.3236\exp(-1.181\emptyset)$ $(R^2 = 0.9912)$ for Particle Sizer 2, respectively. In

region 3, particle sizes from 13.75 to 32 μm, the average CFD resuspension factors increase and reduce following quadratic equation RF_{CFD} = 9E-09Φ3 - 7E-07 Φ 2 + 2E-05 Φ - 0.0001 (R^2 = 0.8709) for Particle Sizer 1 and RF_{CFD} = 3E-10 Φ 3 - 2E-08 Φ 2 + 6E-07 Φ - 4E-06 (R^2 = 0.7811) for Particle Sizer 2.

5.3 Comparison of CFD resuspension factor results against bin-by-bin experimental resuspension factor results.

Figure 93 shows the comparison of CFD and experimental bin-by-bin resuspension factor (K_i) results crossing Particle Sizer 1.

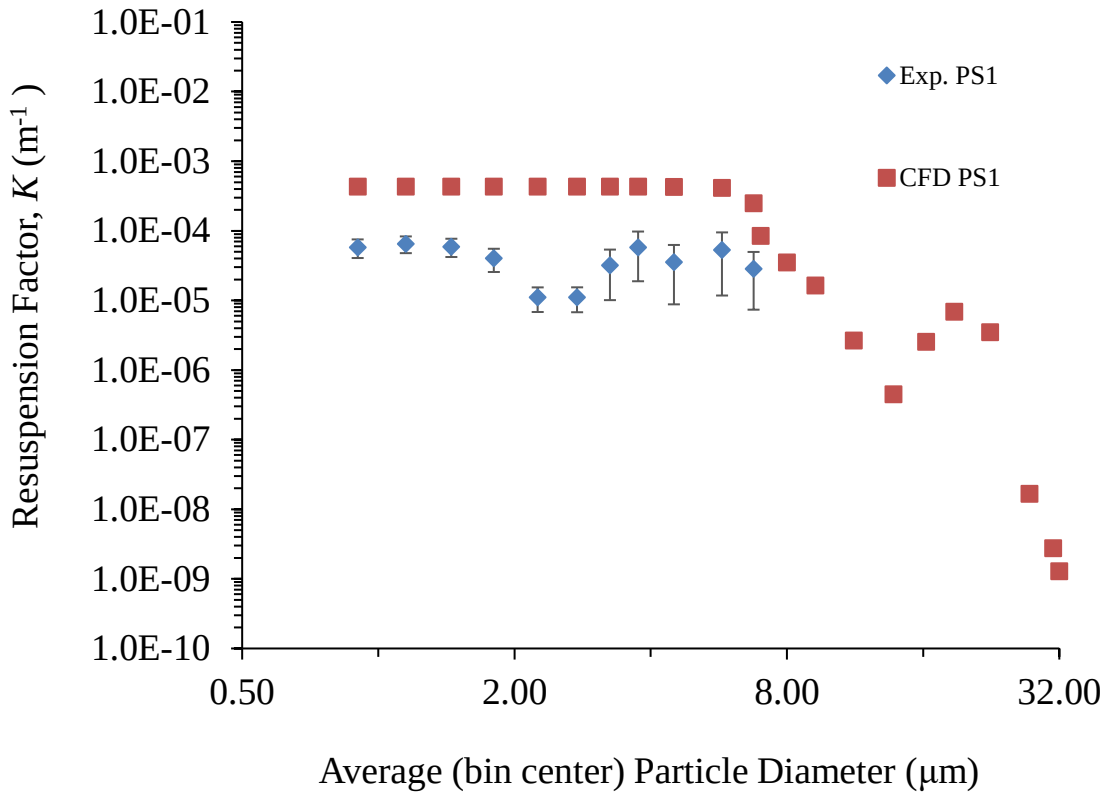

Figure 93: Comparison of CFD and Experimental bin-by-bin resuspension factors for Particle Sizer 1(PS1) location.

According to Figure 93, the CFD resuspension factor and experimental results have similar trends between 0.9 and up to 6.75 µm particle sizes, except for particle sizes 2.25 and 2.75 µm. For the particle sizes between 0.9 and 6.7 µm, the CFD resuspension factor results for particle sizer 1 is an order of magnitude higher than experimental results.

Figure 94 shows the comparison of CFD and Experimental bin-by-bin resuspension factor (Ki) results at the Particle Sizer 2 location.

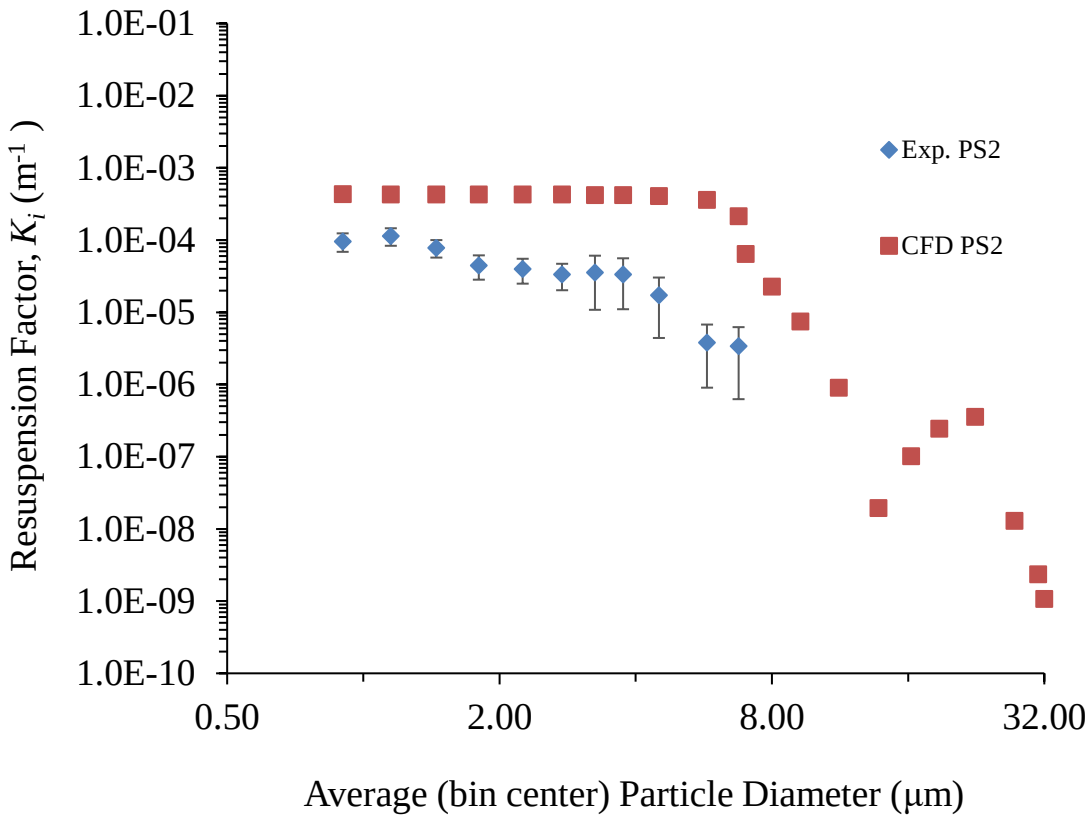

Figure 94: Comparison of CFD and Experimental bin-by-bin resuspension factors for Particle Sizer 2 (PS2) location.

According to Figure 94, CFD and Experimental resuspension factor results have similar trends up to 6.75 μm particle size.

For the particle sizes between 0.9 and 6.7 μm, the CFD resuspension factor results for particle sizer 2 is an order of magnitude higher compared to experimental results.

5.4 Regional CFD resuspension fraction results for different Ceiling velocities.

The CFD simulation effectively replicated the resuspension process, demonstrating a strong correlation between the resuspension factor values obtained through CFD and the experimental data for particle sizes ranging from 0.9 to 7 µm for an average test section velocity of 6.7 ms^{-1} of the WIS facility wind chamber.

In this segment of the thesis, the connection between the Regional CFD resuspension fraction and ceiling velocities is examined. As Henry's literature review (2014) highlighted, parameters like wall shear stress, friction velocity, and near-wall units significantly influence understanding of the flow dynamics near wall surfaces and are pivotal in the initial particle resuspension process. Shifting from traditional statistical evaluations of velocity profiles to a more comprehensive examination of near-wall fluid behaviours through careful experimental observations and Direct Numerical Simulations (DNS) has yielded valuable insights, particularly regarding particle resuspension within the Laminar Sub Layer. DNS studies have unveiled coherent structures in thin boundary layers, including "sweep" and "ejection" patterns, which are associated with the movement of particles toward or away from the wall. Furthermore, the presence of low-speed streaks contributes to what is known as the "preferential concentration effect" (Bernardini, Pirozzoli,, & Orlandi, 2013). (Soldati & Marchioli, 2009).

In the previous section, we successfully simulated these coherent structures using the Large Eddy Simulation (LES) method for the Regional CFD model. Employing a similar approach, we calculated the facet average shear stresses of the Regional Domain floor for corresponding streamwise Ceiling velocities. The Ceiling boundaries were modelled as a fixed constant streamwise velocity with no perturbations. The corresponding shear stress values and respective friction velocities found using eight CFD Regional models are depicted in Figure 95 for Ceiling velocities 0.89 to 7 ms^{-1}.

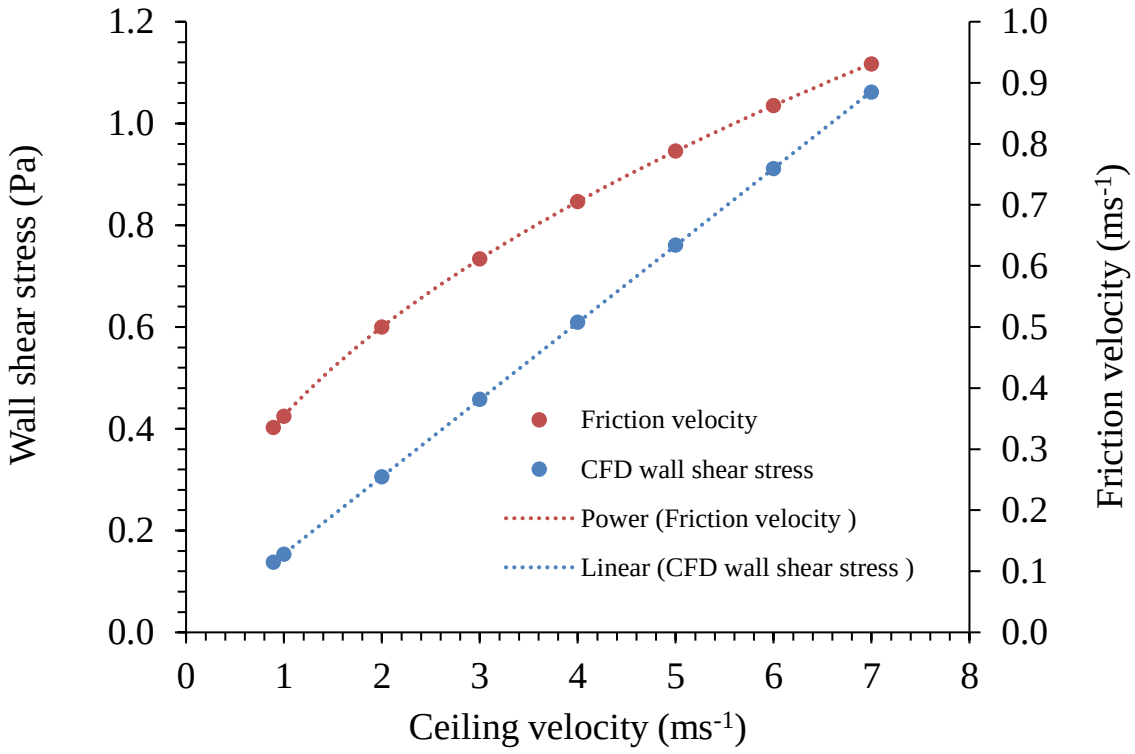

Figure 95: Shear stresses and friction velocities calculated using Regional CFD models for different Ceiling velocities.

As per Figure 95, the shear stress at the Ceiling boundary (100 µm above the floor) varies linearly following the curve: $\tau_w = 0.1514V_c + 0.003$ $(R^2 = 1)$, here $\tau_w$is floor shear streass and $V_c$is velocity at the Ceiling and wall shear stress varies following the power curve $u_\tau = 0.3545{V_c}^{0.4963}$ $(R^2 = 1)$, here $u_\tau$is friction velocity.

The turbulent kinetic energy (k) and turbulent dissipation rates (ε) at the Ceiling boundary were calculated using the relationships provided by Kalitzin et al. (2005).

$$\boldsymbol{k^+ = \frac{2400}{C_{\epsilon 2}^2}\left[\frac{1}{(y^+ + C)^2} + \frac{2y^+}{C^3} - \frac{1}{C^2}\right]} \qquad \textbf{(106)}$$

here, $\mathbf{k}^+ = \frac{k}{u_\tau^2}$, where k is turbulent kinetic energy, u_τ is friction velocity, $C_{\epsilon 2} = 1.9, C = 11$ and $\mathbf{y}^+$is non-dimensional wall normal distance.

$$\boldsymbol{\varepsilon^+ = \frac{14400}{C_{\epsilon 2}^2}\frac{1}{(y^+ + C)^4}} \qquad \textbf{(107)}$$

here, $\boldsymbol{\varepsilon}^+ = \frac{\varepsilon v}{u_\tau^4}$, where ε is turbulent dissipation rate, and v is dynamic viscosity.

Figure 96 shows the Turbulent Kinetic Energy at the Ceiling for Ceiling velocities of 0.89 to 7 ms^{-1}.

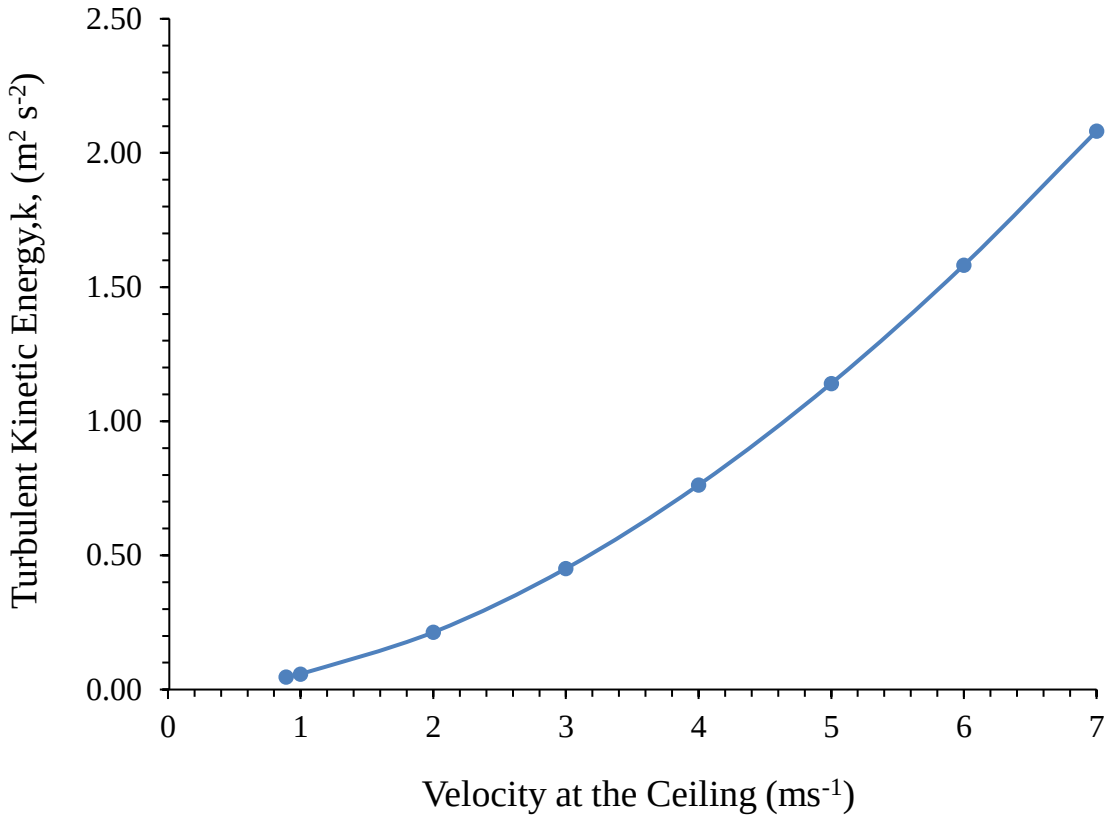

Figure 96: Variation of Turbulent Kinetic Energy (k) against velocity at the Ceiling boundary.

The Turbulent Kinetic Energy at the Ceiling with respect to the Ceiling velocity can be fitted into a power function: $k = 0.0589{V_c}^{1.84}$ $(R^2 = 0.9999)$, where k is Turbulent Kinetic Energy at the Ceiling and $V_c$is the velocity at the Ceiling.

Figure 97 shows the Turbulent Dissipation Rate (ε) at the Ceiling for Ceiling velocities of 0.89 to 7 ms-1.

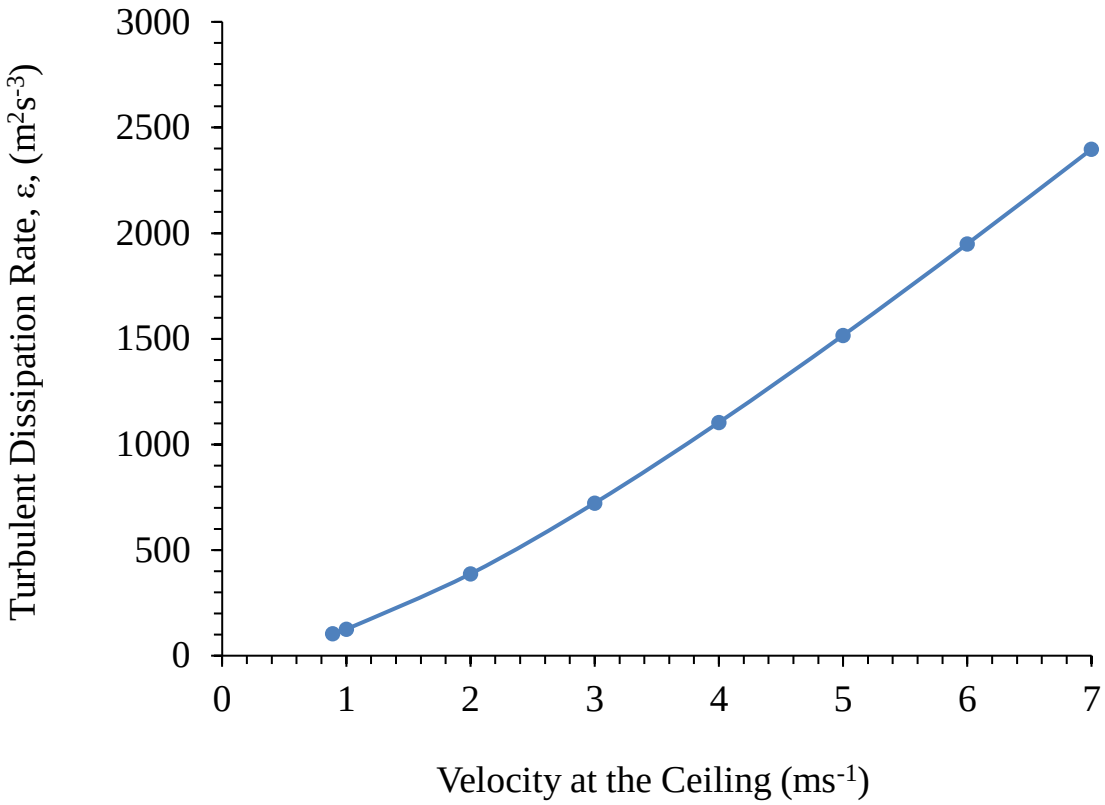

Figure 97:Variation of Turbulent Dissipation Rate (ε) at the Ceiling against Velocity at the Ceiling.

The Turbulent Dissipation Rate at the Ceiling with respect to the Ceiling velocity can be fitted into a power function: $\varepsilon = 128.46{V_c}^{1.5298}$ $(R^2 = 0.9991)$, where ε is the Turbulent Dissipation Rate at the Ceiling and $V_c$is the velocity at the Ceiling.

Figure 98 to Figure 105 show the bin-by-bin resuspension fraction distributions for 0.89, 1, 2, 3, 4, 5, 6 and 7 ms^{-1} Ceiling velocities.

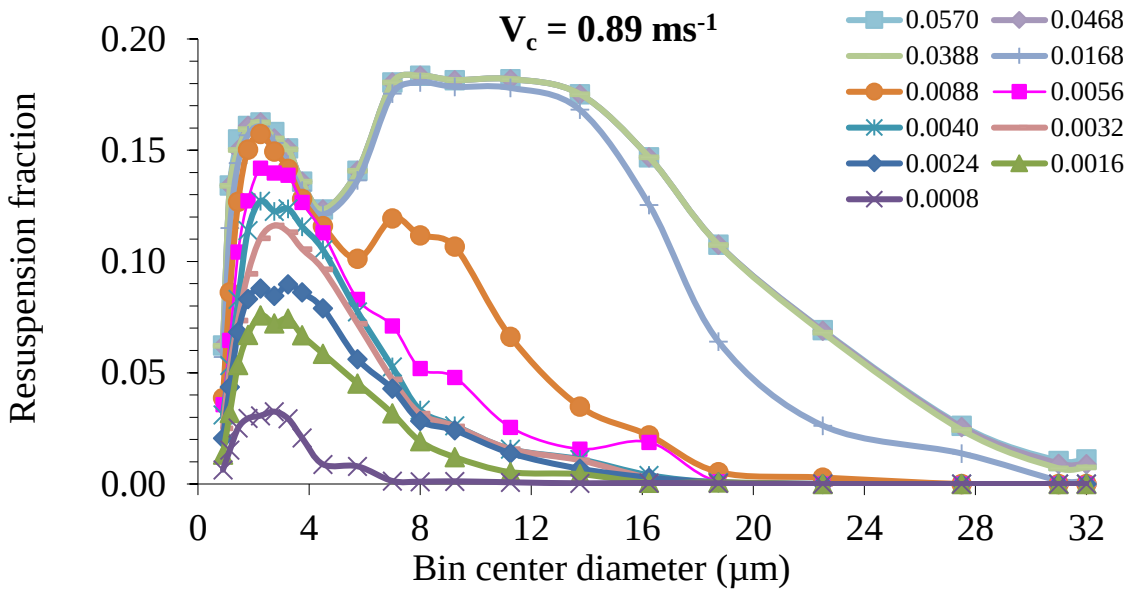

Figure 98: Time evolution of particle Resuspension Fraction vs. Bin center diameters for Ceiling velocity of 0.89 ms^{-1}, when k = 0.0473 m^{2}s^{-2} and ε = 104.4 m^2 s^{-3}

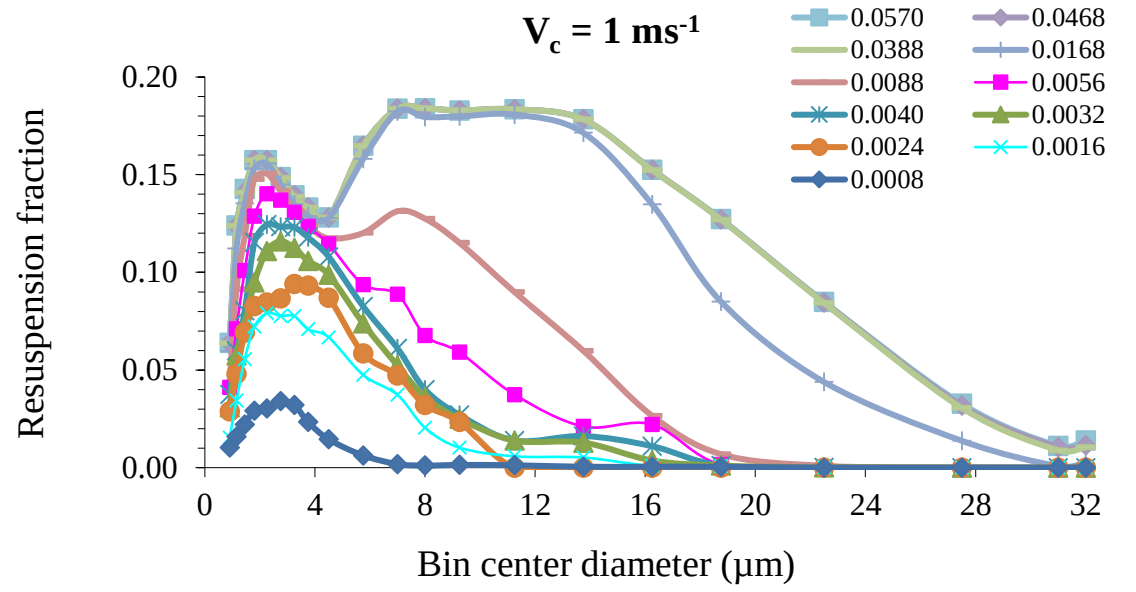

Figure 99: Time evolution of particle Resuspension Fraction vs. Bin center diameters for Ceiling velocity of 1 ms^{-1}, when k = 0.05812 m^{2}s^{-2} and ε = 125.2 m^2 s^{-3}

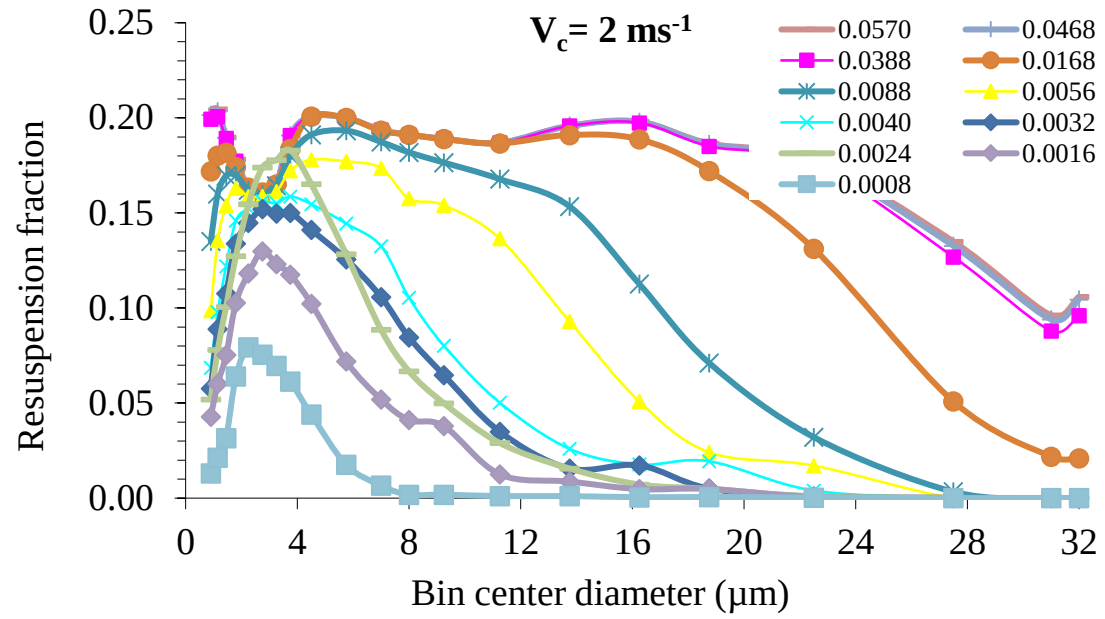

Figure 100: Time evolution of particle Resuspension Fraction vs. Bin center diameters for Ceiling velocity of 2 ms^{-1}, when k = 0.2134 m^{2}s^{-2} and ε = 387.3 m^2 s^{-3}

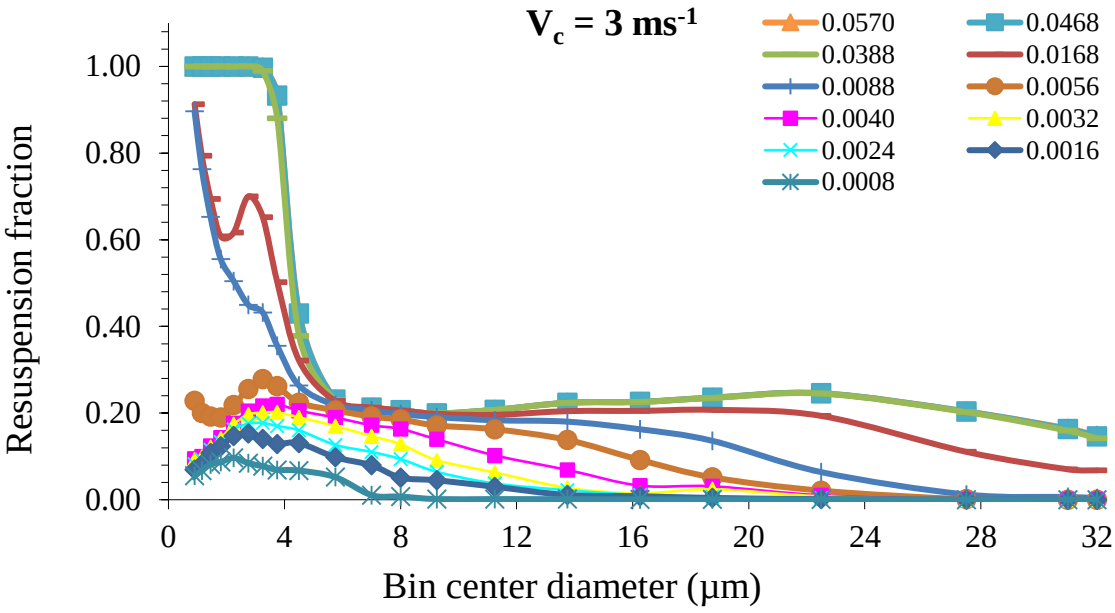

Figure 101: Time evolution of particle Resuspension Fraction vs. Bin center diameters for Ceiling velocity of 3 ms^{-1}, when k = 0.4510 m^{2}s^{-2} and ε = 722.7 m^2 s^{-3}

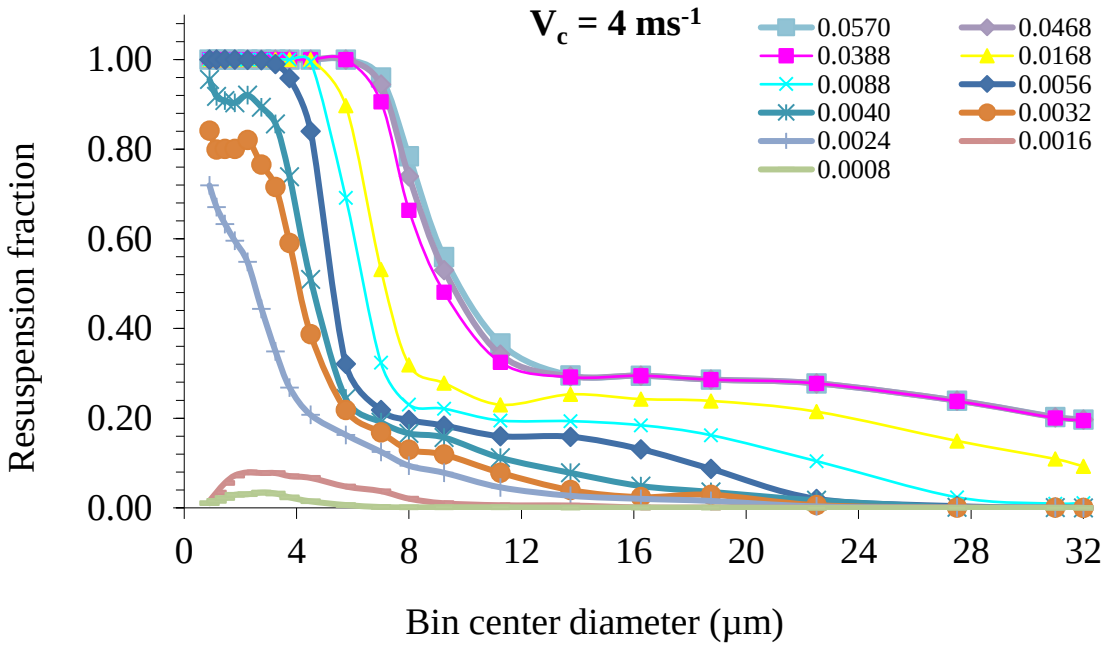

Figure 102: Time evolution of particle Resuspension Fraction vs. Bin center diameters for Ceiling velocity of 4 ms^{-1}, when k = 0.7623 m^{2}s^{-2} and ε = 1104 m^2 s^{-3}

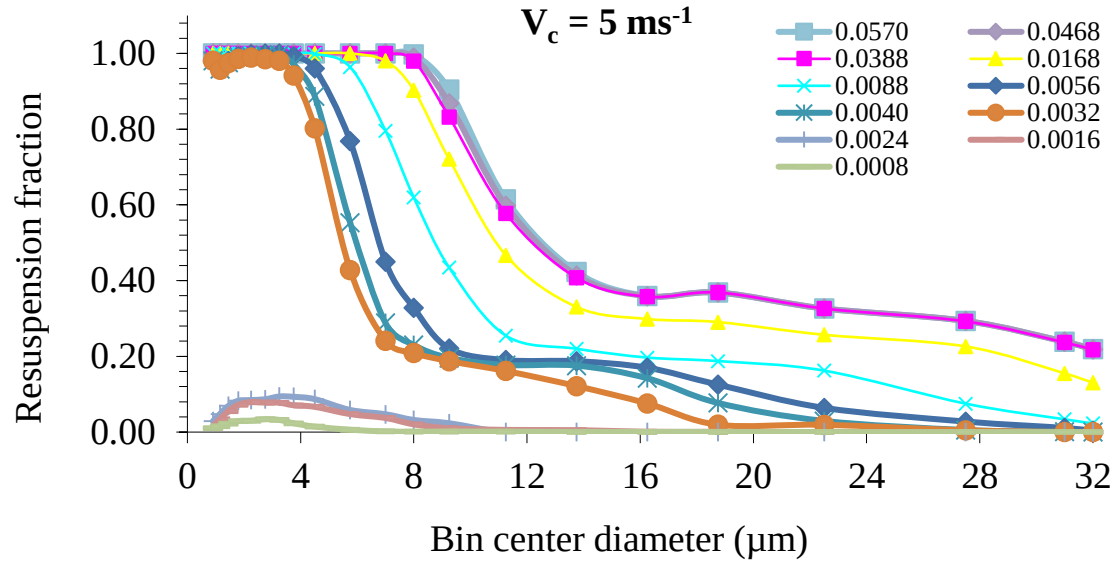

Figure 103: Time evolution of particle Resuspension Fraction vs. Bin center diameters for Ceiling velocity of 5 ms^{-1}, when k = 1.141 m^{2}s^{-2} and ε = 1516 m^2 s^{-3}

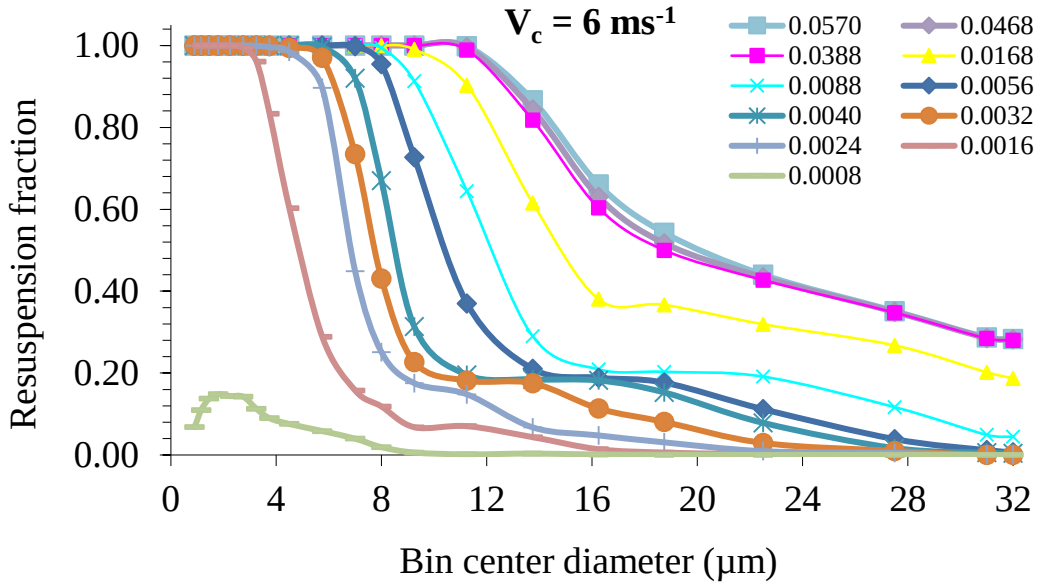

Figure 104: Time evolution of particle Resuspension Fraction vs. Bin center diameters for Ceiling velocity of 6 ms^{-1}, when k = 1.582 m^{2}s^{-2} and ε = 1949 m^2 s^{-3}

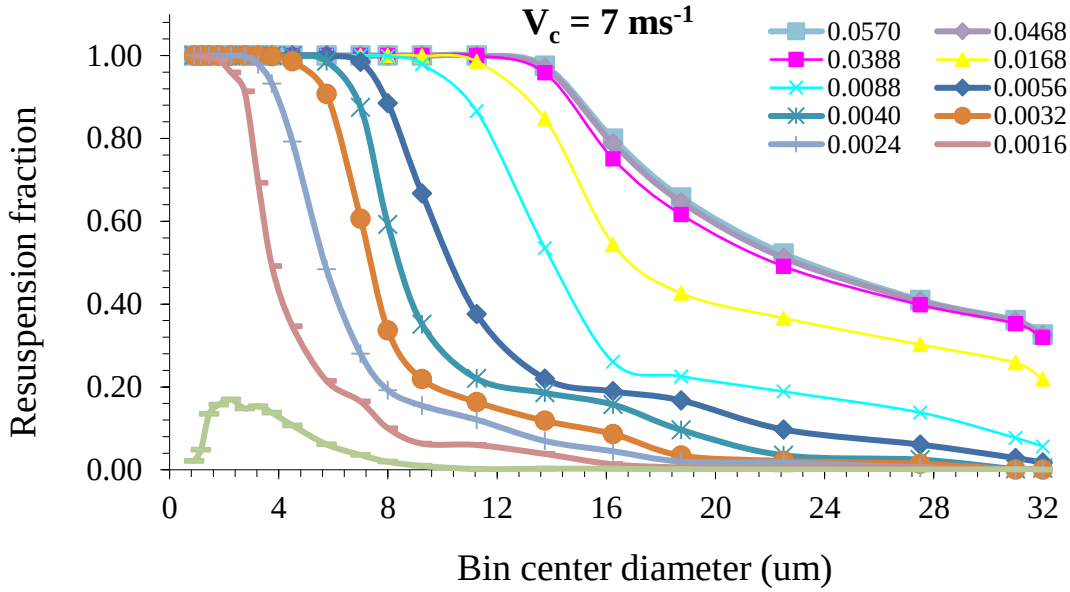

Figure 105: Time evolution of particle Resuspension Fraction vs. Bin center diameters for Ceiling velocity of 7 ms^{-1}, when k = 2.081 m^{2}s^{-2} and ε = 2397 m^2 s^{-3}

For all Ceiling velocities, the resuspension fraction increases as time progresses. As per the resuspension fraction results shown in Figure 98 to Figure 105, there are four stages to the resuspension process for all particle sizes under respective Ceiling streamwise velocities. During the first stage, the resuspension fraction grows slowly; during the second stage, the resuspension fraction grows fast; during the third stage, the resuspension fraction grows slowly; and during the final stage (fourth stage) the growth of the resuspension fraction is almost zero following a series of S-shape curves similar to what is shown in Figure 106.

5.4.1 Analysing Resuspension fraction for 10µm particles

Figure 106 shows the comparison of resuspension fractions. $(number/number)$ aginst time $(seconds)$ for different Ceiling velocities for 10 µm bin center diameter particles.

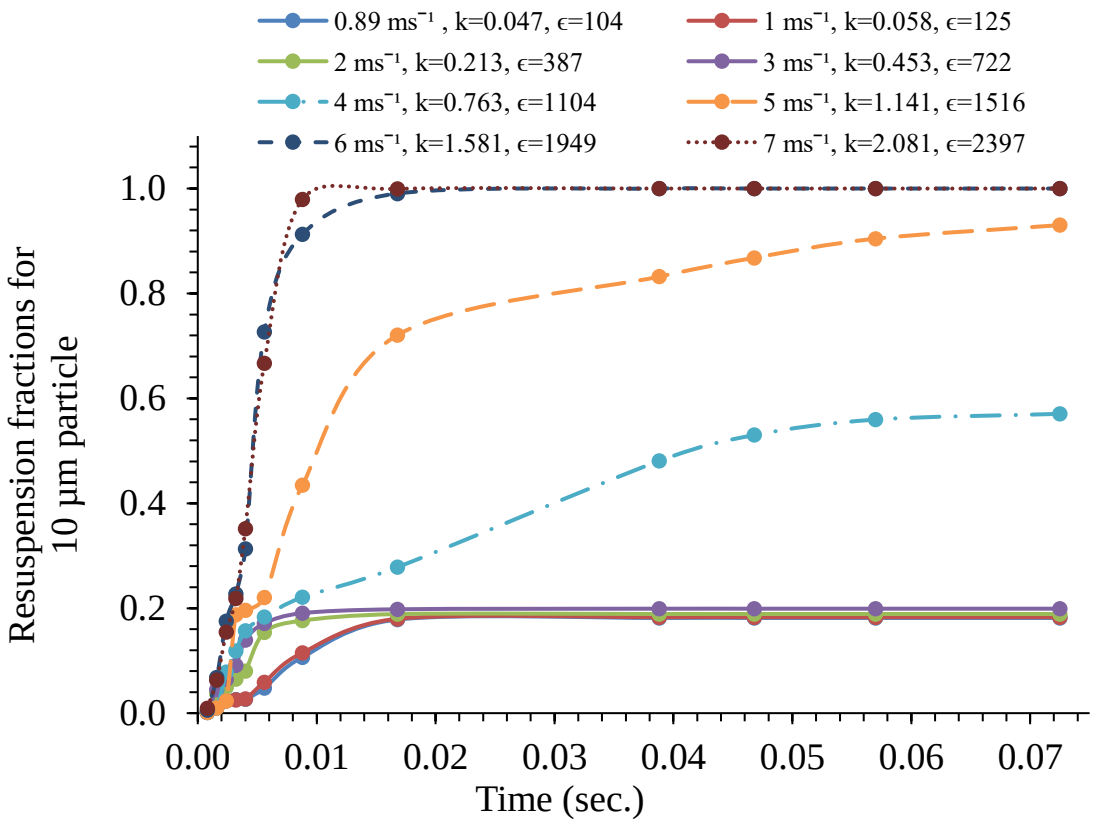

Figure 106 Time history graph of resuspension fraction for 10 um particles at different ceiling boundary velocities

As per Figure 106, for most Ceiling velocity conditions except for 4 and 5 ms -1, the resuspension fractions achieve their fourth stage of resuspension (zero growth) at 3.88E-2 sec.

The standard equation of the S-curve used in this analysis is given in Equation (108).

$$\boldsymbol{RF = A\left(1 - e^{-kt^n}\right)} \qquad \textbf{\textit{(108)}}$$

here, A, k and n are fitting constants as given in Table 19, RF is the resuspension fraction, and t is the time measured in seconds.

Table 19: Fitting constants and coefficient of determination (R^2) for the series of S-curves solved for velocities 0.89 to 7 ms $^{-1}$ for particle size 10 μm particle resuspension fractions.

Ceiling velocity V_C (ms $^{-1}$)	**Friction velocity u_τ (ms $^{-1}$)**	***A***	***k***	***t***	**R^2**
0.89	3.352E-01	1.837E-01	2.660E+05	2.661E+00	9.992E-01
1.00	3.538E-01	1.845E-01	9.402E+03	1.942E+00	9.998E-01
2.00	4.998E-01	1.844E-01	3.334E+05	2.362E+00	9.989E-01
3.00	6.115E-01	1.936E-01	4.530E+05	2.323E+00	9.994E-01
4.00	7.055E-01	6.168E-01	2.101E+01	8.266E-01	9.924E-01
5.00	7.881E-01	3.037E+00	6.043E+02	1.698E+00	9.651E-01
6.00	8.626E-01	9.821E-01	5.912E+05	2.536E+00	9.868E-01
7.00	9.310E-01	1.005E+00	4.530E+05	2.499E+00	9.978E-01

As per Equation (108), for the Ceiling velocity of 4 ms^{-1}, the maximum resuspension fraction of 0.6485 was achieved at around 0.4 seconds, and for the Ceiling velocity of 5 ms $^{-1}$ the maximum resuspension fraction of 0.8848 was achieved at around 0.09 seconds.

Figure 107 shows how the forecasted resuspension fractions found from CFD using Equation (108) fit into the work done by Reeks and Hall (2001) with 10 µm alumina spheres on a polished stainless-steel flat plate in a fully developed turbulent channel flow. The fraction remaining on the surface is given by 1-RF. The CFD fractions remaining after 1 second for respective friction velocities are shown in red boxes overlayed on the original figure generated by Reeks and Hall (2001).

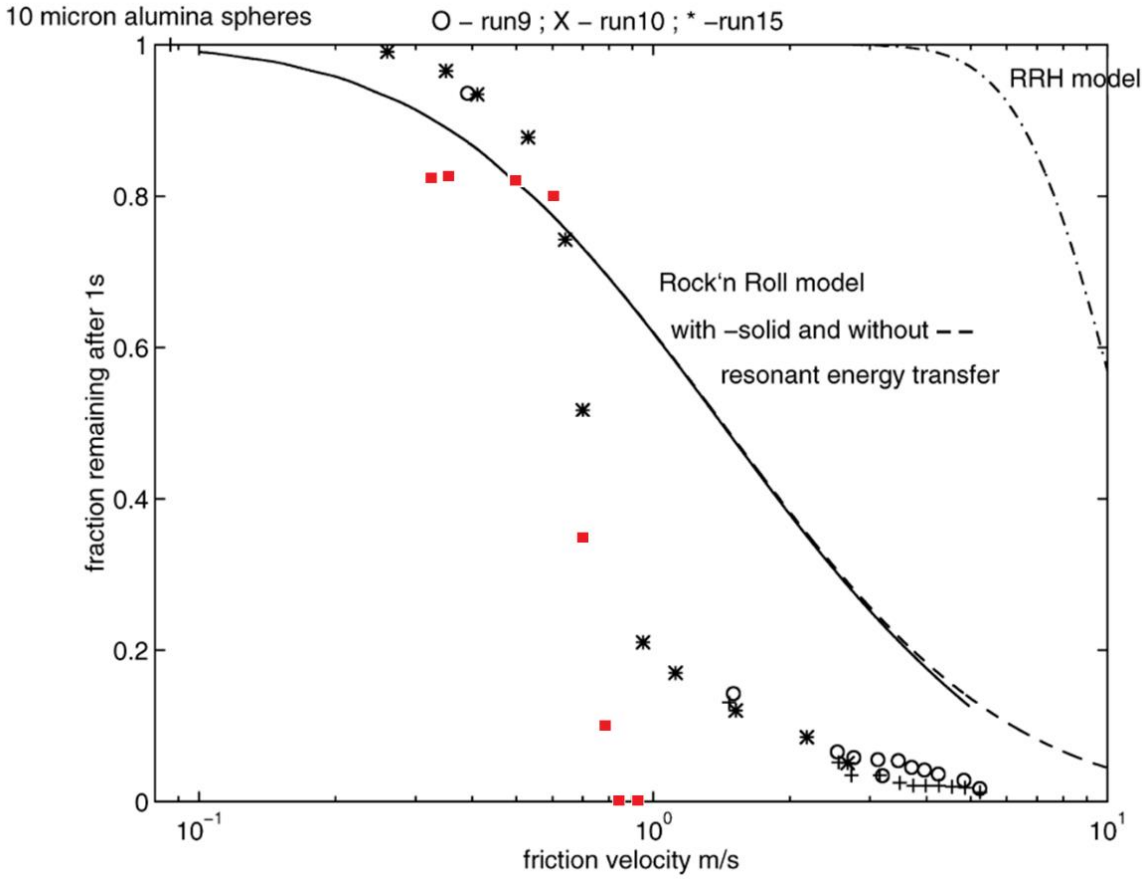

Figure 107: Comparison of CFD resuspension fractions with the published data by Reeks and Hall (2001) as presented in Henry and Minier (2014) for 10 µm particles.

As per Figure 107, the remaining fractions for 10 μm particles match the experimental work Reeks and Hall (2001) conducted for the Ceiling velocities of 2, 3 and 4 ms^{-1}. The resuspension fractions found for the rest of the velocities used in CFD work are less than the results found by Reeks and Hall (2001).

6 CONCLUSIONS

While extensive literature exists within the scientific community for modelling the resuspension of radioactive particles from aged deposits, there is a noticeable scarcity of publicly accessible scholarly works addressing the simulation of resuspension processes for freshly deposited radioactive material arising from a Dirty Bomb event. Therefore, as a part of this thesis, detailed experimental procedures and CFD methods were developed to simulate freshly fallen radioactive particle resuspension using radioactive $^{140}La_2O_3$ powder as a surrogate. The main discoveries found as a part of the thesis are summarized below:

1. A detailed experimental procedure to perform a resuspension experiment of radioactive particles resulting from a Dirty Bomb event
2. A practical way to measure particle resuspension factor using average bib-by-bin resuspension factor after a Dirty Bomb Event.
3. Calculation of Deposition Fraction (DFR) of radioactive particles that were resuspended after a Dirty Bomb Event.
4. Use of Global and Regional CFD models to simulate particle resuspension

6.1 A detailed experimental procedure to simulate an RDD event and calculation of resuspension factors

Radioactive $^{140}La_2O_3$ power was generated by activating nonradioactive $^{139}La_2O_3$ powder using a high flux thermal neutron field.

Radioactive particles were dispersed inside a sealed chamber using a high-energy pressurized pneumatic dispersion system to simulate an RDD event. Dispersed radioactive particles were collected onto sample plates under gravitational settling without external winds.

Beta radiation distribution on the contaminated sampling plates was mapped using a beta radiation detector array before and after the resuspension experiment located outside the contamination chamber.

The contaminated plates were carefully brought into the custom-built 10 m long suction-type wind chamber capable of producing winds up to $6.7 \times (1 \pm 7.5\%)$ m s^{-1} at the test section, using three fans located at the end of the wind chamber. The penetrating gamma radiation from ^{140}La was measured using gamma radiation detectors located under the wind chamber, and particle size distribution of resuspended particles was measured using particle counters. Isokinetic ports of the particle counters were located inside the wind chamber at 52 and 165 cm downstream of the contamination plates. The port closer to the wind chamber was placed at the same level as the contamination plate, mainly to

capture rolling and sliding particles, while the second Particle Sizer port was located 15 cm above ground to capture the airborne resuspended particles. MCNP software was used to calculate the geometric efficiency of the gamma detector.

The mass of La_2O_3 powder on the contamination plates before the resuspension experiment was calculated using the decay-corrected activity of ^{140}La on the contaminated plate with the known mass-to-activity ratio of dispersed particles used in the simulated RDD. The particle size distribution on the contamination plates was determined by subtracting the measured particle size distribution of the RDD powder from the particles that required more time to settle onto the plates due to gravitational forces. To identify the range of particles that did not settle on the plates during this period, a simulation of the gravitational settling process was conducted using CFD.

Finally, the bin-by-bin resuspension factors were calculated by dividing the number of particles within each bin, as recorded by the particle counters for 1 cubic meter of air, with the number of particles within the corresponding bin on a 1 square meter area of the contaminated plates.

The average bin-by-bin resuspension factors (K) for particle sizes between 0.9 μm to 7 μm at Grimm Particle Sizer 1 and 2 locations, 52.5 cm and 165 cm downstream from the initial fallout, were calculated to be 4.12E-05 × (1 ± 46.9%) m^{-1} and 4.56E-05 × (1 ± 79.5%) m^{-1} respectively.

The resuspension factor values determined in the experiment align closely with the enhanced, modified Anspaugh et al. model, which demonstrates a remarkable capacity to

forecast resuspension data accurately down to 0.01 days. As Maxwell and Anspaugh (2011) documented, these modified Anspaugh correlations were formulated by fitting curves to resuspension data gathered from three continents.

6.1.1 Future work to improve the experimental procedure to calculate the particle resuspension factor immediately after an RDD event

During the simulated RDD event, the contaminated plates collected inside the contamination chamber showed a nonhomogeneous distribution of La_2O_3 particles. In future work, sample plates can be slowly rotated without disturbing the particle deposition to achieve homogeneous particle distribution to improve the repeatability of the experiment.

The particle size distribution of the La_2O_3 powder was measured using Grimm Particle Sizer and Malvern Spraytech systems in an offsite facility. The measurements were conducted under the same environmental conditions as the experiments at the WIS facility (RH% and Temperature). However, the energies imparted onto La_2O_3 powder during active and inactive experiments were not measured and compared, resulting in more or less agglomerated particles in one method over the other. In future work, an isokinetic Grimm Particle Sizer should be placed inside the contamination chamber to measure the in-situ

particle size distribution to ensure the correct particle size distribution will be used when calculating the total mass of contaminated particles deposited onto the plates instead of using CFD methods to find the particle size distribution.

As discussed in the literature review section, the initial particle resuspension process occurs close to the ground wall surfaces, mainly due to vortices' burst and sweep effect in the coherent flow structure. However, the resuspension experiment did not quantify the near-wall coherent flow structure. In future work, Particle Image Velocimetry (PIV) and High-Speed Imaging techniques can be used to characterize the initial particle resuspension process and compare the results against the Regional CFD results.

During the resuspension experiments, the wind chamber's velocity measurements at the Grimm Particle Sizer locations were measured using hotwire anemometers, but the flow patterns close to the wind chamber wall surfaces and contaminated plates were never characterized. For future work, small pitot tubes with a micrometre lifting scale can be used to characterize the turbulent boundary layer of the floor at the test section to help compare the CFD velocity values with experimental velocity results.

6.2 A practical way to measure particle resuspension factor: using bin-by-bin resuspension factor

Particle resuspension is often expressed as resuspension factor, resuspension rate and equivalent soil concentration (Nicholson K. W., 1988). As discussed in the literature review chapter of the thesis, resuspension immediately after an RDD event is a complex process, and an accurate method of measuring its magnitude has not yet been fully developed. The bin-by-bin resuspension factor approach used in the thesis is a practical method to provide information about the particle size distribution of resuspended particles available at the human breathing level to calculate the particle deposition fractions into separate compartments of the human respiratory tract. The bin-by-bin resuspension factor distributions found using experimental and CFD methods at Grimm Particle Sizer locations have similar trends. The experimental bin-by-bin resuspension factors correspond to maximum respiratory track deposition particle size for Head Airway, Tracheobronchial and Alveolar regions were found to be 2.8867E-2 × (1 ± 18.3%) m^{-1} at particle size 6.5 µm, 8.5962E-4 × (1 ± 23.9%) m^{-1} at particle size 3 µm and 9.6017E-4 × (1 ± 21.6%) m^{-1} at particle size 1 µm, respectively.

6.3 Lung Deposition fraction (DFR)of radioactive particles after an RDD event

In the event of an RDD incident, there is a possibility that radioactive materials could contaminate food sources within the affected area. This can happen if the RDD disperses radioactive materials into the environment, including farmland or food distribution channels. Consuming contaminated food is a significant concern because it can lead to the ingestion of radioactive particles, which may emit harmful radiation as they decay. (Cheng, Kamboj, & Wallo, 2009).

In an RDD incident, radioactive particles can settle on various surfaces, including the skin of individuals. If these particles are inadvertently ingested, they can enter the body and lead to internal radiation exposure. This mechanism is concerning as it involves direct contact with contaminated surfaces and may result from inadequate personal decontamination measures or hand-to-mouth contact.

Groundshine refers to radiation exposure from radioactive materials on the ground's surface emitting radiation. This is an external dose and occurs when individuals are near contaminated areas without any radioactive materials entering their bodies (US Homeland Security, 2017).

The importance of the two internal exposure mechanisms (eating contaminated food and inadvertent ingestion of skin contamination) depends on the specific

circumstances of the RDD incident. They are both significant concerns and must be assessed alongside the external dose from groundshine to comprehensively understand the radiation exposure risks in an urban environment. The relative importance of these pathways can vary and should be evaluated on a case-by-case basis, considering factors such as the type of RDD, the quantity and type of radioactive materials involved, and the effectiveness of response and mitigation efforts. Public health and safety measures must address all potential exposure routes to minimize the risks associated with internal and external radiation doses.

According to the U.S. Department of Energy preliminary report (Cheng, Kamboj, & Wallo, 2009), direct exposure to a radioactive plume after an RDD event and inhalation of plume material happens at the early phase of exposure (the first four days following the incident). Contamination of skin and clothes happens from the early phase to the late phase (beyond 1 year), groundshine from deposited material and inhalation of resuspended material happens between halfway of the Early phase to half way of the Late phase. The ingestion of contaminated water and food happens from the Intermediate phase (fourth day to 1 year) to halfway of Late phase (Cheng, Kamboj, & Wallo, 2009)

The radiation dose due to the inhalation of micron-size radioactive particles is already well understood. However, the number of radioactive particles that are resuspended and become available for inhalation by a human, with respect to particle diameter, is not well established. The human respiratory system is divided into three main regions: head airways, tracheobronchial and alveolar, based on its structure, airflow patterns, functions, particle retention time and sensitivity to deposited particles (Hinds, 1999).

The deposition fraction of radioactive particles that were resuspended (DFR) due to an RDD event was calculated by multiplying the bin-by-bin resuspension factor values (Ki) by the respective curve fit of ICRP deposition fraction (DP) data given by Hinds (1999).

The DFR against particle size curves for the Head Airway (HA) region, Alveolar (AL) region and Tracheobronchial (TB) regions have similar trends as bin-by-bin particle resuspension curves. DFR values generally decrease as particle size increases from 0.9 to 7 μm for particle sizes, except at particle size 1.15 μm.

The average values of DFR for particle sizes between 0.9 to 3.75 μm for HA, TB and AL regions were 2.84E-05 × (1 ± 19.75%) m^{-1}, 2.54E-06 × (1 ± 28.2%) m^{-1} and 6.88E-06 × (1 ± 64.2%) m^{-1}, respectively. From 3.75 to 7μm, DFR reduces following third-order polynomial: DFR = -9E-08Φ3 + 5E-06 Φ 2 - 5E-05 Φ + 0.0002 (R^2 = 1) for HA region, DFR = -6E-08 Φ 3 + 1E-06 Φ 2 - 8E-06 Φ + 2E-05 (R^2 = 1) for TB region and DFR = -1E-07 Φ 3 + 2E-06 Φ 2 - 1E-05 Φ + 3E-05 (R^2 = 1) for AL region.

Estimating the internal dose to humans near a Radiological Dispersal Device (RDD) event is extremely valuable to calculating the hazard of a given radiological device to public members. Furthermore, in future work, internal dose due to inhalation of radioactive particles resuspended from a unit surface area on the ground immediately after an RDD event can be calculated by multiplying DFR by respective dose conversion factors.

Figure 108 shows the estimated Committed Effective Inhalation Dose (CEID) for adult males and females without respirators and first responders wearing self-contained

breathing apparatus (SCBA) with the assigned protection factor (APF) of 10000 (US NRC, 2021) who are within 450 m from ground zero due to a full-scale dirty bomb explosion similar to the one used at Suffield, by DRDC (Erhardt, et al., 2016). This prototypical impact assessment was performed utilizing the experimental resuspension factor at the Grimm particle sizer 2 location and the average ground contamination estimated from the Suffield dirty bomb experiment conducted by DRDC (Erhardt, et al., 2016). During these initial assessments, it was assumed that initial particle resuspension factors were similar for both experiments conducted at Suffield, Canada and the WIS facility at Munster, Germany.

The committed effective inhalation dose (50 yrs.) was calculated using the Equation (111).

$$\boldsymbol{CEID = GC \times RF \times BR \times \frac{1}{APF} \times T \times DCF} \qquad \textit{(109)}$$

here, CEID is the committed effective inhalation radiation dose (Sv), GC is the ground concentration (Bqm^{-2}), RF is the resuspension factor (m^{-1}), BR is breathing rate (m^3hr^{-1}), APF is the assigned protection factor for respirators (this value is 1 for the public and 10000 for the first responders), T is the duration of exposure (hr), and DCF is dose conversion factor ($SvBq^{-1}$).

The local ground concentration of ^{140}La was determined based on Figure 3 (Erhardt, et al., 2016). To account for increased breathing rates resulting from panic during an RDD

event, an average moderate breathing rate of 1.5 m^3hr^{-1} was employed (Bates D. V., 1966) (ICRP, 1975). The experimentally calculated average resuspension factor of 4.56E-5 m^{-1} corresponding to Grimm particle sizer 2 location was used. The Inhalation Dose Conversion Factors (DCF) for 5 µm activity median aerodynamic diameter (AMAD) was used since Dv(50) found for La_2O_3 powder was close to 3 µm. The corresponding DCF for males and females are 1.5E-9 and 1E-9 $SvBq^{-1}$, respectively (ICRP, 1975).

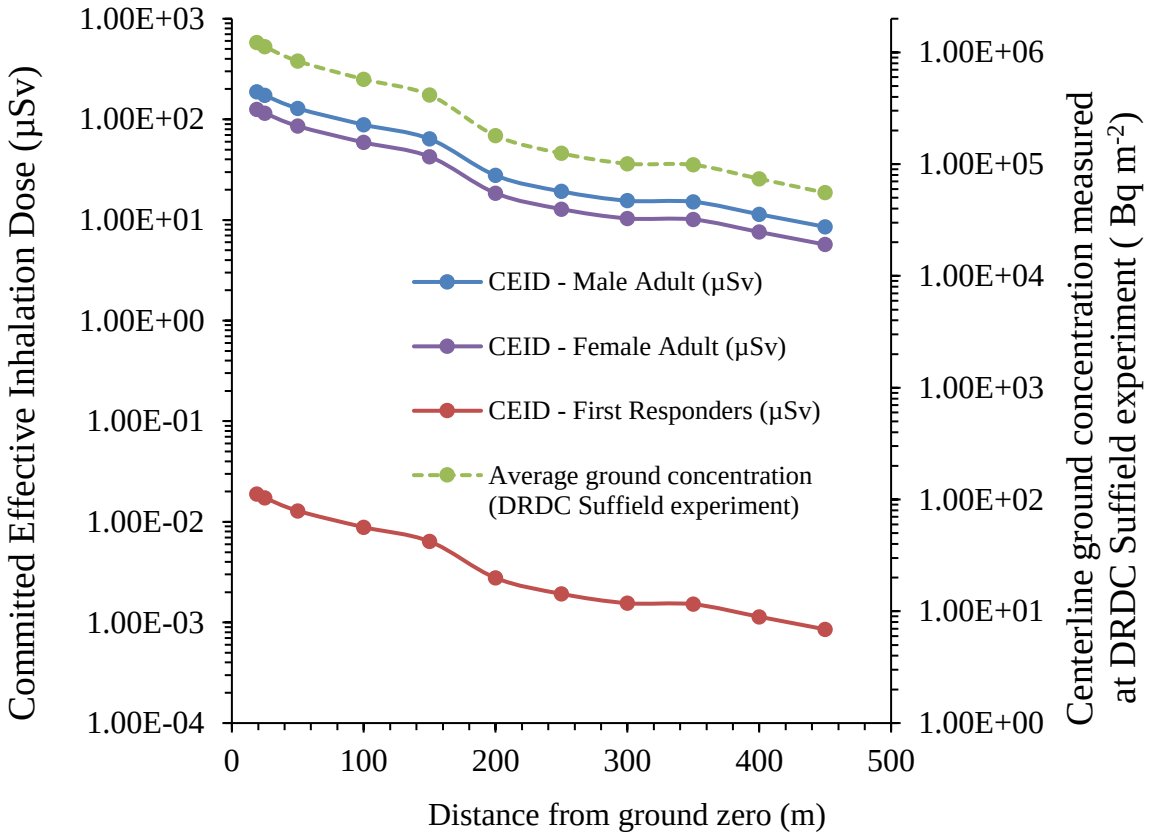

Figure 108: Committed Effective Inhalation Dose(CEID) assessment to the first responders and to the members of the public living close to Ground Zero of a dirty bomb used at Suffield (Erhardt, et al., 2016)

Graphs in Figure 108 have similar trends since Committed Effective Inhalation Radiation Dose (CEID) graphs were generated by multiplying the average centerline ground concentration graph, generated using experimental data collected at the DRDC Suffield experiment, by corresponding multiplication factors outlined in Equation (111). The graphs illustrate a reduction in CEID with increasing distance from ground zero following exponential curves specific to each individual, as shown below:

Male adults: $CEID = 178.68e^{-0.007X}$ ($R^2 = 0.9584$),

Female adults: $CEID = 119.128e^{-0.007X}$ ($R^2 = 0.9584$),

First responders: $CEID = 1.7E-28e^{-0.007X}$ ($R^2 = 0.9584$),

here, X is the distance from ground zero measured in meters. The average activity of the dirty bomb used by DRDC at the Suffield experiment was 35.2 × (1 ± 10%) GBq. As per Erhardt, Lebel, et al. (2016), 3% of the radioactive material used in Suffield experiments was deposited close to GZ, and 15-30% was deposited within a 450 m radius from GZ.

6.4 Use of Global and Regional CFD models to simulate particle resuspension

Computational Fluid Dynamics (CFD) is a powerful simulation tool. It was used in the thesis to obtain numerical approximations to the solutions of the governing fluid flow equations that will represent the flow inside the wind chamber used to conduct radioactive particle resuspension experiments, including the coherent flow structure close to the floor surfaces where initial resuspension would occur. The CFD process is usually conducted in three steps: mesh generation, solving appropriate governing equations, and post-processing results. The mesh generation was performed using Gambit software, and solving governing equations and post-processing of results were performed using the FLUENT double-precision solver.

Initial resuspension of microscopic particles occurs next to the wall surfaces of the floor. Therefore, a smooth mesh of the wind chamber that would include geometric features of the surface roughness elements of contaminated plates would have close to 2.25 billion mesh elements. Using current computer technology, it is impossible for the analyst to solve a CFD problem with a mesh of that magnitude within a reasonable time frame to provide resuspension factor information to incident commanders attending the RDD event.

The CFD modelling process used in the thesis was broken down into two steps. In step 1, a Global CFD model was used to calculate the boundary conditions required to model the Regional CFD model. In step 2, a Regional CFD model was generated using

boundary conditions found from the Global CFD model to simulate the flow patterns close to the surface roughness elements to model initial particle resuspension.

The 10 m long Global CFD model was initially generated in 2D to find the appropriate turbulence model that can predict the Regional CFD model's boundary conditions. The Global 2D CFD model had close to 428,213 mesh nodes and y+ less than 1, especially in the regions where initial particle resuspension would occur. A pressure-based, unsteady, implicit segregated, double-precision solver was used to find the 2D computational domain solutions. The comparison of velocity results close to the wind chamber floor (< 200 μm wall-normal distance) against the Spalding law of the wall velocity profile and the comparison of mean flow 2D CFD results against experimental results across the wind chamber showed that k-ω SST turbulence model was superior against other turbulence models available in FLUENT software at the time of initial analysis.

Later, both Global and Regional CFD models were generated in 3D. The grid-independent 3D mesh of the Global CFD model had 16,289,581 mesh nodes and y+ less than 2.5, especially in the regions where initial particle resuspension would take place. A pressure-based, unsteady, implicit segregated double precision solver was used to find the solutions to the 3D computational domain. At the beginning of the CFD simulation, the k-ω SST turbulence model was introduced to find the turbulence properties of the 3D computational domain. Later, the turbulence model was switched to Large Eddy Simulation (LES) to characterize the turbulent eddies. Large eddies were resolved directly

in the LES model, while smaller eddies - smaller than mesh sizes- were modelled using the Smagorinsky-Lilly sub-grid-scale model. The converged Global CFD model simulated velocity of v_x = 8.932E-1 × (1 ± 47.4%) m s^{-1} at the edge of the Regional CFD models (100 μm above the floor of the wind chamber) with a gradient of -5.306 Pa m^{-1}.

The Regional domain was 414 μm long, 106 μm tall and 100 μm wide and located just above the center of the contaminated plate. A grid-independent structured mesh was generated using GAMBIT software, and it had 379,900 hexahedral structured mesh elements. Using the boundary velocity values found from the Global CFD model, the boundary condition for the Ceiling of the Regional CFD model was established using the Spectral Synthesizer fluctuating algorithm available in FLUENT to simulate the coherent structure of eddies close to the viscous sublayer region.

The overall resuspension factor was calculated by multiplying the resuspension fraction from the Regional 3D computational domain by the Global CFD transfer factors from the Global 3D computational domain.

The CFD resuspension factors for Particle Sizer 1 and 2 exhibit similar trends and can be categorized into three distinct regions. In region 1 (particle sizes from 0.9 to 6.75 μm), the average CFD resuspension factor is 4.14E-04 × (1 ± 13.3%) m^{-1} for Particle Sizer 1 and 4.01E-04 × (1 ± 16.3%) m^{-1} for Particle Sizer 2. For region 2 (particle sizes from 6.75 to 13.75 μm), the average CFD resuspension factor decreases with fitted curves: $RF_{CFD} = 0.0342 \exp(-0.83\emptyset)$ $(R^2 = 0.9911)$ for Particle Sizer 1 and $RF_{CFD} = 0.3236 \exp(-1.181\emptyset)$ $(R^2 = 0.9912)$ for Particle Sizer 2. In region 3 (particle sizes from

13.75 to 32 μm), the average CFD resuspension factors follow quadratic equations: RFCFD = 9E-09Φ3 - 7E-07 Φ 2 + 2E-05 Φ - 0.0001 (R^2 = 0.8709) for Particle Sizer 1 and RFCFD = 3E-10 Φ 3 - 2E-08 Φ 2 + 6E-07 Φ - 4E-06 (R^2 = 0.7811) for Particle Sizer 2.

The average bin-by-bin resuspension factor found using CFD is a magnitude higher compared to the experimental results. The disparities between CFD and experimental resuspension factor values underscore the complex nature of modelling particle resuspension. While CFD simulations provide insights into the dynamic behaviour of aerosol particles, actual experimental conditions introduce a myriad of variables that theoretical models may not fully capture.

Moreover, it's important to note a critical distinction between the CFD simulations and real experiments conducted at the WIS facility. In the CFD simulations, a mono-layer dispersion is assumed, simplifying the model by considering a single layer of particles. However, in actual experiments at the WIS facility, the presence of multiple layers introduces complexities, especially in scenarios involving particle breakage due to clusters. This divergence in the experimental setup highlights a potential source of variation between CFD predictions and empirical observations, emphasizing the need for continued refinement of computational models to better account for the intricate dynamics encountered in multifaceted real-world environments.

Additionally, it's crucial to consider the inherent variability in experimental resuspension factor values. As documented by Garger, Hoffman, and Thiessen (1997), experimental values of resuspension factors can exhibit significant variations, often

spanning 2 to 3 orders of magnitude. This inherent variability underscores the challenges in precisely measuring and replicating resuspension phenomena under diverse experimental conditions. In light of this, the robustness of the CFD method employed in this thesis becomes evident, particularly in successfully modelling resuspension factors between particle sizes of 0.9 and 6.75 μm. The consistency and reliability demonstrated within this size range showcase the potential efficacy of the CFD approach in capturing and predicting resuspension dynamics within controlled parameters.

Furthermore, it's noteworthy to consider the impact of utilizing a relatively small micron-size domain in modelling initial particle resuspension through CFD. The choice of domain size introduces a level of abstraction, and in some instances, it may contribute to an overestimation of resuspension factors compared to larger-scale CFD simulations. The confined domain might amplify the interactions between particles and surfaces, potentially resulting in higher resuspension factors than those observed in broader, more representative scenarios.

In future work, one can incorporate surface roughness elements in both downstream and transverse directions to the Regional CFD model floor to capture the saltation of particles in both downstream and transverse directions, increasing the particle resuspension factor for bigger particles during the CFD modelling.

BIBLIOGRAPHY

Bernardini, M., Pirozzoli,, S., & Orlandi, P. (2013). The effect of large-scale turbulent structures on particle dispersion in wall-bounded flows. *International Journal of Multiphase Flow, 51*, 55-64.

Ahmed, M. M., & Ahmed, S. S. (2008). A comparison study to determine the mean of particle size distribution for truthful characterization of environmental data (Part 1). *Journal of Engineering Sciences*, 147-166.

Ali, F., & Waller, E. (2014). Design of a Hybrid Computational Fluid Dynamics–Monte Carlo Radiation Transport Methodology for Radioactive Particulate Resuspension Studies. *Journal of Health Physics*, 311-317.

Allen, J. R. (1985). *Principle of physical sedimentology*. London: George Allen and Union.

American Society of Heating Refrigerating and Air-Conditioning Engineers. (1997). *ASHRAE handbook, fundamentals.* ATLANT: ASHRAE.

Anspaugh, L. R., Shinn, J. H., Phelps, P., & Kennedy, N. C. (1975). Resuspension and Redistribution of Plutonium in Soils. *Health Physics, 29*(4), 571-582.

Anspaugh, L. R., Simon, S. L., Gordeev, K. L., Likhtarev, I. A., Maxwell, R. M., & Shinkarev, S. M. (2002). Movement of radionuclides in terrestrial ecosystems by physical process. *Health Physics*, 669-679.

Anspaugh, L., Kennedy, N., Phelps, P., & Shinn, J. (1975). Resuspension and redistribution of plutonium in soils. *Journal of Health Physics, 29*, 571-582.

ASME. (2008, July 22). Procedure for Estimation and Reporting of Uncertainty Due to Discretization in CFD Applications. *J. Fluids Eng*, *130*(7), 4 pages. Retrieved 2 15, 2022, from https://doi.org/10.1115/1.2960953

Assaad, A. D., Ghali, K., Ghaddar, N., & Habchi, C. (2020). Coupled CFD and particle resuspension models under combined effect of mechanical and aerodynamic disturbances. *Building and Environment, 169*. Retrieved 12 23, 2022

Bates D. V., F. B. (1966). Task Group on Lung Dynamics: Deposition and Retention Models for Internal Dosimetry of the Human Respiratory Tract. *Health Phys*(12), 173-207.

Bellecci, C., Gaudio, P., Lupelli, I., Malizia, A., Porfiri, M., Quaranta, R., & Richetta, M. (2011, June 6). STARDUST experimental campaign and numerical simulations: influence of obstacles and temperature on dust resuspension in a vacuum vessel under LOVA. *Nuclear Fusion, 51*. doi:10.1088/0029-5515/51/5/053017

Biasi, L., De Los Reyes, A., Reeks, M. W., & De Santi, G. F. (2001). Use of a simple model for the interpretation of experimental data on particle resuspension in turbulent flows. *Journal of Aerosol Science, 32*(10), 1175-1200.

Biswas, G., & V, E. (2002). *Turbulent Flows.* (P. Kumar, R. Prasad, & V. Gupta, Eds.) New Delhi, India: Mehra, N. K., Narosa Publishing House.

Blocken, B., van Druenen, T., Toparlar, Y., Malizia, F., Mannion, P., Andrianne, T., . . . Diepens, J. (2018). Aerodynamic drag in cycling peloton: New insights by CFD simulation and wind tunnel testing. *Journal of Wind Engineering and Industrial Aerodynamics*, 319-337. Retrieved from https://www.sciencedirect.com/science/article/pii/S0167610518303751

Bottcher, J. (2003, May 13-15). SVG 2 radiation and contamination measuring system. *Technical sales training RM&P*.

Bouris, D., & Bergeles, G. (1998). 2D LES of vortex shedding from a square cylinder. *Journal of Wind Engineering and Industrial Aerodynamics, 80*, 31-36.

Braaten, D., Paw U.K.T., P., & Shaw, R. (1990). Particle resuspension in a turbulent boundary layer – Observed and modelled. *Journal of Aerosol Science, 21*(5), 613-628.

Brambilla, S., Speckart, S., & Brown, M. J. (2017). Adhesion and aerodynamic forces for the resuspension of non-spherical particles in outdoor environments. *Journal of Aerosol Science, 112*, 52-67. Retrieved 12 2022, 16, from https://www.sciencedirect.com/science/article/pii/S0021850217300502

Brezani, I. (2011, 12 21). Rosin-Rammler Diagram plot function. Retrieved from https://www.mathworks.com/matlabcentral/profile/authors/2241235-ivan-brezani

Cantwell, B. J. (1981). Organized motion in turbulent flow. *Ann. Rev. Fluid Mechanics,* 457-515.

Castelo, A. d., Capitao, J. A., & De Santi, G. (1999). *International standard problem No. 40 - Final comparison report (EUR 18708 EN).* European Commission joint research center.

Cengel, Y. A., & Cimbala, J. M. (2006). *Fluid Mechanics Fundamentals and Applications.* McGraw-Hill.

Cheng, C. Y., Kamboj, S., & Wallo, A. (2009). *Preliminary Report on Operational Guidelines Developed for Use in Emergency Preparedness and Response to a Radiological Dispersal Device Incident.* Environmental Science Division, Argonne National Laboratory and U.S. Department of Energy, Office of Health, Safety and Security. U.S. Department of Energy.

Christensen, K. T., & Adrian, R. J. (2001). Statistical evidence of hairpin vortex packets in wall turbulence. *J Fluid Mech*(431), 433-443.

Ciparisse, J., Malizia, A., Poggi, L., Cenciarelli, O., Gelfusa, M., Carestia, M., . . . Gaudio, P. (2016). Numerical Simulations as Tool to Predict Chemical and Radiological Hazardous Diffusion in Case of Nonconventional Events. *Modelling and Simulation in Engineering*. Retrieved from https://dl.acm.org/doi/abs/10.1155/2016/6271853

Cleaver, J., & Yates, B. (1973). Mechanism of detachment of colloidal particles from a flat substrate in a turbulent flow. *Journal of colloid and interface science, 44*(3), 464-474.

Comte-Bellot, S., & Corrsin, S. (1971). Simple Eulerian time correlation of full- and narrow-band velocity signals in grid-generated, “isotropic” turbulence. *Journal of Fluid Mechanics, 48*(2), 273-337.

Corn, M. (1966). *Aerosol Science*, 359-392.

Crasto, G. (2007). Numerical Simulations of the Atmospheric Boundary Layer. 195. Febbraio, Cagliari.

DeGraw, J., Cimbala, J., & Freihaut, J. (2006). CFD Modeling of Particle Resuspension. *American Physical Society*. Tampa. Retrieved from http://meetings.aps.org/link/BAPS.2006.DFD.OA.5

Dennis, D. (1987). Coherent structures in wall-bounded turbulence. *Anais da Academia Brasileira de Ciencias*. doi:10.1590/0001-3765201520140622

Designing and Implementing a Radiobioassay Program. (2008, June). Retrieved 05 21, 2018, from Canadian Nuclear Safety Commission: http://nuclearsafety.gc.ca/pubs_catalogue/uploads/RD-150_draft2_e.pdf

Dilara, P., Karasenbrink, A., & Hummel, R. (1998). *STORM test SR11-ISP40 Quick look report (Technical Note JRC-Ispra).* Italy.

Do Rio, M. P., Amaral, E. C., & Paretzke, H. G. (1994). The resuspension and redeposition of 137 Cs in an urban area: The experience after the Goiania accident. *Journal of aerosol science, 25*(5), 821-831.

Erhardt, L., Lebel, L., Korpach, E., Berg, R., Inrig, E., Watson, I., . . . Quayle, D. (2016). Deposition measurements from the full-scale radiological dispersal device field trials. *Health Physics Journal, 110*(5), 442-457.

Erhardt, L., Quayle, D., & Noel, S. (2013). *Full-Scale RDD Experiments and Models.* Ottawa: Defence R&D Canada. Retrieved 7 26, 2022

Evgenii, K., Garger, F., Hoffman, O., & Thiessen, K. (1997). Uncertainty of the long-term resuspension factor. *Journal of Atmospheric Environment, 31*(11), 1647-1656.

Fluent Inc. (2006). *Fluent 6.3 documentation.* Retrieved 2010, from http://my.fit.edu/itresources/manuals/fluent6.3/help/

Friess, H., & Yadigaroglu, G. (2000). A Generic model for the resuspension of multilayer aerosol deposits by turbulent flow. *Journal of Nuclear Science Engineering, 138*, 161-176.

Friess, H., & Yadigaroglu, G. (2002). Modelling of the resuspension of particle clusters from multilayer aerosol deposits with variable porosity. *Journal of Aerosol Science, 33*, 883-906.

Fromentine, A. (1989). *Particle resuspension from a multilayer deposit by turbulent flow.* Swiss federal institute of technology, Zurich.

Garcia-Olivares, A., & Iranzo, C. (1997). Resuspension and transport of plutonium in the Palomares area. *Journal of Atmospheric Environment, 37*(1), 101-114.

Garger , E., Gordeev , S., Holländer , W., & Kashpur, V. (1996). Resuspension and deposition of radionuclides under various conditions. Retrieved 11 29, 2022, from https://inis.iaea.org/collection/NCLCollectionStore/_Public/31/056/31056833.pdf

Garger, E. K., Hoffman, F. O., Thiessen, K. M., Galeriu, D., Kryshev, A. I., Lev, T., . . . Watkins, B. (1999). Test of existing mathematical models for atmospheric resuspension of radionuclides. *Journal of Environmental Radioactivity, 42*, 157-175.

Garger, E. K., Hoffman, O. F., & Thiessen, M. K. (1997, March). Uncertainty of the long-term resuspension factor. *Journal of Atmospheric Environment, 31*(11), 1647-1656.

Garger, E., Hoffman, F., Thiessen, K., Galeriu, D., Kryshev, A., Lev, T., . . . Watkins, B. (1999). Test of existing mathematical models for atmospheric resuspension of radionuclides. *Journal of Environmental Radioactivity, 42*, 157-175.

Garland, J. (1979). *Resuspension of particulate matter from grass and soil (AERE-R 9452).*

Garland, J. A. (1982). *Resuspension of particulate material from grass. Experimental programme 1979-1980.* HMSO, AERE-R10106, London, United Kingdom.

Garland, J. A., & Pomeroy, J. R. (1994). Resuspension of fall-out material following the Chernobyl accident. *Journal of Aerosol Science, 25*(5), 793-806.

Gaudio, P., Malizia, A., & Lupelli, I. (2010). Experimental and numerical analysis of dust resuspension for supporting chemical and radiological risk assessment in a nuclear fusion device. *International Conference on Mathematical Models for Engineering Science, 30*, pp. 2010-30. Puerto De La Cruz, Tenerife.

Gavrilov, V., Klepikova, N., Troyanova, N., & Rodean, H. (1995, October). Stationary model for resuspension of radionuclides and assessments of 137Cs concentration in the near-surface layer for the contaminated areas in the Bryansk Region of Russia and Belarus. *Atmospheric Environment, 29*(19), 2633-2650.

Gelain, T., Rondeau, A., Peillon, S., Sabroux, J. C., & Gensdarmes, F. (2015). CFD modelling of the wall friction velocity field in the ITER tokamak resulting from airflow during a loss vacuum accident - Consequences for particle resuspension. *Fusion Engineering and Design*, 87-99. Retrieved from https://www.sciencedirect.com/science/article/pii/S0920379615002720

Georgiadis, N. J., & Yoder, D. A. (2006, January). Evaluation of Modified Two-Equation Turbulence Models for Jet Flow Predictions. *AIAA 2006-490.* Reno, Nevada.

Germano, M., Piomelli, U., Moin, P., & Cabot, w. (1991). A dynamic subgrid-scale eddy viscosity model. *Journal of Phys. Fluids, 3*, 1760-1765.

Gillette, D., Robert, Lawson, J., & Thompson, R. (2004a). Comparison of aerodynamic and mechanical resuspension mechanisms for particles deposited on field rye grass. *Journal of Atmospheric Environment, 38*, 4789-4797.

Goldasteh, I., Yilin, T., Goodarz, A., & Andrea, R. F. (2014, Jul 01). Human induced flow field and resultant particle resuspension and transport during gait cycle. *Journal of Building and Environment, 77*, 101-109. Retrieved 12 19, 2022, from https://www.sciencedirect.com/science/article/pii/S0360132314000766

Gomes, C., Freihaut, J., & Bahnfleth, W. (2007). Resuspension of allergen-containing particles under mechanical and aerodynamic disturbances from human walking. *Atmospheric Environment, 41*(25), 5257-5270. Retrieved 12 23, 2022, from https://www.sciencedirect.com/science/article/pii/S1352231007002804?via%3Dihub

Goren, S. (1970). The normal force exerted by creeping flow on a small sphere touching a plane. *Journal of Fluid Mechanics, 43*(3), 619-625. doi:10.1017/S0022112070000782

Government of Canada. (2017, 03 07). *Beaufort wind scale table*. Retrieved 11 24, 2022, from https://www.canada.ca/en/environment-climate-change/services/general-marine-weather-information/understanding-forecasts/beaufort-wind-scale-table.html#shr-pg0

Grass, A. J. (1971). Structure features of turbulent flow over smooth and rough boundaries. *Journal of Fluid Mechanics, 50*, 233-255.

Green, A. R., Erhardt, L., Lebel, L., Duke, M. J., Jones, T., White, D., & Quayle, D. (2016). Overview of the full-scale radiological dispersal device field trials. *Health Physics Journal, 110*(5), 403-417.

Green, R. M., & Finn, R. J. (1964). *Photopeak efficiencies of NaI(Tl) crystals.* Australian Atomic Energy Commission. Sutherland: North-Holland Publishing Co.

Grimm Aerosol Technik GbH & Co. KG. (2010, 03 14). *How the 1100 Aerosol Spectrometer Series works*. Retrieved 01 02, 2012, from Grimm Aerosol Canada Inc: http://www.dustmonitor.com/General/principles.htm#1100s

Guingo, M., & Minier, J. P. (2008). A new model for the simulation of particle resuspension by turbulent flows based on stochastic description of wall roughness and adhesion forces. *Journal of Aerosol Science, 39*(11), 957-973.

Haider, A., & Levenspiel, O. (1989). Drag Coefficient and Terminal Velocity of Spherical. *Powder Technology, 58*, 63-70.

Hall, D. (1988). Measurements of the mean force on a particle near a boundary in turbulent flow. *Journal of Fluid Mechanics, 187*, 451-456.

Hatano, Y., & Hatano, N. (2003). Formula for the resuspension factor and estimation of the date of surface contamination. *Journal of Atmospheric Environment, 37*(25), 3475-3480.

Henry, C., & Minier, J.-P. (2014). A stochastic approach for the simulation of particle resuspension from rough substrates: Model and numerical implementation. *Journal of Aerosol Science, 77*, 168-192. Retrieved 12 17, 2022, from https://www.sciencedirect.com/science/article/pii/S002185021400130X

Henry, C., & Minier, J.-P. (2014, 12 1). Progress in particle resuspension from rough surfaces by turbulent flows. *Progress in Energy and Combustion Science, 45*, 1-53. Retrieved from https://www.sciencedirect.com/science/article/pii/S0360128514000483

Hill , J. D. (2007). *Resuspension Programme: Experimental Trails held at WIS Munster, 19th -23rd March 2007, NATO UNCLASSIFIED.* RADIAC Project Office, Harwell, Didcot, Oxfordshire, UK. doi:RPO(RT)/T002/07/P2

Hill, J. (2007, 01 09). Development of a New Resuspension Descriptor. *GBR presentation to RNDSG*. Harwell: Radiac Project Office.

Hinds, W. C. (1999). *Aerosol technology.* California, Los Angeles, USA: John Wiley & Sons, Inc.

Hinze, J. O. (1975). *Turbulence* (2nd ed.). McGraw Hill, Inc.

Horst, T. (1976a). *The estimation of air concentrations due to the suspension of surface contamination by the wind (BNWL-2047).* Pacific Northwest Laboratory, Washington.

Horst, T. (1976b). *Resuspension from a generalized area source (BNWL-200-Part 3).* Pacific Northwest Laboratory, Washington.

Ibrahim, A. H. (2004). *Microparticle detachment from surfaces by fluid flow2004.* Ph.D. thesis, Nortre Dame, IN. Retrieved from http://etd.nd.edu/ETD-db/theses/available/etd-01302004-105607/unrestricted/IbrahimAE012004.pdf

Ibrahim, A., Dunn, P., & Qazi, M. F. (2008). Experiments and validation of a model for microparticle detachment from a surface by turbulent airflow. *Journal of Aerosol Science, 30*, 645-656.

ICRP. (1975). *Report of the Task Group on Reference Man.* Oxford, UK: Pergamon Press.

ICRP. (1994). Human Respiratory Tract Model for Radiological Protection. ICRP Publication 66. *Ann. ICRP 24*, 1-3.

ICRP-72. (1996). *Age Dependent Doses to Members of the Public from Intake of Radionuclides: Part 5, Compilation of Ingestion and Inhalation Dose Coefficients.* Elmsford, NY.: Pergamon Press.

Industries, Bubble Technology. (n.d.). *Bubbletech*. Retrieved May 22, 2018, from Mobile Microspec: http://bubbletech.ca/product/mobile-microspec-2

Innovatest Europe BV. (2021). *Manual TR200.* Retrieved 12 12, 2021, from TR200 - Surface roughness tester:

https://www.salutron.de/fileadmin/redakteure/dokumente/InnovaTest/Manual_TR-200.pdf

International Atomic Energy Agency. (1992). *Modelling of resuspension, seasonality and losses during food processing.* Vienna, Austria: International Atomic Energy Agency.

Ishizuka, M., Mikami, M., Tanaka, T., Igarashi, Y., Kita, K., Yamada, Y., . . . Ninomiya, K. (2017). Use of a size-resolved 1-D resuspension scheme to evaluate resuspended radioactive material associated with mineral dust particles from the ground surface. *Journal of environmental radioactivity, 166*, 436-448.

Kaiser, J. (2019, March 11). Retrieved from http://www.southampton.ac.uk: http://www.southampton.ac.uk/~nwb/lectures/GoodPracticeCFD/Articles/BPG_ANSYS_Simulation_vs_Reality_July2005_08Kaiser.pdf

Kalitzin , G., Medic, G., Laccarino, G., & Durbin, P. (2005). Near-wall behaviour of RANS turbulence models and implications for wall functions. *Journal of Computational Physics*, 265–291. Retrieved from https://citeseerx.ist.psu.edu/document?repid=rep1&type=pdf&doi=db25831db947f9a8b3f714b9aa012fb2ee0a0194

Kaneyasu, N. O. (2017). Weak size dependence of resuspended radiocesium adsorbed on soil particles collected after the Fukushima nuclear accident. *Journal of environmental radioactivity, 172*, 122-129.

Kasagoi, N., & Nishino, K. (1986). Experiments in Fluids. *4*, 309-318.

Kellett, M. A.; Bersillon, O.; Mills, R. W. (2009). *The JEFF-3.1/-3.1.1 Radioactive decay data and fission yields sub-libraries.* Nuclear Energy Agency.

Kim, H. K. (1971). The production of turbulence near a smooth wall in a turbulent. *Journal of Fluid Mechanics, 50*, 133-160.

Kim, Y., Gidwani, A., Wyslouzil, B., & Sohn, C. (2010). Source term models for fine particle resuspension from indoor surfaces. *Building and Environment, 45*(8), 1854-1865. Retrieved 12 17, 2022

Kita, K. I. (2020). Rain-induced bioecological resuspension of radiocaesium in a polluted forest in Japan. *Scientific reports, 10*(1), 1-5.

Kline, S. J., Reynolds, W. C., Schraub, F. A., & Runstadler. (1967). The structure of turbulent boundary layers. *Journal of Fluid Mechanics, 30*, 741-773.

Kok, J. F., Parteli, E. J., Michaels, T. I., & Karam, D. B. (2012). The physics of wind-blown sand and dust. *Reports on Progress in Physics, 75*(10). doi:10.1088/0034-4885/75/10/106901

Kottapali, K., Murali, H., Song, G., Fillingham, P., & Novosselov, I. (2023). Resuspension of trace explosive particle residues by planar impinging jet: Effects of exposure

duration and wall shear stress. *Journal of Aerosol Science, 17*. doi:https://doi.org/10.1016/j.jaerosci.2022.106095

Kottapalli, K., Murali, H., Song, G., Fllingham, P., & Novosselov, I. (2023). Resuspension of trace explosive particle residues by planar impinging jet: Effects of exposure duration and wall shear stress. *Journal of Aerosol Science, 167*. doi:https://doi.org/10.1016/j.jaerosci.2022.106095

Kraichnan, R. (1970). Diffusion by a Random Velocity Field. *Physics of Fluids, 11*, 21-31.

Kryshev, I. I., Alexakhin, R. M., & Makhonko, K. P. (1992). *Radioecological consequences of the Chernobyl accident.* Moscow, Russia: Nuclear Society International.

L. Pieuchot, J. M.-F. (2018). Curvotaxis directs cell migration through cell-scale curvature landscapes. *Nature Communications, 9*(1), 3995. doi:10.1038/s41467-018-06494-6

Laufer, J. (1975). New trends in experimental turbulence research. *Ann. Rev. Fluid Mechanics*, 307-326.

Lebel, L., Brousseau, P., Erhardt, L., & William, A. (2011). Entrainment of powders and soils into explosive fireballs. *International Journal of Energetic Materials and Chemical Propulsion., 10*, 351-364. Retrieved from https://www.researchgate.net/publication/270472212_Entrainment_of_powders_and_soils_into_explosive_fireballs

Lengweiler, P. (2000). *Modelling Deposition and Resuspension of Particles on and from.* Ph.D. thesis, Swiss Federal Institute of Technology, Zürich, Switzerland. Retrieved 12 8, 2022, from https://apps.dtic.mil/sti/pdfs/ADA478675.pdf

Levi, M. A., & Kelly, H. C. (2002, Nov). Weapons of mass disruption. *Sci. Am., 287*(5), 76-81. doi:10.1038/sciencetificamerica1102-76

Linsley, G. (1978). *Resuspension of the transuranium elements: A review of existing data.* National Radiological Protection Board, Harwell, United Kingdom.

Linsley, G. S. (1978). *Resuspension of transuranium elements: A review of existing data (NRPB-R75IRN 11095635).* National Radiological Protection Board.

Loosmore, G., & HUNT, J. (2000). Dust resuspension without saltation. *Journal of Geophysical Research, 105*(20), 663-20671.

LTS Research Laboratories, Inc. (2015, 10 07). *Safety Data Sheet Lanthanum Oxide*. Retrieved 1 6, 2023, from https://www.ltschem.com/msds/La2O3.pdf

Makhonko, K. P. (1992). Resuspension of the radioactive dust from the underlying surface. *72*, 523-531.

Makhon'ko, K. P. (1992). Wind uplift of radioactive dust from the ground. *Atomic Energy, 72*(5), 465-472.

Malvern Spraytec. (2013). *Malvern Spraytec product brochure*. Retrieved May 16, 2013, from Spraytec: www.malvern.com

Maxwell, R., & Anspaugh, L. R. (2011). An improved model for prediction of resuspension. *Journal of Health Physics*, 722-730.

Mitsakou, C., Helmis, C., & Housiadas, C. (2005). Eulerian modelling of lung deposition with sectional representation of aerosol dynamics. *Journal of Aerosol Science, 36*, 75-94.

Moris, S., & Alexander, A. J. (1772). An investigation of particle trajectories in two phase flow systems. *Journal of Fluid Mechanics, 55*(2), 193-208.

Murakami, A., & Mochida, A. (1995). On turbulent vortex shedding flow past a square cylinder predicted by CFD. *Journal of Wind Engineering and Industrial Aerodynamics, 54*, 191-211.

Muralidhar, K., & Biswas, G. (1999). *Advanced Engineering Fluid Mechanics*. New Delhi, India: Narosa Publishing House.

Nicholson, K. (1993). Wind tunnel experiments on the resuspension of particulate material. *Atmospheric Environment, 27*(A), 181-188.

Nicholson, K. W. (1988). A review of particle resuspension. *Journal of Atmospheric Environment, 22*(No. 12), 2639-2651.

Nicholson, K. W., & Branson, J. R. (1990). Factors affecting resuspension by road traffic. *The Science of the Total Environment, 93*, 349-358. Retrieved 11 25, 2022

O'Neill, M. E. (1868). A sphere in contact with a plane wall in a slow linear shear flow. *Chemical Engineering Science, 23*(11), 1293-1298. Retrieved from //doi.org/10.1016/0009-2509(68)89039-6

Oosthuizen, P. C. (1997). *Compressible fluid flow* (Vol. Vol. 179). New York: McGraw-Hill.

Peillon, S., Gélain, T., Payet, M., Gensdarmes, F., Grisolia, C., & Pluchery, O. (2022, September). Adhesion forces of radioactive particles measured by the Aerodynamic Method–Validation with Atomic Force Microscopy and comparison with adhesion models. *Journal of Aerosol Science, 165*. doi:20

Peng, W., Zhang, T., & Yanan Zhen, Y. S. (2014). Graphite dust resuspension in an HTR-10 steam generator. *Particuology, 17*, 149-157. Retrieved 12 23, 2022, from https://www.sciencedirect.com/science/article/pii/S1674200114000261?via%3Dihub

Perera, S. W. (2015, February 9). Experimental Modeling of Wind-Driven Bin-by-Bin Resuspension Factors of Freshly Fallen Radionuclides After an Energetic Release From a Radiological Dispersal Device. *ASME J of Nuclear Rad, 1*(1). Retrieved from https://doi.org/10.1115/1.4026390

Qian, J., & Andrea, R. F. (2008). Resuspension of Dust Particles in a. *Aerosol Science and Technology,* 566-578. doi:10.1080/02786820802220274

Rambousky, R. (2008). *Resuspension of radiological aerosols - Design and testing of a system allowing sensitive time dependent measurement of aerosol removal.* Technical Note, Defence R&D Canada - Ottawa, Ottawa, Canada. doi:DRDC Ottawa TN 2008-110

Reeks, M. W., & Hall, D. (2001). Kinetic models for particle resuspension in turbulent flows: theory and measurement. *Journal of Aerosol Science, 32*(1), 1-31.

Reeks, M., Reed, J., & Hall, D. (1988). On the resuspension of small particles by a turbulent flow. *Journal of Physics D: Applied Physics, 21*(4), 574-589.

Reshetin. (2005). Estimation of radioactive levels associated with a 90Sr dirty bomb event. *Journal of Atmospheric Environment, 39*(25), 4471-4477.

Roache, P. J. (1993, June 23-24). A Method for Uniform Reporting of Grid Refinement Studies,. *Proceedings of Quantification of Uncertainty in Computation Fluid Dynamics, Edited by Celik, et al., ASME Fluids Engineering Division Spring Meeting, Washington,, 158*.

Rodi, W. (1993). On the simulation of turbulent flow past bluff bodies. *Journal of Wind Engineering and Industrial Aerodynamics, 46*, 3-19.

Rosner, G., & Winkler, R. (2001). Long-term variation (1986-1998) of post-Chernobyl 90Sr, 137Cs, 238Pu and 240Pu concentration in air, depositions to ground, resuspension factors and resuspension rates in South Germany. *Journal of Science of the Total Environment, 273*, 11-25.

Rumsey, Chris. (2011, June 10). *Menter Shear Stress Transport Model*. Retrieved October 19, 2011, from NASA: http://turbmodels.larc.nasa.gov/sst.html

Saffman, P. G. (1965). The lift on a small sphere in a slow shear flow. *Fluid Mech., 22*, 385-340.

Sapounas, A. A., Campen, J. B., Wildschut, J., & Bot, G. P. (2010). Energy saving during bulb storage applying modelling with computational fluid dynamics. *XVIIth World Congress of the International Commission of Agricultural Engineering (CIGR)*, (pp. 1-10). Quebec.

Schershakov, V. (1997). *Development of a computer model for calculation of radioactive materials into the atmosphere after an accident (UCRL CR-129075).* Lawrence Livermore National Laboratory.

Schlichting, H., Gersten, K., Schlichting, H., Krause, E., Oertel Jr., H., Schlichting, H., . . . Schlichting, H. T. (1996). *Boundary-Layer Theory.* Berlin: Springer.

Sehmel, G. (1977a). *Transuranic and tracer simulant resuspension.* Pacific Northwest Laboratory, Washington.

Sehmel, G. (1977b). *Radioactive particle resuspension research experiments on the Handford reservation.* Pacific Northwest Laboratories, Washington.

Sehmel, G. (1980). Particle resuspension: A review. *Journal of Environment International, 4*(2), 107-127.

Sehmel, G. (1984). *Transuranic resuspension (PPNL-SA-11792).* Pacific Northwest Laboratory, Washington.

Sehmel, G. (1986). *Resuspension research with tracers at PNL.* Annual Report for 1985, Pacific Northwest Laboratory, Richland, Washington.

Shams, M., Ahmadi, G., & Smith, D. H. (2002). Computational modeling of flow and sediment transport and deposition in meandering rivers. *Advances in Water Resources, 25*, 689-699.

Shinn, J. (2003). *Studies of plutonium aerosol resuspension at the time of Maralinga cleanup (UCRL-ID-155063).* Lawrence Livermore National Laboratory.

Shinn, J., Homan, D., & Hofmann, C. (1986). *A summary of plutonium aerosol studies: Resuspension at Nevada test site (UCRL 90746).* Lawrence Livermore National Laboratory.

Shultis, J. K., & Faw, R. E. (2011). *An MCNP Primer.* Manhattan: Kansas State University. Retrieved from https://www.mne.k-state.edu/~jks/MCNPprmr.pdf

Smirnov, A., Shi, S., & Celik, I. (2001). Random flow generation technique for large eddy simulations and particle-dynamics modeling. *Journal of Fluids Engineering, Transactions of the ASME, 123*(2), 359-371. doi:10.1115/1.1369598

Smirnov, R., Shi, S., & Celik, I. (2001). Random flow generation technique for Large Eddy Simulations and Particle-Dynamics Modelling. *Journal of Fluids Engineering, 123*, 359-371.

Soldati, A., & Marchioli, C. (2009). Physics and modelling of turbulent particle deposition and entrainment: Review of a systematic study. *International Jounal of Multiphase Flow, 35*(9), 827-839. Retrieved 12 11, 2002, from https://www.sciencedirect.com/science/article/pii/S0301932209000329

Stempniewicz, M. M. (2009). *SPECTRA Sophisticated Plant Evaluation Code for Thermal–Hydraulic Response Assessment.* NRG report, Arnhem.

Stempniewicz, M. M., & Komen, E. J. (2010). Comparison of several resuspension models against measured date. *Nuclear Engineering and Design, 240*, 1657-1670.

Stewart, K. (1967). The suspension of particulate material from surfaces. In B. Fish (Ed.). Gatlinburg,Tennessee: Pergamon press.

Stosch, H. (2016). *Neutron Activation Analysis of the Rare Earth Elements (REE) - With Emphasis on Geological Materials.* doi:10.1515/psr-2016-0062

Tang, P., Kita, K., Igarashi, Y., Satou, Y., Hatanaka, K., Adachi, K., . . . Shinohara, A. (2022). Atmospheric resuspension of insoluble radioactive cesium-bearing particles found in the difficult-to-return area in Fukushima. Progres. *Progress in Earth and Planetary Science, 9*(1), 1-15.

Thermo Fisher Scientific. (n.d.). SVG 2 Radiacmeter. Retrieved 30 2022, 12, from https://www.dozimetrs.lv/sites/default/files/attaches/thermo_svg-2.pdf

Till, J., & Meyer, H. (1983). *Radiological assessment. A textbook on environmental dose analysis.* TN, USA: Oak Ridge National Lab.

Troen, I., & Petersen, L. E. (1989). *European Wind Atlas.* Roskilde: RISO National Laboratory.

US Homeland Security. (2017, November). *Radiological Dispersal Device (RDD) Response Guidance, Planning for the first 100 Minutes.* Retrieved 8 8, 2022, from https://www.dhs.gov/sites/default/files/publications/NUSTL_RDD-ResponsePlanningGuidance-Public_171215-508.pdf

US NRC. (2021, March). *Appendix A to Part 20 - Assigned Protection Factors for Respirators*. Retrieved November 27, 2023, from https://www.nrc.gov/reading-rm/doc-collections/cfr/part020/part020-appa.html#footnote_i

Van Hout, R. (2013). Spatially and temporally resolved measurements of bead resuspension and saltation in a turbulent water channel flow. *Journal of Fluid Mechanics, 715*, 389-423.

Versteeg, H. K., & Malalasekera, W. (2007). *An Introduction to Computational Fluid Dynamics* (second ed.). Essex, England: Pearson Education Limited.

Vesilind, P. A. (1980). The Rosin-Rammler particle size distribution. *Resource Recovery and Conservation, 5*(3), 275-277. Retrieved 12 27, 2022, from https://www.sciencedirect.com/science/article/pii/0304396780900074

Wagenpfeil, F., Paretzke, H., Peres, J., & Tschiersch, J. (1999). Resuspension of coarse particles in the region of Chernobyl. *Journal of Atmospheric Environment*(33), 3313-3323.

Waller, E. (2003). *Technical Aspects of Radiological Terrorism.* SAIC Canada. Defence R&D Canada.

Waller, E. (2007). *Analysis of the 152mEu2O3 Resuspension Experiments Conducted at the WIS Decontamination Facility in Munster, Germany.* The University of Ontario Institute of Technology, Oshawa, Ontario, Canada. doi:UOIT-ARRL-01-07

Waller, E. J., & Perera, S. (2010). Radionuclide Resuspension Considerations for RDD Fallou. *Health Physics Society.* Salt Lake City, UT.

Walsh, C. (2002). *Calculation of resuspension doses for emergency responses (NRPB-W1).* National Radiological Protection Board, Didcot.

Wang, H. C. (1990). Effects of inceptive motion on particle detachment from Surfaces., (pp. 386-393). Retrieved 12 2022, 16

Warner, T. T. (2010). *Numerical Weather and Climate Prediction.* Cambridge Univeristy Press.

Wellings, J., Bedwell, P., Hywood, S. M., & Charnock, T. W. (2019). *Estimation of radiation doses from inhalation of resuspended materials in emergency situations.* Oxfordshire: Public Health England.

Wen, H., & Kasper, G. (1989). On the Kinetics of particles reentrainment from surfaces. *Journal of Aerosol Science, 20*(4), 483-498.

Whicker, J. J. (2021). Radionuclide resuspension across ecosystems and environmental disturbances. *ournal of Environmental Radioactivity , 223*. doi:106586

Yu, C., Cheng, J. J., Kamboj, S., Domotor, S., & Wallo, A. (2009). *Preliminary report on operational guidelines developed for yse in emergency preparedness and response to a Radiological Dispersal Device Incident.* TN: U.S. Department of Energy, Office of Health, Safety and Security. Retrieved 11 25, 2022, from https://resrad.evs.anl.gov/docs/ogt_manual_doe_hs_0001_2_24_2009c.pdf

Zarin, N. (1970). *Measurement of non-continuum and turbulence effects on subsonic sphere drag (NASA contractor report).* NASA contractor report, Washington, D.C., USA.

Zhu, Y., Zhao, B., & Tan, Z. (2012). A Particle Resuspension Model in Ventilation Ducts. *Journal of Aerosol Science and Technology, 46*, 222-235.

Zimon, A. D. (1982). *Adhesion of Dust and Powder. 2d ed., rev. and en.* (T. b. Johnston, Trans.) Translated by Robert K. Johnston: Consultants Bureau.

Ziskind, G., & Gutfinger, C. (2002). Shear and gravity effects on particle motion in turbulent boundary layers. *Journal of Powder Technology*, *125*(2), 140-148. doi:10.1016/S0032-5910(01)00500-9

Ziskind, G., Fichman, M., & Gutfinger, C. (1995). Resuspension of particulates from surfaces to turbulent flows - Review and analysis. *Journal of Aerosol Science, 26*(4), 613-644.

7 APPENDIX A

7.1 List of parameters used in particle resuspension studies

Table 20: Summary of past resuspension studies with radioactive particle resuspension

Year	**Study**	**Date of Release & Measurement**	**Land Area and Description**	***K* (m-1)**	**Resuspension Mechanism and Isotopic Composition**	**Size**
	Stewart	-	Clear, level, sandy soil. 9 m^2, nominal level 1.2 mc/m^2	$1.8x10^{-7}$ $1x10^{-7}$	Similar to Health Physics surveillance. ^{91}Y, aqueous solution of chloride	d < 8µm d < 18µm
1967	Stewart	-	Clear, level, sandy soil. 1 m^2, nominal level 24.6 mc/m^2	$2x10^{-11}$ $3x10^{-11}$	Similar to Health Physics surveillance. ^{91}Y, aqueous solution of chloride	d < 8µm d < 18µm
1967	Stewart	-	Clear, level, sandy soil. 9 m^2 and nominal level 8.8 mc/m^2	$1x10^{-8}$ $5x10^{-10}$	Similar to Health Physics surveillance. ^{91}Y, aqueous solution of chloride	d < 8µm d < 18µm
1967	Stewart	-	The previous site, surface disrupted, charged debris not removed. 20 m radius, average level 0.6 mc/m^2	$2x10^{-6}$ $1.5x10^{-6}$	Similar to Health Physics surveillance. ^{210}Po, oxide from the combustion of the elements in the presence of soot particles and dust from the ground surface	d < 8µm d < 18µm
1967	Stewart	-	The previous site, surface disrupted,	$2x10^{-6}$	Similar to Health Physics surveillance.	d < 8µm

Year	Study	Date of Release & Measurement	Land Area and Description	*K* (m-1)	Resuspension Mechanism and Isotopic Composition	Size
			charged debris not removed. 20 m radius, average level 3 mc/m^2	$1.6x10^{-6}$	^{210}Po, oxide from the combustion of the element in the presence of soot particles and dust from the ground surface	d < 18µm
1967	Stewart	-	Clear, level, sandy soil. 1 m^2, nominal level 112 g/m^2	$2.4x10^{-6}$ $1.6x10^{-7}$	Similar to Health Physics surveillance. ^{210}Po, oxide from the combustion of elements in the presence of soot particles and dust from the ground surface	d < 4µm d < 12µm
1967	Stewart	-	Undistributed, sandy soil covered with coarse desert grass. 9 m^2, level 70 g/m^2	$8x10^{-6}$ $5x10^{-7}$	Similar to Health Physics surveillance. Natural Uranium: U_3O_8 from combustion. A fraction smaller than 50 microns obtained by sieving	d < 4µm d < 12µm
1967	Stewart		Concrete paving stones, 2 m^2, level 180 g/m^2	$2x10^{-6}$ $1.5x10^{-7}$	Similar to Health Physics surveillance. Natural Uranium: U_3O_8 from combustion. A fraction smaller than	d < 4µm d < 12µm

Year	Study	Date of Release & Measurement	Land Area and Description	*K* (m-1)	Resuspension Mechanism and Isotopic Composition	Size
					50 microns is obtained by sieving	
1984	Sehmel. Hanford Site, USA	M: 1976-1979	Four sites are tested.	10^{-4} 10^{-11}	Wind resuspension was measured at a height of 0.3-124m. $^{239\text{-}240}$Pu, ^{241}Am	Respirable and inhalation range
1986	Shinn. Palanquin, NV	M: 1982-1986	Low-density shrub cover.	$1.8x10^{-13}$	Wind resuspension. ^{239}Pu Pu flux=3.3x10-7, U* = 0.45 m/s	AMAD = 2.5 µm
1986	Shinn. Palanquin, NV	M: 1982-1986	Low-density shrub cover.	$4.3x10^{-12}$	Wind resuspension. 239Pu Pu flux=6.1x10-7, U* = 0.23 m/s	AMAD = 2.7 µm
1986	Shinn. Pu Valley, NV	M: 1982-1986	Low-density shrub cover.	$6.1x10^{-10}$	Wind resuspension. ^{239}Pu Pu flux = 6.2x10-5, U*=0.20 m/s	AMAD = 5.5 µm
1986	Shinn. GMX, NV	M: 1982-1986	Low-density shrub cover.	$2x10^{-10}$	Wind resuspension. ^{239}Pu Pu flux=1.9x10-5, U* = 0.20 m/s	AMAD = 5.7 µm
1997	Garcia-Olivares. Southern Spain	R: 1966 M:1988	226 ha cultivated & uncultivated lands, and urban areas. Avg soil particle density = 2.7 g/cm^3	10^{-10}	Wind resuspension. ^{239}Pu, ^{241}Am	52% air contamination due to AED < 40 µm < AED <63 µm and 16% due to 63 µm < AED < 200 µm

Year	Study	Date of Release & Measurement	Land Area and Description	*K* (m-1)	Resuspension Mechanism and Isotopic Composition	Size
1999	Wagenpfeil. Pripayat Beach, Chornobyl	R: 1986 M: 1991	Sand, 5cm land height.	$1x10^{-10}$ – $0.6x10^{-10}$	Wind resuspension. ^{137}Cs, measured at heights 1.7m – 3.8m	d > 10µm
1999	Wagenpfeil. Zapoli, Chornobyl	R: 1986 M:1991	Grass, 0.5m height. 5cm land height tested.	$6x10^{-10}$ – $4x10^{-10}$	Wind resuspension. ^{137}Cs, measured at heights 1.7m – 3.8m	d > 10µm
1999	Wagenpfeil. Kopachy, Chornobyl	R: 1986 M: 1991	Grass, 0.2m height. 5cm land height tested.	$1.4x10^{-10}$ $1.1x10^{-10}$	Wind resuspension. ^{137}Cs, measured at heights 1.7m – 3.8m	d > 10µm
1999	Wagenpfeil. Pripayat Beach, Chornobyl	R: 1986 M:1991	Sand, 5cm land height.	$0.1x10^{-10}$	Wind resuspension. ^{137}Cs, measured at heights 1.2m	d < 10µm
1999	Wagenpfeil. Zapoli, Chornobyl	R: 1986 M: 1991	Grass, 0.5m height. 5cm land height tested.	$6.3x10^{-10}$	Wind resuspension. ^{137}Cs, measured at heights 1.2m	d < 10µm
1999	Wagenpfeil. Kopachy, Chornobyl	R: 1986 M: 1993	Grass, 0.2m height. 5cm land height tested.	$2.7x10^{-10}$	Wind resuspension. ^{137}Cs, measured at heights 1.2m	d < 10µm
1999	Wagenpfeil. Novozybkov, Chornobyl	R: 1986 M: 1994	Bare soil, 5cm land height tested.	$1.4x10^{-10}$	Wind resuspension. ^{137}Cs, measured at heights 1.2m	d < 10µm
1999	Wagenpfeil. Zapoli, Chornobyl	R: 1986 M: 1991	Grass, 0.5m height. 5cm land height tested.	$1.5x10^{-9}$- $3.5x10^{-7}$	Anthropogenic enhanced resuspension. ^{137}Cs, measured at heights 1.2m	d > 10µm

Year	Study	Date of Release & Measurement	Land Area and Description	*K* (m-1)	Resuspension Mechanism and Isotopic Composition	Size
1999	Wagenpfeil. Kopachy, Chornobyl	R: 1986 M: 1993	Grass, 0.2m height. 5cm land height tested.	$1x10^{-8}$ - $5x10^{-7}$	Anthropogenic enhanced resuspension. ^{137}Cs, measured at heights 1.2m	d > 10µm
1999	Wagenpfeil. Novozybkov, Chornobyl	R: 1986 M: 1994	Bare soil, 5cm land height tested.	$1.6x10^{-9}$-$1.6x10^{-8}$	Anthropogenic enhanced resuspension. ^{137}Cs, measured at heights 1.2m	d > 20µm
2003	Shinn. Plot 2 Palmores, Spain	R: 1966 M: 1993	-	10^{-10}	Wind resuspension. $^{239-240}$ Pu, ^{241}Am, measured heights 1.1m and 2.1m	d < 7µm MMAD = 3.6 µm AMAD = 3.3 µm
2003	Shinn. Tharanki West, Australia	M: 1996-1997	Nuclear test site, undisturbed control	$3.0x10^{-10}$	Wind resuspension. $^{239-240}$ Pu, ^{241}Am Pu/Am = 6 (σ = 2.5) Ef=2, Air Activity = 1 Bq, TSP = 14 µgm-3	AMAD = 4.7 µm MMAD = 4 µm
2003	Shinn. Tharanki North, Australia, plot #19	M: 1996-1997	Nuclear test site, cleaned site	$4.0x10^{-9}$	Wind resuspension. $^{239-240}$ Pu, ^{241}Am Pu/Am = 10 (σ = 3.7) Ef=2, Air Activity = 2.2 Bq, TSP = 28 µgm-3	AMAD = 2.8 µm MMAD = 3 µm

Year	Study	Date of Release & Measurement	Land Area and Description	*K* (m-1)	Resuspension Mechanism and Isotopic Composition	Size
2003	Shinn. Tharanki North, Australia, plot #18	M: 1996-1997	Nuclear test site, undisturbed recontaminated	$1.3x10^{-9}$	Wind resuspension. $^{239-240}$ Pu, ^{241}Am Pu/Am = 10 (σ = 3.7) Ef=2, Air Activity = 2.3 Bq, TSP = 7 µgm-3	AMAD = 6.9 µm MMAD = 3.2 µm
2003	Shinn. Tharanki Northeast, Australia	M: 1996-1997	Nuclear test site, cleaned site	$1.4x10^{-9}$	Wind resuspension. $^{239-240}$ Pu, ^{241}Am Pu/Am = 6.4 (σ = 0.7) Air Activity = 2.3 Bq, TSP = 14 µgm-3	AMAD = 3.7 µm MMAD = 4.6 µm
2003	Shinn. Tharanki Northeast (storm), Australia	M: 1996-1997	Nuclear test site, 24 hr dust storm	$5.9x10^{-7}$	Wind resuspension. $^{239-240}$ Pu, ^{241}Am Ef=6, Pu/Am = 6.4 (σ = 0.7) Air Activity = 2.3 Bq, TSP = 967 µgm-3	AMAD = 3.7 µm MMAD = 4.6 µm
2003	Shinn. TM-100, Australia	M: 1996-1997	Nuclear test site, undisturbed control	$2.8x10^{-11}$	Wind resuspension. $^{239-240}$ Pu, ^{241}Am Ef=0.0003, Pu/Am = 3 (σ = 1.7) Air Activity = 0.0167 Bq, TSP = 1 µgm-3	AMAD = 2.9 µm MMAD = 1 µm
2003	Shinn. TM-100, Australia	M: 1996-1997	Nuclear test site, cleaned site	$6.6x10^{-11}$	Wind resuspension. $^{239-240}$ Pu, ^{241}Am Ef=0.0003, Pu/Am = 3 (σ = 1.7) Air Activity = 0.0167 Bq, TSP= 15 μgm^{-3}	AMAD = 2.9 µm MMAD = 1 µm

Table 21: Parameters influencing resuspension (Sehmel, 1986)

Pollutant particle properties	Soil properties	Particle-soil interaction	Surface properties	Topography	Metrological variables
Chemical reactivity	Moisture content	Attraction forces	Areas of erodible surface	Agricultural	Air density, affected by
Density	Ratio of erodible to non-erodible fractions	- Molecular forces: Van-der-Waals forces	Cohesiveness of particles	Broken	- Humidity
Hydrophobic		- Chemical binding forces	- Binding action of materials	Desert	- Pressure
Hydrophilic		- (Valence forces)			
Particle diameter	Soil size frequency distribution	- Electrostatic forces	- Surface moisture	Diurnal	- Temperature
- Respirable	Specific gravity	- Magnetic forces	Cover	Flat	Soil burden carried
- Nonrespirable	Structure	Capillary forces at the surface of aggregates filled with liquid	Obstructions	Forested	- Influence on air velocity
- Frequency distribution	- Organic matter	Chemical reaction	Roughness, large scale	Hills	- Avalanching
Shape	- Lime content	Contact area effect on adhesion	- Mechanical turbulence	Humidity	- Saltation
Surface roughness	- Texture	- Particle shape	- Overall sheltering	Seasonal	Surface moisture content
	Temperature	- Particl size	- Roughness, small scale	Temperature	- Dew
		- Nature of particel and surface	- Orientation of obstacles	Undulating	- Frost upheaval
		- Surface roughness	- Percent of are covered by non-erodible aggregates or obstacles	Uniform	Relative humidity
		- Adhesion of agglomerates vs individual particles		Urban	Temperature
		Crystallization of dissolved substances	- Sheltering of individual particles	Valley	- Surface dry
		Deposition of suspended colloidal particles	- Stability of aggregates against abrasion and	Water	- Surface drying
		Hardening binders	integration by moisture and watering		- Surface frozen
		Liquid bridges	Temperature		- Wind speed Wind removal forces
		Mineral bridges	Topographic features		- Mean wind speed
		Relative humidity	- Broken		- Frequency, period, and intensity of gusts
		Temperature	- Uniform		penetrating to the surface
		Time of contact	Vegetative cover		- Transient and steady drag
		Viscous surface coating	- Live vegetation		- Verticle wind profile
			- Plant residue		- Stability - Vertical turbulent exchange - Surface roughness - Temperature stratification - Wind direction

8 APPENDIX B

8.1 Initial Work

8.1.1 Aerodynamic properties affecting particle dynamics

Microscopic particles that are resuspended will travel through the air and eventually fall back to the ground, and they leap or roll until they lose their kinetic energy. It is vital to study the parameters affecting these particles' dynamics when tracking their path after the initial resuspension process. This chapter covers the initial work performed to understand the forces acting on spherical particles using exact and numerical techniques.

8.1.1.1 Forces acting on a suspended spherical particle

The particle trajectory of the resuspended particle was developed using Newton's second law of motion, and its equation can be written as below:

$$\frac{dU_P}{dt} + F_D(U - U_P) + g_X\left(\frac{\rho_P - \rho}{\rho_P}\right) + F_X = 0 \qquad \textbf{(110)}$$

Here, Up is the particle velocity, and $F_D(U\text{-}Up)$ is the drag force acting on a unit mass particle. F_X represents the acceleration due to other forces, such as the Saffman lift force. The Saffman (1965) lift force is the subsequent drift force acting on a particle across streamlines due to Brownian motion. Here ρ is the density of continuous flow, and ρ_p is the particle density. Here F_D can be derived as in Equation (111).

$$F_D = \frac{18\mu}{\rho_P d_P^2}\frac{C_d \mathbf{Re}}{24} \qquad \textbf{(111)}$$

Here μ is the continuous flow dynamic viscosity, C_d is the coefficient of drag for particle size d_p, **Re** is the Reynolds number of the particle found using Equation (112).

$$\boldsymbol{Re = \frac{\rho d_P |U_P - U|}{\mu}} \qquad \textbf{(112)}$$

Equation (111) clearly shows that the drag force acting on a spherical particle depends on the Reynolds number. La_2O_3 powder was used as a radioactive stimulant to

conduct the resuspension experimental work at Wehrwissenschaftliches Institut für Schutztechnologien (WIS) in Munster, Germany. These particles have an average density of 6.51 g cm^{-3} and average aerodynamic diameters between 0.25 μm and 150 μm.

Figure 109 shows how the Reynolds number of spherical particles changes as velocity increases.

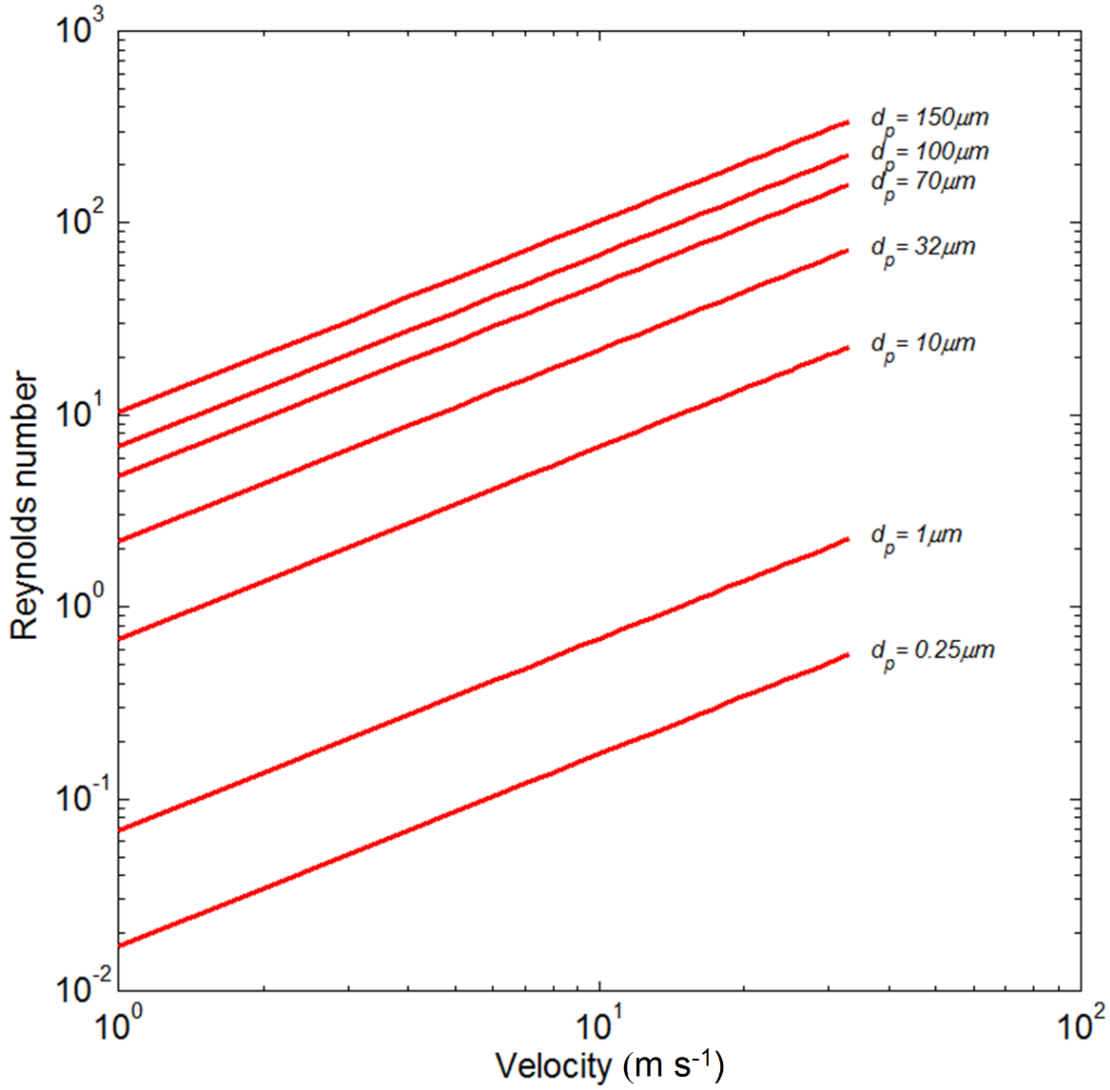

Figure 109: Reynolds number versus velocity for spherical particles with aerodynamic diameters of 0.25, 1, 10, 32, 70, 100, and 150 µm calculated up to 33.3 m s^{-1} particle velocity with respect to free stream air at Standard Atmospheric Conditions (SAC)

Figure 109 shows that **Re** for a selected size particle changes linearly during the particle deceleration process from 33.3 to 0 m s^{-1} relative velocity with respect to air at standard atmospheric conditions. The highest relative velocity (33.3 m s^{-1}) is experienced at the starting point of the projectile. Reynolds numbers for these particles were calculated

up to a particle launching velocity of 33.3 m s^{-1} (~120 km h^{-1}) to find the behaviour of particles if particles were mechanically launched by a wheel of a vehicle moving on the highway at a speed of 120 km h^{-1}, which represents a good case for mechanical resuspension

Figure 110 shows the calculated values for the coefficient of drag (C_d) for a spherical particle versus the Reynolds number found using Equations used in FLUENT to find C_d , Stokes law and experimental data from (Zarin, 1970).

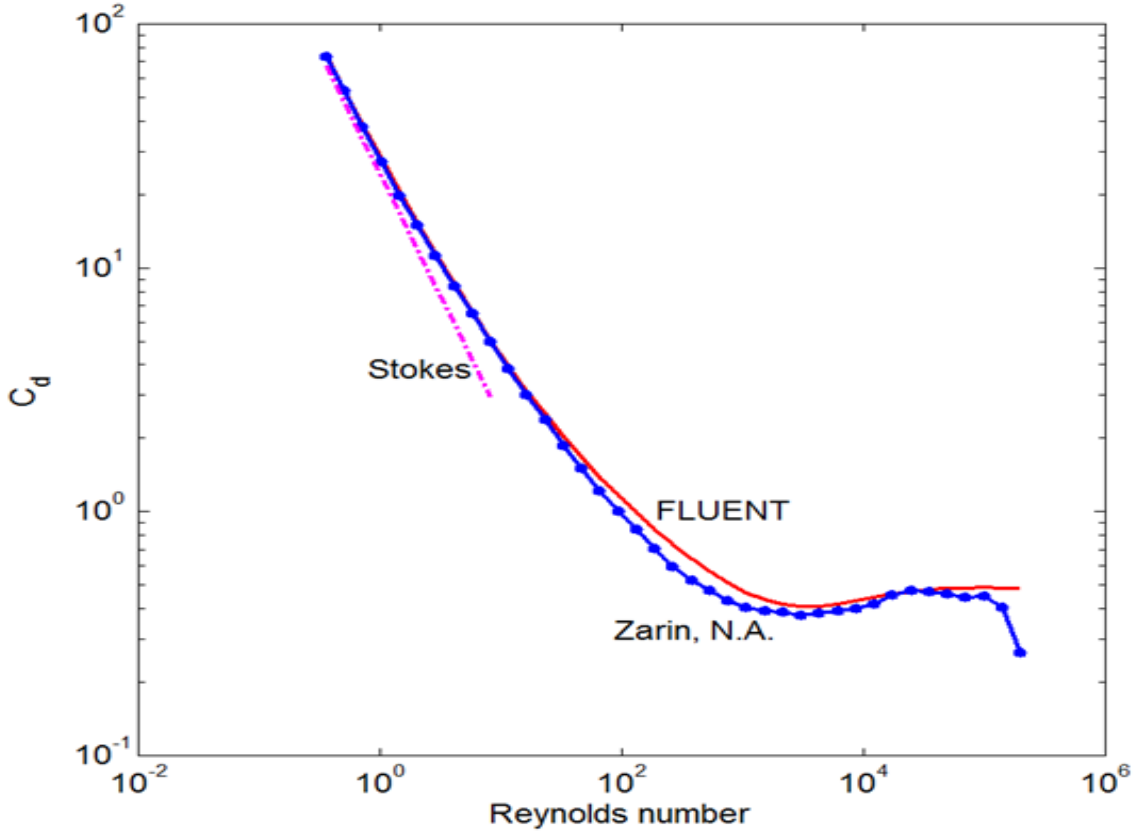

Figure 110: Comparison of sphere drag coefficients used in FLUENT, Stokes law, and digitized experimental data by Zarin, N.A. (1970).

Figure 110 shows that C_d is at its highest when particles start moving from rest. The values of C_d on spherical particles reduced linearly up to Reynolds number of 1 and further started reducing exponentially from Reynolds numbers from 1 to 1,000.

Figure 111 shows the percentage difference of C_d calculated using the drag equation used in FLUENT with respect to experimental data by Zarin (1970) up to the maximum Reynolds number that a La_2O_3 particle will experience when launched by a vehicle moving at a speed of 33.3 m s^{-1}.

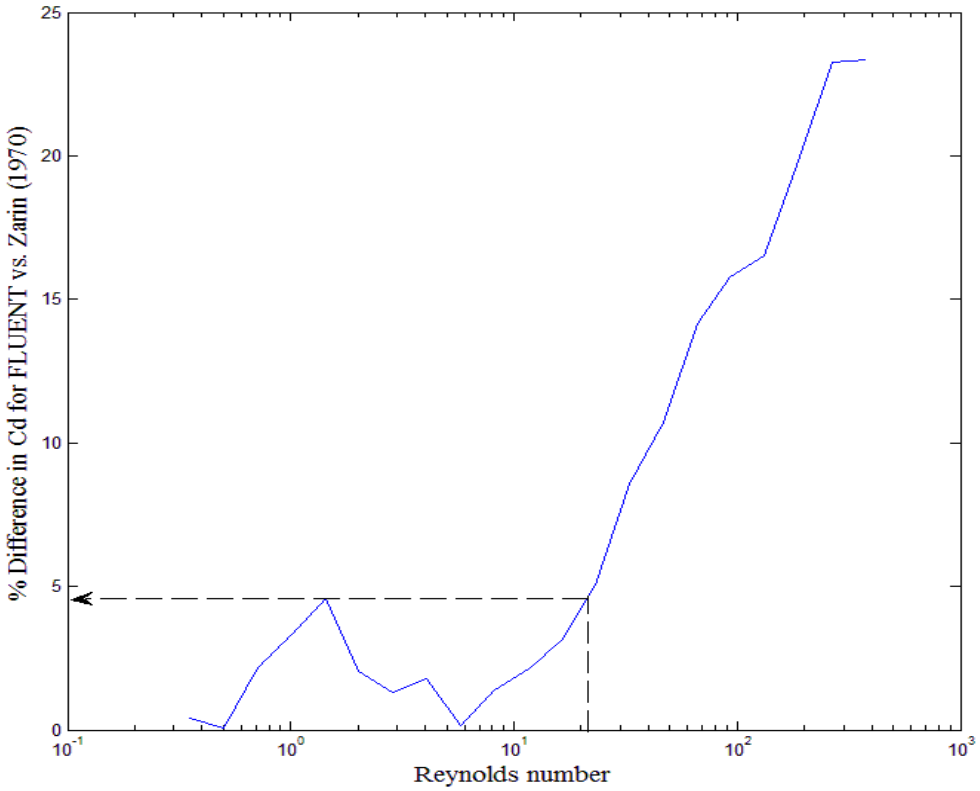

Figure 111: Percentage difference in drag coefficient found using FLUENT and experimental results by Zarin (1970) for Reynolds numbers from 0.35 to 3,000

The Cd values found match the experimental data found by Zarin (1970) within 5% up to Reynolds number of 22.

The mean velocity of the wind chamber used for resuspension studies at the WIS facility was 6.7 m s^{-1}, and the aerodynamic diameters of 75% of the total volume of the particles were less than 35 μm. Using Equation (117). the maximum Reynolds number of these particles during the resuspension experiment was calculated to be 16.6 (< 22). Since the maximum Reynolds number of the particles used in the WIS facility experiment was

less than 22, one can confidently say that the equations used in FLUENT to calculate the C_d can satisfactorily be used to calculate the drag forces acting on the particles during the resuspension process.

8.1.1.2 Comparison of drag force against gravity using exact solutions

When a microscopic particle is released into the air, it will quickly reach the velocity of the air since drag forces acting on these particles are substantial compared to other forces acting on them. Solutions for drag forces for the range of particles utilized in the experiments under the thesis were calculated by solving Equation (115).

These results are summarized as shown in Figure 112.

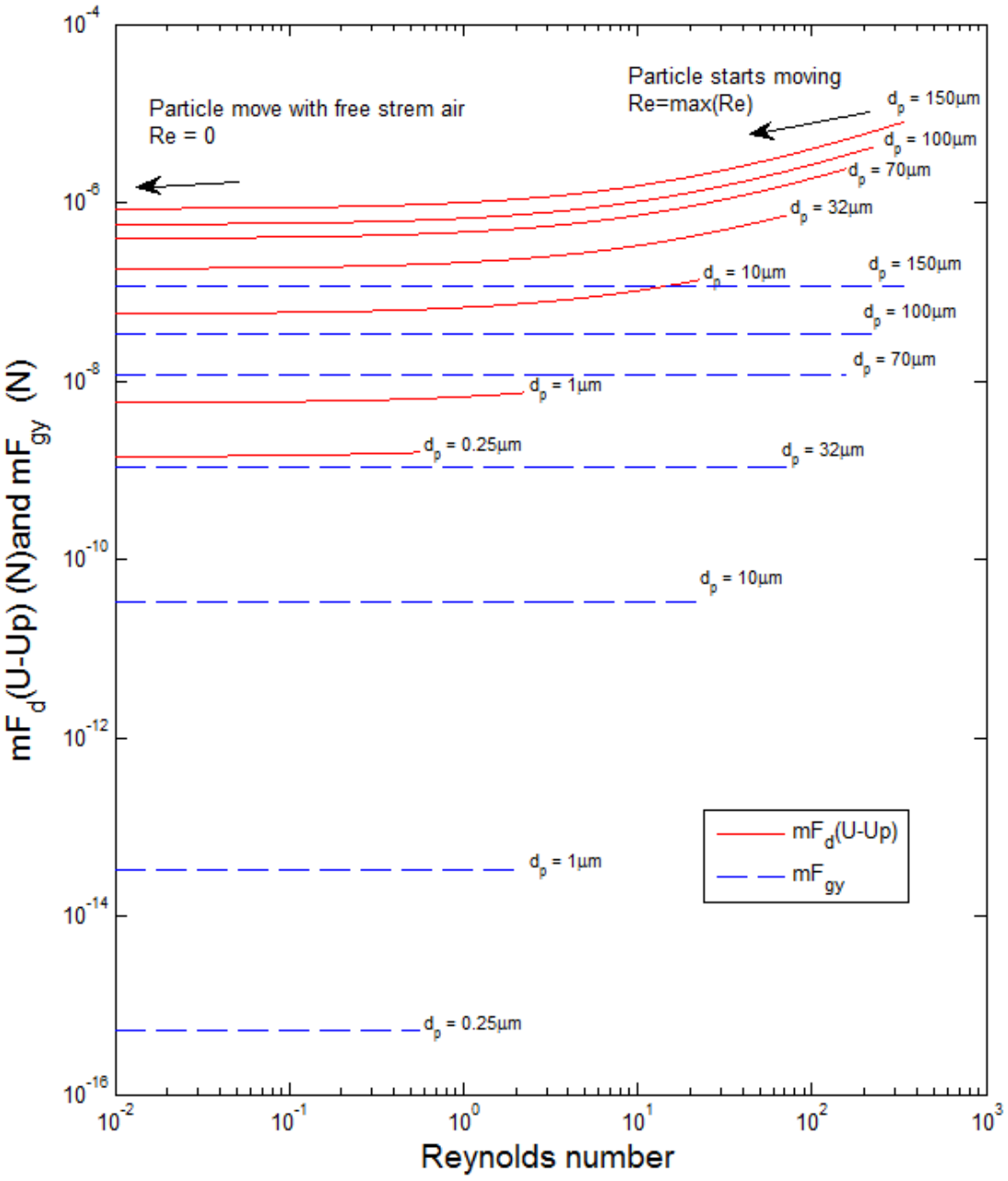

Figure 112: Drag force (F_D: solid lines) and force due to gravity (F_{GY}: broken lines) acting on spherical Lanthanum Oxide particle against their Reynolds number for selected particle sizes in SAC air up to maximum particle Reynolds number corresponds to 33.3 m s^{-1} particle relative velocity

The exact solution for drag forces acting on spherical particles shows particles started moving through the free stream flow until their relative velocity with air reaches zero. The ratio of maximum drag force (corresponds to maximum **Re** at free stream velocity of 33.33 m s^{-1}) to respective forces due to gravity (mF_{gy}) are 2.2045E5 and 4.04E3 for 1 μm and 10 μm diameter spherical particles, respectively, indicating that initial trajectories of these particles are dominated by the drag forces acting on them compared to gravitational forces.

8.1.1.3 CFD modelling of particles that were released to free-stream air

The previous section confirmed that FLUENT CFD software could model the drag force acting on microscopic particles. However, it is vital to confirm that the FLUENT software can also track these particles in the computational domain that mimics the modelling of practical particle resuspension scenarios.

A 2D computational domain, as shown in Figure 113, was generated using the mesh generation software Gambit. The computational domain was 10 m long and 1.2 m tall. It has 100 rectilinear mesh elements in the stream-wise direction and 1000 rectilinear mesh elements in the wall-normal direction. The computational mesh, generated using Gambit, was later imported to FLUENT. The downstream velocity field of the computational

domain was initialized to 33.3 ms^{-1} under Standard Atmospheric Conditions (SAC), simulating the free stream flow conditions.

Microscopic spherical particles with diameters of 0.25, 1.0, 10, 32, 70, 100, and 150 µm were released into the inlet of an initialized computational domain at locations 0.3 m, 0.4 m, 0.5 m, 0.6 m, 0.7 m, 0.8 m and 0.9 m above the ground respectively. Figure 113 shows the particle paths of these particles tracked under drag, gravity, and buoyancy forces.

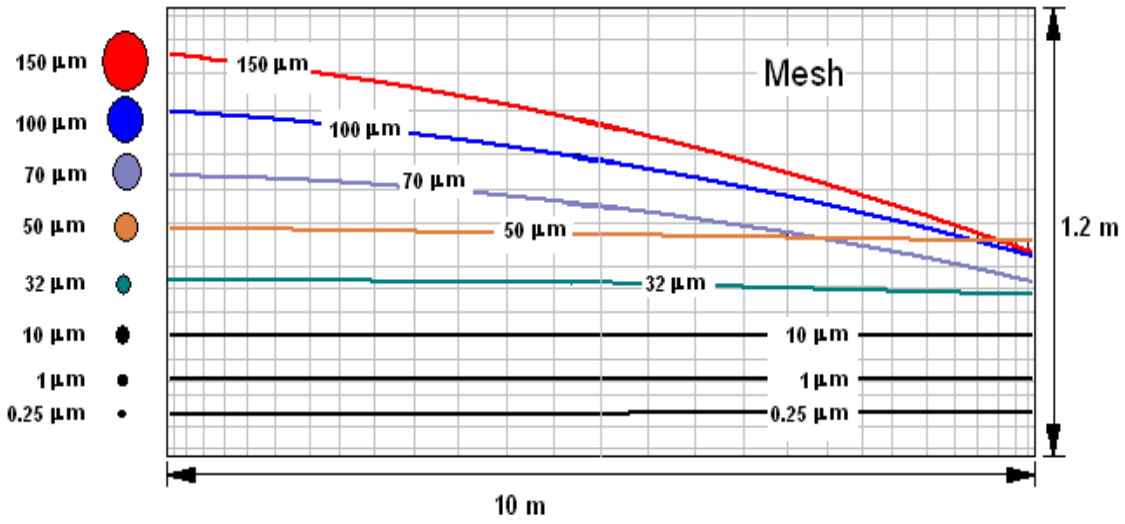

Figure 113: Particle tracks of selected particles found using FLUENT software as particles move downstream at 33.3 ms^{-1} constant velocity flow domain under SAC. Note: The figure is not to scale, and the number of meshes used in the actual model is much higher.

According to CFD results in Figure 113, particles in the respirable range (up to 10 µm) move in horizontal paths along the streamlines of the free stream flow. As particle size

increases, the particle path starts taking a parabolic projectile shape showing the effects of forces due to gravity.

Since the particles in the respirable range move in horizontal lines, one can confirm that buoyancy and gravity do not play a significant role in defining the path of these particles; hence, the path of these particles can be found by solving the simple linear equation.

$$\frac{dU_P}{dt} + F_D(U - U_P) + F_X = 0 \qquad (113)$$

here, U_p is the particle velocity, $F_D(U\text{-}Up)$ is the drag force, and F_X are other forces acting on a unit mass particle, as discussed at the beginning of this Appendix.

8.1.1.4 Effect of particle launching velocity on respirable range particle dynamics

Particles that will settle down on wall surfaces can be launched into free stream air by mechanical forces such as tires of moving vehicles, vortices generated by bluff bodies, or wind shear.

Particle launching parameters such as launch angle and velocity can vary based on the launching profiles of the surface, mechanical forces and aerodynamic forces acting on them at the time of the launch.

Basic particle tracking calculations were performed to find the velocity and the distance of a particle at time t after it was launched at a velocity of U_{PL} with an angle θ with respect to the positive X-axis.

.

Figure 114 shows a particle launched into free steam air from the upstream edge of a 1m tall and 1m wide bluff body.

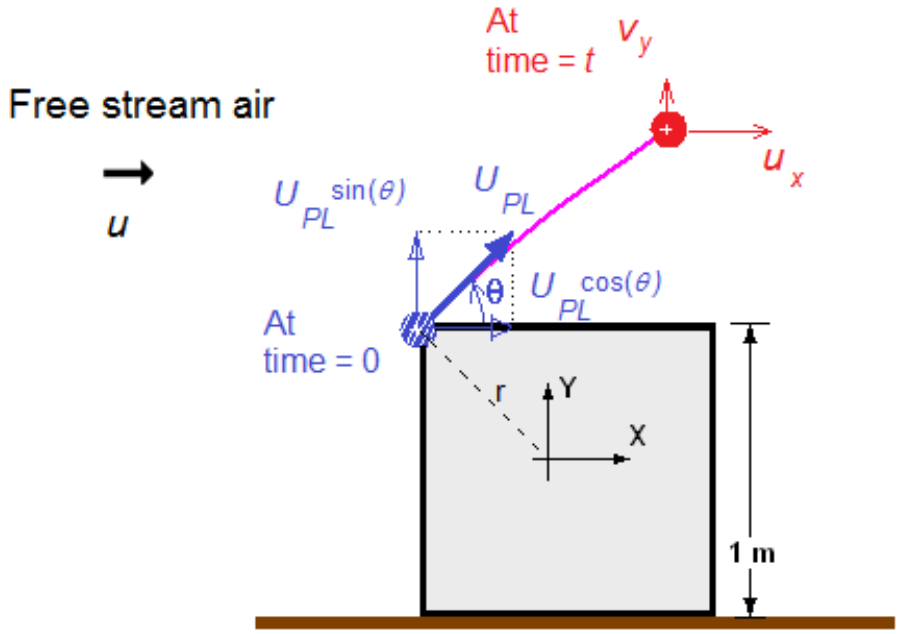

Figure 114: Velocities and the location of a particle that was launched from the upstream edge of a 1m x 1m square buff body.

As shown in Figure 7, this particle moved into a new location after time *t*. At time *t*, the orthogonal components of velocity are u_x and v_y in X and Y directions, respectively.

.

8.1.1.4.1 X-velocity component of the particle (constant k_D=40.08)

At time *t,* the x-component of the drag force (F_{DX}) acting on a spherical particle can be written as,

$$\boldsymbol{F_{DX} = \frac{1}{2}\rho(u - u_X)^2 C_D A,} \qquad \textbf{(114)}$$

here, ρ is the density of free stream air at SAC, u is free-stream velocity, C_d is the drag coefficient, and A is the reference area ($A=\pi r^2$ for a spherical particle with radius r). After dividing the (113) by the mass of the spherical particle ($m_p = \rho_p \ 4/3 \ \pi \ r^3$), a simplified version can be written as

$$\boldsymbol{\frac{dU_X}{dt} = -k_D[u - u_x(t)]^2} \qquad \textbf{(115)}$$

The value of k_D is defined by Equation (116).

$$k_D = \frac{3}{4}\frac{C_D}{d}\frac{\rho}{\rho_p} \qquad (116)$$

Usually, the magnitude of k_D changes according to the relative velocity of the spherical particle with respect to free stream air moving at u velocity. However, for simplicity, the results presented under this section of the thesis assume that k_D stays constant (k_D = 40.08) for the entire range of velocity of the 10 μm particle to simplify ordinary differential equations (ODE) used to find the velocities and locations of particles.

Equation (124) is a first-order non-linear differential equation with $u_x(t)$ as the dependent variable and t as the independent variable. The solution for u_X at time t was found by integrating the differential equation with respect to time t. The X-velocity component of the particle at time t after applying initial boundary conditions [$u\ (0) = U_{PL} \cdot cos\ (\theta)$] can be written as follows.

$$u_x(t) = \frac{-k_D[u^2 - uU_{PL}\,cos(\theta)]t + U_{PL}\,cos(\theta)}{1 - k_D[u - U_{PL}\,cos(\theta)]t} \qquad (117)$$

The solution of Equation (117) for 10 μm diameter spherical particle, released by a wheel of a car travelling at 33.33 m s^{-1} (U_{PL}) at an angle of 45^0 (θ) with respect to positive X-direction, is shown in Figure 115.

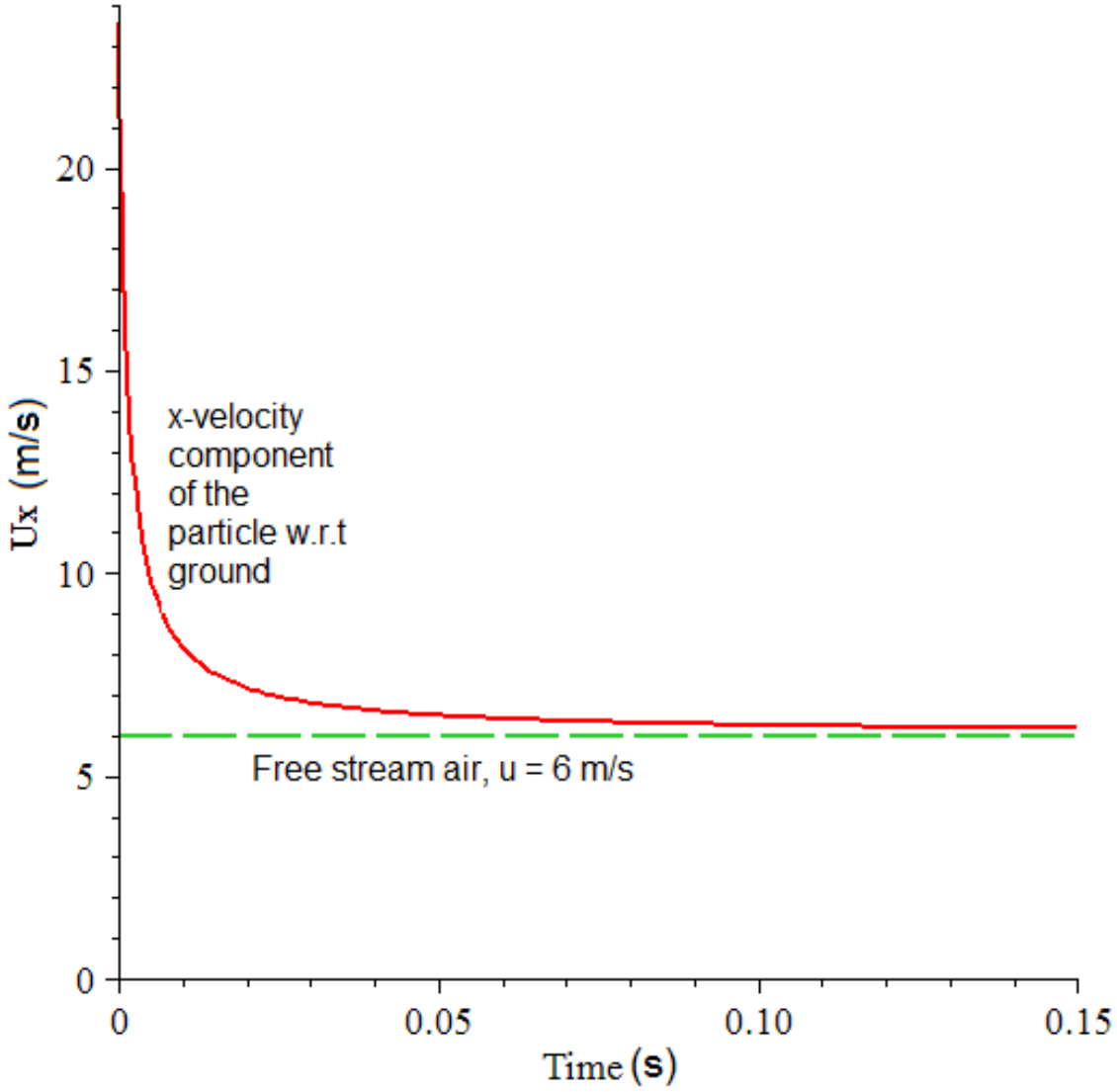

Figure 115: X-velocity component (U_X) of 10 µm diameter spherical particle launched at 33.3 ms^{-1} velocity at an angle of 450 to air at SSA that is moving downstream at 6 ms^{-1} velocity in the horizontal direction. (Assumption: constant k_D=40.08)

According to Figure 115, the horizontal velocity component of the particle (u_x) reduces exponentially from 23.5 m s-1 [33.3·cos (45^0)] to the velocity of the free stream air, (6 ms^{-1}) in 0.13 s with 126.9 ms^{-2} deceleration in positive X-direction..

8.1.1.4.2 X- location of the particle (constant k_D=40.08)

Integrating Equation (117) with respect to *t* and applying initial boundary conditions [x(0)= - r cos(θ)], the *x*-location of the particle at time *t* can be written as in Equation (118).

$$\boldsymbol{x(t) = \frac{tk_D u + ln[1 - tk_D u + tk_D U_{PL} cos(\theta)] - r\, cos(\theta) k_D}{k_D}} \qquad \textbf{(118)}$$

here, *x(t)* is the particle's location at time *t*, and *r* is the radial distance from a global reference point to the initial launching location of the particle

The plot of x-locations of the particle with respect to the global reference point is shown in Figure 116.

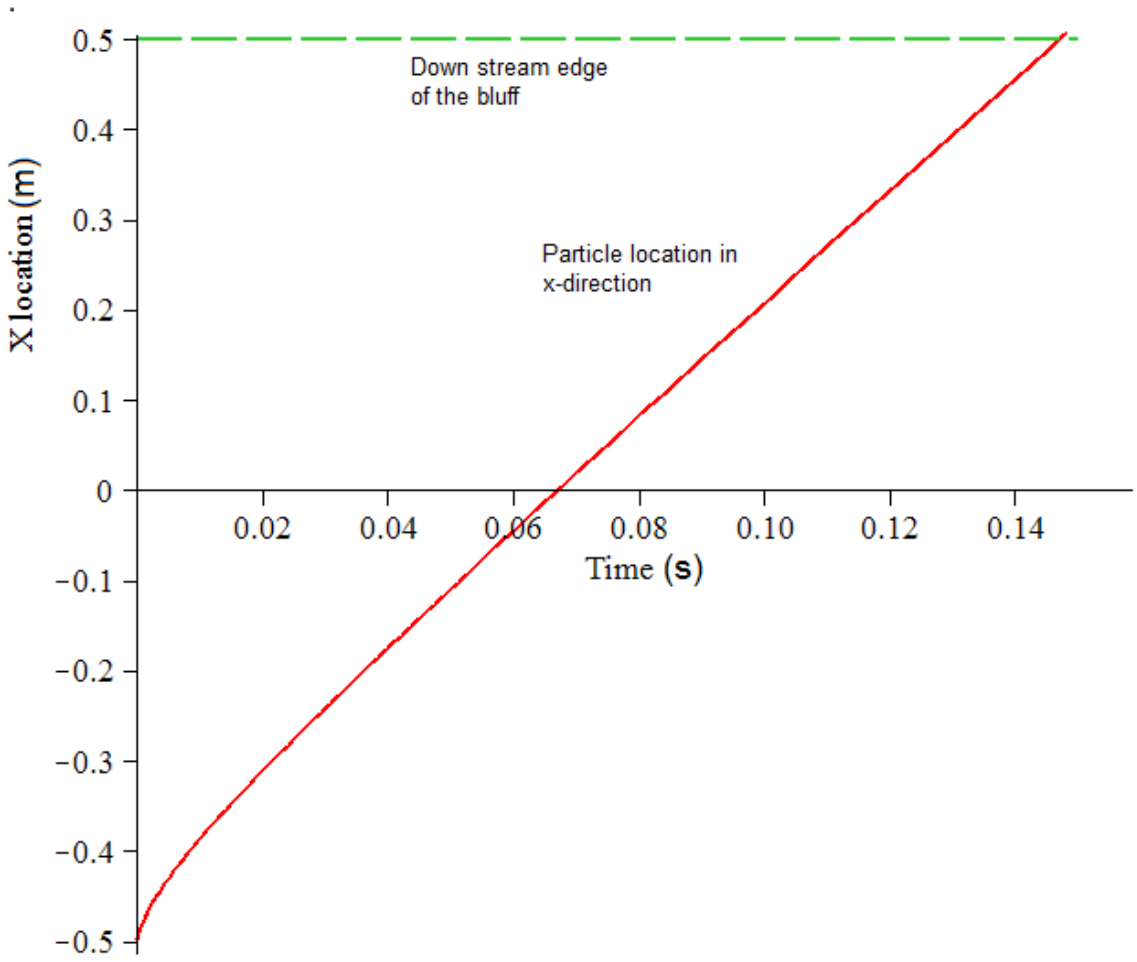

Figure 116: X-location of 10 μm diameter spherical particle launched at 33.3 m s^{-1} velocity at an angle of 45^0 to air at SSA. The particle is moving downstream at 6 m s^{-1} velocity in the horizontal direction. (Assumption: constant k_D=40.08)

According to Figure 116, a 10 μm particle quickly moved 0.1m in the x-direction within 0.001 s at the beginning of the launch. Beyond the 0.001s timeline, the particle X-location increased linearly, passing the bluff body at 0.15 s.

8.1.1.4.3 Y-velocity component of the particle moving up against the gravity (constant k_D=40.08)

The ODE corresponding to the velocity of the particle when it is moving up against gravity at time t in the y-direction can be written as Equation (119).

$$\frac{dv_y(t)}{dt} + k_D\left[v_y(t)\right]^2 + g = 0 \qquad (119)$$

Equation (119). is a first-order, linear differential equation with $v_y(t)$ as the dependent variable and t as the independent variable. Substituting initial boundary condition values to the solutions of the ODE [$v_y(0)=U_{PL}\sin(\theta)$], the y-velocity component of the particle at time t can be written as in Equation (120).

$$v_y(t) = -\frac{\tan\left(t\sqrt{gk_D} - \arctan\left(\frac{k_D U_{PL}\sin(\theta)}{\sqrt{gk_D}}\right)\right)\sqrt{gk_D}}{k_D} \qquad (120)$$

The y-velocity component (v_y) of the particle at time t was found ususing Equation (120), and the change of v_y with respect to time is shown in Figure 117.

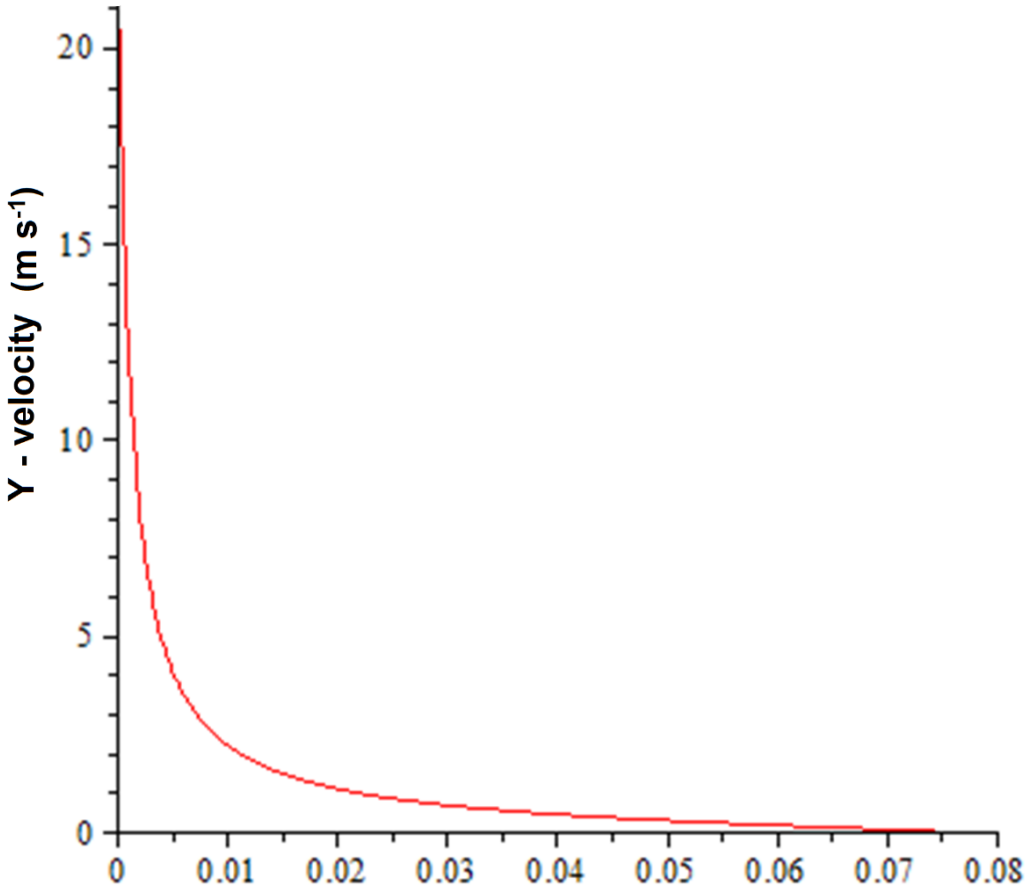

Figure 117: Y-velocity component (V_y) of a 10 µm diameter spherical particle launched at 33.3 m s^{-1} velocity at an angle of 450 to air at SAC moving downstream at 6 m s^{-1} velocity in the horizontal direction when the particle is moving in the direction against the gravity (Assumption: constant k_D =40.08)

According to Figure 117, the y-velocity component reduces exponentially from 23.5 m s^{-1} to 0 m s^{-1} in 0.08 s with the deceleration of 294.3 m s^{-2} in the positive y-direction.

8.1.1.4.4 Y- location of the particle moving up against the gravity (constant k_D=40.08)

Integrating Equation (120) with respect to *t* and substituting initial conditions [*y (0)* = 1], the Y-location of the particle at time *t* can be written as follows (Here, *y(0)*is the vertical location of the particle in the global coordinate system).

$$y(t)=\frac{1}{2}\frac{1}{k_D}\left(\begin{array}{l}\dfrac{\ln\left(\sqrt{gk_D}+U_{PL}\sin(\theta)k_D\tan\left(t\sqrt{gk_D}\right)\right)}{k_D}- \\ \dfrac{1}{2}\dfrac{\ln\left(1+\tan\left(t\sqrt{gk_D}\right)^2\right)}{k_D}-\dfrac{1}{2}\dfrac{-2k_D+\ln\left(gk_D\right)}{k_D}\end{array}\right) \quad (121)$$

The plot of y-location with respect to time for a 10 μm particle according to Equation (121) is shown in Figure 118.

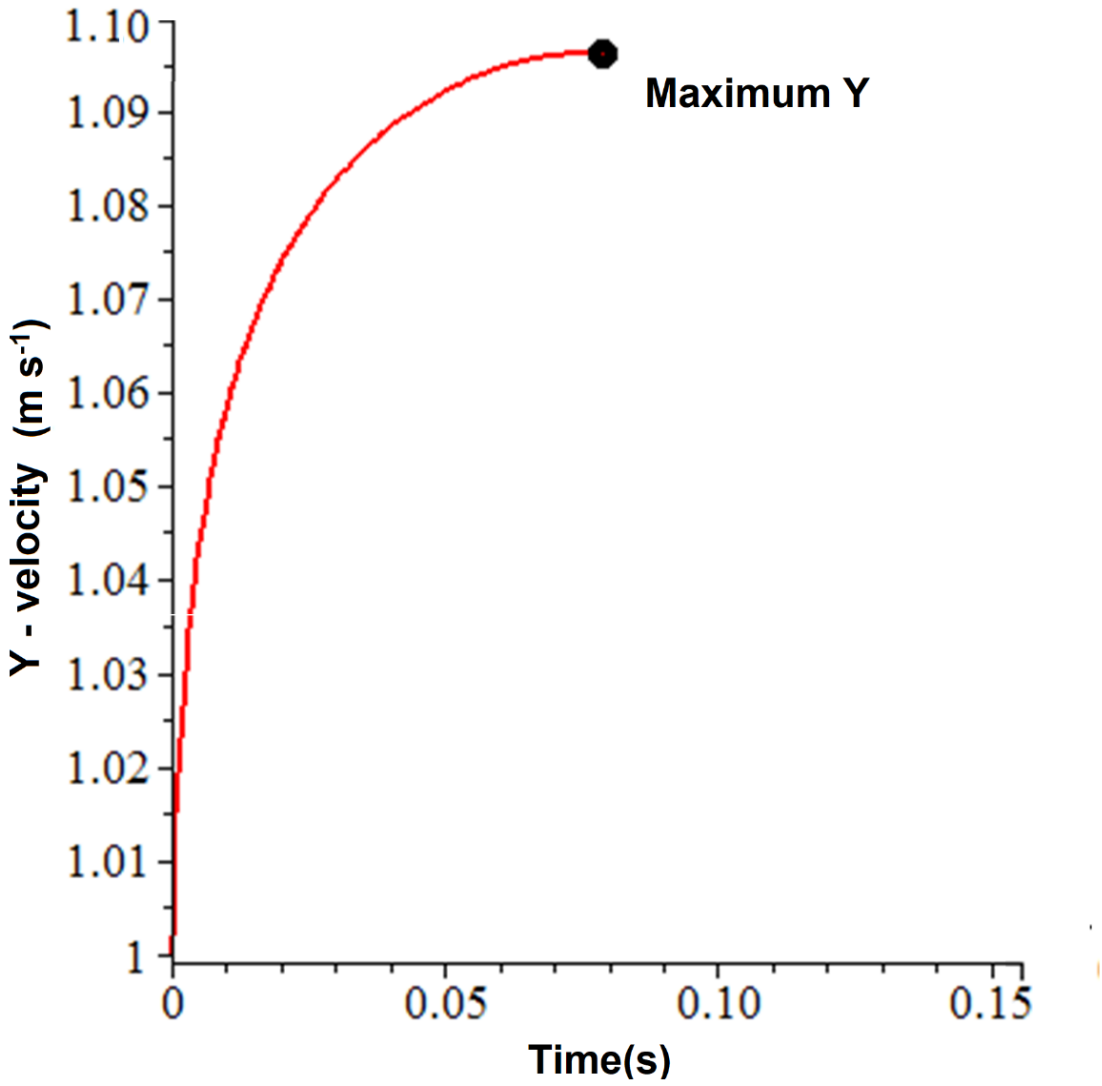

Figure 118: Y location of a 10 μm diameter spherical particle launched at 33.3 m s^{-1} velocity at an angle of 45^0 to air at standard atmospheric conditions moving downstream at 6 m s^{-1} velocity in the horizontal direction when the particle is moving in the direction against the gravity. (Assumption: constant k_D=40.08)

Figure 118 shows that the particle reaches its maximum Y-location (9.7 cm above the bluff body) within 0.08 seconds.

8.1.1.4.5 Y- velocity of the particle falling towards the ground after reaching its maximum Y-location (constant k_D=40.08)

The ODE corresponding to the Y-velocity of the particle coming down towards the ground is different from the Y-velocity of the same particle going up. The direction of the drag force with respect to the direction of gravity force is now acting in opposite directions, compared to the same direction when the particle was going up against the gravity.

The ODE corresponding to the Y-velocity of a spherical particle, falling towards the ground due to gravity after it reaches its maximum Y-location, can be written as in Equations (122).

$$\frac{d v_y(t)}{dt} - k_D\left[v_y(t)\right]^2 + g = 0 \qquad (122)$$

This is a first-order, linear differential equation with $v_y(t)$ as the dependent variable and t as the independent variable. Substituting initial boundary condition values to the solutions of the ODE [$v_y(0)=0$], the y-velocity component of the particle at time t can be written using Equation (123).

$$v_y(t) = -\frac{tanh\left(t\sqrt{gk_D}\right)\sqrt{gk_D}}{k_D} \qquad (123)$$

The plot of Y-velocity with respect to time for a 10 □m particle according to Equation (123).

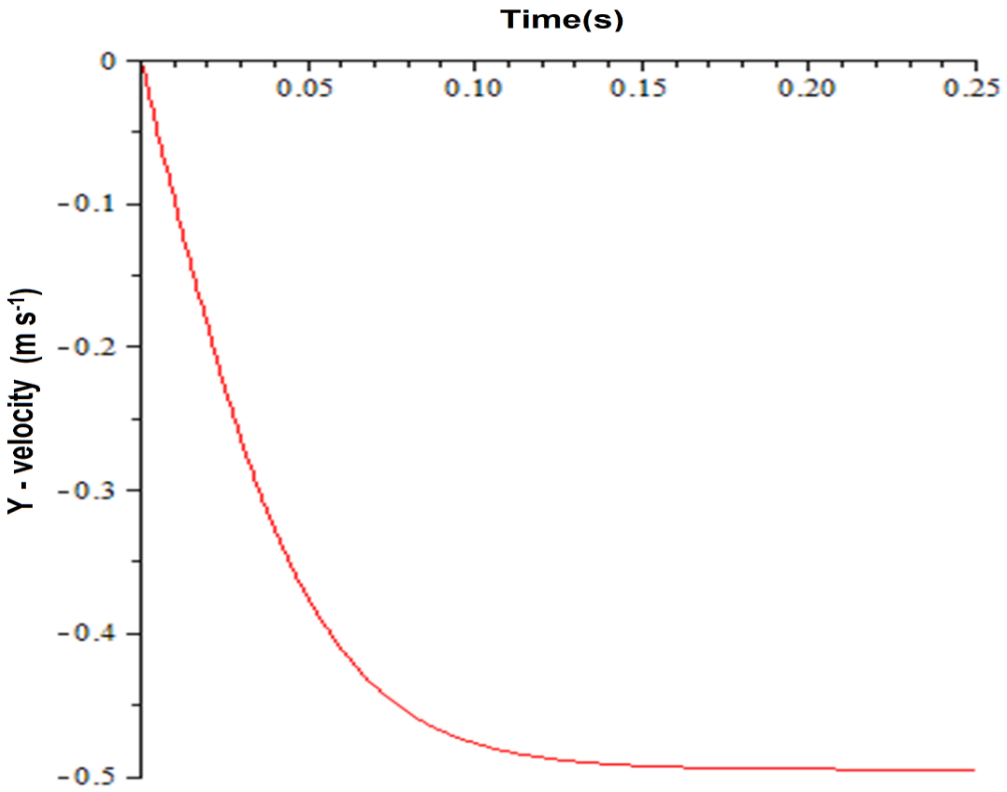

Figure 119: Y-velocity component (vy) of 10 □m diameter spherical particle coming down towards the ground after reaching maximum y-location (Assumption: constant k_D =40.08)

According to Figure 119, the y-velocity component towards the ground started accelerating from 0 m s^{-1} velocity to a terminal velocity of 0.5 m s^{-1} within 0.25 s with 2m s^{-2} acceleration.

8.1.1.4.6 Y-location of the particle coming down toward the ground after reaching its maximum Y-location (constant k_D=40.08)

Integrating Equation (123) with respect to *t* and substituting initial conditions [*y (0)* = 1.097], the y-location of the particle at time *t* can be written as follows (Here, *y(o)* is the vertical location of the particle in the global coordinate system).

$$y(t) = \begin{pmatrix} \frac{1}{2}\frac{ln\left(tanh\left(t\sqrt{gk_D}\right)-1\right)}{k_D} + \\ \frac{1}{2}\frac{ln\left(tanh\left(t\sqrt{gk_D}\right)+1\right)}{k_D} + \\ \frac{1097}{1000} - \frac{\frac{1}{2}I\pi}{k_D} \end{pmatrix} \quad (124)$$

Here I^2 = -1. The plot of y-location with respect to time for a 10 μm particle according to Equation (124) can be shown in Figure 120.

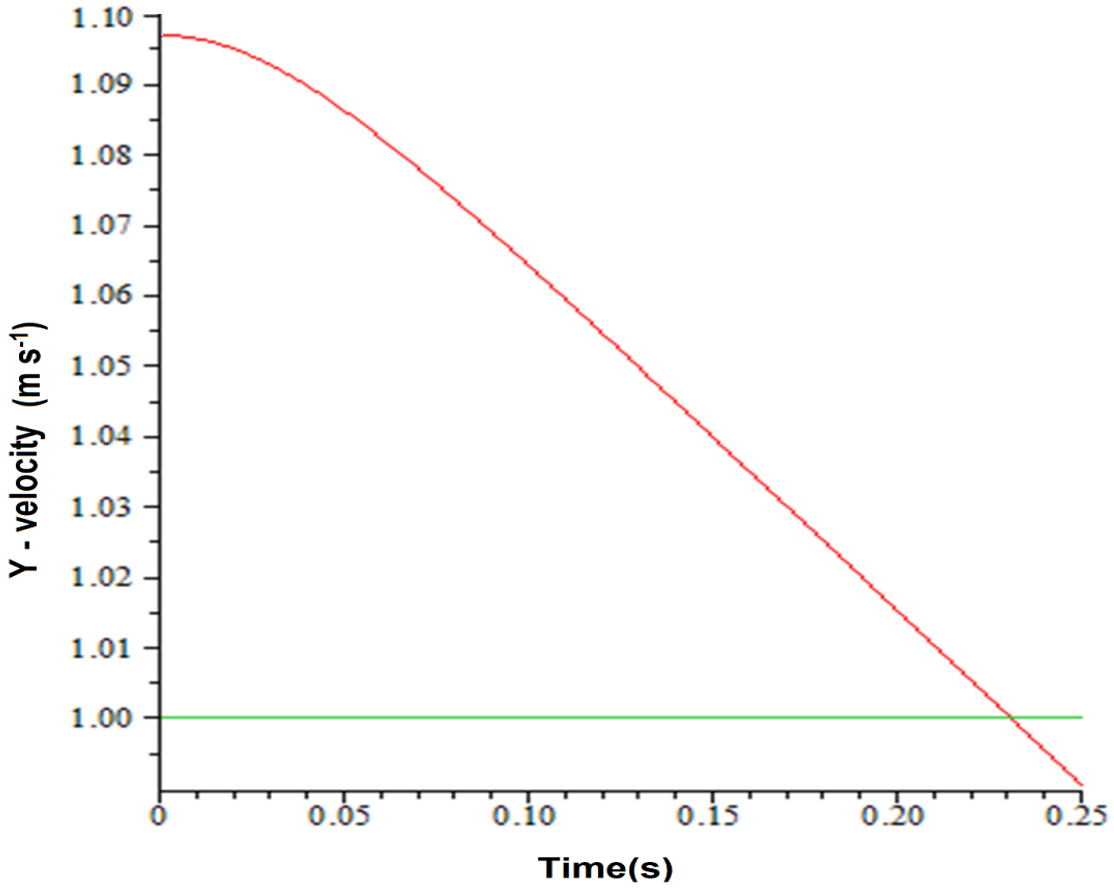

Figure 120: Y-location of 10 μm diameter spherical particle coming down towards the ground after reaching maximum vertical height (Assumption: constant k_D =40.08)

Figure 120 shows 10 μm spherical particle coming down from its highest Y-location (1.097 m) to the top surface of a 1 m tall bluff body in 0.23 s compared to the 0.08 s it took to reach the highest Y-location on its way up from the top leading edge of 1 m tall bluff body.

The magnitude of deceleration of the particle going up was much higher (294.3 m s^{-2}) than the magnitude of the particle coming down (2 m s^{-2}) to the ground. This is because the forces due to gravity and the drag force act on the particle against the particle's path when it is going up, but these forces act in opposite directions when the particle is coming down towards the ground.

This analysis showed that if a reparable-sized particle was to resuspend mechanically, it could move only a very short distance before reaching its terminal velocity. For example, the vertical distance travelled for a 10 μm particle used under this analysis was close to 10 cm before reaching its terminal velocity.

This analysis proves that a mechanically resuspended particle can only reach an average human breathing height (~1.5 m) if it travels along a streamline that connects the initial launch point and the average human breathing height. In nature, a straight steam line that will connect the ground to human breathing height will not exist. A big vortex that can be generated behind a buff body due to moving air over it or a series of rotating vortices that can be generated in the atmospheric boundary layer can quickly bring respirable range particles into an average human breathing space.

8.2 2D WIS Facility Computational Model

Due to the symmetric nature of the physical geometry of the WIS facility wind chamber across the vertical plane running in a windward direction through the center of the wind chamber, a 2D CFD model of the WIS facility wind chamber was used at the beginning of the software evaluation phase to find out which turbulence model available in the FLUENT CFD software could be used to model the radioactive particle resuspension inside the WIS facility wind chamber.

8.2.1 Mesh Generation of 2D WIS Facility Computational Model

The 2D computational domain of the WIS facility wind chamber was generated using rectilinear mesh elements. A very fine mesh was generated close to the wind chamber's wall surfaces to ensure an adequate number of nodes in the viscosity-dominated boundary layer region to model turbulent properties accurately. The original mesh was refined until the y^+ of all wall surfaces was less 1.

The y^+ represents the non-dimensional wall distance for wall-bounded flows, and it is defined as,

$$y^+ \equiv \frac{u_* y}{\nu} \qquad (125)$$

here, $u_*$is the friction velocity at the location of interest, and it is defined as given in Equation (126). Here ν is the local kinematic viscosity of the fluid, and y is the wall-normal distance to the location of interest.

$$u_* = \sqrt{\frac{\tau_w}{\rho}} \qquad (126)$$

where, τ_w is the wall shear stress at the location of interest and ρ is the fluid density. Some turbulence models available in FLUENT software solve the boundary layer using wall functions when $\mathbf{y}^+ > 30$. However, FLUENT recommends using $\mathbf{y}^+$ close to 1 to correctly resolve the flow in the Laminar Sub Layer (LSL); some turbulence models are capable of resolving the boundary when $1 < \mathbf{y}^+ < 5$ (Fluent Inc., 2006).

Figure 121 shows boundaries and the final 2D mesh of selected areas of the 2D WIS facility wind chamber.

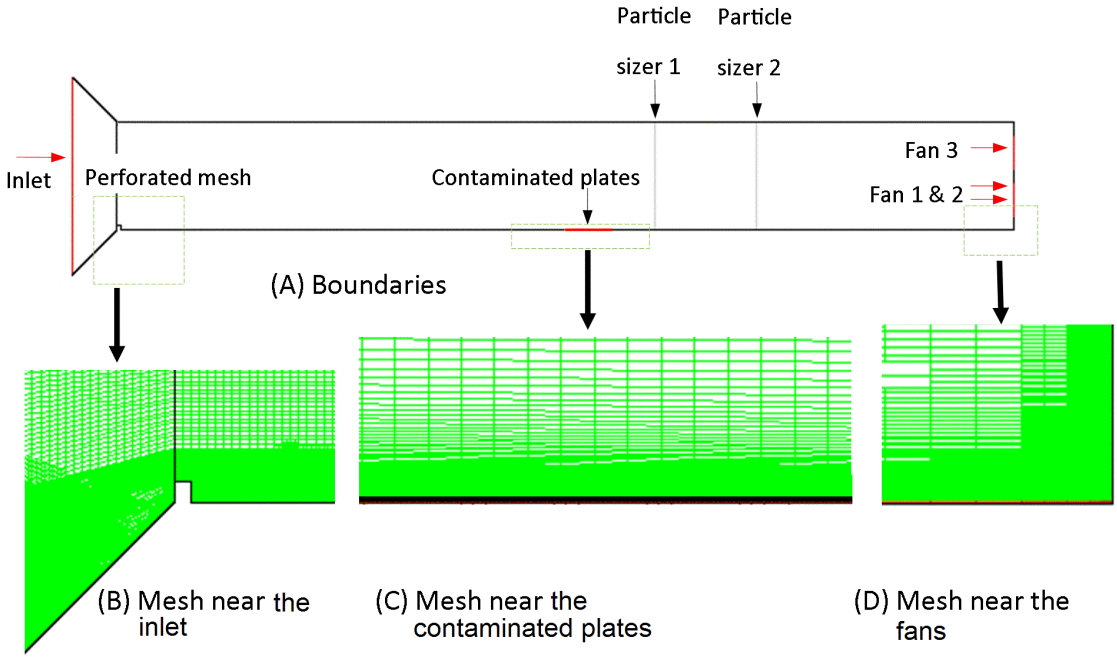

Figure 121: Boundaries and 2D mesh of selected regions of the WIS facility computational domain

Figure 121-(A) shows the boundaries and relative locations of Particle Sizers used in the computational domain. Figure 121-(B) shows the zoomed-in 2D mesh close to the lower surface of the wind chamber intake and perforated mesh. The rectangular shape turbulator is located just after the perforated mesh; a turbulator on the floor of the wind chamber was used to trip the boundary layer. Figure 121-(C) shows the zoomed-in 2D mesh near contaminated plates. Figure 121-(D) shows the zoomed-in 2D mesh near the rear wall of the wind chamber where Fan 1&2 and the duct for Fan3 were mounted.

The original mesh of the 2D WIS facility wind chamber was developed at a 1:1 scale using GAMBIT mesh generation software. The initial mesh had 132,905 mesh nodes and $\mathbf{y}^+$ s less than 1 for the ceiling and the floor, but the $\mathbf{y}^+$ s of the intake nozzle of the wind chamber were between 250 and 550. Also, on the outlet walls of the wind chamber where the fans were mounted, $\mathbf{y}^+$ s were between 5 and 500. Later, this mesh was refined using the $\mathbf{y}^+$ adaptation algorithm available in FLUENT until the $\mathbf{y}^+$s of all wall surfaces were less than 1. The corresponding final 2D mesh ended up with 428,213 nodes.

8.2.1.1 Boundary conditions for 2D WIS Facility Computational Model

Boundary conditions of the 2D computational domain were selected to represent fluid dynamic properties of the physical model of the WIS facility wind chamber.

8.2.1.1.1 Inlet Boundary Condition

The inlet of the wind chamber was modelled in FLUENT as a pressure-inlet boundary condition. The flow direction into the computational domain through the

pressure-inlet boundary was selected perpendicular to the inlet. Since the inlet of the wind chamber was made with a 2.2 m × 2.2 m square cross-section, and it was opened to the WIS facility surrounding, a hydraulic diameter of 2.2 m and turbulent intensity of 1% were selected to specify the turbulent properties of the inlet (Fluent Inc., 2006).

Turbulence intensity, I, was derived from the relationship,

$$\boldsymbol{I = \frac{u'}{U_{avg}}} \qquad \textbf{(127)}$$

here, $u'$is the root-mean-square of the turbulent velocity fluctuations in x, y and z directions, and $U_{avg}$is the mean average velocity. Here u'can be computed using Equation (128), and U_{avg}, was calculated using Equation (129).

$$\boldsymbol{u' = \sqrt{\frac{1}{3}\left(\overline{(u_x')^2} + \overline{(u_y')^2} + \overline{(u_z')^2}\right)} = \sqrt{\frac{2}{3}k}} \qquad \textbf{(128)}$$

here, u_x', $u_y'$and $u_z'$are turbulent velocity fluctuations in x, y, and z directions, and *k* is turbulent kinetic energy.

The mean average velocity, U_{avg}, is given by,

$$\boldsymbol{U_{avg} = \sqrt{U_x^2 + U_y^2 + U_z^2}} \qquad \textbf{(129)}$$

where, U_x, U_y, and U_z are mean velocities in *x*, *y* and *z* directions. Since the WIS facility under this section was modelled in 2D, the *z* components in (128) and (129) are zero.

8.2.1.1.2 Perforated mesh Boundary Condition

The boundary condition of the perforated mesh was modelled in FLUENT as a porous jump. The pressure drop across the porous medium was modelled using the Forchheimer equation (Fluent Inc., 2006),

$$\boldsymbol{\frac{dp}{dx} = \frac{\mu}{K_p} U_s + \frac{1}{2} \rho C U_s^{\,2}} \qquad \textbf{(130)}$$

here, K_p (m^2) is the permeability of the medium, U_s is the superficial velocity, ρ is the density of the fluid, and *C* (m^{-1}) is the pressure-jump coefficient. The superficial velocity through the porous jump boundary condition was calculated by dividing the volume flow rate through the wind chamber by the cross-sectional areas at the perforated mesh location.

Since the pressure drop values across the perforated mesh for a range of operational velocities were not measured during the WIS facility wind chamber experiment, the values of K_p and *C* used in during the WIS facility wind chamber experiment, the values of K_p and *C* used in Equation (130) were calculated by modelling the perforated mesh inside a virtual wind chamber using 2D FLUENT software (Sapounas, Campen, Wildschut, & Bot, 2010).

Table 22 shows a list of input parameters used in FLUENT software to model perforated mesh boundary conditions.

Table 22: Porous jump boundary values used in the CFD models

Face permeability (K_p)	1.2E-8 m^2 (Sapounas, Campen, Wildschut, & Bot, 2010).
Porous medium thickness	0.001 m The thickness of the perforated mesh.
Pressure-jump coefficient (*C*)	3220 m^{-1} (Sapounas, Campen, Wildschut, & Bot, 2010).
Discrete phase boundary condition type	interior

8.2.1.1.3 Fan Boundary Conditions

Boundary conditions of the fans used in the WIS facility wind chamber were modelled in FLUENT as exhaust fans. The mass flow rates of the fans in the CFD model were selected to match the WIS facility experimental setup. Area-weighted target mass flow rates of 5.22 kg s^{-1} and 2.61 kg s^{-1} were introduced to Fan 1&2 and the Fan 3 boundary conditions.

The gauge pressure of the backflow of Fans 1&2 boundary was used as zero since Fan 1 and Fan 2 were forcing the wind chamber air directly out to the WIS facility surroundings. The gauge pressure of the backflow for Fan 3 was used as 37 Pa since the air was forced out from the rear of the wind chamber to the WIS facility surroundings through a 2 m long duct that has a 90º elbow at the end. The pressure drops across the duct, and the elbow was calculated according to the engineering data sheets provided by the ASHRAE handbook (American Society of Heating Refrigerating and Air-Conditioning Engineers, 1997).

The intensity and length-scale option available in FLUENT was selected to introduce turbulence parameters of the backflow of Fan 1 & 2 boundary conditions; the intensity and hydraulic diameter option were selected for the Fan 3 boundary condition (Fluent Inc., 2006). The turbulent intensity of 20% and length scale of 4 cm (10% of the blade span) were introduced to Fans 1&2. The turbulent intensity of 10% and hydraulic

diameter of 40 cm were introduced for Fan 3 boundary conditions as per the recommendations given by the FLUENT software manual.

8.2.1.1.4 Wall Boundary Conditions

All 2D WIS facility wind chamber walls were modelled as non-slip boundaries with smooth surfaces. However, most of the distances from the wall boundaries to the centroids of the wall-adjacent mesh cells in the 2D WIS facility computation domain were smaller than the measured average peak-to-peak roughness heights of the wall surfaces (Rz = 9.2□□m for the contamination plate). Therefore, it is meaningless to define roughness parameters that will be used in the FLUENT software to modify the active thickness of the Laminar sub-layer (Fluent Inc., 2006). In this situation, FLUENT will solve the turbulent parameters all the way to the walls, assuming all walls are smooth. Also, the goal of 2D CFD modelling of the WIS facility wind chamber was to find the resuspension factors of Stage 2, where the flow is affected by the free stream velocity and not by roughness parameters of wall surfaces (Biswas & V, 2002).

8.2.2 CFD Modeling of the 2D WIS Facility Wind Chamber Flow Fields

The boundary layer of the WIS facility wind chamber was tripped using a turbulator located on the floor of the wind chamber after the perforated mesh. Based on the hydraulic diameter at the test section, the average Reynolds number was calculated to be 5.6E5 using Equation (131) at normal operating conditions of the WIS facility wind chamber.

$$Re_D = \frac{\rho U D_h}{\mu} = \frac{U D_h}{v} \qquad (131)$$

Here, ρ is the density of the fluid, U is the velocity of free stream air at the test section, D_h is the hydraulic diameter of the test section (130.3 cm), and μ and v are dynamic and kinematic viscosities of air, respectively. The flow at the test section was turbulent since $\mathbf{Re_D}$ was higher than 2200 (Biswas & V, 2002).

8.2.2.1 Selection of CFD Approach and Turbulence Model to solve the 2D CFD Model of the WIS Facility Wind Chamber

Since the general flow in the test section is turbulent and will be modelled in 2D, the Reynolds-averaged Navier-Stokes equations (RANS) approach will be used to find solutions to the computational domain. The RANS approach uses time-averaged fluctuating quantities to solve the computational domain of the 2D WIS facility.

Compared to full Navier-Stokes equations, additional terms in the RANS approach are modelled using classical turbulence models (Versteeg & Malalasekera, 2007). The FLUENT 6.3.26 software provides the following viscous models: Inviscid, Laminar, the single equation Spartlart-Allmaras, two equations *k*-epsilon (*k*-ε), *k*-omega (*k*-ω), and seven equations Reynolds Stress, Detached Eddy Simulation and Large Eddy Simulation (LES). Here, k represents turbulent kinematic energy; ε represents the turbulent dissipation rate and ω represents the specific dissipation rate. Equations (132), (133) and (134) define *k* and Equations (133) and (134) define ε, respectively.

$$\boldsymbol{k = \frac{1}{2}\left(\overline{(u_x')^2} + \overline{(u_y')^2} + \overline{(u_z')^2}\right)} \qquad \textbf{(132)}$$

here, u_x', $u_y'$and $u_z'$are turbulent velocity fluctuations in x, y, and z directions, respectively.

The turbulent dissipation rate (ε) is the rate at which *k* is converted into internal thermal energy. For compressible flows ε can be written as in Equation (133).

$$\boldsymbol{\varepsilon = 2\nu\overline{s'_{ij} \cdot s'_{ji}}} \qquad \textbf{(133)}$$

here, ν is the kinematic viscosity s'_{ij} and s'_{ji} are deformation tensors.

The specific turbulent dissipation rate ω is the rate at which *k* is converted into internal thermal energy per unit volume during a unit time. Therefore, the specific turbulent dissipation rate (ω) can be written using *k* and ε as given in Equation (134).

$$\boldsymbol{\omega = \frac{\varepsilon}{k\beta^*}} \qquad \textbf{(134)}$$

here, $\beta^* = C\mu$, where C is a constant equal to 0.09 and μ is dynamic viscosity.

8.2.2.1.1 Comparison of turbulent properties available in FLUENT close to wall surfaces

This section of the thesis aims to find an appropriate turbulence model that can be used to model the velocity distribution and turbulent properties close to wall surfaces where initial particle resuspension would take place.

The suitable turbulence model was selected by comparing velocity profiles and turbulent kinetic energy profiles found using different turbulence models available in FLUENT against Laminar (LAM), Large Eddy Simulation (LES) and Spalding's Law of the Wall velocity distributions. The LES model is usually used for 3D CFD modelling (Rodi, 1993), (Murakami & Mochida, 1995), but it was used here for benchmarking and comparing available viscous models in FLUENT.

8.2.2.1.2 Comparison of Velocity Profile Close to Wall Surfaces

Figure 122 shows the comparison of velocity magnitudes close to the floor of the WIS facility at the center of the contamination plate calculated using selected turbulence models available in FLUET 6. 3.26 software.

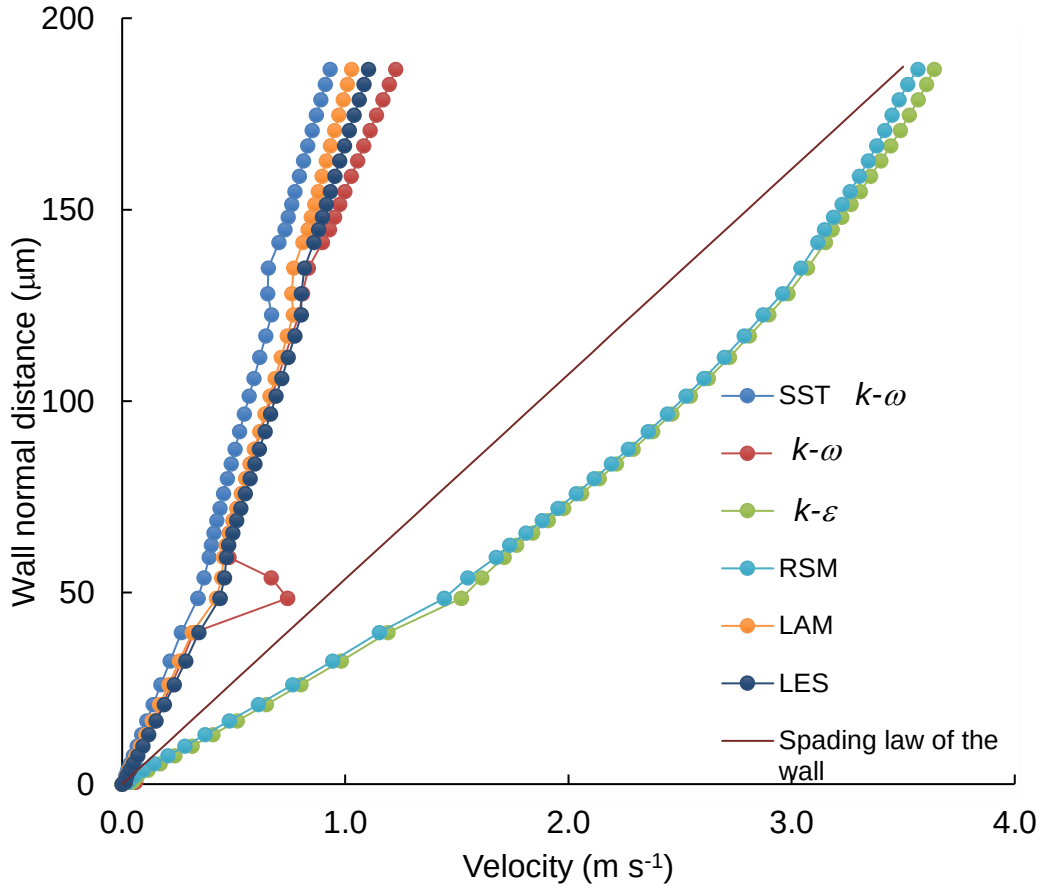

Figure 122 Comparison of velocity magnitude (m s^{-1}) found using k-ω SST, Standard k-ω, Standard *k-ε* and Reynolds Stress (RSM) turbulence models at the center of contaminated plate calculated against the Laminar (LAM) flow, Large Eddy Simulation (LES) and Spalding law of the wall velocity profiles.

A comparison of velocity profiles in Figure 122 shows that the velocity increases linearly up to 40 μm wall-normal distances for all viscous models. These profiles indicate that the thickness of the Laminar Sub Layer (LSL) at the center of the plate is 40 μm under steady-state operating conditions of the wind chamber.

Velocity profiles calculated for SST *k-ω* and Standard *k-ω* are similar to LAM and LES velocity profiles, but the velocity magnitudes calculated for a given wall-normal location for these models are lower than the Spalding's law of the wall velocity distribution.

Also, the Standard *k-ω* model shows a sudden increase in velocity just past the LSL region compared to the SST *k-ω* turbulence model, which uses a built-in transition function to smoothen the velocity from LSL to Buffer Layer (Fluent Inc., 2006).

Both Standard *k-ε* and Reynolds Stress Model (RSM) overpredicted velocity magnitudes compared to Spalding's law of the wall.

8.2.2.1.3 Comparison of Turbulent Kinetic Energy (k) close to wall surfaces

Comparison of Turbulent Kinetic Energies (k) for available turbulence models are shown in Figure 123 and Figure 124. These figures were separated due to their significant differences in values for k. Figure 123 shows the k values close to the wall surface found using Standard *k- ω* and *k-ω* SST turbulence models.

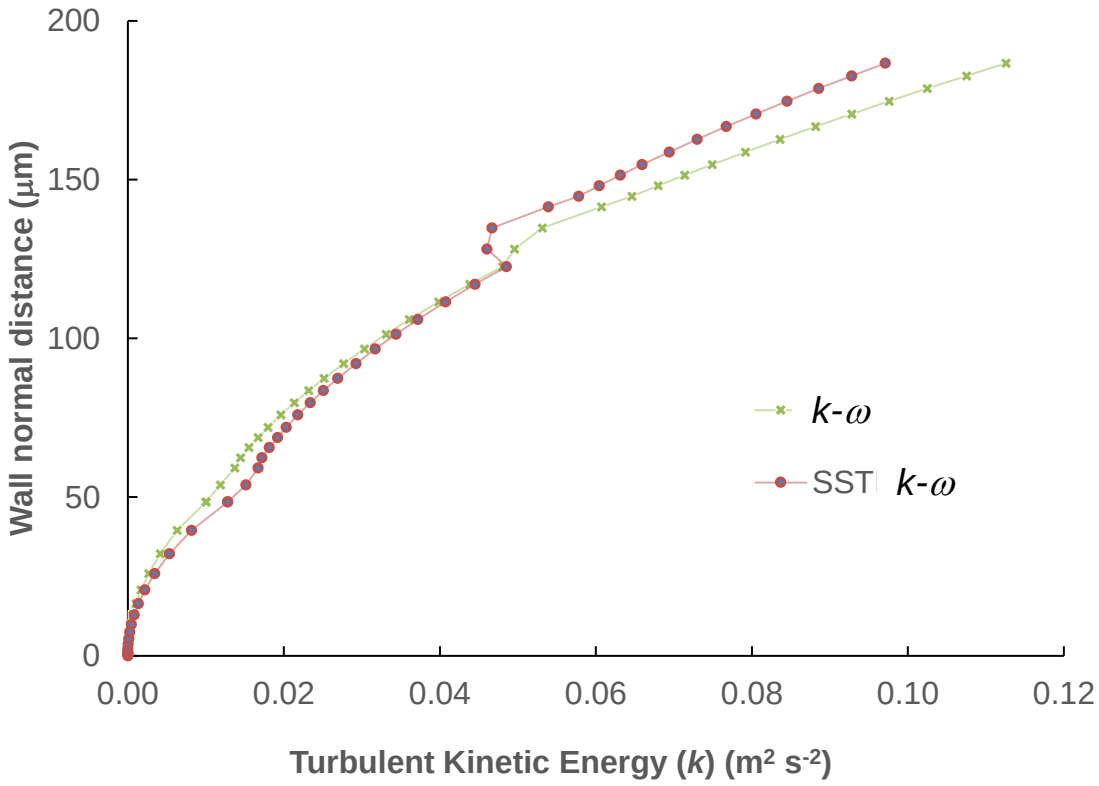

Figure 123:Wall normal distance versus Turbulent Kinetic Energy (k) at the center of the contaminated plate calculated for Standard *k-ω* and *k-ω* SST turbulence models under normal operating conditions of the wind chamber.

Turbulent Kinetic Energy (k) close to wall surfaces for *k-ω* SST and Standard *k-ω* turbulence models have similar trends. However, the k values for both models are minimal (< 0.01) $m^2 s^{-2}$ inside the LSL region compared to values found for both RSM and Standard *k-ε* turbulence models.

Figure 124 shows the Turbulent Kinetic Energy (k) values close to the WIS facility contamination plate floor calculated using RSM and Standard *k*-*ε* turbulence models.

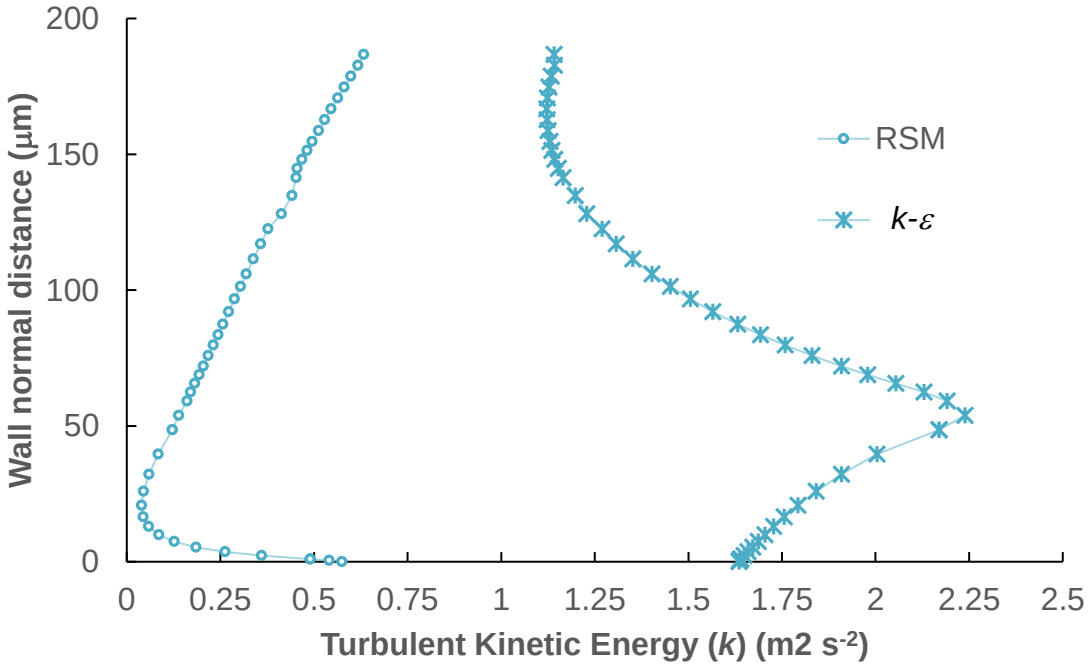

Figure 124: Wall-normal distance versus Turbulent Kinetic Energy (k) at the center of the contaminated plate calculated using RSM and Standard *k*-*ε* turbulence models under normal operating conditions of the wind chamber

Turbulent Kinetic Energy (k) values at the wall were calculated to be 0.57 m^2 s^{-2} and 1.64 m^2 s^{-2} for RSM and Standard *k*-*ε*, respectively, but the k values calculated for *k*-

ω SST and Standard k-ω turbulence models at the exact location were minimal (3.64E-8 m^2 s^{-2} and 5.11E-8 m^2 s^{-2} respectively).

As the wall-normal distance increased, the k value for RSM started to decrease to 0.04 m^2 s^{-2} at 20.8 µm and then increased to 0.63 m^2 s^{-2} at 200 µm. On the other hand, an opposite behaviour was observed for k values found for the Standard k-ε model; k values started increasing up to 2.23 m^2 s^{-2} at 53 µm and then began to reduce to 1.12 m^2 s^{-2} at 167 µm wall-normal distance.

Comparison of k values for k-ω SST, Standard k-ω, Standard k-ε, and RSM models show that both Standard k-ε and RSM models calculated unrealistic k and velocity values in near-wall regions. It was also found that the Standard k-ω turbulence model had difficulties figuring out the velocity transition from the LSL region to the Buffer region.

A comparison of available turbulence models in FLUENT software showed that the k-ω SST turbulence model could be used successfully to model the turbulent transport properties of the 2D CFD WIS facility wind chamber because of its superior capabilities in modelling turbulence kinetic energy and velocity profile close to the wall surface. Historically, the k-ω SST turbulence model has proven to predict accurate solutions for wall-bounded flows even in highly separated flow regions (Georgiadis & Yoder, 2006).

8.2.2.2 Shear Stress Transport (SST) k-ω turbulence model

The Shear Stress Transport (SST) *k-ω* turbulence model uses both standard *k-ω* and *k-ε* models. The standard *k-ω* and *k-ε* models are famous two equations turbulence models and information about these two models can be found in any turbulent flow fluid mechanics textbook. In the SST *k-ω* turbulence model, turbulent properties of the near-wall region of the boundary layer are modelled using the standard *k-ω* model and the rest of the turbulent flow properties are modelled using the standard *k-ε* model.

In the SST *k-ω* model, turbulent kinematic energy (*k*) and specific dissipation rate (ω) are modelled using Equations (135) and (136), respectively:

$$\frac{\partial}{\partial t}(\rho k) + \frac{\partial}{\partial x_i}(\rho k u_i) = \frac{\partial}{\partial x_j}\left(\Gamma_k \frac{\partial \omega}{\partial x_j}\right) + \widetilde{G}_k - Y_k + S_k \qquad (135)$$

and,

$$\frac{\partial}{\partial t}(\rho \omega) + \frac{\partial}{\partial x_i}(\rho \omega u_i) = \frac{\partial}{\partial x_j}\left(\Gamma_\omega \frac{\partial \omega}{\partial x_j}\right) + G_\omega - Y_\omega + D_\omega + S_\omega. \qquad (136)$$

here, terms Γ_k, and Γ_ω represent effective diffusivity of k and ω respectively. Terms $\tilde{G}_k$ and G_ω represent the generation of k and ω due to mean velocity gradients, respectively. Terms Y_k and Y_ω represent the dissipation of k and ω due to turbulences, respectively. The term D_ω represents the cross-diffusion term. The cross-diffusion term will blend the standard k-ω model and standard k-ε model parameters. Terms S_k and S_ω are user-defined source terms (Fluent Inc., 2006)

8.2.2.2.1 The effective diffusivities of k and ω

Effective diffusivities of k and ω (Γ_k and Γ_ω, respectively) are defined as Equations (137) and (138), respectively.

$$\boldsymbol{\Gamma_k = \mu + \frac{\mu_t}{\sigma_k}} \qquad \textbf{(137)}$$

and,

$$\boldsymbol{\Gamma_\omega = \mu + \frac{\mu_t}{\sigma_\omega}} \qquad \textbf{(138)}$$

where, μ is dynamic viscosity, σ_k and σ_ω are turbulent Prandtl numbers for k and ω respectively. Values of turbulent Prandtl numbers are calculated using Equations (139) and (140), respectively. The turbulent viscosity μ_t is computed by combining k and ω as given in Equation (144).

The turbulent Prandtl number for σ_k and σ_ω are defined by Equations (139) and (140), respectively.

$$\boldsymbol{\sigma_k = \frac{1}{\frac{F_1}{\sigma_{k,1}} + \frac{(1-F_1)}{\sigma_{k,2}}}} \qquad \textbf{(139)}$$

and,

$$\boldsymbol{\sigma_\omega = \frac{1}{\frac{F_1}{\sigma_{\omega,1}} + \frac{(1-F_1)}{\sigma_{\omega,2}}}} \qquad \textbf{(140)}$$

where, $\sigma_{k,1}$=1.176, $\sigma_{k,2}$=1.0, $\sigma_{\omega,1} = 2.0$, $\sigma_{\omega,2} = 1.0$ and the blending function F_1 is defined by Equation (141).

$$\boldsymbol{F_1 = tanh\left(\Phi_1^4\right)} \qquad \textbf{(141)}$$

The function Φ_1 depends on the location of the flow, and it is defined by Equation (142).

$$\Phi_1 = min\left[max\left(\frac{\sqrt{k}}{0.09\omega y}, \frac{500\mu}{\rho y^2 \omega}\right), \frac{4\rho k}{\sigma_{\omega,2} D_\omega^+ y^2}\right], \tag{142}$$

here, y is the distance to the next surface from the point of interest; μ is the dynamic viscosity of the fluid and the positive portion of cross-diffusion D_ω^+, defined by Equation (143).

$$D_\omega^+ = max\left[2\rho \frac{1}{\sigma_{\omega,2}} \frac{1}{\omega} \frac{\partial k}{\partial x_j} \frac{\partial \omega}{\partial x_j}, 10^{-10}\right] \tag{143}$$

The turbulent viscosity, μ_t, is computed using Equation (144).

$$\mu_t = \frac{\rho k}{\omega} \frac{1}{max\left[\frac{1}{\alpha^*}, \frac{SF_2}{a_1 \omega}\right]} \tag{144}$$

here, the term α^* is calculated using Equation (145), the term *S*, the strain rate magnitude is calculated using Equation (148), and the blending function F_2 is found by Equation (150).

$$\boldsymbol{\alpha^* = \alpha^*_\infty \left(\frac{\alpha^*_0 + \frac{Re_t}{R_k}}{1 + \frac{Re_t}{R_k}} \right)} \qquad \textbf{(145)}$$

here, $\alpha^*_\infty = 1.0$, $R_k = 6.0$, α^*_0 is calculated using Equation (146) and the term $\mathbf{Re}_t$ is defined by Equation (147).

$$\boldsymbol{\alpha^*_0 = \frac{\beta_i}{3}} \qquad \textbf{(146)}$$

where, $\beta_i = 0.072$.

$$\boldsymbol{Re_t = \frac{\rho k}{\mu \omega}} \qquad \textbf{(147)}$$

here, ρ and μ are the density and dynamic viscosity of the free stream air, respectively. The strain rate magnitude (strain invariant), S (Rumsey, Chris, 2011), is defined by Equation (148) and the blending function, F_2 is defined by Equation (150).

$$S = \sqrt{2S_{ij}.S_{ij}} \qquad (148)$$

where, S_{ij} is defined by Equation (149).

$$S_{ij} = \frac{1}{2}\left[\frac{\partial U_i}{\partial x_j} + \frac{\partial U_j}{\partial x_i}\right] \qquad (149)$$

The blending function used in Equation (144) is defined by Equation (150).

$$F_2 = tanh\left(\Phi_2^2\right) \qquad (150)$$

The function Φ_2 depends on the location of interest and is defined by Equation (151).

$$\Phi_2 = max\left[2\frac{\sqrt{k}}{0.09\omega y}, \frac{500\mu}{\rho y^2 \omega}\right] \qquad (151)$$

here, y is the distance to the next surface from the point of interest; μ is dynamic viscosity and ρ is the fluid density.

8.2.2.2.2 Generation k and ω ($\tilde{G}_k$ *and* G_ω respectively)

In the SST k-ω turbulence model, the production of turbulent kinetic energy due to the mean velocity gradient $\tilde{G}_k$ is defined by Equation (152).

$$\widetilde{\boldsymbol{G}}_{\boldsymbol{k}} = \boldsymbol{min}(\boldsymbol{G}_{\boldsymbol{k}}, \boldsymbol{10\beta\rho\beta^{*}k\omega}) \qquad \textbf{(152)}$$

here, G_k is evaluated using the Boussinesq hypothesis as given in Equation (153).

$$\boldsymbol{G}_{\boldsymbol{k}} = \boldsymbol{\mu}_{\boldsymbol{t}}\boldsymbol{S}^{\boldsymbol{2}} \qquad \textbf{(153)}$$

The term μ_t is turbulent viscosity, and it was defined earlier using Equation (144), and the term S is strain rate magnitude, and it was defined earlier using Equation (148).

Production or generation of ω, G_ω , is calculated using Equation (154)

$$\boldsymbol{G_\omega = \frac{\alpha}{\nu_t} G_k} \qquad \textbf{(154)}$$

here, the coefficient α is given by Equation (155), and G_k was calculated using Equation (153), and $\nu_t = \frac{\mu_t}{\rho}$, where μ_t is turbulent viscosity and ρ is the fluid density.

$$\boldsymbol{\alpha = \frac{\alpha_\infty}{\alpha^*}\left(\frac{\alpha_0 + \frac{Re_t}{R_\omega}}{1 + \frac{Re_t}{R_\omega}}\right)} \qquad \textbf{(155)}$$

here, R_ω=2.95, $\alpha_0 = \frac{1}{9}$, $\alpha^*$and $\mathbf{Re_t}$ were defined by Equations (145) and (147), respectively and α_∞ defined by Equation (156).

$$\boldsymbol{\alpha_\infty = F_1 \alpha_{\infty,1} + (1 - F_1)\alpha_{\infty,2},} \qquad \textbf{(156)}$$

where,

$$\boldsymbol{\alpha_{\infty,1} = \frac{\beta_{i,1}}{\beta^*_\infty} - \frac{\kappa^2}{\sigma_{\omega,1}\sqrt{\beta^*_\infty}}}} \quad \textbf{(157)}$$

and,

$$\boldsymbol{\alpha_{\infty,2} = \frac{\beta_{i,2}}{\beta^*_\infty} - \frac{\kappa^2}{\sigma_{\omega,2}\sqrt{\beta^*_\infty}}}} \quad \textbf{(158)}$$

here, $\kappa = 0.41$ and $\beta_{i,1} = 0.075$, $\beta_{i,2} = 0.0828$, $\sigma_{\omega,1}$=2.0, $\sigma_{\omega,2}$=2.0 and $\beta^*_\infty = 0.09$.

8.2.2.2.3 Dissipation of k and ω (Y_k and $Y\omega$ respectively)

The dissipation of turbulent kinetic energy, Y_k, can be written as in Equation (159).

$$\boldsymbol{Y_k = \rho\beta^* k\omega} \quad \textbf{(159)}$$

here, ρ is fluid density and β^* is defined by Equation (160).

$$\boldsymbol{\beta^* = \beta_i^*[1 + \zeta^* F(M_t)]} \qquad \textbf{(160)}$$

here, $\zeta^* = 1.5$ and β_i^* is defined by Equation (161), and the compressibility function, $F(M_t)$ is defined by Equation (162).

$$\boldsymbol{\beta_i^* = \beta_\infty^* \left[\frac{\frac{4}{15} + \left(\frac{R_{et}}{R_\beta}\right)^4}{1 + \left(\frac{R_{et}}{R_\beta}\right)^4} \right]}, \qquad \textbf{(161)}$$

here, $\beta_\infty^* = 0.09$, $R_\beta = 4$ and $\mathbf{R_{et}}$ was calculated using Equation (147) and,

$$\boldsymbol{F(M_t) = \begin{cases} 0 & M_t \le M_{t0} \\ M_t^2 - M_{t0}^2 & M_t > M_{t0} \end{cases}} \qquad \textbf{(162)}$$

here,

$$\boldsymbol{M_{t0} = 0.25} \qquad \textbf{(163)}$$

and,

$$M_t^2 = \frac{2k}{a^2} \tag{164}$$

where,

$$a = \sqrt{\gamma RT} \tag{165}$$

here, γ=1.4, R=297.04 J/kg K and T is the temperature of the free stream air measured in Kelvin The dissipation of ω, Y_ω, can be written as in Equation (166).

$$Y_\omega = \rho\beta\omega^2 \tag{166}$$

here, ρ is fluid density and β is defined by Equation (167).

$$\beta = \beta_i\left[1 - \frac{\beta_i^*}{\beta_i}\zeta^* F(M_t)\right] \tag{167}$$

here, β_i is defined by Equation (168) and β_i^* was previously defined by Equation (161).

$$\boldsymbol{\beta_i = F_1 \beta_{i,1} + (1 - F_1) \beta_{i,2}} \qquad \textbf{(168)}$$

here, $\beta_{i,1} = 0.075$, $\beta_{i,2} = 0.0828$, and the blending function F_1 was earlier defined by Equation (141).

8.2.2.2.4 Cross diffusion of ω

The cross diffusion term, D_ω, will combine the standard k-ω and the standard k-ε turbulence models. The value of D_ω is calculated using Equation (169).

$$\boldsymbol{D_\omega = 2(1 - F_1) \rho \sigma_{\omega,2} \frac{1}{\omega} \frac{\partial k}{\partial x_j} \frac{\partial w}{\partial x_j}}, \qquad \textbf{(169)}$$

here, the blending function F_1 defined earlier by Equation (141), ρ is fluid density and $\sigma_{\omega,2} = 1.0$.

8.2.2.3 Continuity and momentum equations

The continuity equation (conservation of mass) and momentum equations (conservation of momentum equations) for incompressible Newtonian fluid flow use in the RANS model are represented by Equations (170) and (171), respectively.

$$\frac{\partial \bar{u}_i}{\partial x_i} = 0 \qquad (170)$$

and,

$$\frac{\partial \bar{u}_i}{\partial t} + \bar{u}_i \frac{\partial \bar{u}_i}{\partial x_j} = -\frac{1}{\rho}\frac{\partial \overline{p}}{\partial x_i} + \nu \frac{\partial^2 \bar{u}_i}{\partial x_j \partial x_j} - \frac{\partial}{\partial x_j} R_{ij} \qquad (171)$$

where, subscripts i and j are free indices that can take 1, 2 and 3. Here $\bar{u}_i$ represents i th component of mean velocities and $\overline{p}$ is the mean (or average) static pressure at position x_i and time t. The density and kinematic viscosity of the fluid passing at this location are denoted by ρ and ν respectively. The Reynolds stress tensor, $R_{ij,}$ is given by $R_{ij} = \overline{u_i' u_j'}$. Fluctuation velocity components at location i can be written as $u_i' = \tilde{u}_i - \overline{u_i}$ (Shams, Ahmadi, & Smith, 2002). Here u_i' is instantaneous velocity.

8.2.2.4 Solving governing equations

The computational domain of the 2D WIS facility wind chamber had 428,213 mesh nodes. Solutions to this computational domain were found using an algorithm capable of solving nonlinear governing equations utilizing available computer power at Ontario Tech University. Therefore, a pressure-based, unsteady, implicit segregated solver was selected due to its lower computer memory requirement than the pressure-based coupled algorithm, but the rate of solution convergence for the segregated solver is significantly lower (Fluent Inc., 2006).

8.2.2.4.1 Selection of time integration method

The implicit time integration used here is unconditionally stable, unlike the explicit time integration, where the time step size is limited by the Courant-Friedrichs-Lewy (CFL) condition. The Courant number (C) is defined as given in equation (172).

$$C = \frac{u\Delta t}{\Delta x} \qquad (172)$$

here, u is velocity, Δt is the time step size, and Δx is the length interval. The corresponding Δt to solve equations of the 2D WIS facility wind chamber, using explicit time marching, was calculated to be 2.7 ns (using u = 6.5 m s^{-1} and Δx =188 μm) compared to the 10 μs time step size used in the implicit method to achieve solutions up to 1E-7 convergence criterion.

Since the 2D computational domain of the WIS facility was built using rectilinear mesh elements, the default Green-Gauss Cell-Based method was used to calculate convection terms of governing equations, secondary diffusion terms, and velocity derivatives. (Fluent Inc., 2006).

8.2.2.5 Comparison of 2D CFD Results with WIS facility experiment

The computational domain of the 2D WIS facility wind chamber flow field was solved until the 1E-7 residual convergence criterion for continuity, momentum and turbulence transport parameters were achieved. Converged results of the 2D WIS facility domain are presented in the following few sections.

8.2.2.5.1 Velocity Profiles

Figure 125 shows the comparison of velocity results found using the converged 2D CFD model and experimental results at the downstream hotwire anemometer grid location (Particle Sizer 2 location).

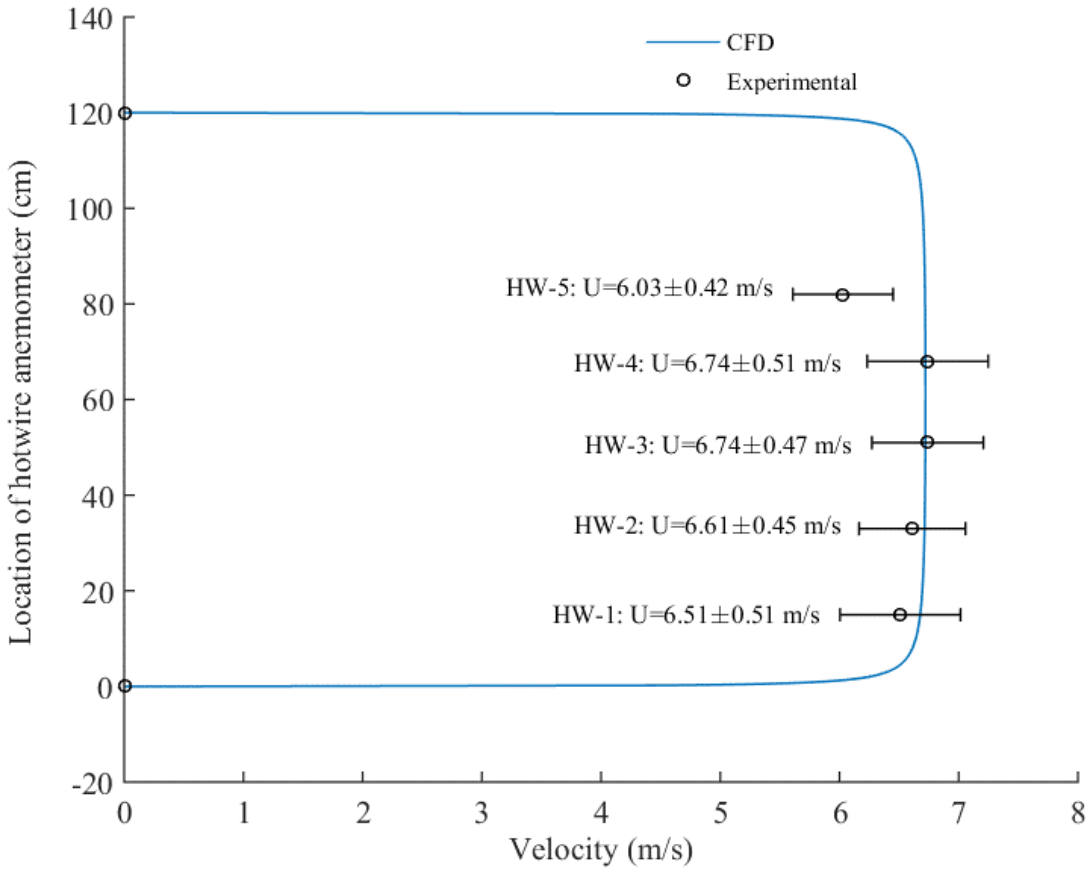

Figure 125: Comparison of velocity magnitudes found using 2D CFD (*k-ω* SST turbulence model), and experimental results at the downstream hotwire anemometer grid. CFD results were calculated across the vertical line running through tips of hotwire anemometers ($\mathbf{Re}_D$ = 5.6E5 for WIS facility normal operating conditions)

Figure 125 shows that 2D CFD results generated using FLUENT software successfully modelled the velocity magnitudes at the location of the hotwire anemometer grid except at the HW-5 location. The HW-5 is located at an elevation where the cross-section of the wind chamber changes its shape from rectangular to trapezium. The transition of the shape in the 3D physical domain was not introduced into the 2D WIS facility computational model due to the 2D approximation. Also, the location of the HW-5 is closer to the roof of the wind chamber rather than the floor where initial particle resuspension would occur.

8.2.2.5.2 2D CFD results

The 2D CFD model of the WIS facility was solved using a FLUENT double-precision solver. The results under this section show converged solutions (up to 10^{-7}) of the 2D, WIS computational domain at 9.4282E-1 s. flow time. The computational domain consists of 428,213 rectilinear mesh elements, and the average Reynolds number of the mean flow of the test chamber (center of the wind chamber) based on the hydraulic diameter of the WIS facility experiment was calculated to be between 104 and 106 at SAC. Solutions were found at standard operating conditions, and closure to RANS equations was achieved using k-ω SST turbulence model. Please refer to the CFD modelling of the 2D WIS facility section for more details.

Figure 126 shows the velocity contour plots of the 2D WIS facility wind chamber.

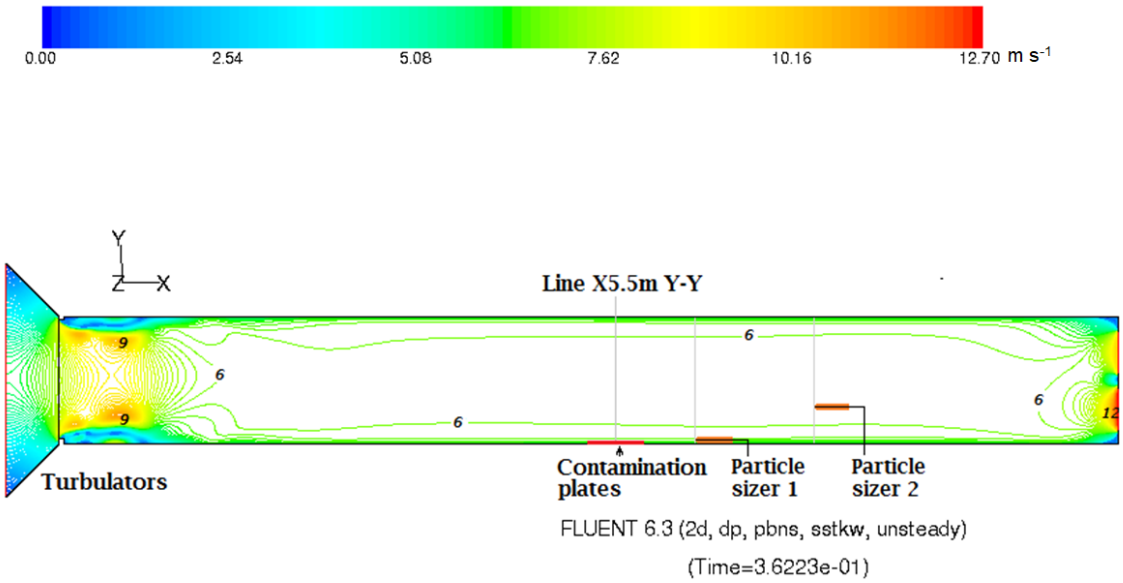

Figure 126: Velocity magnitude contours (m s -1) of the 2D WIS facility computational domain. ($\mathbf{Re}_L$ = 5.6E5 at SAC)

According to CFD results, air from the WIS facility surroundings enters the wind chamber at a maximum velocity of 5.9 m s^{-1} at the center of the inlet. Beyond this point, velocity magnitude increased through the converging section up to 7.4 m s^{-1} at the center of the perforated mesh location. As airflow turns the corner from the converging section to the settling section of the wind chamber, airflow near the wall surfaces goes over the 10 cm tall turbulator, increasing its velocity up to a maximum of 9 m s^{-1} due to vortices formed at the aft of the trubulator. After this point, flow inside the wind chamber started to settle

down towards the test section, where contamination plates were placed around the mid-section of the wind chamber.

Velocity vectors of selected sections of the wind chamber (Inlet, Verticle line at x=5.5 m, and at the Fans) are shown in Figure 127.

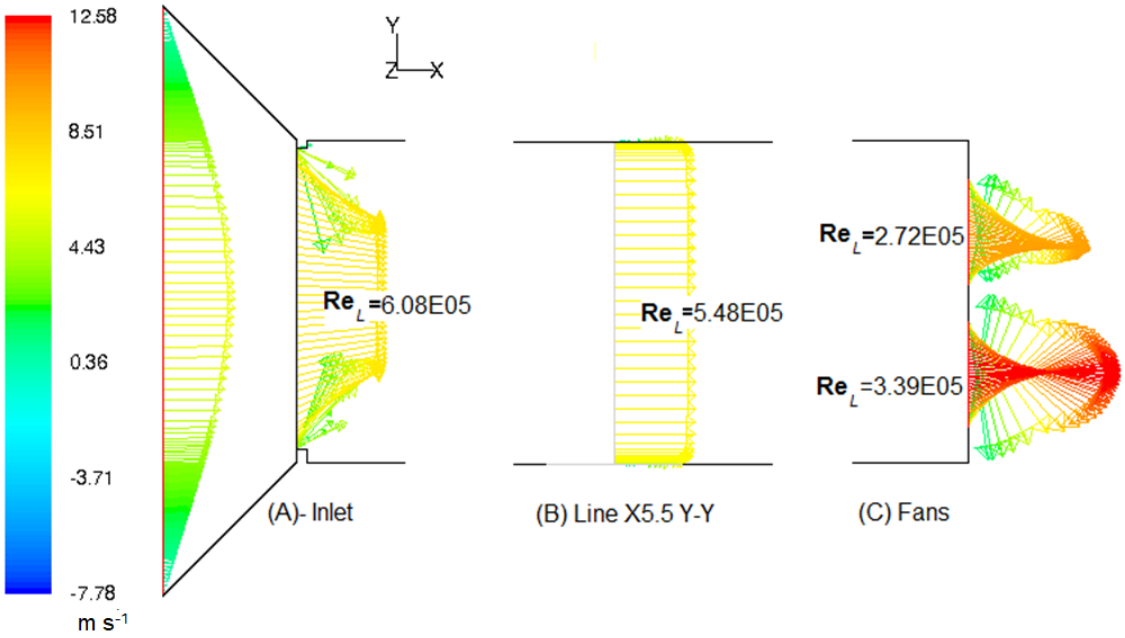

Figure 127: Velocity vectors, coloured by velocity magnitude, of selected locations and corresponding maximum hydraulic diameter based Reynolds number ($\mathbf{Re}_L$ = 5.6E5) at WIS facility normal operating conditions. Profile (A)- Inlet and Perforated Mesh, profile (B)-Line X5.5m Y-Y and profile (C)-Fans

As shown in Figure 127, the velocity vector profile of the Inlet has a hyperbolic shape with a velocity of 5.9 m s^{-1} at the focus. The velocity profile at the mid-section of

the Perforated Mesh has almost a linear velocity profile averaging at 7.4 m s^{-1}. The velocity vector profile at Line X5.5 Y-Y (the vertical line at X=5.5 m) is almost linear across the test section except near the ceiling and the floor of the wind chamber. The velocity vector patterns at Fan 1 (top) and Fan 2&3 (below) show a fanning effect with maximum velocities of 10.2 m s-1 and 12. 6 m s^{-1}, respectively.

Figure 128 shows the x-velocity contour plots, and Figure 129 shows the y-velocity contour plots of the 2D WIS facility wind chamber.

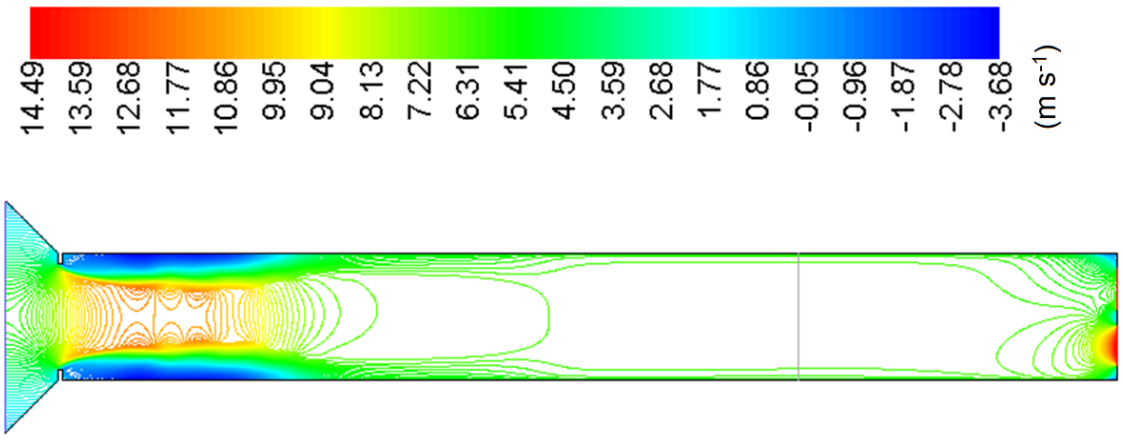

Figure 128: Contours of X velocity (m s^{-1}) of 2D CFD model of WIS facility

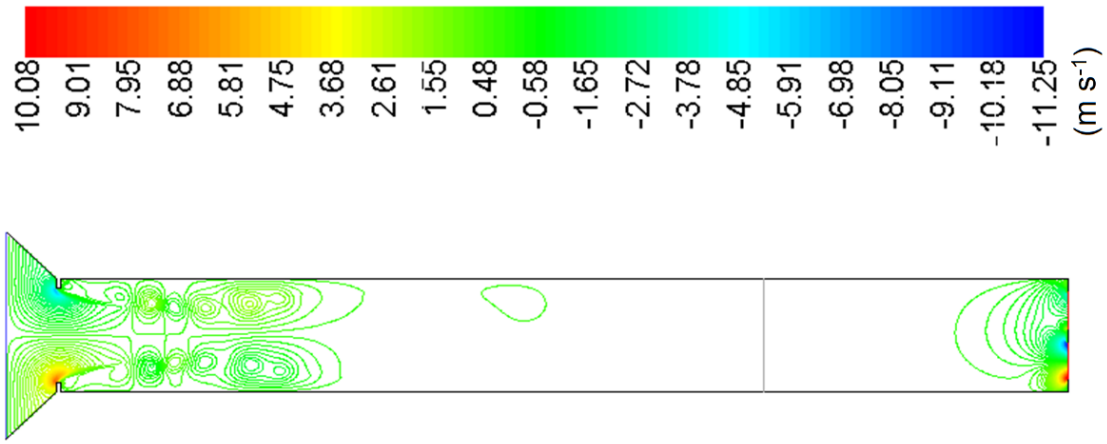

Figure 129: Contours of Y velocity (ms^{-1}) of 2D CFD model of WIS facility

Figure 130 and Figure 131 show the contour plots of turbulent velocity and turbulent intensity (%) of the 2D CFD model.

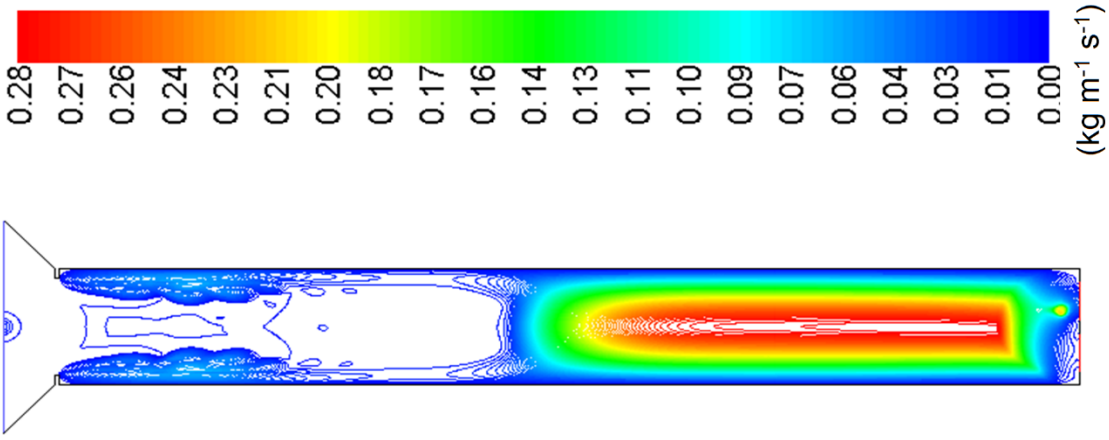

Figure 130: Contours of Turbulent Viscosity (kg m^{-1} s^{-1}) of 2D CFD model of WIS facility

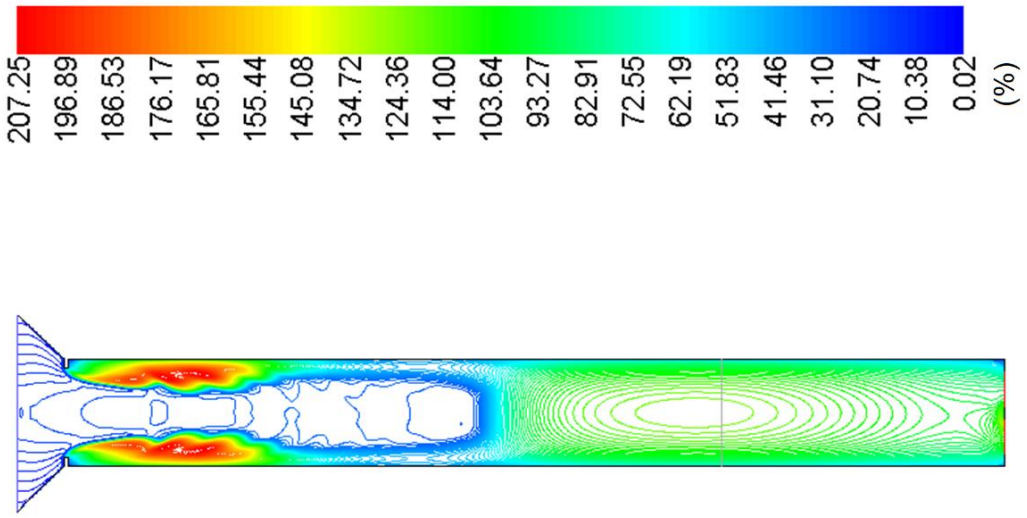

Figure 131: Contours of Turbulent Intensity (%) of 2D CFD model of WIS facility

Figure 132 shows the contour plots of Turbulent Kinetic Energy of the 2D CFD model.

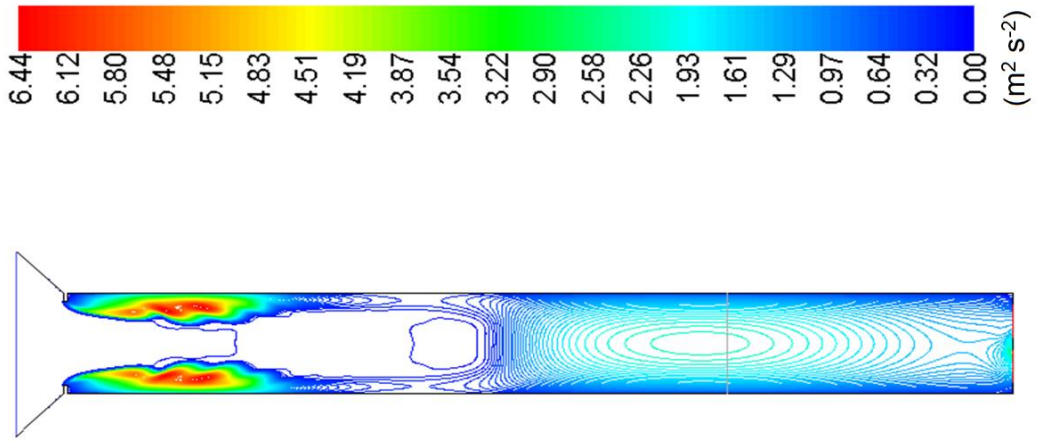

Figure 132: Contours of Turbulent Kinetic Energy (m^2 s^{-2}) of 2D CFD model of WIS facility

8.2.2.6 Velocity and Pressure Profile at 100 µm above the contaminated plate

The ceiling boundary of the Regional computation domain is located 100 µm above the contaminated plate. The velocity and pressure values required to model the ceiling boundary of the Regional computation domain were calculated from the converged Global WIS facility CFD model.

Figure 133 shows the CFD results of windward (V_x), wall-normal (V_y), and transverse velocity (V_z) contour plots of an imaginary plane located 100 µm above the contamination plates found from the Global CFD model as a vortex passing by.

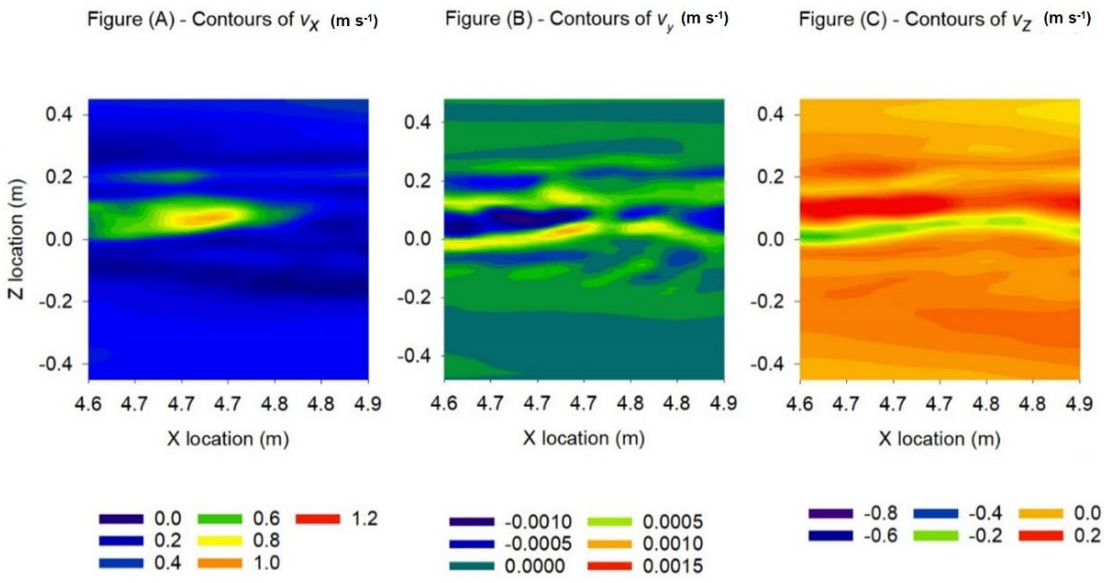

Figure 133: Contour plots of stream-wise velocity, V_x (m s^{-1}), wall-normal velocity, V_y (m s^{-1}) and span-wise velocity, V_z (m s^{-1}) of a bounded plane (0.5 m x 0. 5 m), located at 100 µm above and parallel to the contamination plate (as per FLUENT Average Reynolds Number is 35.7)

The area average stream-wise velocity (V_x) has a mean velocity of 0.8932 ± 0.4230 m s^{-1}, with the highest V_x close to the center of the contamination plate. The average wall-normal velocity (V_y) has a mean velocity of -0.000004517 ± 0.001259 m s^{-1}. Finally, the area average span-wise velocity (V_z) has a mean velocity of 0.01350 ± 0.3232 m s^{-1} with the highest variation of V_z around the center of the bounded imaginary boundary plane.

Figure 134 shows the projections of V_x, V_y, V_z, and static pressure values onto the X (stream-wise) and Z (span-wise) axes.

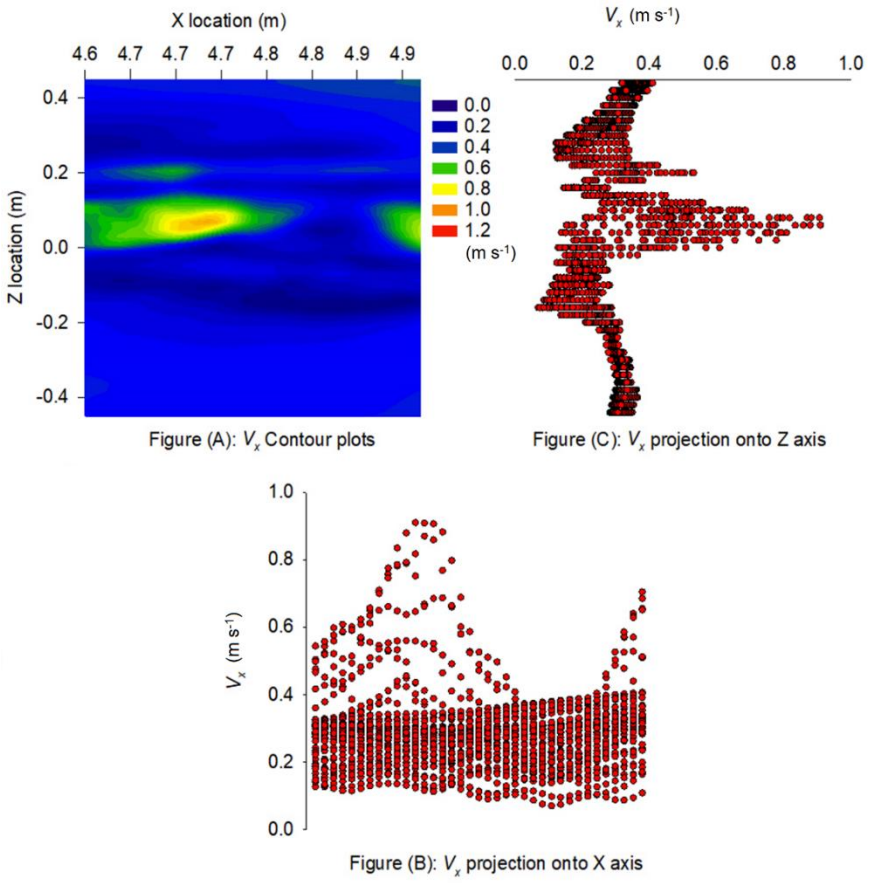

Figure 134: V_x velocity projections onto the X and Z axis

Figure 135 B and C show that two peaks of V_x are present on the imaginary plane located 100 μm above the contamination plates. The first peak, V_x = 0.8985 m s^{-1}, appears at x= 4.7290 m and z= 0.0530 m locations, and the second peak, V_x = 0.6962, appears at x = 4.9690 and z = 0.0190 m location. The distance between these two peaks is 0.2400 (m).

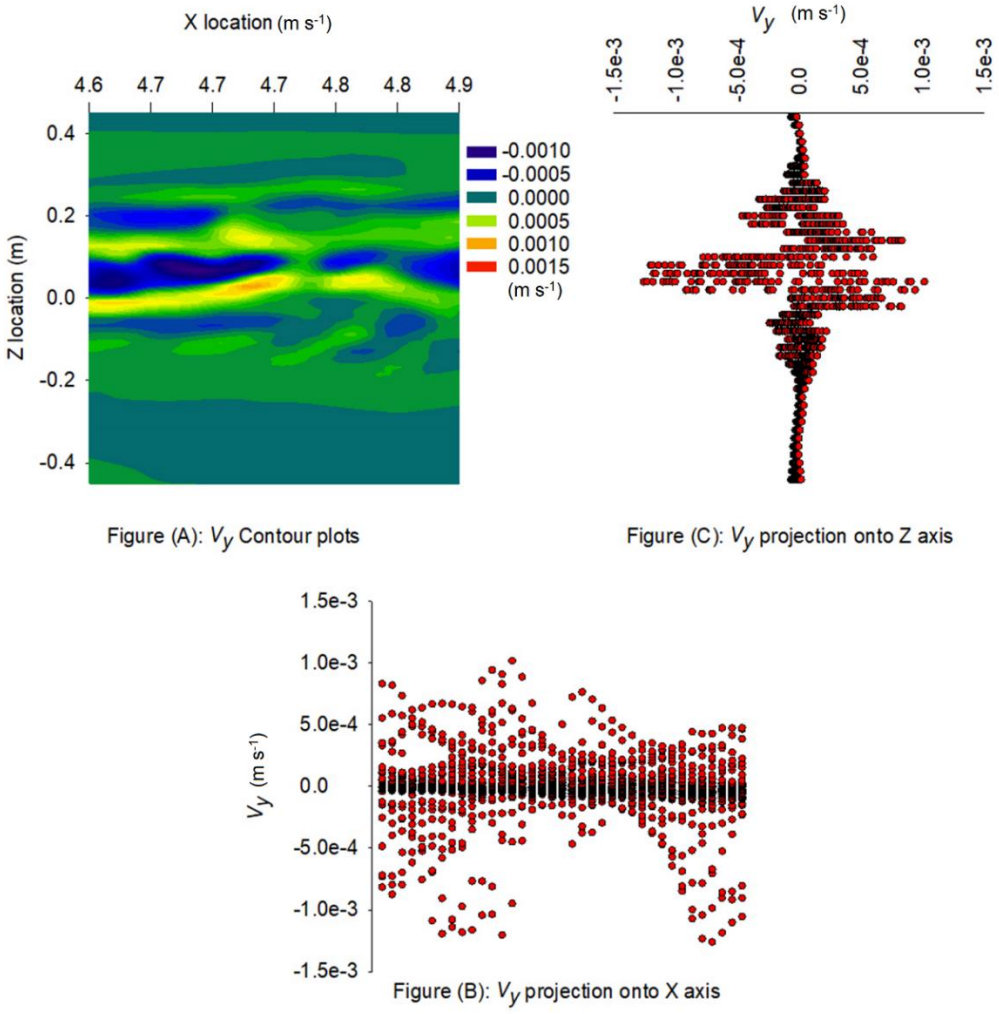

Figure 135: V_y velocity projections onto the X and Z axis

Figure 135 B and C show that there are five peaks and four valleys of V_y along with Y locations of the imaginary plane.

The locations of the peaks and the valleys are tabulated in Table 23

Table 23: V_y peaks and valleys along with X location from Figure 135.

Inflection point	**Peak (p) / Valley (v)**	**X Location (m)**	***Vy* (m s^{-1})**
1	p	4.610	0.0008560
2	v	4.620	-0.0008740
3	p	4.669	0.0006870
4	v	4.700	-0.001162
5	p	4.740	0.001016
6	v	4.800	-0.0004670
7	p	4.810	0.0007630
8	v	4.940	-0.001259
9	p	4.960	0.0004700

The peaks for Vy along the Z locations are shown in Table 24.

Table 24: Vy peaks and valleys along Z location from Figure 135.

Inflection point	**Peak (p) / Valley (v)**	**Z Location (m)**	***V_y* (m s^{-1})**
1	p	0.200	-0.0004560
2	v	0.140	0.0008330
3	p	0.060	-0.001181
4	v	0.040	0.001016

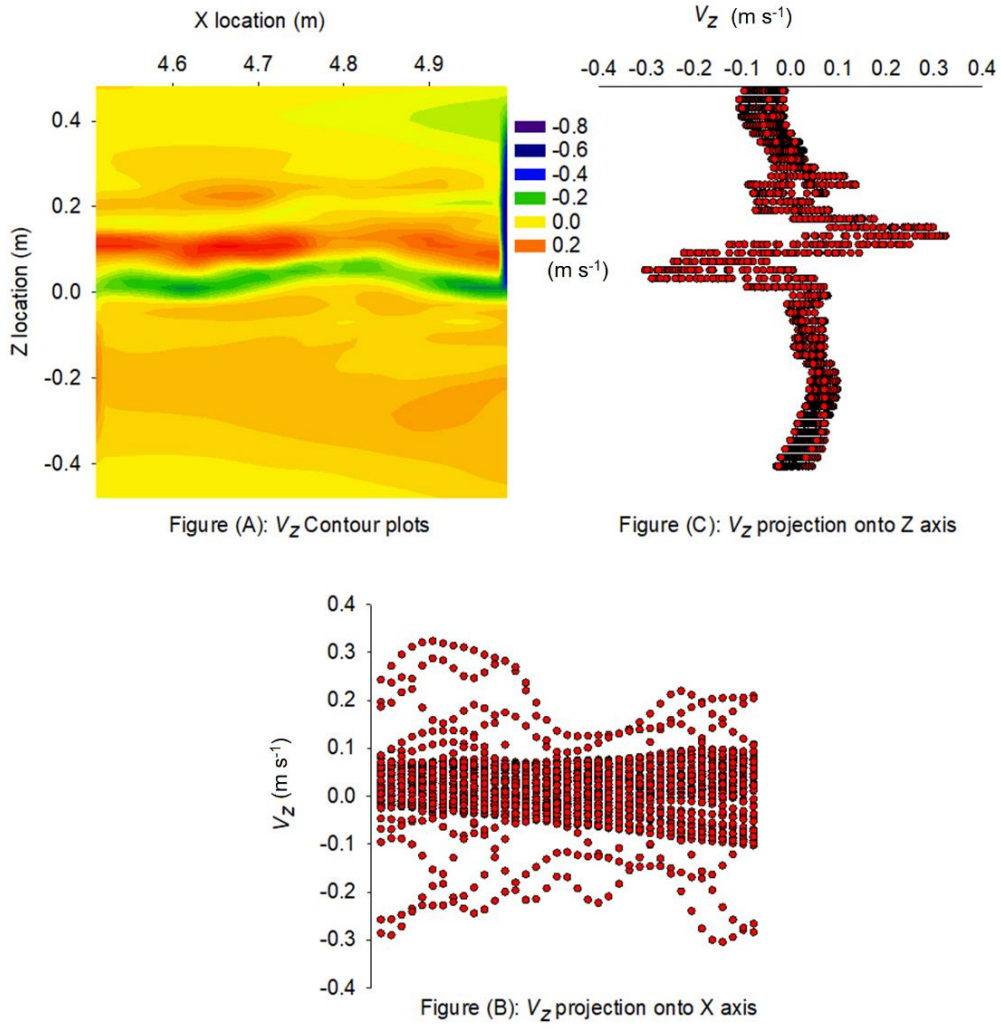

Figure 136: V_Z velocity projections on to X and Z axis

Figure 136 B and C show that there are 3 peaks and 5 valleys of V_z along with the Y location of the imaginary plane. Locations of the peaks and Vz valleys are tabulated in Table 25.

Table 25: VZ peaks and valleys along with the X Location from Figure 136.

Inflection point	Peak (p) / Valley (v)	X Location (m)	V_Z (m s^{-1})
1	v	4.615	-0.2901
2	p	4.660	0.3232
3	v	4.700	-0.2444
4	v	4.750	-0.2165
5	v	4.820	-0.2226
6	p	4.900	0.2191
7	v	4.940	-0.3044
8	p	4.560	0.2050

The peaks for V_z along the Z locations are shown in Table 26.

Table 26: VZ peaks and valleys along Z location from Figure 136.

Inflection point	Peak (p) / Valley (v)	Z Location (m)	V_Z (m s^{-1})
1	p	0.220	0.1359
2	v	0.200	-0.0704
3	p	0.100	0.3206
4	v	0.020	-0.2997

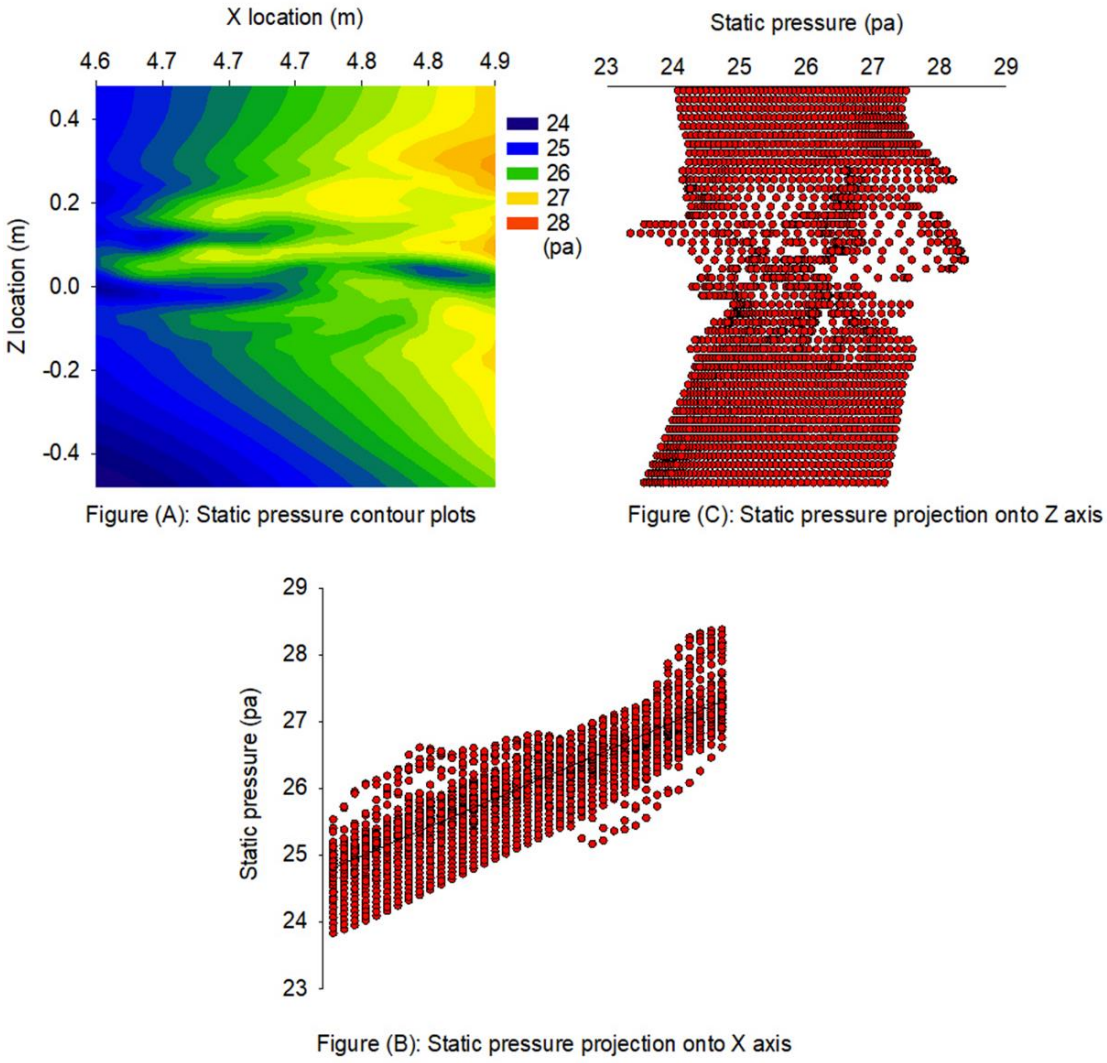

Figure 137: Pressure projections on to X and Z axis

Figure 137 B shows that the projected average static gauge pressure increases almost linearly from 24.76 Pa to 27.34 Pa from the upstream to the downstream end of the bounded imaginary plane with a slope of 5.31 Pa m^{-1}.

Also, there are two prominent static pressure peaks, p = 26.61 (Pa), at X = 4.69 (m) and p = 28.36 (Pa), at X = 4.959 (m); one static pressure valley, p = 25.46 (Pa), was found at x= 4.89 (m) location.

9 APPENDIX C

9.1 Computer codes used in the thesis

9.1.1 MATLAB code to find the Reynolds number for 0.25, 10. 32, 100 and 150 μm diameter spherical particles

```
% Prepared by Sharman Perera, MASc
%  November 03rd 2010
clear;
clf;
%  Reynolds number vs. Velocity for  0.25e-6 1e-6 10e-6 32e-6 70e-6 100e-6
150e-6 micro meter particles
grid on
format long eng;


rhoair=1.225;
la2o3=6.51;                                          %La2O3 6.51g/cm^3
la2o3=(la2o3/1000)/(1/100)^3;
rhop=la2o3;
mu=1.79e-5;
    Up=0;
    vv=0;


dp=[0.25e-6 1e-6 10e-6 32e-6 70e-6 100e-6 150e-6];
for dd=1:length(dp);
for uu=0:120/3.6;
vv=vv+1;
Rey(dd,vv)=rhoair*dp(dd)*abs(Up-uu)/mu;
```

```
UU(dd,vv)=uu;
        end
loglog(UU(dd,:),Rey(dd,:),'.-');
xlabel('velocity (m/s)');
ylabel('Reynolds number');
title('Reynolds number vs. velocity')
hold on
s=num2str(dp(dd)/1e-6);
ss=['dp = ',s,'\mum'];
text(max(UU(dd,:))/.9,max(Rey(dd,:)),ss,'FontSize',8);
end


Rmax_10mm=rhoair*10e-6*abs(0-120/3.6)/mu;
SS=sqrt(1.4*287*300);
format short
Mmax=max(uu)/SS       %       M>0.3       is       compressible       flow--
%http://en.wikipedia.org/wiki/Compressible_flow
text(     7,4,'32     \mum     diameter     La2O3     powder     in     still..
air','FontSize',8,'BackgroundColor',[.7                                    .9
.7],'HorizontalAlignment','center');
```

9.1.2 MATLAB code to validate the equation used in FLUENT to find the coefficient of drag on spherical particles against published experimental data

```
% Prepared by Sharman Perera, MASc
clear;
clf;
grid on
format short

CdVsRe= xlsread('CdVsRey_Digitized_45points2.xls');
ReyD=CdVsRe(:,1)*.88;
CdD=CdVsRe(:,2)*.88;
loglog(ReyD,CdD);

f=1;   %Shape factor
 cc=0;

for count= 1:length(ReyD)
ReyF(count)=ReyD(count);
b1=exp(2.3288-6.481*f+2.4486*f^2);  %Constant to calculate Cd
b2=0.0964+0.5565*f; %Constant to calculate Cd
b3=exp(4.905-13.8944*f+18.4222*f^2-10.2599*f^3);    %Constant to calculate
Cd
b4=exp(1.4681+12.2584*f-20.7322*f^2+15.8855*f^3);   %Constant to calculate
Cd
CdF(count)=24/ReyF(count)*(1+b1*ReyF(count)^b2)+b3*ReyF(count)/(b4+ReyF(co
unt));
%Stokes Law
if ReyF(count)<10;
ReyS(count)=ReyD(count);
```

```
CdS(count)=24/ReyS(count);
            end


PerDifD_F_Cd(count)=(CdF(count)-CdD(count))/CdD(count)*100;


    end


    figure(1)
loglog(ReyD,CdD,'-.r',ReyS,CdS,':',ReyF,CdF,'linewidth',2);% D - Digitized,
S-Stokes,F-FLUENT
legend('Zarin,N.A','Stokes','FLUENT')


xlabel('Reynolds number');
ylabel('Cd');
title('Cd vs. Reynolds number');


     figure(2)
semilogx(ReyD(1:21),PerDifD_F_Cd(1:21));
xlabel('Reynolds number');
ylabel('% Difference in Cd use in FLUENT vs. Zarin, N.A.');
title('% Difference in Cd use in FLUENT against Zarin, N.A.');
```

9.1.3 MATLAB code to calculate the drag force acting on 0.25, 10, 32, 70, 100 and 150 μm diameter spherical particles released into the air moving at 33.33 m/s and to compare the drag force against forces due to gravity.

```
% Prepared by Sharman Perera, MASc
clear;
clf;
grid on;
format long;
rhoair=1.225;
la2o3=6.51;%La2O3 6.51g/cm^3
la2o3=(la2o3/1000)/(1/100)^3;
rhop=la2o3;
mu=1.79e-5;
    Up=0;

Up=0;
U=120/3.6;

dp=[0.25e-6 1e-6 10e-6 32e-6 70e-6 100e-6 150e-6];
for jj=1:length(dp)
Rey=rhoair*dp(jj)*abs(Up-U)/mu
    cc=0;
for Rey=0:.01:Rey;
            %Calculate Cd
cc=cc+1;
f=1;    %Shape factor
b1=exp(2.3288-6.481*f+2.4486*f^2);  %Constant to calculate Cd
b2=0.0964+0.5565*f; %Constant to calculate Cd
```

```
b3=exp(4.905-13.8944*f+18.4222*f^2-10.2599*f^3);    %Constant to calculate
Cd

b4=exp(1.4681+12.2584*f-20.7322*f^2+15.8855*f^3);   %Constant to calculate
Cd

Cd(jj,cc)=24/Rey*(1+b1*Rey^b2)+b3*Rey/(b4+Rey);

Fd1(jj,cc)=18*mu/(rhop*dp(jj)^2)*Cd(jj,cc)*Rey/24;

m(jj)=4/3*pi()*(dp(jj)/2)^3*rhop;

Fg(jj,cc)=m(jj)*9.817;% Gravitational force acting on 10 mic diameter
particle

Fd(jj,cc)=Fd1(jj,cc)*abs(Up-U)*m(jj);

Rey1(jj,cc)=Rey;


    end
      figure (1)


loglog(Rey1(jj,:),Fd(jj,:),'r-')
      hold on
loglog(Rey1(jj,:),Fg(jj,:),'b--')
xlabel('Reynolds number', 'FontSize',14)
ylabel('mF_d(U-Up) (N)and mF_g_y  (N)', 'FontSize',14);
legend('mF_d(U-Up)','mF_g_y');
%title(['Force due to drag vs. Reynolds number upto max|(Up-U)|=
',num2str(U),' m/s, ','\phi =',num2str(f)]);
s=num2str(dp(jj)/1e-6);
ss=['d_p = ',s,'\mum'];
text(max(Rey1(jj,:))*1.05,max(Fd(jj,:))/0.9,ss,'FontSize',8);
text(max(Rey1(jj,:))*1.05,max(Fg(jj,:))/0.9,ss,'FontSize',8);
      hold on
end


figure (2)
loglog(Rey1(jj,:),Cd(jj,:),'.b-');
xlabel('Reynolds number');
ylabel('Cd');
```

```
title(['Cd vs. Reynolds number for max|(Up-U)|= ',num2str(U),',\phi
=',num2str(f)']);

Max_drag_10um_at_33p33m_s_speed=max(Fd(3,:))

Fd_over_Fgy_for_10um=max(Fd(3,:))/max(Fg(3,:))

Fd_over_Fgy_for_1um=max(Fd(2,:))/max(Fg(2,:))
```

9.1.4 MATLAB code to track the particle path of spherical particles with diameters of 0.25, 1, 2, 4, 6 and 10 μm launched with 33.3 m s^{-1} velocity with 45°angle with reference to +ve X-axis into 6 m s^{-1} free stream velocity at standard atmospheric conditions.

```
% Prepared by Sharman Perera
clc;
clear;
clf;
format bank;

% Environmental parameters
rho=1.225   % Density of air at Std. conditions
mu=1.79e-5; % Dynamic viscosity of air at Std. conditions
g=9.817;    % Acceleration due to gravity
u=6;        % X component of free stream velocity in m/s
v=0;        % Y component of free stream velocity in m/s
z=0;        % Z component of free stream velocity in m/s

% Particle parameters
rhop=6510   % Density of La2O3 powder in kg/m^3
% particle parameters to calculate the coefficient of drag
f=1;   %Shape factor
b1=exp(2.3288-6.481*f+2.4486*f^2);  %Constant to calculate Cd
b2=0.0964+0.5565*f; %Constant to calculate Cd
b3=exp(4.905-13.8944*f+18.4222*f^2-10.2599*f^3);    %Constant to calculate
Cd
b4=exp(1.4681+12.2584*f-20.7322*f^2+15.8855*f^3);   %Constant to calculate
Cd
```

```
% Particle launching properties

Upl=33.3;     % Particle initial velocity in m/s

beta=45;    % Initial launching angle of the particle in degrees w.r.t +ve
X

gamma=60;   % Initial launching angle of the particle in degrees w.r.t.+Z

% lunching location

h=1; % height of the box in (m)

w=1; % width of the box in (m)

r=sqrt((h/2)^2+(w/2)^2);


% Solution control

del_t=1e-6;  % Size of the time step

N_steps=1000;   % Number of time steps


tend=10;


% Initial conditions at time =0

theta(1)=beta;

ux(1)=Upl*cosd(beta);

vy(1)=Upl*sind(beta);

wz(1)=Upl*cosd(gamma)


time(1)=del_t;

x(1)=0;

y(1)=0;

z(1)=0;


dp=[0.25e-6 1e-6 2e-6  4e-6  6e-6 10e-6 ];% Particle diameter in m 0.25e-6
1e-6 2e-6  4e-6  6e-6 10e-6 32e-6 70e-6 100e-6 150e-6


% Create figure

figure1 = figure;
```

```
% Create axes
axes1 = axes('Parent',figure1,'YScale','log','YMinorTick','on',...
'XMinorTick','on',...
'PlotBoxAspectRatio',[1 1 1],...
'FontName','Arial',...
'FontSize',14);
box(axes1,'on');
hold(axes1,'all');

for dd=1:length(dp);
d=dp(dd);
for i=1:N_steps;

Rey_u(i)=rho*ux(i)*d/mu;
Rey_v(i)=rho*vy(i)*d/mu;
Rey_w(i)=rho*wz(i)*d/mu;

Cd_u(i)=24/(Rey_u(i))*(1+b1*(Rey_u(i))^b2)+b3*(Rey_u(i))/(b4+(Rey_u(i)));
Cd_v(i)=24/Rey_v(i)*(1+b1*(Rey_v(i))^b2)+(b3*Rey_v(i))/(b4+Rey_v(i));
Cd_w(i)=24/Rey_w(i)*(1+b1*(Rey_w(i))^b2)+(b3*Rey_w(i))/(b4+Rey_w(i));

kD_u(i)=3/4*Cd_u(i)/d*rho/rhop;
kD_v(i)=3/4*Cd_v(i)/d*rho/rhop;
kD_w(i)=3/4*Cd_w(i)/d*rho/rhop;

theta(i)=atand(real(vy(i))/real(ux(i)));

t=del_t;
ux(i+1)=(-t*kD_u(i)*u^2+t*kD_u(i)*u*ux(i)+ux(i))/(1-
t*kD_u(i)*u+t*kD_u(i)*ux(i));
wz(i+1)=(-t*kD_w(i)*w^2+t*kD_w(i)*w*wz(i)+wz(i))/(1-
t*kD_w(i)*w+t*kD_w(i)*wz(i));
```

```
vy(i+1)=-tan(t*sqrt(g*kD_v(i))-
atan(vy(i)*kD_v(i)/sqrt(g*kD_v(i))))*sqrt(g*kD_v(i))/kD_v(i);

%vy(i+1)=-(-vy(i)*kD_v(i)+tan(t*sqrt(kD_v(i)*g)-arctan(kD_v(i)*(v-
vy(i))/sqrt(kD_v(i)*g)))*sqrt(kD_v(i)*g))/kD_v(i)



x(i+1)=(t*kD_u(i)*u+log(1-
t*kD_u(i)*u+t*kD_u(i)*ux(i))*cosd(theta(i))+x(i)*kD_u(i))/kD_u(i);

z(i+1)=(t*kD_w(i)*w+log(1-
t*kD_w(i)*w+t*kD_w(i)*wz(i))*cosd(theta(i))+z(i)*kD_w(i))/kD_w(i);

y(i+1)=log(sqrt(g*kD_v(i))+vy(i)*sind(theta(i))*kD_v(i)*tan(t*sqrt(g*kD_v(
i))))/kD_v(i)-(1/2)*log(1+tan(t*sqrt(g*kD_v(i)))^2)/kD_v(i)-(1/2)*(-
2*y(i)*kD_v(i)+log(g*kD_v(i)))/kD_v(i);



time(i+1)=time(i)+del_t;

end



quiver(x,y,gradient(x),gradient(y),.2)



plot(x,y,'-','LineWidth',2,'MarkerSize',2)

xlabel('X location, m');

ylabel('Y location, m');

% title('Particle track of selected particles');

hold on



Dp=dp*1e6;

s=num2str(Dp(dd));

ss=['d_{p}','= ',s,'\mum'];



text(max(x(i)),max(y(i)),ss,'FontSize',10,'FontName','Arial','FontAngle','
italic');

hold on



end



format short;
```

```
TT=del_t*N_steps;

s2=num2str(TT);

s2=['Time of flight =',s2,' s']

text(max(x(i))*0.6,max(y(i))*0.0005,s2,'FontSize',10,'FontName','Arial','F
ontAngle','normal');

ylim([0,0.02]); xlim([0,0.02]);
```

9.2.1 MATLAB code used to plot the size and mass distribution of powder

```
clear;

clf;

clc;

close all

cc=1;

for dp=[0.001:0.001:10,11:100];


IFD(cc)=1-0.5*(1-1/(1+0.00076*dp^2.8)); % Inhalable fraction as used by ICRP
model

DFha(cc)=IFD(cc)*(1/(1+exp(6.84+1.183*log(dp)))+1/(1+exp(0.924-
1.1885*log(dp)))); % The deposition fraction for the head airways

DFtb(cc)=(0.00352/dp)*[(exp(-0.234*(log(dp)+3.40)^2)+63.9*exp(-
0.819*(log(dp)-1.61)^2))]; % Deposition fraction for the tracheobronchial
region

DFal(cc)=(0.0155/dp)*[exp(-0.416*(log(dp)+2.84)^2)+19.11*exp(-
0.482*(log(dp)-1.362)^2)]; % Deposition fraction for the alveolar region

DF(cc)=IFD(cc)*[0.0587+0.911/(1+exp(4.77+1.485*log(dp)))+0.943/(1+exp(0.50
8-2.58*log(dp)))];% Total deposition fraction for particle size dp

rho_p=6500;% density of the particle

rho_0=1000;

N=1000; % Number concentration of particles of diameter dp

Vm=1; % minute volume or volume inhaled in 1 min

da(cc)=dp*(rho_p/rho_0)^0.5; % For spheres

Mdep(cc)=pi()/6*N*rho_p*dp^3*Vm*DF(cc);

dp1(cc)=dp;

cc=cc+1;

 end


% Create figure

figure1 = figure;
```

```
% Create axes

axes1 = axes('Parent',figure1,'YMinorTick','on',...

'XScale','log',...

'XMinorTick','on',...

'PlotBoxAspectRatio',[1 1 1],...

'FontName','Arial',...

'FontSize',14);

box(axes1,'on');

hold(axes1,'all');

% Plots

semilogx(dp1,DFha,'-',dp1,DFtb','-.',dp1,DFal,'--
',dp1,DF,':','LineWidth',2,'MarkerSize',2)

xlabel('Particle diameter ( \mum )');

ylabel('Respiratory deposition fraction');

%title('Respiratory deposition, fraction vs. particle diameter');

legend(axes1,'Head      airways','Tracheobronchial      region','Alveolar
region','Total');

xlim([0.001,100]);
```

9.2.2 MATLAB code used to plot the size and mass distribution of powder

```
% Prepared by Sharman Perera

clf;

format long;

close all;


% Bin sizes use in Grimm Aerosol Spectrometer (Model 1.109).

% Bin   0.25-0.28 µm    0.28-0.30 µm    0.30-0.35 µm    0.35-0.40 µm

% 0.40-0.45 µm  0.45-0.50 µm    0.50-0.58 µm    0.58-0.65 µm

% 0.65-0.70 µm  0.70-0.80 µm    0.80-1.0 µm 1.0-1.3 µm  1.3-1.6 µm

% 1.6-2.0 µm    2.0-2.5 µm  2.5-3.0 µm  3.0-3.5 µm  3.5-4.0 µm  4.0-5.0 µm

% 5.0-6.5 µm    6.5-7.5 µm  7.5-8.5 µm  8.5-10.0 µm 10.0-12.5 µm

% 12.5-15.0 µm  15.0-17.5 µm    17.5-20.0 µm    20.0-25.0 µm

% 25.0-30.0 µm  30.0-32.0 µm    >32.0 µm


% Lower cut-off values of the bins

Dlc= [0.25  0.28  0.3  0.35   0.4  0.45   0.5  0.58   0.65  0.7 0.8 1   1.3
1.6 2   2.5 3   3.5 4   5   6.5  7.5  8.5  10  12.5...

    15  17.5    20  25  30  ];


% Hihger cut-off values of the bins

Dhc= [ 0.28  0.3  0.35    0.4   0.45    0.5  0.58   0.65    0.7  0.8  1
1.3  1.6   2   2.5   3   3.5   4   5   6.5   7.5   8.5   10  12.5    15
17.5   20  25  30  32  32];


% Bin center diameter in  µm

D=[0.265    0.29    0.325   0.375   0.425   0.475   0.54   0.615   0.675
0.75    0.9 1.15    1.45   1.8    2.25    2.75    3.25    3.75    4.5 5.75
7   8   9.25    11.25   13.75   16.25   18.75    22.5    27.5    31  32];


% Particles size distribution of 01 litre of air analysed by Grimm within 2
minutes
```

```
N_liter_2minutes=[212014.5    291907.6     597024    778472.5     675966.1
448411.5     449799.3     356406.5    169642   268890.5     307186     232546
142883   146908   134447.3    78540.8 42348.3 24047.3 23762.4 6751.1   1269.9
259.5    135.7    39.6    5.1 2    3    1    1    0    7];


% Particle size distribution in 1 cubic meter of air

N_m3=N_liter_2minutes*1000;


d_la2o3=6500 % Density of La2O3 in kg/m^3


% Mass distribution of particle in 1 cubic meter o air

M_m3=[4/3*pi()*[((D*1e-6)/2).^3]*d_la2o3*1000].*N_m3


% Total mass of La2O3 dispersed in 1 cubic meter of air = sum(M_m3)

M_m3_total=sum(M_m3);


% Particle distribution in 1g of powder=(N_m3/M_m3_total)*1

N_1g=N_m3/M_m3_total*1;


%   Particle distribution on plate = N_1g*Mass of powder on plate

%   Total mass of powder dispersed in 01 litre of air


% Mass of La2O3 on plate calculations

%   Mass of La2O3 on plate was calculated to be 120 mg

M_onplate = 120 % units mg

M_onplate = 120*1e-3  % converts to g


Np_onplate=N_1g*(M_onplate);


%              plots

% Bar graph showing number of particles on plate

    figure1 = figure (1);

nn=length(D); % Distribution control
```

```
    % Create axes
axes1 = axes('Parent',figure1,'YScale','log','YMinorTick','on',...
'XMinorTick','on',...
'PlotBoxAspectRatio',[1 1 1],...
'FontName','Arial',...
'FontSize',14);
box(axes1,'on');
hold(axes1,'all');

bar(D(1:nn),Np_onplate(1:nn))%  % Bar graph for diameter frequency
xlabel('Particle diameter ( \mum )');
ylabel('Number of particle on a plate');
%  title('Histogram of frequency versus particle size');

% Calculating cumulative mass fraction for frequency plots
Np=Np_onplate;
D=D(1:nn);
Np=Np(1:nn);
M_on_plate=[4/3*pi()*[((D*1e-6)/2).^3]*d_la2o3*1000].*Np

M_on_plate_sum=sum(M_on_plate);                   % Total mass of particles
on the plate
M_on_plate_frac=M_on_plate/M_on_plate_sum; % Mass distribution of particles
on plate

    figure2 = figure (2);
axes1 = axes('Parent',figure2,'YMinorTick','on',...
'XMinorTick','on',...
'PlotBoxAspectRatio',[1 1 1],...
'FontName','Arial',...
'FontSize',14);
box(axes1,'on');
hold(axes1,'all');
```

```
bar(D(1:nn),M_on_plate_frac(1:nn))%  % Bar graph for mass fraction of
xlabel('Particle diameter ( \mum )');
ylabel('Mass fraction of particle on the plate ');
% title('Weibull curve of Mass fraction vs diameter in micro meter');


%    fit this model y = c * (x/a)^{(b-1)} * exp(-(x/a)^b)%%
%   is defined with three parameters: the first scales the
%   curve along the horizontal axis, the second defines the
%   shape of the curve, and the third scales the curve along
%   the vertical axis. Notice that while this curve has almost
%   the same form as the Weibull probability density function,
%   it is not a density because it includes the parameter c, which
%   is necessary to allow the curve's height to adjust to data.
%   We can fit the Weibull model using nonlinear least squares.
%    Reference - MATLAB HELP " Curve Fitting and Distribution Fitting "
%   Matlab 7.10
time=(D(1:nn));
conc=M_on_plate_frac(1:nn);
modelFun =  @(p,x) p(3) .* (x ./ p(1)).^(p(2)-1) .* exp(-(x ./ p(1)).^p(2));
%modelFun =  @(p,x)  exp(-(x ./ p(1)).^p(2));
startingVals = [10 2 5];
coefEsts = nlinfit(time, conc, modelFun, startingVals)
xgrid = linspace(0,D(nn),100);
line(xgrid, modelFun(coefEsts, xgrid), 'Color','r');
WeibullF=modelFun(coefEsts, xgrid);
a=coefEsts(1)
b=coefEsts(2)
c=coefEsts(3)
a_s=num2str(a);
b_s=num2str(b);
```

```
c_s=num2str(c);

b_s_1=b-1;

b_s_1=num2str(b_s_1);

M_on_plate_sum_s=num2str(M_on_plate_sum);

format short

ss1=['MF  =',  c_s,'  *  (d_p  /  ',a_s,')^{',b_s_1,'}  *  exp[-(d_p  /
',a_s,').^{',b_s,'}]'];

ss2=['Total mass = ', M_on_plate_sum*1000, 'mg'];

text(8,.115,'\leftarrow                                                Weibull
model','FontSize',12,'FontName','Arial','FontAngle','italic')

text(8,0.1,ss1,'FontSize',10,'FontName','Arial');

text(10,0.05,ss2,'FontSize',12,'FontName','Arial','FontAngle','italic');

text(10,0.01,'Density          of          La_2O_3          =          6510
kg/m^3','FontSize',12,'FontName','Arial','FontAngle','italic');


%legend('Mass fraction bar graph',' y = c_s * (x/a_s)^{(b_s-1)} * exp(-
(x/a_s)^b_s');

% mode - The most frequent size, or the diameter associated with the highest
point on the frequency function curve.

mode=interp1([ M_on_plate_frac]',[D(1:nn)]',max( M_on_plate_frac))

line([mode,mode],[0,max(WeibullF)],'Color','b','LineWidth',1);

ssmo=['Mode = ', num2str(mode), '\mum'];

text(mode+.1,0.1,ssmo,'FontSize',12,'FontName','Arial','FontAngle','italic
');



 % Cumulative distribution curve

 % Retaining fraction calculations

for ii=1:length(D(1:nn))+1

if ii==1;

M_r_f(ii)=0;

    else

M_r_f(ii)=M_r_f(ii-1)+M_on_plate_frac(ii-1);

    end

end
```

```
 % Create figure

figure3 = figure (3);

% Create axes

axes1 = axes('Parent',figure3,'YMinorTick','on',...

'XMinorTick','on',...

'PlotBoxAspectRatio',[1 1 1],...

'FontName','Arial',...

'FontSize',14);

box(axes1,'on');

hold(axes1,'all');

plot([0,D(1:nn)],[M_r_f(1:nn+1)],'o-')%  % Bar graph for diameter frequency


xlabel('Particle diameter ( \mum )');

ylabel('Cumulative mass fraction');

% title('Cumulative distributing curve');

           hold on

% mean - Diameter corresponding to a cumulative fraction of 0.5

mean=interp1q([M_r_f(1:nn+1)]',[0,D(1:nn)]',0.5)


line([mean,0],[0.5,0.5],'Color','r','LineWidth',1);line([mean,mean],[0,0.5
],'Color','r','LineWidth',1);

ssm=['Mean = ', num2str(mean), '\mum'];

text(mean+.1,0.03,ssm,'FontSize',12,'FontName','Arial','FontAngle','italic
');


    %Diameter calculations


Da=[0.265    0.29     0.325    0.375    0.425    0.475    0.54     0.615 0.675
0.75    0.9 1.15    1.45    1.8 2.25    2.75   3.25  3.75    4.5 5.75    7
8   9.25    11.25   13.75   16.25   18.75   22.5    27.5    31  32]


Np_onplate=[587099577.4  808335413.9  1653247953   2155705746   1871850329
.1241717912    1245560935   986942429     469763844     744597652 850643568
643954344    395664207    406810028    372304503    217491117    117268720
```

```
66590538    65801608    18694797 3516541   718594   375773   109658   14123
5538  8307   2769   2769   0   19384]


N=sum(Np_onplate(1:nn))

%Arithmetic average, or count mean diameter =sum(N*d/n)

dacm=sum((Np_onplate(1:nn)).*(D(1:nn)))/N

           mean

           mode

% Diameter of average surface = sqrt(sum(n*d^2)/N)

das=sqrt(sum((Np_onplate(1:nn)).*((D(1:nn))).^2)/N)

% Diameter of average volume = (sum(nd^3)/N)^1/3

dav=(sum((Np_onplate(1:nn)).*(D(1:nn)).^3)/N)^(1/3)

% Length mean diameter = sum(n*d^2)/sum(n*d)

dlm=sum((Np_onplate(1:nn)).*(D(1:nn)).^2)/sum((Np_onplate(1:nn)).*(D(1:nn)
))

% Surface mean diameter =sum(n*d^3)/sum(n*d^2)

dsm=sum((Np_onplate(1:nn)).*(D(1:nn)).^3)/sum((Np_onplate(1:nn)).*(D(1:nn)
).^2)

           % Volume mean diameter

dvm=sum((Np_onplate(1:nn)).*[(D(1:nn)).^4])/sum((Np_onplate(1:nn)).*[(D(1:
nn)).^3])
```

9.2.3 MATLAB code used to generate Weibull distributions to resuspension factors calculated using CFD and experimental methods at Grimm locations

```
% Prepared by Sharman Perera
clf;
format long;
close all;

% Bin sizes use in Grimm Aerosol Spectrometer (Model 1.109).
% Bin   0.25-0.28 µm    0.28-0.30 µm    0.30-0.35 µm    0.35-0.40 µm
% 0.40-0.45 µm  0.45-0.50 µm    0.50-0.58 µm    0.58-0.65 µm
% 0.65-0.70 µm  0.70-0.80 µm    0.80-1.0 µm 1.0-1.3 µm  1.3-1.6 µm
% 1.6-2.0 µm    2.0-2.5 µm  2.5-3.0 µm  3.0-3.5 µm  3.5-4.0 µm  4.0-5.0 µm
% 5.0-6.5 µm    6.5-7.5 µm  7.5-8.5 µm  8.5-10.0 µm 10.0-12.5 µm
% 12.5-15.0 µm  15.0-17.5 µm    17.5-20.0 µm    20.0-25.0 µm
% 25.0-30.0 µm  30.0-32.0 µm    >32.0 µm

% Lower cut-off values of the bins
Dlc= [0.25  0.28  0.3  0.35   0.4  0.45   0.5  0.58   0.65  0.7 0.8 1   1.3
1.6 2   2.5 3   3.5 4   5   6.5  7.5  8.5  10  12.5...
    15  17.5    20  25  30  ];

% Hihger cut-off values of the bins
Dhc= [ 0.28  0.3  0.35    0.4   0.45    0.5  0.58   0.65    0.7  0.8  1
1.3  1.6   2   2.5   3   3.5   4   5   6.5   7.5   8.5   10  12.5    15
17.5   20  25  30  32  32];

% Bin center diameter in  µm
D=[0.265    0.29    0.325   0.375   0.425   0.475   0.54   0.615   0.675
0.75    0.9 1.15    1.45   1.8    2.25    2.75    3.25    3.75    4.5 5.75
7   8   9.25    11.25   13.75   16.25   18.75    22.5    27.5    31  32];
```

```
% Particles size distribution of 01 litre of air analysed by Grimm within 2
minutes

N_liter_2minutes=[212014.5    291907.6     597024    778472.5     675966.1
448411.5     449799.3     356406.5    169642   268890.5     307186     232546
142883   146908   134447.3    78540.8 42348.3 24047.3 23762.4 6751.1  1269.9
259.5   135.7   39.6    5.1 2   3   1   1   0   7];


% Particle size distribution in 1 cubic meter of air

N_m3=N_liter_2minutes*1000;


d_la2o3=6510 % Density of La2O3 in kg/m^3


% Mass distribution of particle in 1 cubic meter o air

M_m3=[4/3*pi()*[((D*1e-6)/2).^3]*d_la2o3*1000].*N_m3


% Total mass of La2O3 dispersed in 1 cubic meter of air = sum(M_m3)

M_m3_total=sum(M_m3);


% Particle distribution in 1g of powder=(N_m3/M_m3_total)*1

N_1g=N_m3/M_m3_total*1;


%   Particle distribution on plate = N_1g*Mass of powder on plate

%   Total mass of powder dispersed in 01 litre of air


% Mass of La2O3 on plate calculations

%   Mass of La2O3 on plate was calculated to be 120 mg

M_onplate = 120 % units mg

M_onplate = 120*1e-3  % converts to g


Np_onplate=N_1g*(M_onplate);


%              plots

% Bar graph showing number of particles on plate
```

```
    figure1 = figure (1);
nn=length(D); % Distribution control
    % Create axes
axes1 = axes('Parent',figure1,'YScale','log','YMinorTick','on',...
'XMinorTick','on',...
'PlotBoxAspectRatio',[1 1 1],...
'FontName','Arial',...
'FontSize',14);
box(axes1,'on');
hold(axes1,'all');

bar(D(1:nn),Np_onplate(1:nn))%  % Bar graph for diameter frequency
xlabel('Particle diameter ( \mum )');
ylabel('Number of particle on a plate');
%  title('Histogram of frequency versus particle size');

% Calculating cumulative mass fraction for frequency plots
Np=Np_onplate;
D=D(1:nn);
Np=Np(1:nn);
M_on_plate=[4/3*pi()*[((D*1e-6)/2).^3]*d_la2o3*1000].*Np

M_on_plate_sum=sum(M_on_plate);                    % Total mass of particles
on the plate
M_on_plate_frac=M_on_plate/M_on_plate_sum; % Mass distribution of particles
on plate

    figure2 = figure (2);
axes1 = axes('Parent',figure2,'YMinorTick','on',...
'XMinorTick','on',...
'PlotBoxAspectRatio',[1 1 1],...
'FontName','Arial',...
'FontSize',14);
```

```
box(axes1,'on');
hold(axes1,'all');

bar(D(1:nn),M_on_plate_frac(1:nn))%  % Bar graph for mass fraction of
xlabel('Particle diameter ( \mum )');
ylabel('Mass fraction of particle on the plate ');
% title('Weibull curve of Mass fraction vs diameter in micro meter');


%    fit this model y = c * (x/a)^{(b-1)} * exp(-(x/a)^b)%%
%   is defined with three parameters: the first scales the
%   curve along the horizontal axis, the second defines the
%   shape of the curve, and the third scales the curve along
%   the vertical axis. Notice that while this curve has almost
%   the same form as the Weibull probability density function,
%   it is not a density because it includes the parameter c, which
%   is necessary to allow the curve's height to adjust to data.
%   We can fit the Weibull model using nonlinear least squares.
%    Reference - MATLAB HELP " Curve Fitting and Distribution Fitting "
%   Matlab 7.10
time=(D(1:nn));
conc=M_on_plate_frac(1:nn);
modelFun =  @(p,x) p(3) .* (x ./ p(1)).^(p(2)-1) .* exp(-(x ./ p(1)).^p(2));
%modelFun =  @(p,x)  exp(-(x ./ p(1)).^p(2));
startingVals = [10 2 5];
coefEsts = nlinfit(time, conc, modelFun, startingVals)
xgrid = linspace(0,D(nn),100);
line(xgrid, modelFun(coefEsts, xgrid), 'Color','r');
WeibullF=modelFun(coefEsts, xgrid);
a=coefEsts(1)
b=coefEsts(2)
c=coefEsts(3)
```

```
a_s=num2str(a);

b_s=num2str(b);

c_s=num2str(c);

b_s_1=b-1;

b_s_1=num2str(b_s_1);

M_on_plate_sum_s=num2str(M_on_plate_sum);

format short

ss1=['MF  =',  c_s,'  *  (d_p  /  ',a_s,')^{',b_s_1,'}  *  exp[-(d_p  /
',a_s,').^{',b_s,'}]'];

ss2=['Total mass = ', M_on_plate_sum*1000, 'mg'];

text(8,.115,'\leftarrow                                                Weibull
model','FontSize',12,'FontName','Arial','FontAngle','italic')

text(8,0.1,ss1,'FontSize',10,'FontName','Arial');

text(10,0.05,ss2,'FontSize',12,'FontName','Arial','FontAngle','italic');

text(10,0.01,'Density          of          La_2O_3          =          6510
kg/m^3','FontSize',12,'FontName','Arial','FontAngle','italic');


%legend('Mass fraction bar graph',' y = c_s * (x/a_s)^{(b_s-1)} * exp(-
(x/a_s)^b_s');

% mode - The most frequent size, or the diameter associated with the highest
point on the frequency function curve.

mode=interp1([ M_on_plate_frac]',[D(1:nn)]',max( M_on_plate_frac))

line([mode,mode],[0,max(WeibullF)],'Color','b','LineWidth',1);

ssmo=['Mode = ', num2str(mode), '\mum'];

text(mode+.1,0.1,ssmo,'FontSize',12,'FontName','Arial','FontAngle','italic
');



 % Cumulative distribution curve

 % Retaining fraction calculations

for ii=1:length(D(1:nn))+1

if ii==1;

M_r_f(ii)=0;

    else

M_r_f(ii)=M_r_f(ii-1)+M_on_plate_frac(ii-1);
```

```
    end
end
 % Create figure
figure3 = figure (3);
% Create axes
axes1 = axes('Parent',figure3,'YMinorTick','on',...
'XMinorTick','on',...
'PlotBoxAspectRatio',[1 1 1],...
'FontName','Arial',...
'FontSize',14);
box(axes1,'on');
hold(axes1,'all');
plot([0,D(1:nn)],[M_r_f(1:nn+1)],'o-')%  % Bar graph for diameter frequency


xlabel('Particle diameter ( \mum )');
ylabel('Cumulative mass fraction');
% title('Cumulative distributing curve');
           hold on
% mean - Diameter corresponding to a cumulative fraction of 0.5
mean=interp1q([M_r_f(1:nn+1)]',[0,D(1:nn)]',0.5)


line([mean,0],[0.5,0.5],'Color','r','LineWidth',1);line([mean,mean],[0,0.5
],'Color','r','LineWidth',1);
ssm=['Mean = ', num2str(mean), '\mum'];
text(mean+.1,0.03,ssm,'FontSize',12,'FontName','Arial','FontAngle','italic
');


    %Diameter calculations


Da=[0.265    0.29     0.325    0.375    0.425    0.475    0.54     0.615 0.675
0.75    0.9 1.15    1.45    1.8 2.25    2.75   3.25  3.75    4.5 5.75    7
8   9.25    11.25   13.75   16.25   18.75   22.5    27.5    31  32]
```

```
Np_onplate=[587099577.4  808335413.9  1653247953   2155705746   1871850329
.1241717912    1245560935   986942429     469763844     744597652 850643568
643954344    395664207    406810028    372304503    217491117    117268720
66590538    65801608    18694797 3516541   718594   375773   109658   14123
5538  8307   2769   2769   0   19384]


N=sum(Np_onplate(1:nn))

%Arithmetic average, or count mean diameter =sum(N*d/n)

dacm=sum((Np_onplate(1:nn)).*(D(1:nn)))/N

           mean

           mode

% Diameter of average surface = sqrt(sum(n*d^2)/N)

das=sqrt(sum((Np_onplate(1:nn)).*((D(1:nn))).^2)/N)

% Diameter of average volume = (sum(nd^3)/N)^1/3

dav=(sum((Np_onplate(1:nn)).*(D(1:nn)).^3)/N)^(1/3)

% Length mean diameter = sum(n*d^2)/sum(n*d)

dlm=sum((Np_onplate(1:nn)).*(D(1:nn)).^2)/sum((Np_onplate(1:nn)).*(D(1:nn)
))

% Surface mean diameter =sum(n*d^3)/sum(n*d^2)

dsm=sum((Np_onplate(1:nn)).*(D(1:nn)).^3)/sum((Np_onplate(1:nn)).*(D(1:nn)
).^2)

           % Volume mean diameter

dvm=sum((Np_onplate(1:nn)).*[(D(1:nn)).^4])/sum((Np_onplate(1:nn)).*[(D(1:
nn)).^3])
```

9.2.4 MATLAB code used to generate Rosin Rammler Distribution for both Malvern and Grim (Brezani, 2011)

```
% Malvern SprayTech

d_m=[0.631  0.736   0.858   1   1.17    1.36    1.58    1.85    2.15    2.51
2.93    3.41    3.98    4.64    5.41    6.31    7.36    8.58    10  11.66
13.59   15.85   18.48   21.54   25.12   29.29   34.15   39.81   46.42   54.12
63.1    73.56   85.77   100];

Rd_m=[99.56 98.24   95.88   92.38   87.72   81.95   75.22   67.75   59.85
51.85   44.12   37  30.76   25.56   21.46   18.43   16.34   14.96   13.99
13.11   12.05   10.65   8.95    7.09    5.28    3.68    2.44    1.56    0.96
0.56    0.3 0.14    0.06    0.01];


%Grimm

%d_g=[0.265 0.29    0.325   0.375   0.425   0.475   0.54    0.615   0.675
0.75    0.9 1.15    1.45    1.8 2.25    2.75    3.25    3.75    4.5 5.75
7   8   9.25    11.25   13.75   16.25   50];

%Rd_g=[99   98  98  97  96  96  95  94  94  93  92  89  87  81  74  64  53
44  31  23  22  21  21  19  19  19  19];



[k_m, n_m] = RRD(d_m, Rd_m)

%[k_g, n_g] = RRD(d_g, Rd_g)


function [k, n] = RRD(d, Rd  % (Brezani, 2011)

% Rosin-Rammler Diagram plot and parameter estimation function.

% Parameters are estimated using non-linear fitting routine.

% Following equation is used:

% R(d) = 100*exp(-1*((d/k)^n))

% where:

% d - mesh sizes

% Rd - percent material retained (cumulative)

% k - size parameter

% n - uniformity parameter
```

```
% Example:
% d = [0.08 0.50 1.25 2 4 6.3 8 12.5 16 40]
% Rd = [95.61 87.71 82.45 79.78 73.28 66.98 63.21 55.4 49.91 23.95]
% [k, n] = RRD(d, Rd)
% >> k = 27.0236
% >> n = 0.5946
% Ing. Ivan Brezani
% ivan.brezani@tuke.sk
% 2011-12-21

if isempty(d)==1
error('Mesh size vector is empty. Enter some values.');
elseif isempty(Rd)==1
error('Percent material retained vector is empty. Enter some values.');
elseif length(d) ~= length(Rd)
error('Vectors are not equal length');
elseif d ~= sort(d)
error('Mesh size vector must be monotonically increasing');
elseif Rd ~= sort(Rd, 'descend')
error('Percent of material retained vector must be monotonically
decreasing');
elseif sum(d <= 0) >= 1
error('Mesh size of zero or negative values not permited');
elseif sum(Rd <= 0) >= 1
error('Zero or negative values of percent material retained not permited');
elseif sum(Rd >= 100) >= 1
error('100% material retained or higher values not permited');
elseif length(d) <= 3
error('Not enoug values for parameter estimation');
end

fit = inline('100*exp(-1*((d./fit(1)).^fit(2)))','fit','d');
```

```
fit = lsqcurvefit(fit,[10 1],d,Rd);

k = fit(1);

n = fit(2);


Y(1) = fit(1)*((-1*log(0.999))^(1/fit(2)));

Y(2) = fit(1)*((-1*log(0.0001))^(1/fit(2)));


y = -1*log10(log10(100./Rd));

semilogx(d, y, 'ro', Y, -1*log10(log10(100./[99.9 0.01])), 'b-');


% Double logarithmic Y-axis

y = [];

y = [0.01 0.1 1 5 10 20 30 40 50 60 70 75 80 85 90 92 94 96 98 99 99.5 99.8
99.9];

y = -1*log10(log10(100./y));

set(gca,'ytick', y);

set(gca,'yticklabel',{'                      ',                      '0.1',
'1','5','10','20','30','40','50','60','70',                       '75',
'80','85','90','92','94','96','98','99','99.5','99.8',' '});

set(gca,'YDir','reverse');

set(gca,'YLim', [min(y) max(y)]);



% Graph labels

xlabel('Mesh size');

ylabel('Retained on screen [%]');

title('Rosin-Rammler Diagram');

grid on;

end
```

9.2.5 MATLAB code used to generate the velocity profiles of the WIS wind chamber

```
% Prepared by Sharman Perera, MASc

% Close all the figures and run for the second time if figures appear not

% distorted

clear

clf

cla

V=    [0 6.51 6.61  6.74  6.74 6.03 0]; % Average velocity found usng Excel

Y=    [0 15   33    51    68   82   120]; % Y location of Hot-wire anemometers

Std_X=[0 0.17 0.14  0.15  0.17 0.14 0];% The standard deviation found using
Excel


figure(1)

yi=0:0.01:120; % Y values for interpolation

xi=interp1(Y,V,yi,'cubic'); % Finding corresponding x values using cubic
spline

clf


figure1 = figure(1);

% Create axes

axes1 = axes('Parent',figure1,...

'ylim',[0,8],'xlim',[0,110],...

'Position',[0.131074113856069 0.11 0.775 0.815],...

'FontSize',14,...

'FontName','Times New Roman');

xlim(axes1,[0 120]);

view(axes1,[90 -90]);

box(axes1,'off');

hold(axes1,'all');
```

```
plot(yi,xi,'LineStyle',':','Color',[1 0 0])

ylabel('Velocity (m/s)','VerticalAlignment','cap',...

'HorizontalAlignment','center',...

'FontSize',14,...

'FontName','Times New Roman');

xlabel('Location             of             hotwire             anemometer
(cm)','VerticalAlignment','bottom',...

'Rotation',90,...

'HorizontalAlignment','center',...

'FontSize',14,...

'FontName','Times New Roman');

% Create errorbar

errorbar(Y,V,Std_X,'Marker','o','LineStyle','none','Color',[0 0 0]);

hold on


% Add the text for Hot-wire anemometer (HW) and Std. deviation

for i =2:1:length(Std_X)-1

s=num2str(Std_X(i))

HWN=num2str(i)

Uu=num2str(V(i))

ss=['HW-',HWN-1 ,': U=',Uu,' (\sigma = ',s,') m/s'];

text(Y(i)+4,V(i)+.2,ss,'fontsize',10);

end

hold off


%--- Generating the plots reading data from the Excel file directly

HW=xlsread('Day1_Run4','UOIT_Active1', 'B:F');

HW1=HW(:,1);

HW5=HW(:,2);

HW4=HW(:,3);

HW3=HW(:,4);

HW2=HW(:,5);
```

```
figure2=figure(2)
X=1:length(HW3);
plot(X/60,HW3); % Change second units to minutes
xlabel('Elappsed time (min)','FontSize',18,...
'FontName','Times New Roman');
ylabel('HW-3 velocity (m/s)', 'FontSize',14,...
'FontName','Times New Roman');
ss=['U=',num2str(V(4)),' (\sigma = ',num2str(Std_X(4)),') m/s'];
text(15,5,ss,'fontsize',12);

figure3=figure(3)
% Create axes
axes3 = axes('Parent',figure3,...
'FontSize',14,...
'FontName','Times New Roman');
box(axes3,'off');
hold(axes3,'all');
X=1:length(HW1);

subplot(2,2,1), plot(X/60,HW1); % Change second units to minutes
xlabel('Elappsed time (min)','FontSize',14,...
'FontName','Times New Roman');
ylabel('HW-1 velocity (m/s)', 'FontSize',14,...
'FontName','Times New Roman');
ss=['U=',num2str(V(2)),' (\sigma = ',num2str(Std_X(2)),') m/s'];
text(15,4,ss,'fontsize',10);

subplot(2,2,2), plot(X/60,HW2);
xlabel('Elappsed time (min)','FontSize',14,...
'FontName','Times New Roman');
ylabel('HW-2 velocity (m/s)', 'FontSize',14,...
```

```
'FontName','Times New Roman');
ss=['U=',num2str(V(3)),' (\sigma = ',num2str(Std_X(3)),') m/s'];
text(15,4,ss,'fontsize',10);

subplot(2,2,3), plot(X/60,HW4);
xlabel('Elappsed time (min)','FontSize',14,...
'FontName','Times New Roman');
ylabel('HW-4 velocity (m/s)', 'FontSize',14,...
'FontName','Times New Roman');
ss=['U=',num2str(V(5)),' (\sigma = ',num2str(Std_X(5)),') m/s'];
text(15,4,ss,'fontsize',10);

subplot(2,2,4), plot(X/60,HW5);
xlabel('Elappsed time (min)','FontSize',14,...
'FontName','Times New Roman');
ylabel('HW-5 Velocity (m/s)', 'FontSize',14,...
'FontName','Times New Roman');
ss=['U=',num2str(V(6)),' (\sigma = ',num2str(Std_X(6)),') m/s'];
text(15,4,ss,'fontsize',10);

%-- From 3D to 2D fans ( Calculations for FLUENT modeling ---
VFR_fan=10000/3600 % Volume flow rate of one fan used at WIS facility is
m^3/hr
d_fan=40/100 % Diameter of the fan According to Klaus (2006) is 40 cm
A1=85*(35+70+35)+1/2*(74+140)*(120-85)% Chamber test section area in cm^2
A2=120*140-2*1/2*(70-37)*(120-85)
P=2*[sqrt((70-37)^2+(120-85)^2)+70+85+37] % Chamber perimeter in cm
L=4*A1/P % Hydraulic daimeter in cm

vis=15.11e-6      %      Kinematic      viscosity      [m^2/s]Ref      -
http://www.engineeringtoolbox.com/air-properties-d_156.html

rho_air=1.225 % Density of air at 20 deg. C [kg/m^3]
```

```
Rey_test_section=6.5260*(L/100)/vis


V_fan=VFR_fan/[pi()*(d_fan/2)^2]
V_2fan=V_fan*2


M1=VFR_fan*rho_air
M2=2*M1
```

9.2.6 MATLAB code is used to plot the Average surface roughness profile and to generate a part of the Journal file used in GAMBIT software

```
% Prepared by Sharman Perera, MASc
clear
clf
Ra=1.663;       % Arithmetic mean roughness of the deviation from the mean
line
Rz=9.17-Ra;     % The average of maximum peak to valley height-Ra
fz=3;           % Controls the number of small peaks
Rs=76;          % The distance between maximum peak to peak
Rs_small=5;     % Width of a small peak
x = 0:.1:3*Rs;
y = Rz/2*sin(2*pi*x/Rs); % Meam profile
plot(x,y,'-.r','LineWidth', 2);
hold on
y = y-Ra*sin(2*pi*(x/Rs_small)/fz);
plot(x,y,'LineWidth', 2);
grid on
xlabel('X location (\mum)')
ylabel('Y location (\mum)')
%  Generating text file for GAMBIT Journal file
```

```
z=[x;y;0*(1:length(x))];
p=1:length(x-1);
fid = fopen('gambit2.txt', 'w');
fprintf(fid,'vertex create coordinates %6.2f  %12.8f %6.2f\n' , z);
fprintf(fid,'edge create nurbs ');
fprintf(fid,'"vertex. %1d" ', p);
fprintf(fid, ' interpolate');
fclose(fid);
type gambit2.txt % Typing the text to command window
```

9.2.7 MATLAB code to generate contaminated powder location file

```
% Prepared by Sharman Perera, MASc
clear
Xs=5;           % X Start
Ys=400e-6;        % Y Start
Zs=0;           % Z Start
delX=0.025E-1;  % del X
delY=0;         % del Y
delZ=0;
Us=0;           % U start
Vs=0.1,         % V start
Ws=0;           % W start
mass_flow = 0;  % Mass flow rate
DD=1e-6*[0.265  0.290   0.325   0.375   0.425   0.475   0.540   0.615   0.675
0.750   0.900   1.150   1.450   1.800   2.250   2.750   3.250   3.750   4.500
5.750    7.000    8.000    9.250    11.250   13.750   16.250   18.750   22.500
27.500  31.000  32.000];
NB=length(DD);
NI=200;      % Number of injections
```

```
%%%%%%%% Generating file %%%%%%%%%%

count=0;

fid      =      fopen('C:\Users\100281330\Desktop\Mage\Write      Up\Final
Chapters\IniPartDist2.txt', 'w');

fprintf(fid,'( X    Y    Z    U    V    W    diameter    T    mass-flow
name )\n');

for j=1:NI;

for i = 1:NB

X =Xs+delX*j

Y =Ys+delY*j

Z =Zs+delZ*j

    U = Us;

    V = Vs;

    W = Ws;

diameter=DD(i);

    T=300;

    name=i;

ZZ=[           X;           Y;         Z;         U;          V;         W;
diameter;     T       ;mass_flow]

fprintf(fid,'(( %6.2e %6.2e %6.2e %6.2e %6.2e %6.2e %6.2e %6.2e %6.2e', ZZ)

fprintf(fid,'  injection-0:%1d )\n',j);

count=count+1

   end

  end


count %Counting total number of injected particles


fclose(fid);

%type IniPartDist2.txt % Typing the text file to the command window
```

9.2.8 MATLAB code to generate velocity profile close to the laminar sub-layer using FLUENT results and Spalding law

```
% Make sure to have the “'DataAnalysisActiveTrialsDac11_2012.xls” file in
the same directory as the Mathlab code


clear

clf

cla

k=0.41;         % von Kármán  constant

B=5.0;          % constant between 5 to 5.5

v= 1.7894e-5;   % kinematic viscosity of the air from FLUENT default( kg/m-
s)

t0=0.34577        % wall shear stress from FLUENT (pa)

dair=1.225;      % density of air from FLUENT default (kg/m^3)

ustar=sqrt(t0/dair)    % friction velocity


% semi-empirical Log Law relationship(Muralidhar & Biswas, 1999)

yy=(1:10:1000)*1e-6;    % y coordinates in (m/s)

ulog=ustar*(1/k*log(ustar*yy/v)+B);% velocity profile of turbulent BL(m/s)

figure(1)

plot(ulog,yy*1e6,'-') % convert yy in to micm

xlabel('X-velocity (m/s)','FontSize',14);

ylabel('Y location (\mum)','FontSize',14);


% Spalding’s Law of the wall (Cengel & Cimbala, 2006).

count=1;

for u=0:0.1:5

y       =       v/ustar*(u/ustar+exp(-k*B)*(exp(k*(u/ustar))-1-k*(u/ustar)-
((k*(u/ustar))^2)/2-((k*(u/ustar))^3)/6));

U(count)=u;
```

```
Y(count)=y;
count=count+1;
end
figure(2)
%plot(U,Y*1e6,'-b','LineWidth',1) % convert Y coordinates into micm



% Laminar sublayer thickness (Ibrahim, Dunn, & Qazi, 2008).
sprime=11.5*v*sqrt(t0/dair); % thickness of the LSL  (m)
T_LSL=sprime*1e6       % thickness of the LSL in micm



U_LSL_Spal=interp1(Y,U,sprime) % velocity at LSL m/s
hold on
%line([U_LSL_Spal,U_LSL_Spal],[0,T_LSL],'Marker','.','LineStyle','--')
%line([0,U_LSL_Spal],[T_LSL,T_LSL],'Marker','.','LineStyle','--')


LSLT=5*v/ustar*1e6 % thickness of Laminar Sub Layer according (Muralidhar &
Biswas, 1999)
BRT=70*v/ustar*1e6 % thickness upto Buffer Layer from floor (Muralidhar &
Biswas, 1999)


VVYY=xlsread('DataAnalysisActiveTrialsDac11_2012','FLUENTV', 'A:B');
F_V=VVYY(:,1);
F_Y=VVYY(:,2);


%hold on
plot(F_V,F_Y*1E6,'.-r','LineWidth',1)
xlabel('X-velocity ( m/s)','FontSize',14);
ylabel('Y location ( \mum)','FontSize',14);
Y_LSL_FLUENT=interp1(F_V,F_Y,U_LSL_Spal) % velocity at LSL m/s
line([U_LSL_Spal,U_LSL_Spal],[0,Y_LSL_FLUENT*1e6],'Marker','.','LineStyle'
,'--')
```

```
line([0,U_LSL_Spal],[Y_LSL_FLUENT*1e6,Y_LSL_FLUENT*1e6],'Marker','.','Line
Style','--')
```

9.2.9 MATLAB code to generate surface roughness profile

```
% Prepared by Sharman Perera, MASc

clear

clf

cla


% Surface roughness information

% Ra- universally recognized and most used parameter of roughness.

% It is the arithmetic mean of the magnitude of the deviation of the

% profile from the mean line. Also referred to as CLA (center line average)
or AA (arithmetic average).

% Rz value is the maximum peak to valley height of the profile within a

% sampling length.

% RS is mean spacing of local peaks of the profile within sampling length

Ra=1.66;        % mic m

Rz=9.18;        % mic m

Rsm=140;        % mic mm (0.14 mm)

Rs= 80;         % mic m ( 0.08 mm)

% Computational domain

XL=250;

% Create vector of x

x = [0:1:XL];

% Evaluate equations element-by-element

Yz = Rz/2*sin(6*x/Rs);

Ya = Ra/2*sin(36*x/Rs);

Yt=Yz+Ya;
```

```
% Create a new figure and turn "hold on"
plot(x,Yz,'-.r',x,Yt,'b');set(gca,'FontSize',14,'FontName',...
'Times New Roman');box off
xlabel('X-location \mum')
ylabel('Y-location \mum')
legend('Centerline profile','Surface profile')
     legend boxoff
```

9.2.10 MATLAB code to convert the FLUENT discrete phase particle information in a boundary into a simple set of arrays

```
Note: Save the filename.pd FLUENT output file to  filename.txt

function D = convertText(fileName)
inputFile = fopen(fileName);
firstRun = 1;
fileFinished = 0;

while not(feof(inputFile))
currentLine = fgetl(inputFile);
if strcmp(currentLine(1:2),'((')
        if firstRun
outText = sscanf(currentLine(3:end-2),'%e')';
            firstRun = 0;
        else
outText = [outText; sscanf(currentLine(3:end-2),'%e')'];
        end
    end
end
```

```
X=outText(:,1)'*1e6;
Y=outText(:,2)'*1e6;
Z=outText(:,3)'*1e6;
u=outText(:,4)'*1e6;
v=outText(:,5)';
w=outText(:,6)';
D=outText(:,7)'*1e6;
fclose(inputFile);
```

9.2.11 MATLAB code to graph Resuspension Factor results from files based on 2D and 3D CFD results

```
format long
clear all
cla
% read all files *
D_FS_R2_SUR=convertText('surfaceR2.txt');      % From 2D CFD -R2
D_FS_R2_AIRG1=convertText('airGrimm1R2.txt');  % From 2D CFD -R2
D_FS_R2_AIRG2=convertText('airGrimm2R2.txt');  % From 2D CFD -R2

D_LSL_R1_SUR=convertText('surfaceR1.txt');        % From 3D CFD -R1
D_LSL_R1_AIR=convertText('airR1.txt') ;           % From 3D CFD -R1

BIN=[0.27 0.29         0.33         0.38         0.43         0.48
          0.54         0.62         0.68         0.75         0.9
          1.15         1.45         1.8          2.25         2.75
          3.25         3.75         4.5          5.75         7
          8            9.25         11.25        13.75        16.25
          18.75        22.5         27.5         31           32];

% Sample the data into respective bins
N_FS_R2_SUR=hist(D_FS_R2_SUR,BIN);
```

```
N_FS_R2_AIR_G1=hist(D_FS_R2_AIRG1,BIN);
N_FS_R2_AIR_G2=hist(D_FS_R2_AIRG2,BIN);

N_LSL_R1_SUR=hist(D_LSL_R1_SUR,BIN);
N_LSL_R1_AIR=hist(D_LSL_R1_AIR,BIN);

% Calculating resuspension factors
% RF for
R_FS_R2_G1=(N_FS_R2_AIR_G1./N_FS_R2_SUR)/0.2e3;  % Normalized to 1cm
R_FS_R2_G2=(N_FS_R2_AIR_G2./N_FS_R2_SUR)/0.2e3;  % Normalized to 1cm

R_LSL_R1=N_LSL_R1_AIR./N_LSL_R1_SUR;

R_G1=R_LSL_R1.*R_FS_R2_G1;
R_G2=R_LSL_R1.*R_FS_R2_G2;

semilogy(BIN,R_FS_R2_G1,'-*',    BIN,R_FS_R2_G2,'-o',    BIN,R_LSL_R1,'-+',
BIN,R_G1, BIN,R_G2)
xlabel('Particle size (\mum)');ylabel('Resuspension factor ')
legend('RF FS Grimm 1','RF FS Grimm 2','RF LSL','RF CFD G1','RF CFD G2');
```

MATLAB code to grab data from FLUENT particle trajectory files. Note: This is the subroutine used in the code to calculate and plot particle resuspension data

```
function D = convertText(fileName)
inputFile = fopen(fileName);
firstRun = 1;
fileFinished = 0;

while not(feof(inputFile))
currentLine = fgetl(inputFile);
if strcmp(currentLine(1:2),'((')
        if firstRun
outText = sscanf(currentLine(3:end-2),'%e')';
            firstRun = 0;
        else
outText = [outText; sscanf(currentLine(3:end-2),'%e')'];
        end
    end
end
X=outText(:,1)'*1e6;
Y=outText(:,2)'*1e6;
Z=outText(:,3)'*1e6;
u=outText(:,4)'*1e6;
v=outText(:,5)';
w=outText(:,6)';
D=outText(:,7)'*1e6;
fclose(inputFile);
```

9.2.12 User Defined Function (UDF) used in FLUENT software to generate a FIXED and UDF vector field and body forces for the DMP model.

```
/************************************************************

UDF generates FIXED and UDF velocity fields for the Regional 3D CFD model
and applies forces to particles during the take-off as per the Rock ‘n’ Roll
model (Reeks and Hall 2001) and Biasi, De Los Reyes, Reeks, & De Santi
(2001).

************************************************************/


#include "udf.h"

#define Vr 0.8933



DEFINE_PROFILE(Vx_t, thread, position)

{

          real x[ND_ND]; /* this will hold the position vector */

          real XX;

          real YY;

          double time;

          face_t f;


          begin_f_loop(f, thread)

          {

                    F_CENTROID(x, f, thread);

                    XX = x[0];

                    YY = x[1];

                    time = CURRENT_TIME;

                    F_PROFILE(f, thread, position) = Vr * cos(6.5 * XX /
400E-6) * (YY / 100E-6);

          }

          end_f_loop(f, thread)

}
```

```
DEFINE_PROFILE(Vy_t, thread, position)
{
          real x[ND_ND]; /* this will hold the position vector */
          real XX;
          real YY;
          double time;
          face_t f;

          begin_f_loop(f, thread)
          {
                    F_CENTROID(x, f, thread);
                    XX = x[0];
                    YY = x[1];
                    time = CURRENT_TIME;
                    F_PROFILE(f, thread, position) = Vr * 1 / 6.5 *
sin(6.5 * XX / 400E-6) * (YY / 100E-6);
          }
          end_f_loop(f, thread)
}

DEFINE_DPM_BODY_FORCE(BF_Vmag_acceleration, p, i)
{
          real bforce;
          real V_mag;
          V_mag = NV_MAG(P_VEL(p));
          if (V_mag <= 1.0e-20)
          {
          if (i == 0) bforce = 0.0;

          else if (i == 1) bforce = -1.0 * (4.0 * M_PI * P_DIAM(p) / 2.) *
(0.016 - 0.0023 * pow((1.0E6 * P_DIAM(p) / 2.), 0.545));
                    }
```

```
        else
        bforce = 0.0;
        /*an acceleration should be returned*/
        return (bforce / P_MASS(p));

}
```

9.2.13 FLUENT User Defined Function (UDF) to generate acceleration due to adhesive body force on particles from walls based on particle minimum distance to the wall

```
/************************************************************
User Defined Function (UDF) to generate acceleration due to adhesive body
force on particles from walls based on particle minimum distance to all
walls. Note: This program calculates the distance from individual particle
to all walls during each time integration of particles and it takes a lot
computer memory.
.************************************************************/
#include "udf.h"


DEFINE_DPM_SCALAR_UPDATE(distance_to_wall, c, t, i, p)
{
    real x[ND_ND];
    real distance = C_U(cell, t);
    real min_distance = 1.0e20; // Initialize with a large value


    C_CENTROID(x, c, t);


    Thread* wall_thread;
    cell_t wall_cell;
```

```
    /* Loop through all cell threads in the domain */
    thread_loop_c(wall_thread, t->domain)
    {
        /* Loop through all cells in the current thread */
        begin_c_loop(wall_cell, wall_thread)
        {
            real wall_x[ND_ND];
            real wall_distance;

            C_CENTROID(wall_x, wall_cell, wall_thread);

            /* Calculate the Euclidean distance between the particle and
the wall cell centroid */
            wall_distance = sqrt((x[0] - wall_x[0]) * (x[0] - wall_x[0]) +
(x[1] - wall_x[1]) * (x[1] - wall_x[1]) + (x[2] - wall_x[2]) * (x[2] -
wall_x[2]));

            /* Find the minimum distance to a wall cell */
            if (wall_distance < min_distance)
                min_distance = wall_distance;
        }
        end_c_loop(wall_cell, wall_thread)
    }

    P_UDMI(p, 0) = min_distance; // Store the minimum distance as UDMI in
the particle

    return min_distance;
}

DEFINE_DPM_BODY_FORCE(body_force, p, i)
{
real min_distance = P_UDMI(p, 0); // Minimum distance to a wall (retrieved
from UDMI)
```

```
    if (min_distance > 1.0e-10)
    {
        real r = P_DIAM(p) / 2.0; // Particle radius
        real gamma = 0.56; //(Hall 1988)
        real p_exponent = 0.545; // Exponent (p) value, adjust as needed
          real r_mic = 1.0E-6 * r / radius in micro-meters

real body_force_magnitude = 4.0 * M_PI * gamma * r * (0.016 - 0.0023 *
pow(r_micm, 0.545));

        real body_force_vector[ND_ND];
NV_V(body_force_vector, =, 0.0); // Initialize the force vector to zero

        /* Set the body force components (e.g., in the -Z direction) */
        body_force_vector[2] = -body_force_magnitude;

        /* Assign the computed force vector to the particle */
        NV_DS(P_F_BODY(p), =, body_force_vector);

        return 1;
    }
    else
        /* No force applied if the minimum distance is below 1E-10 meters
*/
        NV_V(P_F_BODY(p), =, 0.0);

return 0;
}
```

9.2.14 MATLAB code to grab data from FLUENT particle trajectory files and to plot Global and Regional CFD resuspension fractions and factors

```
format long
clear all
clearvars
cla
%
BIN=[0.27   0.29    0.33    0.38    0.43    0.48    0.54    0.62    0.68    0.75
0.9 1.15    1.45    1.8 2.25    2.75    3.25    3.75    4.5 5.75    7   8   9
10 11 12 13 14 15 16 17 18 19 20 21 22 23 24 25 26 27 28 29 30 31 32.5];


%%%%%%%%%%%%%3D Regional CFD - Both UDF and FIXD boundary Mirometer model%%%%%%
Regional_FIXED_air=convertText('Regional_FIXED_air.txt');
Regional_UDF_air=convertText('Regional_UDF_air.txt');
Regional_floor=convertText('Regional_floor.txt');

Numb_Regional_FIXED_air=hist(Regional_FIXED_air,BIN);
Numb_Regional_UDF_air=hist(Regional_UDF_air,BIN);
Numb_Regional_floor=hist(Regional_floor,BIN);

RFR_Regional_FIXED_air=Numb_Regional_FIXED_air./Numb_Regional_floor;
RFR_Regional_UDF_air=Numb_Regional_UDF_air./Numb_Regional_floor;
RFR_Regional_Combined=(RFR_Regional_FIXED_air+RFR_Regional_UDF_air)/2.0;


figure(1);
plot(BIN,RFR_Regional_FIXED_air,'*');xlabel('Particle                    size
(\mum)');ylabel('Regional resuspension fraction for FIXED')
set(gca, 'YScale', 'log')
figure(2);
plot(BIN,RFR_Regional_UDF_air,'*');xlabel('Particle                    size
(\mum)');ylabel('Regional resuspension fraction for UDF ')
set(gca, 'YScale', 'log')
figure(3);
plot(BIN,RFR_Regional_Combined,'*');xlabel('Particle                    size
(\mum)');ylabel('Regional resuspension fraction for COMBINED ')
```

```
set(gca, 'YScale', 'log')

%%%%%%%%%%%%%3D Global CFD - BiG WIS facility domain %%%%%%%%%%%%%%%%%%%%%
Global_G1=convertText('Global_G1_3D_100bins.txt');
Global_G2=convertText('Global_G2_3D_100bins.txt');
Global_floor=convertText('Global_floor_3D_100bins.txt');

Numb_Global_G1=hist(Global_G1,BIN);
Numb_Global_G2=hist(Global_G2,BIN);
Numb_Global_floor=hist(Global_floor,BIN);

RF_Global_G1_3D=Numb_Global_G1./Numb_Global_floor;
RF_Global_G2_3D=Numb_Global_G2./Numb_Global_floor;

Tmax_G1_2D=177.98; % Particle tracking time for last particle hitting Grimm 1
(sec.)
Tmax_G2_2D=179.06; % Particle tracking time for last particle hitting Grimm 2
(sec.)
V_FR_2D=6.395082449; % Volume flow rate through Grimm 1 and 2(m^3/sec.)
A_FL=0.5;            % Flow area of release (m^2)

RF_3DCFD_GLOBAL_G1_32=(RF_Global_G1_3D/(V_FR_2D*Tmax_G1_2D))/(1/A_FL);
RF_3DCFD_GLOBAL_G2_32=(RF_Global_G2_3D/(V_FR_2D*Tmax_G2_2D))/(1/A_FL);

figure(4);
plot(BIN,RF_3DCFD_GLOBAL_G1_32,'*');xlabel('Particle                    size
(\mum)');ylabel('Global resuspension factor for Particle Sizer 1 (1/m)')
set(gca, 'YScale', 'log')
figure(5);
plot(BIN,RF_3DCFD_GLOBAL_G2_32,'*');xlabel('Particle                    size
(\mum)');ylabel('Global resuspension factor for Particle Sizer 2 (1/m) ')
set(gca, 'YScale', 'log')

%%%%%%%%%%%%% Combined Regional and Global RF %%%%%%

RF_3D_G1=RFR_Regional_Combined.*RF_3DCFD_GLOBAL_G1_32;
RF_3D_G2=RFR_Regional_Combined.*RF_3DCFD_GLOBAL_G2_32;
```

```
figure(6);
plot(BIN,RF_3D_G1,'*');xlabel('Particle    size    (\mum)');ylabel('3D    CFD
Resuspension factor for Particle Sizer 1 (1/m)')
set(gca, 'YScale', 'log')
figure(7);
plot(BIN,RF_3D_G2,'*');xlabel('Particle    size    (\mum)');ylabel('3D    CFD
Resuspension factor for Particle Sizer 2 (1/m)')
set(gca, 'YScale', 'log')
```